Kai Wang

Modelling and dynamic analysis of a semi-submersible floating vertical axis wind turbine

Kai Wang

Doctoral Thesis

NTNU
Norwegian University of
Science and Technology
Faculty of Engineering
Science and Technology
Department of Marine
Technology

NTNU – Trondheim
Norwegian University of
Science and Technology

NTNU

Kai Wang

Modelling and dynamic analysis of a semi-submersible floating vertical axis wind turbine

Thesis for the degree of Philosophiae Doctor

Trondheim, January 2015

Norwegian University of Science and Technology
Faculty of Engineering Science and Technology
Department of Marine Technology

NTNU – Trondheim
Norwegian University of
Science and Technology

Dedicated to my dear parents and my beloved wife

Abstract

Wind turbines are mainly classified into horizontal axis wind turbines (HAWTs) and vertical axis wind turbines (VAWTs) based on different orientation of their axis of rotation. Ever-increasing demand for energy boosts the application of the wind turbines in the deep water. The applications of HAWTs in deep water using different floating support structures have led to an increasing and versatile research due to their commercial success. However, the application of the VAWTs in the offshore wind industry also has some potential due to its economical installation and maintenance. More and more efforts have been invested in developing floating vertical axis wind turbines (FVAWTs), but the research on the FVAWTs is still at an early stage.

Although different concepts of the FVAWTs were proposed based on a combination of a rotor and a floater, an optimized design is still an open question. The rotor covers straight-blade rotor, Darrieus curved-blade type rotor and helical-blade rotor while a floater could be a spar, semi-submersible or tension leg platform (TLP). To evaluate a FVAWT, a simulation tool is needed to perform time domain numerical simulations. The simulation tool should have the capability to calculate aerodynamic loads on the rotor, hydrodynamic loads on the floater and structural dynamics of the rotor, and include a controller. Based on the calculated dynamic response, a response analysis is carried out to better understand the response characteristics of a FVAWT as a basis for design and safety criteria according to serviceability. The objective of this thesis has been the development of a coupled method for integrated dynamic analysis of the FVAWTs and application in a systematic study of a Darrieus rotor on a semi-submersible floating support structure.

The aerodynamic analysis of a VAWT differs from that of a HAWT, especially when the VAWT is mounted on a floater. Thus, the aerodynamics of a VAWT is first addressed and a model improvement for evaluating the effect of tower tilting on the aerodynamics of a VAWT is performed. This improved model is validated against experimental data collected for an H-Darrieus wind turbine in skewed flow conditions. Based on the assumption that the velocity component parallel to the rotor shaft is small in the downstream part of the rotor, the effect of tower tilting is quantified with respect to power, rotor torque, thrust force and the normal force and tangential force coefficients on the blades.

Secondly, a novel 5 MW FVAWT concept, based on a Darrieus rotor on a semi-submersible support structure, is proposed. An aero-hydro-servo-elastic tool Simo-Riflex-DMS is developed for modeling the dynamics of the FVAWT and validated. This integrated dynamic model takes into account the wind inflow, aerodynamics, hydrodynamics, structural dynamics (wind turbine, floating platform and the mooring lines) and a generator controller.

Thirdly, the response characteristics of the 5 MW FVAWT are studied based on statistical analysis and spectral analysis of the response. The response characteristics of the FVAWT under steady wind condition and those under turbulent wind condition are compared to investigate the effect of the turbulent wind. The advantage in reducing the 2P effect on the FVAWT is identified by comparing with the equivalent land-based wind turbine. Furthermore, by comparing the FVAWT with a rigid FVAWT, the aspect of rigid versus flexible rotor is quantified, and thus the effect of the modeling method of the rotor on the responses is observed. Besides the normal operating condition, the global motions and structural responses of the FVAWT as a function of azimuthal angle are studied for the parked condition. To identify the effect of wind-wave misalignment on the platform motion, structural response and mooring lines, the dynamic response analysis of the FVAWT in selected misaligned wind and wave conditions are conducted.

Moreover, it is also of great interest to compare the performance of a FVAWT with a FHAWT. A comparative study of the studied FVAWT and a FHAWT with the 5 MW NREL reference wind turbine mounted on the same semi-submersible is carried out. A set of time domain simulations with different conditions, i.e., the decay tests, wave only conditions, wind only conditions and the combined wind and wave conditions, are conducted. The dynamic responses of the FVAWT and the FHAWT, such as the global motions of the floater in six DOFs, the bending moment of the bottom of the tower and the tension at the fairleads of the mooring lines, are compared based on statistical results and power spectra.

Lastly, a novel hydrodynamic brake installed in the FVAWT is proposed in this thesis. The FVAWTs with fixed-pitch blades experience large aerodynamic loads in high wind speed condition or in stormy weather. The blades may be deformed or broken, and the tower can collapse in more severe cases. Thus, initiating an emergency shutdown is one of the most important concerns for the FVAWTs. Therefore, a dynamic response analysis of the FVAWT with this installed hydrodynamic brake is studied for possible use in connection with emergency shutdown event. The effects of the hydrodynamic brake on the platform motions and structural loads under normal operating conditions and during the emergency shutdown events are evaluated. The use of both the hydrodynamic brake and mechanical brake is also investigated.

Acknowledgements

First of all, my deepest gratitude goes first and foremost to my supervisor Professor Torgeir Moan for giving me the chance to pursue my Ph.D. degree in the Centre for Ships and Ocean Structures (CeSOS) at NTNU and his illuminating instruction for my Ph.D study. During the past four years, Prof. Moan helped me to overcome a number of scientific challenges and encouraged me to become an independent researcher. I have benefitted from the active research atmosphere he creates at CeSOS and his insight into the research through each discussion. I was also impressed by his personal characters, such as working hard, having solid fundamental theories, being good at capturing new information and research trend, being patient and being strict to students. It is my great pleasure to be one of his students.

I would also like to thank my co-supervisor Professor Martin O.L. Hansen from Technical University of Denmark (DTU) for his instruction, encouragement and proofreading of all papers and the thesis. He did me a great favor in my research work. He would always check my research process and have discussion with me when he came to CeSOS. Furthermore, he has been keeping contact with me through email when he was at DTU.

Many other people have contributed to my work through discussions. I have to give my most thanks to Chenyu Luan for numerous discussions and a pleasant collaboration. I would like to thank Dr. Erin E. Bachynski for giving advice on the compiling of dynamic link library between the aerodynamic code and Simo/Riflex. Many thanks also got to Dr. Karl Merz and Dr. Harald Svendsen from SINTEF Energy Research for several discussions. I also would like to acknowledge the discussion, instruction and comment from Adjunct Associate Professor Zhen Gao. I am also grateful for my friends and colleagues at NTNU: Muk Chen Ong, Yihan Xing, Zhiyu Jiang, Xiaopeng Wu, Lin Li, Qin Zhang, Biao Su, Peng Li, Zhao He, to name a few. They are always helpful. Furthermore, I would like to thank Sigrid B. Wold and Annika Bremvåg for their kind helps.

I also wish to acknowledge the financial support from the Research Council of Norway through the Norwegian Research Centre for Offshore Wind Technology (NOWITECH) and CeSOS at the Department of Marine Technology, Norwegian University of Science and Technology (NTNU), Trondheim, Norway.

Finally, I want to give my special thanks to my parents in China and my wife, Xinyi Liu. Their encouragement and love have been the main support to keep me going over the years. Without them, I may never have gotten to where I am today.

Abbreviations

AC	Actuator Cylinder flow
BEM	Blade Element Momentum
BL	Beddoes-Leishman
CeSOS	Centre for Ships and Ocean Structures
CFD	Computational Fluid Dynamics
COB	Center of Buoyancy
DLL	Dynamic Link Library
DMS	Double Multiple-Streamtube model
DNV	Det Norske Veritas
DS	Dynamic Stall
DTU	Technical University of Denmark
EU	European Union
EWEA	European Wind Energy Association
FEM	Finite Element Method
FHAWT	Floating Horizontal Axis Wind Turbine
FP7	7th Framework Programme
FVAWT	Floating Vertical Axis Wind Turbine
GDW	Generalized Dynamic Wake
GWEC	Global Wind Energy Council
HAWT	Horizontal Axis Wind Turbine
IEA	International Energy Agency
IEC	International Electrotechnical Commission
JONSWAP	Joint North Sea Wave Project
LC	Load Case
MIT	Massachusetts Institute of Technology
MW	Megawatt
NREL	National Renewable Energy Laboratory
NTM	Normal turbulence model
NWP	Normal wind profile model
OC3	Offshore code comparison collaboration within IEA Wind Task 23
OC4	Offshore code comparison collaboration Within IEA Wind Task 30
OWENS	Offshore Wind ENergy Simulation
PIV	Particle Image Velocimetry
RANS	Reynolds-Averaged Navier-Stokes
SNL	Sandia National Laboratories
TDHMILL	Thrust-Dynamic-Horizontal-Mill
TLP	Tension Leg Platform
VAWT	Vertical Axis Wind Turbine
VTM	Vorticity Transport Model

List of appended papers

This thesis consists of an introductory part, five papers (three journal papers and two conference papers)

The following five papers are reported in Appendix A:

Paper 1:
A method for modeling of floating vertical axis wind turbine
Kai Wang, Torgeir Moan and Martin O.L. Hansen
Published in Proceedings of the 32nd International Conference on Ocean, Offshore and Arctic Engineering, Nantes, France, June 2013

Paper 2:
Model improvements for evaluating the effect of tower tilting on the aerodynamics of a vertical axis wind turbine
Kai Wang, Martin O.L. Hansen and Torgeir Moan
Published in Wind Energy, Vol. 18 (2015), pp. 91-110.

Paper 3:
Dynamic analysis of a floating vertical axis wind turbine under emergency shutdown using hydrodynamic brake
Kai Wang, Martin O.L. Hansen and Torgeir Moan
Published in Energy Procedia, Vol.53 (2014), pp. 56-69.

Paper 4:
Comparative study of a FVAWT and a FHAWT with a semi-submersible floater
Kai Wang, Luan Chenyu, Torgeir Moan and Martin O.L. Hansen
Proceedings of the Twenty-fouth (2014) International Offshore and Polar Engineering Conference, Busan, Korea, June 15-20, 2014

Paper 5:
Stochastic dynamic response analysis of a floating vertical axis wind turbine with a semi-submersible floater
Kai Wang, Torgeir Moan and Martin O.L. Hansen
Submitted for review in Wind Energy

Declaration of Authorship

Regarding the authorship of the five papers and my contributions, I have been the first author of all these papers and I was responsible for establishing the models, performing the calculations, providing the results and writing the papers under the supervisions of Professor Torgeir Moan and Professor Martin O.L. Hansen. They made helpful corrections and comments on these papers. Martin O.L. Hansen recommend me submit the *paper 1* to Wind Energy. Chenyu Luan (the second author in *paper 4*) helped me to set up the Genie model of the platform and carried out simulations for FHAWT.

Additional paper

The following paper is not included in this thesis:

A Comparison of two coupled model of dynamics for offshore floating vertical axis wind turbines (VAWT)
Michael Borg, Kai Wang, Maurizio Collu and Torgeir Moan
Published in Proceedings of the 32rd International Conference on Ocean, Offshore and Arctic Engineering, San Francisco, California, USA, June 2014

Contents

1 Introduction

1.1 General Background

Wind has been one of the fastest growing renewable energy sources in recent years. It has increasingly played a vital role in combating global warming, environmental pollution and the energy crisis all over the world. The global wind power has increased at a rapid pace by deploying larger, grid-connected wind turbines either on land ('onshore') or at sea ('offshore'). Figure 1.1 presents global wind power cumulative capacity [1] which shows that global wind power installations increased by 35.47 GW in 2013, bringing the total installed capacity up to 318.1 GW. During 2010-2011 more than half of all new wind power was added outside of the traditional markets of Europe and North America, mainly driven by the continuing boom in China which accounted for nearly half of all of the 18 GW installed at in 2011. China now has 91.42 GW of wind power installed. In the European Union (EU), the target for 20% of the European Union's overall energy supply to come from renewable sources by 2020 has been established. Further, wind energy will be a main contributor to produce 442 TWh meeting 14.9% of electricity consumption according to EWEA's new central scenario [2]. In 2013, a total of 25.4 GW of renewable power capacity was installed and wind energy accounted for 44% (11.2 GW) of new renewable power capacity installed [3]. At the end of 2013 there were 117.3 GW of installed wind energy capacity: 110.7 GW onshore and 6.6 GW offshore, which covers 8% of the EU's electricity consumption in a normal wind year [4].

At present, offshore wind power makes up only a small percentage of the total wind energy produced, but it has become the most promising renewable energy sources. This is because the offshore wind turbines can overcome several limitations encountered by land-based wind turbines such as the lack of expensive land near major population centers and the visual pollution, especially for Europe, where vacant land is scarce and vast shallow-water resources are available. Further, an offshore wind farm can generate more power than the same wind farm onshore due to more strong and consistent winds. The offshore wind is also less turbulent and have smaller shear than on land which both reduces fatigue damage effects. Moreover the size of an offshore wind turbine is not limited by road or rail logistical constraints if it can be manufactured near the coastline because it is easier to transport large MW wind

turbines to a planned site at sea by barges and ships than on land by trucks. Hence, the growth of offshore wind power has been accelerating in recent years. Figure 1.2 shows a development overview of annual onshore and offshore installations from 2001 to 2013 in EU. It shows that 2013 was a record year for offshore installations, with 1,567 MW of new capacity grid connected. Offshore wind power installations represent over 14% of the annual EU wind energy market, up from 10% in 2012 [3].
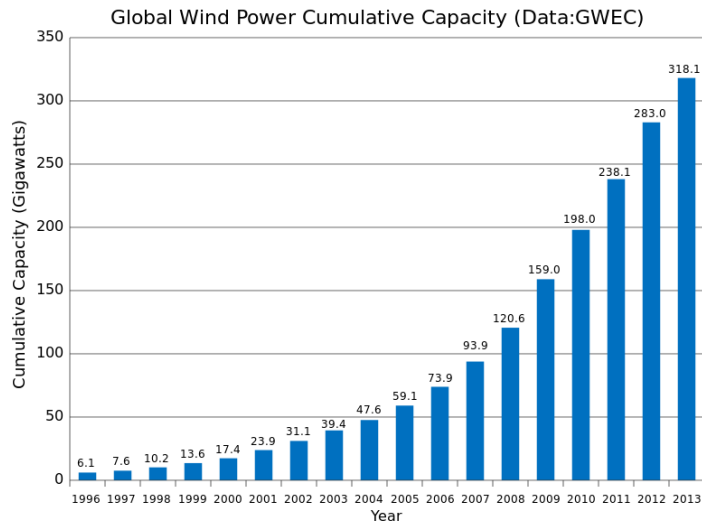
Figure 1.1: Global cumulative installed wind capacity 1996-2013 [1]

Current offshore wind turbines are mainly mounted on monopile bases in shallow water with depths of less than 30 m and within 20 km from shore [5]. Figure 1.3 presents average water depth and distance to shore for offshore wind farms in 2012 and the bubble size in the figure represents the total capacity of the wind farm [6]. The average water depth of offshore wind farms was 22 m. The average distance to shore was 29 km. It is clear from projects under construction, consented or planned, that average water depth and distance to shore will increase. The space-frame support structures, such as tripod and jacket, were employed to maintain the strength and stiffness requirements at the lowest possible cost as water depth increases further up to 50 m. As water depth is greater than 100 m, the floating support structures are expected to be the only viable choice. Subsequently, there is an increasing trend to exploit deep-water offshore wind energy in some countries such as USA, Norway, UK(Scotland), China and Japan [7], where vast deepwater wind sources are available to deploy floating offshore wind turbines. Since the feasibility of floating platform systems for wind turbines was demonstrated by Musial, Butterfield, and Boone [8], design and study of various floating concepts have been carried out. Three primary types of floating structures are under consideration for offshore wind turbines based on the experiences in offshore oil and gas (O&G) industries, namely: the spar, the tension-leg platform, and the semi-submersible. Figure 1.4 illustrates current types of offshore wind turbines including three types of floating wind turbines [6]. The

spar-buoy concept, which can be moored by catenary or taut lines, achieves stability by using ballast to lower the center of mass (CM) below the center of buoyancy (COB). The tension leg platform (TLP) achieves stability through the use of mooring-line tension brought about by excess buoyancy in the tank. The semi-submersible concept is generally moored by catenary lines and achieves stability through its water-plane area. An example of the spar-type wind turbine is the 2.3 MW Hywind which is the world's first full scale floating offshore wind turbine. This turbine has been operating successfully at a water depth of 200 m and 10 km off the west coast of Norway since September 2009 [9]. The WindFloat [10] design consists of a 2 MW Vestas wind turbine and a semi-submersible floater fitted with patented water entrapment (heave) plates at the base of each column. This turbine was installed of the Portuguese coast in 2011 and started producing energy in 2012. More full scale wind turbines with these three types of floater will be built in coming years.
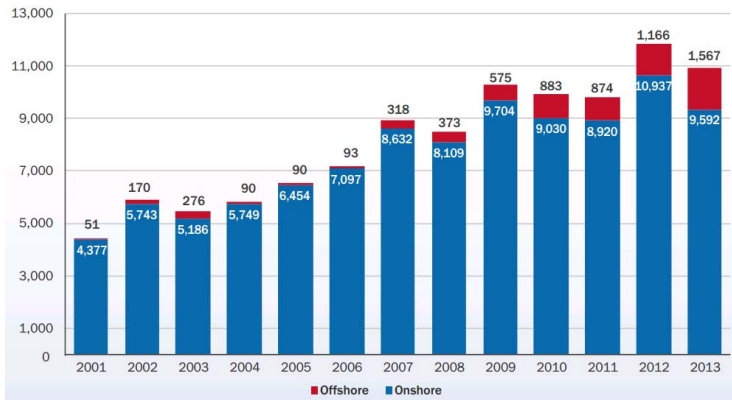
Figure 1.2: Annual onshore and offshore installations (MW) (Source: EWEA [3])

Despite certain achievements, the floating concept with large wind turbines still faces several challenges. The most important consideration is the higher capital costs of offshore wind power due to expensive offshore grid connections, installations and maintenance. Some characteristics such as water depth and distance to shore significantly affect the grid connection, civil works and other costs. Although the price of wind energy has decreased significantly since the 1980s, policy measures are still needed to ensure rapid deployment of wind turbines in most regions of the world [11]. It is therefore important to exploit the sizable technical potential for further design improvements and the most suitable configurations with different feasible concepts. The current industrial wind parks are based on horizontal axis wind turbines (HAWTs) as mentioned above. Yet vertical axis wind turbines (VAWTs) offshore has been a promising concept to compete floating horizontal axis wind turbines (FHAWTs) due to their advantages as mentioned above. The concepts of floating vertical axis wind turbines (FVAWTs) are described in Section 1.2.
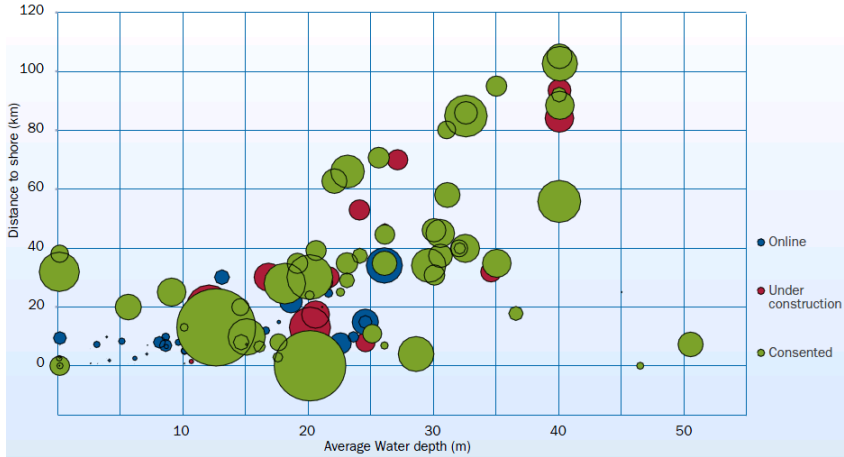
Figure 1.3: Average water depth and distance to shore for online, under construction and consented offshore wind farms (Source: EWEA [6])

This thesis aims to study a concept of FVAWT in a systematic manner, which started with developing simulation tool to code-to-code comparison study; and investigating the aerodynamics of wind turbine to analyzing the dynamic response of the whole floating system comprehensively; considering normal operating condition to emergency shutdown event; as well as comparing the FVAWT with a FHAWT. The concepts of FVAWTs are still at an early stage and a sophisticated simulation tool is the first and foremost research task. Further, the loads and responses of a FVAWT differ significantly from those of a FHAWT. It is, therefore, necessary to study the FVAWT not only individually but also comparatively with a FHAWT. This study will lead to a better understanding of FVAWTs, i.e. both their advantages and disadvantages, which are very important for further development of the vertical floating concepts and improve their competitiveness in the wind energy industry.
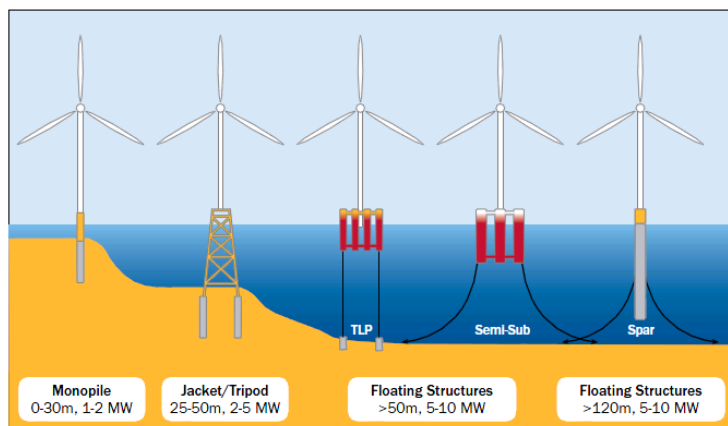
Figure 1.4: Offshore wind turbine foundation designs (Source: EWEA [6])

1.2 Floating Vertical Axis Wind Turbines

Vertical-axis wind turbines (VAWTs) are a type of wind turbine where the blades rotate about a vertically-oriented center axis that is called rotational shaft (tower) driving a generator to convert the mechanical torque to electrical power through a gearbox. This vertical shaft is perpendicular to the wind direction (sometimes termed as a ''cross-flow'' turbine) while in HAWTs the rotor is aligned with the axis of rotation parallel to the direction of the wind, which makes the different HAWT and VAWT significantly.

VAWTs are generally categorized as drag driven type or lift driven type according to the aerodynamic characteristics. Figure 1.5 shows three main types of VAWTs. A Savonius turbine is mostly considered as a drag device, although it could employ significant lift as stated by Jamieson [12]. The lift driven devices include the straight-blade Giromill (H-type) and the fixed-blade Darrieus VAWT. The Savonius turbines cannot compete with other types on the basis of an aerodynamic performance, but they have been used extensively in high-torque low-speed applications, such as for water pumping and ventilations purposes [13]. In contrast, the H-rotor and Darrieus curved blade rotor have undergone considerable research and significant engineering development for further application. Other VAWTs with various configurations, such as Darrieus-Masgrowe (two-tier) rotor, crossflex wind turbines, combine Savonius and Darrieus rotor, Zephyr turbine and so on, are also used in certain places [14].

The Darrieus VAWTs were developed and commercialized mainly in USA and Canada [15]. During the 1970s and 1980s, Sandia National Laboratories (SNL) devoted considerable effort to the research and development of the Darrieus VAWTs. The study on the proposed and tested designs was performed gradually in size and power population from a 2, 5, 17-m diameter research VAWT to the 34-m 'Test Bed' Darrieus VAWT. The 17-m research turbine obtained some successes and commercialization, and the installation and operation of the 34-m 'Test Bed' turbine demonstrated a significant step in the development of larger and more efficient commercial Darrieus VAWTs. Using the 34-m turbine as a start point, FloWind Corp. developed a new generation advanced VAWT with composite blades and extended height-to-diameter ratio. Unfortunately, after the bankrupt of Flowind in the 1997 and termination of the US DOE-sponsored VAWT research, VAWTs were not pursed to any great extent and lost its ground to HAWTs. Thus, a variety of VAWTs are limited to small scale individual use. However, extensive research activities in numerous universities and research institutions of the world is still continued with various aspects, such as novel type of VAWT [16-20], aerodynamic modeling [21-28], CFD simulation [29-32], measurement study [32-36], dynamics [37], upper scaling[38], generators [39], wind farm of VAWTs [40, 41] and so on.

Compared to HAWTs, VAWTs do have some disadvantages that have limited their use

in commercial land-based wind farms. Most critical issues are the economic concerns and fatigue problem. The former was attributed to longer blade length and lower power efficiency, and the latter is due to aerodynamic cyclic loading on the blade and subsequent torque ripple on the drive train. However, it is should be noted that these challenges were identified 20 years ago. By the use of modern composite materials, the fatigue issue of the blades can be overcome. Sutherland et al. [42] state that ''in reality, VAWTs are no more prone to fatigue failure than HAWTs. With the current understanding of fatigue loads, VAWT blades that reliably withstand the fatigue loads imposed upon them can have been designed''. Furthermore, the generalizations which refer to the Darrieus VAWT as aerodynamically less efficient than the HAWT must be used carefully as Worsell [43] and other researchers [44] concluded that the maximum average measured power coefficient of the VAWT are about 0 and 15% higher than those of the HAWTs. Moreover, efficiency of a wind farm of VAWTs can be improved by optimizing turbine placement within the wind farm. Kinzel et al. [41] concluded that the distance behind a turbine pair that the flow needs to recover to 95% of the wind velocity upwind of the turbine pair is approximately 6 D while a recovery distance of 4 D was observed for the wake behind a single VAWT. In comparison, the distance required for a recovery of the flow velocities is significantly smaller than the 14 D that the flow behind HAWTs needs to recover to 95% of the upwind velocity. The problem of torque ripple on the drive train could be handled effectively simply by adding compliance to the drive train in the earliest designs [45] such as the Test bed design. In addition, the problem of cyclically varying torque on VAWTs can be alleviated by recently novel design with helical twist in the blades [16, 17]. The most famous helical type is the quietrevolution turbine which consists of three vertical blades, each having a helical twist of 120 degrees. This feature spreads the torque evenly over the entire revolution. To summarize, modern designs of VAWTs have overcome the majority of issues associated with early designs [42].
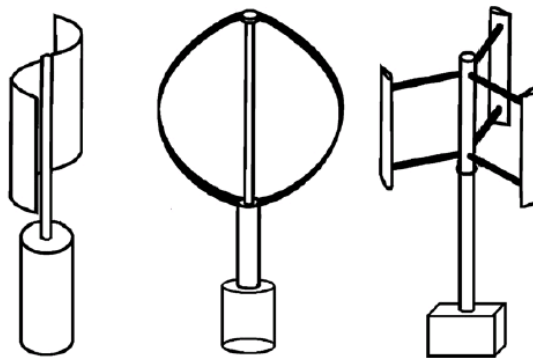
Figure 1.5: Three main configurations of VAWT: Savonius, Darrieus and H-type [46]

The advantages of VAWTs make them very promising as floating concepts for offshore deployment in deep water. The key advantages of VAWTs for floating offshore application can be summarized as follows:

- No yaw control because the rotor is always facing the wind
- Better suited to remove gear box due to the application of direct drive generator
- Reduced floater cost associated with a lower centre of gravity
- Lower operational and maintenance costs associated with a more accessible drive train because almost all of the components of a FVAWT requiring maintenance are located at the bottom, facilitating the maintenance work appreciably
- Minor obstacle in upscaling
- More power density achieved by deploying VAWTs optimally in a wind farm

Due to unique features and advantages of VAWTs as mentioned above, a FVAWT having an effective mooring system seems to be well fitted for floating offshore application. Increasing interest in the use of FVAWTs has been demonstrated. Sandia National Laboratories obtained a research grant from the U.S. Department of Energy to investigate the feasibility of VAWTs for offshore deployment in 2011 [42]. The cost-competitiveness of a multi-MW FVAWT will be investigated through a series of design studies. A potential for COE reduction of over 20% for VAWTs in the offshore application could be achieved [47]. Up to now, several FVAWT concepts have been proposed by different research institutions and industries. These FVAWTs consist of different types of VAWTs and platforms as used for FHAWTs. Some examples of proposed concepts include DeepWind [48], VertiWind [49], Aerogenerator X [50], 'floating tilted axis' [51], Gwind [52], and SKWID [53] concepts, as shown in Figure 1.6.
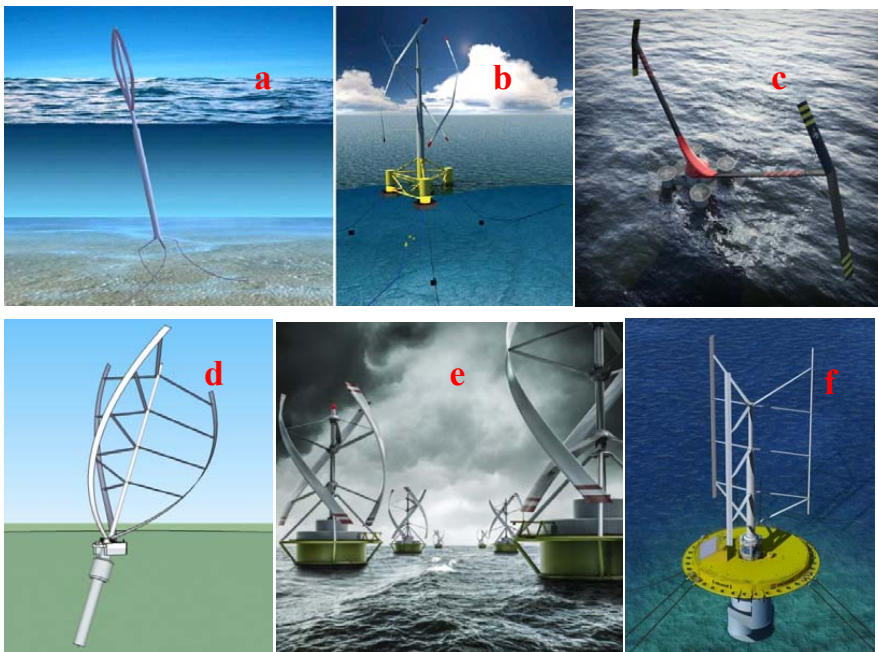
Figure 1.6: (a) DeepWind concept (b) VertiWind concept   (c) Aerogenerator X concept   (d) 'floating tilted axis'   (e) Gwind   (f) SKWID

The DeepWind concept [48] was proposed in the DeepWind project which was started in the autumn of 2010 under the European FP7 programme and aimed at investigating a new offshore floating vertical axis wind turbine (VAWT) concept for exploiting wind resources at deep offshore sites. Risø DTU coordinates this project which involves 12 international partners. This concept includes a 2-bladed Darrieus type of rotor, a long rotating spar buoy as support structure, direct drive subsea generator, torque absorption and mooring cables which are anchored into the sea bed. It was firstly designed to be a 2 MW with the rotor height of 75 m and rotor diameter of 67 m [54-56], and was later increased to a larger size with power capacity of 5 MW as the first baseline design [57], followed by a further design optimization [58]. An optimized blade profile has been obtained with less weight and higher stiffness than the first baseline design. However, the lateral force (the lift known as Magnus effect) acting on this rotating spar in currents and the subsea generator technology impose technical challenges to this concept [59] and many R&D efforts have been taken, such as model testing of transverse forces on the floating spar rotating in combined waves and currents and exploration of direct transmission drives of high torque converting into electrical energy.

The VertiWind concept [49] is a 2 MW FVAWT design with a 105 m height created by Nenuphar and the mooring system, floater and installation are designed by Technip company. An innovative VAWT is mounted in the centre of a semi-submersible floater to ensure that the centre of gravity, the buoyancy and the convergence point of the mooring lines are all on the same axis. This configuration can highly reduce the sway and yaw response of the floater subject to non co-linearity or heading variation of wave and wind. Three helical blades and four levels of supporting arms used for the VAWT, and each blade cover a 120 degrees angle. Therefore, this wind turbine is based on a conventional 3-bladed H-Darriues VAWT, but considered as an evolution in the improved twisted blade setup which offering several important advantages, such as simple straight blades, reduced dynamic stall and minimized torque variation during one revolution.

The Aerogenerator X concept [50] has a turbine of 10MW with the height of 130 meters, resulting from an 18-month feasibility study (called the NOVA project [60]), according to UK Company Wind Power Limited. The concept is drastically different from other VAWT concepts, the rotor blades extend from the center axis in a V-shape which is half of the height of an equivalent horizontal-axis turbine.

Another concept was proposed by Akimoto et al. [51] with a tilted axis of a FVAWT. The tilt angle varies according to the balance of turbine thrust and stability of the floater. Electric generators are installed above the water surface at a low altitude to provide easy maintenance access. Preliminary estimation and comparisons indicate that economic performance of the new concept can be higher than those of horizontal and vertical axis offshore wind turbines. However, many issues, such as the stability

of the floater, bending moment and fatigure stength of the blades and dynamics of this floating system, have not been discussed.

The Gwind concept [52] is another helical Darrieus VAWT design from a Norwegian Gwind research project. Gwind is developing a gyro-stabilized FVAWT for offshore and near-shore applications. Its current concept prototype, Spinwind 1, has been built to explore the motion characteristics of a vertical axis turbine and floater combined. Besides the low center of gravity and reduced cost for installation, production and maintenance, this concept has an important benefit from gyro stabilization which could suppress motion and reduce variable loads on structure.

The SKWID concept [53] by Modec is a floating wind and current hybrid power generation system capable of maximizing the harvesting of ocean energy from wind and current. It's an interesting concept having a Darrieus wind turbine above water and a Savonius-style generator capturing currents below water, both supported by an anchored floating platform.

1.3 State-of-art in FVAWT Modelling

In order to better understand the performance of different concepts of FVAWTs for conceptual design and analysis as well as assessing the structural integrity, platform motion and installation, and to provide the basis for detailed structural designs, a model should be developed to represent the aerodynamic, hydrodynamic, structural dynamic and control systems for a FVAWT in a fully coupled manner. The modeling calls for a fully-coupled aero-hydro-servo-elastic approach.

Compared to the so called aero-servo-elastic codes for land-based wind turbine analysis, the hydrodynamic loads are present, and the corresponding additional dynamic behavior must be considered for floating wind turbines. The analysis of floating wind turbines must also account for the dynamic coupling between the motions of the support platform and the wind turbine, as well as the dynamic characterization of the mooring system for compliant floating platforms. Compared to the aero-hydro-servo-elastic codes for FHAWTs analysis, FVAWTs have the same dynamic characteristics, however with a different module for aerodynamics. A variety of methods have been developed from frequency domain techniques [61-65] to the fully coupled time domain aero-hydro-servo-elastic models [66-71] for conceptual assessment and dynamic analysis of FHAWTs. Many codes have been developed to include coupled aero-hydro-servo-elastic modeling capabilities for FHAWTs. The well-known open source codes is the FAST [72] (coupled with Aerodyn [73] and Hydrodyn [74]) developed by NREL [67]. Risø DTU also extended its HAWC2 code [75] to have the capability of hydrodynamic calculation. The limit is that the Morison formula can only be used for slender structures. A more recent and comprehensive

code is Simo-Riflex-Aerodyn based on the integration of Aerodyn and Simo&Riflex [76, 77]. This code has been verified through a benchmark study [78] and widely used for numerous design and dynamic analysis of various FHAWTs [79-82]. Other codes such as 3Dfloat [83], Bladed [84], Simo&Riflex [69, 70] and VpOne [85] are developed by international researchers from universities, research institutions and industry. Using these codes, several code-to-code verification activities based on the existing models were carried out for a spar-type FHAWT in Phase IV of the Offshore Code Comparison Collaboration (OC3) within the Subtask 2 of the International Energy Agency Wind Task 23 [86, 87], and for a semi-submersible FHAWT in the OC4 Phase II of Task 30. The verification of modeling tools by comparing results of simulated responses between various tools is performed [88]. In contrast, the available simulation tools to model the FVAWTs in a fully-coupled way are limited. Following the resurgence of interest in the potential of VAWTs for offshore application, more and more effects have been taken on the development of aero-hydro-servo-elastic modeling for FVAWTs.

A simplified method for the analysis of the aerodynamic loads for DeepWind concept under turbulent wind and platform motion was created by Merz [89]. In addition to the real blades, a number of "ghost" blades were also introduced and their aerodynamic behavior were calculated based on a blade-element momentum model in this method, such that there is always the equivalent of one blade associated with each column of streamtube elements on the swept surface. Although this method has advantages of eliminating iteration and potential numerical instability in the induced velocity calculation and general applicability in unusual cases, it only considers the surge displacement of the FVAWT by creating a simple mass-spring-damper model. Therefore, the hydrodynamic model was not included, and the interaction between the separate dynamic models was not considered. Furthermore, Merz and Svendsen [90-92] extended this method by including the hydrodynamic calculations based on Morison formula and focused on the investigation of a control algorithm for the DeepWind FVAWT.

The Offshore Wind ENergy Simulation (OWENS) toolkit is being developed as a design tool for assessing innovative FVAWT configurations by Sandia National Laboratory in conjunction with its partners such as Texas A&M and University of Maine. The OWENS toolkit aims at establishing a robust and flexible finite element framework and VAWT mesh generation utility, coupled with a modular interface that allows users to integrate easily with existing codes, such as aerodynamic and hydrodynamic codes. Firstly, an energy preserving time integration method has been extended to rotational systems, and implemented into the finite element method in OWENS [93]. An unconditionally stable integration scheme was constructed by utilizing system energy in this method, and hence for conservative systems energy was preserved regardless of time step size. Then, an update on the development of the OWENS toolkit was realized by introducing a loose coupling approach to external loading modules, which allows a greater degree of modularity and flexibility of the tool

[94]. An analysis of a realistic VAWT with aerodynamic and platform forcing were carried out through one-way coupling to the Sandia National Laboratories CACTUS [95] VAWT aerodynamics software. However, only the rigid rotor rotation of the VAWT is considered in aerodynamics analysis by this one-way coupling approach. Blade deformations are not accounted for in aerodynamic force calculations, and thus the aeroelastic nature of the simulation is limited. Recently, an improvement over the loose coupling procedure considers iteration at each time step, using a "predictor corrector" approach, such that a hydrodynamic module was also included by coupling the wave-to-wire numerical model, WaveEC2Wire, with OWENS [96]. Future developments are being made by using the two-way coupled aerodynamics model that receives blade deformations and performs aeroelastic calculations, by integrating a nonlinear mooring module and by adding up other necessary features.

The HAWC2, a state-of-the-art aero-hydro-servo-elastic code used for FHAWTs, has been developed to have capability of calculating a FVAWT response in time domain for the DeepWind Project. The aerodynamic loads acting on the rotor are calculated using double disk multiple streamtube formulation and provided to HAWC2 through a dynamic link library (DLL) [48]. Recently, instead of the steamtube model, the Actuator Cylinder flow model [97] is implemented into HAWC2 due to its advantages in VAWT aerodynamic and aeroelastic simulation models. The structural model for wind turbines in HAWC2 is based on multibody dynamics, which means that quite complex structures and arbitrary large rotations of the bodies can be handled. However, wave loads in HAWC2 are calculated using the Morison formula, which is well suitable for slender structures such as spar floater. Therefore, HAWC2 is still not suitable for FVAWTs when a semi-submersible floater is used.

To provide a simplified coupled dynamic design tool to the use in the preliminary design stages of FVAWTs, Borg et al. from Cranfield University developed FloVAWT (Floating Vertical Axis Wind Turbines) code based on the MATLAB/Simulink programming environment. Continual development and verification of FloVAWT have been performed by Collu et al. [98, 99].The hydrodynamic model is the core of this coupled model because all other modules feed into it as external forces and subsequently the platform motion is simulated through the MSS toolbox developed by Fossen and Perez [100]. The Double Multiple-Streamtube model with Gormont-Berg dynamic stall is used in the aerodynamic model, and Cummins equation with radiation-force state approximation is used in the hydrodynamic model. However, main drawbacks of this code are that the is dynamic mooring model, structural dynamics and control dynamic are missing; therefore linearized force-displacement relation is used in the mooring dynamics, the rotor is assumed as rigid and constant rotational speed assumed.

Based on the Simo&Riflex code which has been extensively used and validated for offshore structures subjected to wave loads, the Simo-Riflex-DMS code was recently developed in connection with this thesis work as non-linear aero-hydro-servo-elastic

simulation tool for modeling FVAWTs. This simulation tool integrates models of the wind inflow, aerodynamics, hydrodynamics, structural dynamics and controller dynamics, and carry out the simulations in a fully coupled manner in the time domain. The development of this simulation tool provides approaches of high fidelity of analysis for FVAWTs and thus become one of focus areas of this thesis. The detailed modeling method is described in Chapter 3 and the related verification is present in Paper 2. In addition, a comparison of this code and aforementioned FloVAWT code has been carried out to offer insight into various aspects and considerations in the modeling.

1.4 Scope and Objectives of the Thesis

The main goal of this thesis is to model and analyze the dynamic behaviors of a floating vertical axis wind turbine. To realize this objective, the following sub-objectives have been defined and achieved:

- To establish an aerodynamic model to calculate the aerodynamic loads on a VAWT and evaluate the effect of the tower tilting on the aerodynamics of a VAWT based on an improved model, verified by comparing with experimental data (Paper 2)

- To establish coupled model of a FVAWT including aerodynamics, hydrodynamics, structural dynamics (wind turbine, floating platform and the mooring lines) and a generator controller (Paper 1)

- To investigate the effect of a hydrodynamic brake on a FVAWT and analyze the FVAWT installed with the hydrodynamic brake in the event of emergency shutdown (Paper 3)

- To compare models of a FVAWT and a FHAWT and to carry out a comparative study of these two models (Paper 4)

- To analyze stochastic dynamic responses of a 5 MW FVAWT with the emphasis on the influences of different modeling methods, parked conditions and wind-wave misalignment conditions (Paper 5)

In addition, the model and simulation code developed in this thesis have also been compared with another simulation tool developed by Cranfield University (Additional paper 1). However, this thesis is written in the form of a collection of 3 journal papers and 2 conference papers. Figure 1.7 shows how the scope of the papers is interconnected in this thesis. The 5 papers are included in Appendix and summarized as follows:

Paper 1: This paper addresses the evaluation of the effect of tower tilting on the aerodynamics of the VAWTs when the wind turbine tilts following the pitch motion of the platform. The Double Multiple-Streamtube (DMS) model is reformulated to account for the effect of tower tilting for the curved-blade Darrieus VAWTs. The model is validated against experimental data collected on an H-Darrieus wind turbine in skewed flow conditions. Three different dynamic stall models are also integrated into the DMS model. According to the experimental data, the DMS model with the inclusion of the dynamic stall model is also well validated. Both the small Sandia 17-m wind turbine and the large DeepWind 5 MW are studied. Furthermore, applications of Glauert momentum theory and pure axial momentum theory are compared to evaluate the effect of the velocity component parallel to the rotor shaft on the accuracy of the model.

Paper 2: This paper presents the development of a coupled method for modeling the dynamics of a floating vertical axis wind turbine. This integrated dynamic model takes into account the wind inflow, aerodynamics, hydrodynamics, structural dynamics (wind turbine, floating platform and the mooring lines) and a generator control. This approach calculates dynamic equilibrium at each time step and takes account of the interaction between the rotor dynamics, platform motion and mooring dynamics. Verification of this method is made through model-to-model comparisons.

Paper 3: The paper presents a novel concept installing a hydrodynamic brake at the end of the extended shaft of a floating vertical axis wind turbine through the centre column of the floater. The motivation is to initiate an emergency shutdown of the FVAWT when the generator torque is lost due to grid loss helping the mechanical brake. Firstly, a model of the concept, integrating the hydrodynamic brake into the original FVAWT, is established to carry out coupled non-linear simulation of the integrated system in the time domain. Secondly, based on the integrated model, the effect of the hydrodynamic brake on the FVAWT under normal operating conditions is evaluated and emergency shutdown process using the hydrodynamic brake is investigated. The dynamic analysis focused on the comparison of global motions, tower base bending moments and the tensions of mooring lines for different load cases with different fault configurations.

Paper 4: This paper focuses on the comparison between a FVAWT and a FHAWT based on numerical simulations. The FVAWT with a 5 MW Darrieus rotor and the FHAWT with the 5 MW NREL reference wind turbine, both mounted on a semi-submersible, is presented. A series of load cases with combined wave and wind conditions are selected to calculate dynamic responses of the FVAWT and the FHAWT, such as the global motions of the floater in six DOFs, the bending moment of the bottom of the tower and the tension at the fairleads of the mooring lines. Statistical analysis and power spectra are used to analyze the time domain results for this comparison study. The results give more insight into the difference between the FVAWT and the FHAWT.

Paper 5: This paper presents a stochastic dynamic response analysis of a 5 MW FVAWT on the basis of the fully coupled nonlinear time domain simulations. The dynamic responses of the FVAWT, including global motions, structural responses and mooring line tension, are studied based on statistical analysis and frequency analysis. The analysis covers following aspects: The response characteristics of the FVAWT under steady wind and turbulent wind condition, comparison between the elastic FVAWT and the rigid FVAWT, comparison between the FVAWT and an equivalent land-based wind turbine, investigating the dynamic response as a function of azimuthal angle in parked condition, dynamic response analysis of the FVAWT in selected misaligned wind and wave conditions.
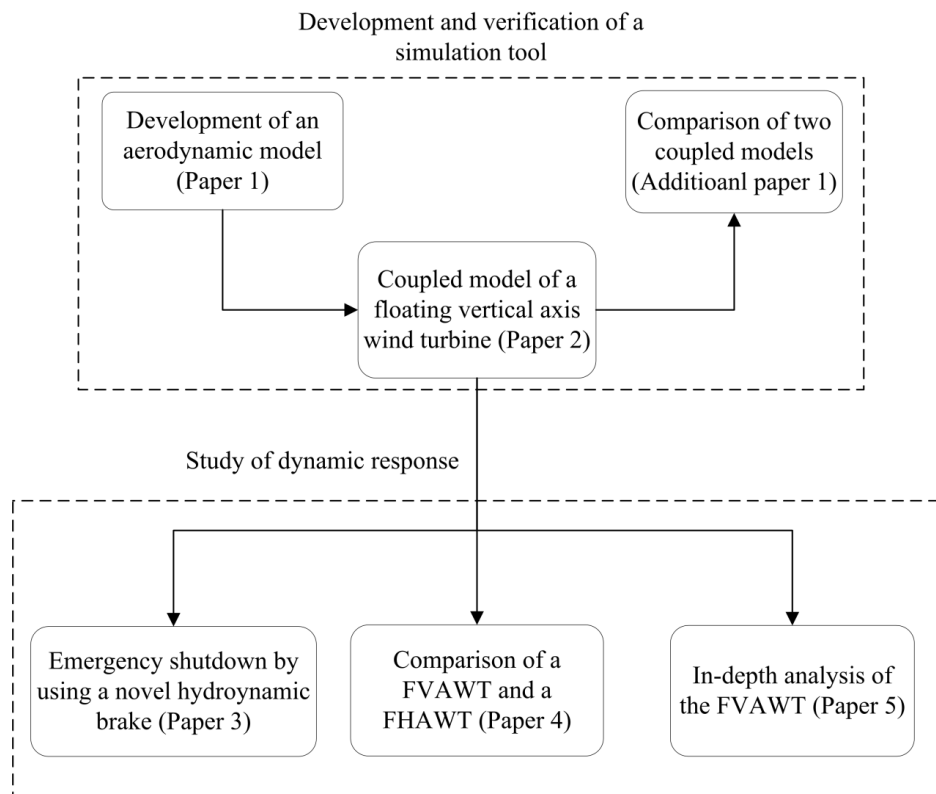
Figure 1.7: Scope of thesis and interconnection between the papers

1.5 Thesis Outline

The summary part of this thesis consists of the following chapters:

Chapter 1 includes the background, motivation and objectives of this thesis.

Chapter 2 introduces the aerodynamic models for calculating the aerodynamic loads on vertical axis wind turbines. In particular, an improved model is presented to evaluate the effect of tower tilting on the aerodynamics of a VAWT when the tower is mounted on a floating support structure and pitch motion occurs.

Chapter 3 introduces the wind turbine and platform considered in this thesis: DeepWind 5 MW wind turbine and an adapted platform from OC4 project. Then, the modeling methodology for the FVAWT is presented by incorporating aerodynamic model, hydrodynamic model, structural model and control model. Based on this coupled model, a state-of-the-art simulation tool Simo-Riflex-DMS is introduced.

Chapter 4 addresses the dynamic response analysis of the FVAWT based on the fully coupled nonlinear time domain simulations. The analysis covers the following aspects: The response characteristics of the FVAWT under steady wind and turbulent wind condition, comparison between the elastic FVAWT and the rigid FVAWT, comparison between the FVAWT and an equivalent land-based wind turbine, investigating the dynamic response as a function of azimuthal angle in parked condition, dynamic response analysis of the FVAWT in selected misaligned wind and wave conditions. Furthermore, emergency shutdown process of the FVAWT with consideration of fault is investigated based on a novel hydrodynamic brake. Lastly, a comparative study of a FVAWT and a FHAWT is also presented.

Chapter 5 summarizes the work in the thesis with the main contributions, conclusions and recommendations for future work.

2 Aerodynamics of a Vertical Axis Wind Turbine

This chapter starts with an overview of aerodynamic models for calculating the aerodynamic loads on vertical axis wind turbines to date in Section 2.1. Dynamic stall models considering dynamic stall effect for improving the accuracy of the aerodynamic model used in this thesis are described in Section 2.2. To consider and evaluate the effect of tower tilting on the aerodynamics of a VAWT when the tower is mounted on a floating support structure and pitch motion occurs, an improved model based on the Double Multiple-Streamtube model is presented in Section 2.3 and validated in Section 2.4. Based on this improved model, evaluation of the effect of tower tilting on the aerodynamics of a small-scale and a large-scale VAWTs can be referred to *Paper 2*. The validated aerodynamic model is used in the development of coupled model in Chapter 3 (also see *Paper 1*).

2.1 Overview of Aerodynamic Models

The well-known Darrieus-type vertical axis wind turbine, driven by aerodynamic lift, was patented in the USA by Georges Darrieus in 1931 [101]. The prediction of aerodynamic loads on a Darrieus-type vertical axis wind turbine poses a significant challenge. Not only does the angle of attack of its blades vary cyclically with rotor azimuth during its operation, but also the interaction between each of the turbine blades and either their own wakes, or the wakes developed downwind of the other blades, influences significantly the aerodynamic loading on the blades and introduce more complexity and difficulty of aerodynamic simulation, especially at high tip speed ratios. The interaction between the blades and their own wakes represents one of the most critical problems in the numerical modeling of aerodynamics of vertical axis wind turbines [102].

Since Sandia National Laboratories started the study of vertical axis wind turbine in the 1970's, a variety of theoretical and computational aerodynamic models have been used to predict aerodynamic loads on vertical axis wind turbines. These include stream-tube models [103-107], Actuator Cylinder flow model [108], vortex models [25, 27, 109, 110], cascade models [111] and panel models [27, 112-115].

The stream-tube models (also named as Blade Element/Momentum model) are based on the conservation-of-momentum principle in a quasi-steady flow by equating the forces on the rotor blades to the change in the streamwise momentum through the turbine. This combination can be classified using three different types of models:

Single Streamtube model by Templin [103], assuming that the entire rotor represented by an actuator disk is enclosed in one streamtube; Multiple-Streamtube model by Strickland [104], in which the volume swept by the rotor is divided into a series of adjacent streamtubes and Double Multiple-Streamtube model (DMS model) by Paraschivoiu [106], which assumes that the vertical axis wind turbine can be represented by a pair of actuator disks in tandem at each level of the rotor, as shown in Figure 2.1. The DMS model has capability to consider the variation of the induced velocity as a function of azimuth angle for each streamtube, thus it gives a more accurate calculation of the aerodynamic loads when compared to the other simpler stream-tube models. The DMS model is described in great detail in the work of Paraschivoiu [15]. However, the DMS model gives over prediction of power for a high solidity turbine and a convergence problem at higher tip speed ratio may occur.

The Actuator Cylinder flow (AC) model was developed by Madsen [108] in his PhD study from 1979 to 1982. By extending the well-known Actuator Disk concept for HAWTs to a general approach of an actuator surface coinciding with the swept area of the actual turbine [116], the AC model was established for aerodynamic calculations of VAWTs based on their surface geometry. To apply this AC flow model in the floating vertical axis wind turbines for the DeepWind project, the real energy conversion of the 5 MW DeepWind rotor was simulated with the AC flow model [117] and the implementation of the AC flow model in the HAWC2 aeroelastic code was presented recently by Madsen et al. [97].

The vortex models, assuming potential flow, calculate velocity field about the rotor through the influence of vorticity in the wake of the blades. The blades are split up into a number of blade elements and each element is represented by a bound vortex filament, also known as lifting line. The strengths of the bound vortices are related to the lift which is determined using airfoil coefficient datasets and calculated relative flow velocity. The fluid velocity at any point in the flow field is the undisturbed wind velocity and the velocity induced by all vortex filaments in the flow field. Based on the above two relationships, the closure of the vortex model can be completed and the velocity field is calculated. A vortex model for a single blade element of a VAWT was first introduced by Larsen [118], and further two dimensional models applicable to VAWTs were presented by Fanucci and Walter [119], Holme [120] and Wilson [121]. These models were limited to lightly loaded wind turbine and small angles of attack to disregard stall effect. By extending the two dimensional vortex models, a three dimensional model was presented by Strickland et al. [110], and further improvements were also made by Strickland et al. [122] considering the dynamic effects, such as dynamic stall, pitching circulation and added mass. The improved model showed better correlation with the calculated and experimental results for the instantaneous blade forces and the overall power coefficients. Further enhanced models were followed by Cardona [123], Vandenberghe and Dick [124]. One novel approach was proposed by Ponta and Jacovkis [109] to combine the free-vortex model with a finite element analysis of the flow in the vicinity of the rotor. It divided the analysis into

two separate regions: macro and micro models. This model could avoid certain shortcomings of the previous vortex model, and improved better calculated results compared with experimental results. However, one disadvantage of this approach is that the stall phenomena could not be covered.

To simulate the wind turbine aerodynamics and performance by providing an accurate representation of the dynamics of the wake that is generated by the turbine rotor, Brown's Vorticity Transport Model [125] (VTM) was developed to investigate the aerodynamic performance and wake dynamics of three different VAWTs both in steady and unsteady wind conditions [28]. In the VTM, the time-dependent Navier–Stokes equations are discretised in three-dimensional finite-volume form using a structured Cartesian mesh within the fluid domain surrounding the turbine rotor. Under the assumption that the wake is incompressible, the Navier–Stokes equations can be cast into the vorticity–velocity form allowing the temporal evolution of the vorticity distribution in the flow surrounding the rotor to be calculated. The VTM was validated by Scheurich et al. [25] based on the comparison between VTM predictions and experimental measurements of the blade aerodynamic loading of a straight-bladed vertical-axis wind turbine that was made by Strickland et al [122]. Furthermore, Scheurich and Brown [126] have compared VTM predictions against experimental measurements of the power curve that were made by Penna [16] for a commercial vertical-axis wind turbine with blades that are helically twisted around the rotor axis. The very satisfactory agreement between VTM predictions and all these different and independent experimental measurements provides considerable confidence in the ability of the VTM to model accurately the aerodynamics of vertical-axis wind turbines.

The cascade models, originally used for turbomachinary design [127], were first proposed by Hirsh and Mandel [128] to apply the cascade principles for the analysis of VAWTs. The blades of a turbine are assumed to be positioned in a plane surface, termed as the cascade, with the distance between adjacent blades equal to the turbine circumferential distance divided by the number of blades, as illustrated in Figure 2.1. The Bernoulli's equation is used to establish the relationship between wake velocity and the free stream velocity while a particular semi-empirical expression is used to relate the induced velocity to the wake velocity. Despite its more computational time than the streamtube models, this model can provide more accurate instantaneous blade force. It can predict the overall values for both low and high solidity turbines, and has no any convergence problem even at high solidities and high tip speed ratios. An improvement for the model to include two important effects of the dynamic stall and flow curvature with blade pitching was presented by Mandal and Burton. The improved model could allow the calculated values of the wake velocities comparable with those by the improved three dimension vortex model by Strickland et al. [122].
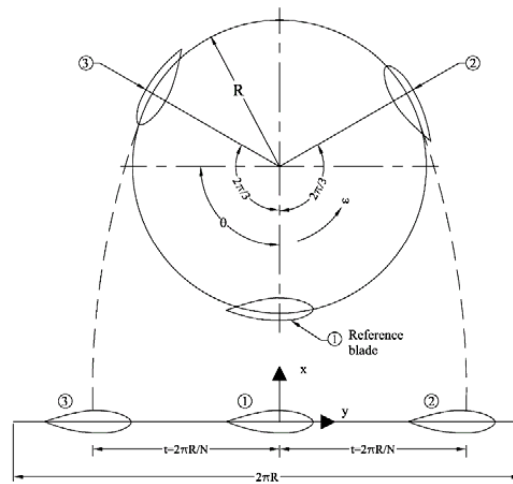
Figure 2.1: Cascade configuration of blades(Islam et al. [129])

The panel models have been applied widely to solve naval hydrodynamic [130] and aircraft aerodynamic problems [131] and a specific introduction to this panel method was presented by Erickson [132]. This model first begins with a discretization of a 3D surface into a number of panels. By placing source or doublet with a prescribed strength on each panel and solving the Laplace equation in terms of the velocity potential for a no penetration Dirchelet boundary condition on the body with the Kutta condition being enforced at the trailing edge, an arbitrary geometry for the hydrodynamic problems can be modeled and two-dimensional aerofoil data obtained from experimental are not necessary. Simão Ferreira and Scheurich [114] used a potential flow panel model developed by Simão Ferreira in his PhD thesis [113] and the VTM model to calculate the aerodynamics of a high aspect ratio H-type VAWT so as to demonstrate that the instantaneous blade aerodynamic loading and the power conversion of a VAWT are decoupled. In this panel model, each blade is represented by a 2D distribution of source and doublet panels over the blade's surface. The Kutta condition is imposed at the trailing edge, and the near-wake is modeled with doublets, with the mid and far wake modeled with vortex points. The 2D panel model was further developed by Zanon et al. [27] to a double–wake vortex panel model coupled with the integral boundary layer equations on the aerofoil surface by using a semi-inverse iterative algorithm for simulating the unsteady 2D flow past a VAWT. This is the first time a double-wake model is thoroughly validated by the comparison with PIV data concerning a pitching aerofoil and a VAWT in dynamic stall. In addition, a 3D unsteady panel method was presented and validated though comparison with the Stereo-PIV experimental results and smoke-trail studies by Dixon et al. [112, 115].

In recent years, improvements in the availability of high-performance computing have boosted the more extensive application of CFD (Computational Fluid Mechanics) models in the aerodynamic calculations of vertical axis wind turbines. Hansen and

Sørensen [133] have simulated the two-dimensional aerodynamics of an aerofoil for a VAWT in a planar and cyclic motion by solving the Reynolds-Averaged Navier-Stokes (RANS) equations. In contrast, detached-eddy simulations of a similar aerofoil configuration have been carried out by Horiuchi et al [134]. Further, a 2D CFD simulation of dynamic stall on a VAWT has been performed to study the modeling based on the verification and validation with Particle Image Velocimetry (PIV) measurements by Simão Ferreira et al. [29, 135].

2.2 Dynamic Stall Model

The accuracy of aerodynamic models can be much improved by incorporating a number of secondary effects and a dynamic stall model. The secondary effects, such as the blade geometry and airfoil type, the rotating tower and the presence of struts and spoilers, are particularly significant at high tip-speed ratios and the influence of secondary effects on the aerodynamics of the Darrieus rotor was described in detail by Paraschivoiu in his work about VAWTs [15]. Dynamic stall can occur at low tip-speed ratios, when the amplitude of the oscillation of the angle of attack becomes large making the flow separate from the blade surface. The angle of attack varies with the azimuthal position during operation, and furthermore, the blades within the downwind zone experience a lower wind speed from the wake of the upwind part of the rotor. Dynamic stall is a complex unsteady phenomenon related to the time response of the viscous boundary layer and thus to the chordwise pressure and skin friction distribution for the rapid variation of the angle of attack as well. The mechanism of dynamic stall was first identified on helicopters with the physics of the stall developments being fundamentally different from the static stall mechanism for the same airfoil. This mechanism produces a delay in stall onset, i.e., the stall occurs at a higher angle of attack than for the static stall case, and is characterized by shedding and passage over the upper lifting surface of a vortex-like structure. The process begins with a rapid increase in lift and ends with full flow separation and catastrophic loss of lift as the vortex disturbance is convected past the trailing edge of the airfoil [136]. Subsequently, hysteresis loops occur in the force coefficients and produce cyclic pressure loading that is not predicted using steady airfoil data.

A variety of computationally efficient engineering models were originally developed to predict the dynamic stall effects in helicopters [137-143]   and a subset of these were adapted for use in wind turbine aerodynamics, e.g., the ONERA method [144, 145]. However, under normal operating conditions the Mach number and rotational frequency for wind turbines are significantly lower than those for helicopters, and thus specific dynamic stall models tuned for wind turbines have been developed by several researchers, such as Øye [146], Snel [147], Gupta et al. [148], Larsen et al. [149] and Sheng et al. [150]. These semi-empirical models represent the essential physics using sets of linear and non-linear equations to model the lift, drag and pitching moment coefficients of airfoils under dynamic conditions. Several empirical

parameters for these equations must be deduced from unsteady airfoil measurements. Further, several empirical methods were developed to adapt for predicting dynamic stall of VAWTs, such as Gormont's model [137] or a model from the Massachusetts Institute of Technology (MIT) [15], which are based on numerical correction of the dynamic stall delay. Gormont's model was first developed for blades on helicopter rotors and several adaptations have been proposed for VAWTs, including those by Strickland et al. [110], Paraschivoiu [15] and Berg [151].

In this thesis, Gormont's model with the adaptation of Strickland et al. [110] and with adaptation of Berg [151] are used to predict the unsteady aerodynamics of VAWTs at a low tip speed ratio. The assumptions that the lift curve and zero-lift angle remain unchanged and that the dynamics effects only modify the angle of attack at which stall occurs are upheld for the former model, denoted as ''Gormont DS'' in the analysis of this work. Thus, a modified angle of attack α_M is used to derive the two-dimensional force coefficient data as a function of $c\dot{\alpha}_e / (2W)$ and other parameters (α_e, γ, K_1), as shown in Equation (2.1)

$$\alpha_M = \alpha_e - \gamma K_1 \left(\left|\frac{c\dot{\alpha}_e}{2W}\right|\right)^{1/2} S_{\dot{\alpha}} \qquad (2.1)$$

where W represents the relative inflow velocity, α_e is the effective blade angle of attack, γ and K_1 are empirical constants, $\dot{\alpha}_e$ represents the instantaneous rate of change of α_e and $S_{\dot{\alpha}}$ is the sign of $\dot{\alpha}$. The latter model, which was intended to avoid the drawback of Gormont's model, was proposed to compute the modified dynamic coefficients using linear interpolation between the dynamic coefficient predicted by Gormont's model and the static coefficient. This model is denoted as ''Berg DS'' in the analysis of this work.

The Beddoes-Leishman dynamic stall (BL DS) model is also used to calculate the VAWTs' aerodynamics in this thesis. This approach is quite different from those of the above methods and represents the physical phenomenon to a certain extent through a superposition of separate indicial functions. The original BL DS model [152] is capable of simulating the dynamic stall effect on helicopters, and the adaptation of this model has been validated for wind turbines by Gupta and Leishman [148]. The model consists of three components: unsteady attached flow, unsteady separated flow and dynamic vortex lift. The loads in the unsteady attached flow regime are obtained by treating the aerodynamic forces on the airfoil as the sum of a circulatory component related to the change of the angle of attack and an impulsive component generated by the change rate of the angle of attack and pitch movement. Next, the total normal force coefficient C_N^{Pot} under attached flow condition is given by

$$C_N^{Pot} = C_N^C + C_N^I \qquad (2.2)$$

where C_N^C is the circulatory normal force coefficient and C_N^I is the impulsive normal force coefficient. The unsteady chordwise force coefficient, C_C, which is

identical to the tangential force coefficient in this case, is obtained using the effective angle of attack α_e

$$C_C = C_N^C \alpha_e \tag{2.3}$$

The unsteady separate flow together with the non-linear effects usually includes leading edge separation and trailing edge separation, both of which must be predicted correctly to accurately estimate the influence on the aerodynamic coefficients. The normal force coefficient and the chordwise force coefficient are related to the dynamic separation point based on the static condition according to the Kirchhoff theory and the history of the angle of attack. Finally, a vortex may detach from the surface at a certain critical point and move downstream along the chord after it is formed near the leading edge. This vortex does not significantly change the pressure distribution until it detaches from the airfoil. The vortex lift contribution is modeled as the difference between the attached flow C_N^C and the unsteady non-linear value from the Kirchhoff relationship. These three components are connected in an open loop system, in which the input for one component cones from the output of the previous component. Thus, the total loading on the airfoil is obtained by summing all of the above components.

In order to adapt the BL DS model for vertical axis wind turbine applications, certain modifications are implemented according to the AeroDyn Theory Manual of NREL [73]. This model is capable of producing aerodynamic force coefficients over the entire range of possible angles of attack. Two different effective separation point tables (f_N and f_C) are calculated as a function of angle of attack for the normal force coefficient and the chordwise force coefficient respectively. The chordwise force coefficient is obtained by adding one additional term from the vortex lift, similar to the normal force coefficient. It is written as

$$C_C = C_{N\alpha}(\alpha_e - \alpha_0)\alpha_e \sqrt{f_C^{"}} + C_N^v \alpha_e (1 - \tau_v) \tag{2.4}$$

where the $C_{N\alpha}$ is the normal force coefficient curve slope, $f_C^{"}$ is the dynamic separation point function taking into account the temporal effects for chordwise force coefficient, C_N^v is the normal force coefficient from the vortex lift contribution and τ_v is a non-dimensional parameter to track the position of the vortex across the airfoil. Finally, the lift coefficient and drag coefficient are calculated from C_N and C_C by force resolution as

$$C_L = C_N \cos\alpha + C_C \sin\alpha \tag{2.5}$$
$$C_D = C_N \sin\alpha - C_C \cos\alpha + C_{d0} \tag{2.6}$$

where C_{d0} is the minimum drag coefficient corresponding to the zero angle of attack.

2.3 Improved DMS Model Considering the Tower Tilting

2.3.1   Description of the effect of tower tilting

The above-mentioned aerodynamic and dynamic stall models are all tailored for onshore wind turbines. If the vertical axis wind turbine is mounted on a floating support structure, a pitch motion of the floating support occurs and the resulting effect of tower tilting on the aerodynamics should be considered to more accurately calculate the performance and aerodynamic loads. Previous research on FVAWTs is limited because this concept was first proposed in recent years. A similar effect has recently been found to be significant in VAWTs operating on buildings where skewed inflow is occasionally present. The effect of the skewed flow on the performance of an H-Darriues designed for installation on roofs of high buildings was modelled using a single actuator disk multiple streamtube model and was measured in a wind tunnel by Mertens et al. [153]. The conclusion of this work shows that the skewed flow causes an effective increase of the energy extraction area and subsequently leads to an increase in the power output. Ferreira et al. [33] further conducted a wind tunnel hotwire measurement to determine the effect of skewed inflow on the thrust variation.

In this next section, the DMS model is reformulated to account for the effect of tower tilting for the curved-blade Darriues VAWTs, including a dynamic stall model. However, the effect of tower tilting is evaluated with respect to the case of steady tilt. The dynamic stall modeling includes Gormont's model with the adaptation of Strickland, Gormont's model with the modification of Berg and the BL DS model. In order to validate the DMS model with different dynamic stall models, the aerodynamic performance and aerodynamic loads at zero tower tilt angle are first calculated and compared with the experimental data; comparative studies of different dynamic stall models are also carried out. The results from different tower tilt angles are compared with those at zero tilt angle of the tower.

2.3.2   Adaptation of the Glauert Momentum Theory for VAWT

The pitch motion of a floating VAWT leads to tower tilt expressed by the tilt angle ϕ. The freestream velocity can be decomposed into a component parallel to the tilted tower and a component perpendicular to the tilted tower. This decomposition is equivalent to the case of having both a horizontal velocity component $U\cos\phi$ and a vertical component $U\sin\phi$ acting on a wind turbine with a non-tilted tower. The general procedure for modifying the DMS model and its subsequent description and analysis are all based on this equivalence, as shown in Figure 2.2.
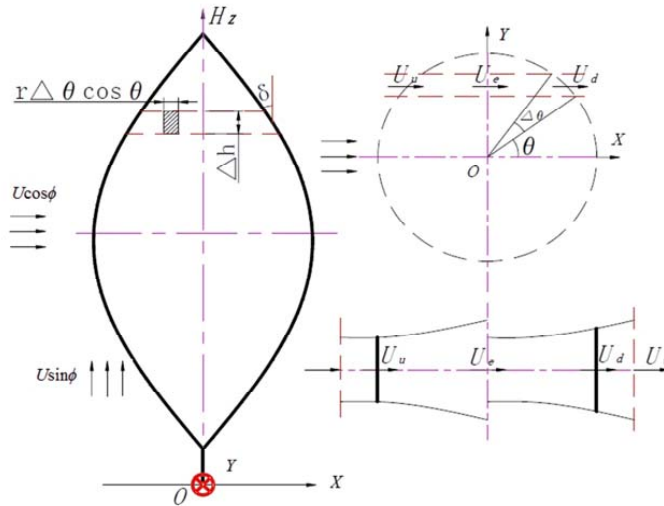
Figure 2.2: Double Multiple-Streamtube Model for a Darrieus wind turbine with two actuator disk in tandem with a horizontal and vertical inflow

The flow through the rotor is subdivided into a sufficiently large number of aerodynamically independent streamtubes. Next, the flow in each streamtube is considered to be acted upon by two actuator disks: the first one representing the upwind half of the surface swept by the rotor blades ($\pi/2\leq\theta\leq3\pi/2$) and the second one representing the downwind half of the rotor ($-\pi/2<\theta<\pi/2$), where the azimuthal angle θ is measured as shown in Figure 2.2. The variation of the induced velocities as a function of the azimuthal angle is considered in each streamtube to distinguish between the loads in the upwind and downwind part of the rotor.

If tower tilting is present, the induction factor a_u is calculated along the direction normal to the tilted tower and the wind velocity at the upwind rotor is decomposed into a horizontal velocity U_u and a vertical velocity V_u. The vertical velocity within the downwind zone is mingled with the turbulent wake from the upwind zone and assumed negligible compared to the complex wake. Then the Glauert momentum theory for yawed flow (according to the Wind Energy Handbook [154]) is applied in the horizontal direction for both the upwind and downwind zones and is coupled with the blade element theory. The contribution from the vertical velocity is considered only for the upwind part of the rotor when calculating the momentum and elemental force. The assumption that the vertical velocity in the downstream zone is negligible is undoubtedly applied for small tilt angles. The extent to which the neglect of the vertical velocity in the downstream zone will affect the calculated result at large tilt angles is an open question. Therefore, pure axial momentum theory will be applied to evaluate the effect of the vertical velocity on the power coefficient by comparing the calculated results with the so-called Glauert momentum theory, which includes the vertical velocity. The difference between these two momentum theories is that the vertical velocity in the upwind zone is included in the mass flow when calculating the

momentum in Equation (2.11) and in the velocity triangle when calculating the angle of attack for the Glauert momentum theory, whereas it is neglected in the axial momentum theory. However, both the momentum and the induced velocity are assumed to be normal to the rotating shaft. The upwind horizontal velocity U_u, the upwind vertical velocity V_u, the equilibrium velocity U_e and the downwind horizontal velocity U_d along any given streamtube can be formulated by Equations (2.7-2.10), respectively:

$$U_u = (\cos\phi - a_u)U \qquad (2.7)$$

$$V_u = U\sin\phi \qquad (2.8)$$

$$U_e = (\cos\phi - 2a_u)U \qquad (2.9)$$

$$U_d = (1 - a_d)U_e = (1 - a_d)(\cos\phi - 2a_u)U \qquad (2.10)$$

Based on the above velocities, the rate of change of momentum for the upwind streamtube and the downwind streamtube are obtained from Equations (2.11) and (2.12), respectively:

$$\Delta I_u = \rho A_s U^2 \sqrt{(\cos\phi - a_u)^2 + \sin^2\phi}\, 2a_u \qquad (2.11)$$

$$\Delta I_d = \rho A_s U_e^{\,2}(1 - a_d)2a_d \qquad (2.12)$$

where A_s is the cross sectional area of the streamtube denoted as $r\Delta\theta|cos\theta|\Delta h$.

2.3.3   Blade Element Theory

When the flow passes over the airfoil, lift force is produced perpendicular to the direction of the relative velocity and drag force acts in the direction of the relative velocity. The normal and tangential forces can be obtained from projection of the lift and drag force according to the azimuthal position. The relative velocity, the angle of attack and the section forces are shown in Figure 2.3. The lift force L and drag force D_r per length are represented by Equations (2.13) and (2.14), respectively:

$$L = C_L \frac{1}{2}\rho W_{Disk}^2 c \qquad (2.13)$$

$$D_r = C_D \frac{1}{2}\rho W_{Disk}^2 c \qquad (2.14)$$

The non-dimensional airfoil characteristics, C_L and C_D, as a function of angle of attack for the local blade element are obtained from experiments with the appropriate wind turbine blade Reynolds number and airfoil shape. The relative velocity and

angle of attack are the foremost parameters that must be determined for evaluating the amplitude and direction of force. Because a difference exists in the velocity distribution between the upwind half of the rotor and downwind half of the rotor, the relative velocity and angle of attack should be treated separately. The W_{Disk} is represented by the local relative velocity at the upwind zone W_u and the local relative velocity at the downwind zone W_d.

Figure 2.3: Velocity and force of blade section

The local relative velocity W_u and the local angle of attack α for the upstream half-cycle of the rotor, $\pi/2 \leq \theta \leq 3\pi/2$, are related by

$$W_u \cos\alpha = \omega r + U_u \sin\theta \qquad (2.15)$$

$$W_u \sin\alpha = U_u \cos\delta \cos\theta + V_u \sin\delta \qquad (2.16)$$

$$\alpha = \tan^{-1}(\frac{U_u \cos\delta \cos\theta + V_u \sin\delta}{\omega r + U_u \sin\theta}) \qquad (2.17)$$

where δ is the angle between the blade normal and the equatorial plane. The second term on the right hand side in Equation (2.16) stems from the vertical component of the wind speed. When the tilt angle ϕ becomes zero, this component will disappear and the equations coincide with their original form in the DMS model.

The local relative velocity W_d and the local angle of attack α for the downstream half-cycle of the rotor, $-\pi/2 < \theta < \pi/2$, are related by

$$W_d \cos\alpha = \omega r + U_d \sin\theta \qquad (2.18)$$

$$W_d \sin \alpha = U_d \cos \delta \cos \theta \tag{2.19}$$

$$\alpha = \tan^{-1}(\frac{U_d \cos \delta \cos \theta}{\omega r + U_d \sin \theta}) \tag{2.20}$$

As stated previously, the vertical component of the wind speed is assumed to be small in the downwind zone such that the formulation for the relationship between the relative velocity and induced velocity is identical to that of the original DMS model.

In order to calculate the power performance and evaluate the influence of the dynamic stall correction, it is convenient to resolve the lift and drag coefficients into a normal force coefficient C_n and a tangential force coefficient C_t, as shown in Equations (2.21) and (2.22):

$$C_t = C_L \sin \alpha - C_D \cos \alpha \tag{2.21}$$

$$C_n = -C_L \cos \alpha - C_D \sin \alpha \tag{2.22}$$

The combination of momentum theory and blade element theory requires projection of the normal force and the tangential force coefficients into a thrust force coefficient C_x and a lateral force coefficient C_y, as shown in Equations (2.23) and (2.24), to calculate the induction factor.

$$C_x = -C_t \sin \theta - C_n \cos \delta \cos \theta \tag{2.23}$$

$$C_y = C_t \cos \theta - C_n \cos \delta \sin \theta \tag{2.24}$$

The average thrust force in the streamtube corresponds to the streamwise force f_x produced by an individual blade element as it passes through the streamtube in which each of N_b blade elements spend $\Delta\theta/2\pi$ percent of their time. Therefore, the average thrust force in the direction of the streamtube at a certain azimuthal position from the blade element theory can be expressed as

$$f_{xave} = \frac{N_b \Delta \theta}{2\pi} \cdot \frac{1}{2} \rho W_{Disk}^2 \frac{c\Delta h}{\cos \delta}(-C_t \sin \theta - C_n \cos \delta \cos \theta) \tag{2.25}$$

By equating Equation (2.25) to Equations (2.11) and (2.12) separately, the induction factor can be calculated from Equations (2.26) and (2.27):

$$a_u \sqrt{(\cos\phi - a_u)^2 + \sin^2 \phi} = \frac{N_b c}{8\pi \cdot r \cdot |\cos\theta|} \cdot \left(\frac{W_u}{U_\infty}\right)^2 \left(-C_{tu} \frac{\sin \theta}{\cos \delta} - C_{nu} \cos \theta\right) \tag{2.26}$$

$$a_d (1 - a_d) = \frac{N_b c}{8\pi \cdot r \cdot |\cos\theta|} \cdot \left(\frac{W_d}{U_e}\right)^2 \left(-C_{td} \frac{\sin \theta}{\cos \delta} - C_{nd} \cos \theta\right) \tag{2.27}$$

The power coefficient is given as

$$C_P = \frac{\bar{T}\omega}{0.5\rho U_\infty^3 S_{wind}}$$ (2.28)

where $\bar{T}$ is the average rotor torque and S_{wind} is the rotor swept area, which is defined as projected area of the rotor seen by the wind.

The integration of the DMS model and the BL DS model in the time domain is represented by a flowchart, as shown in Figure 2.4. At a given time, the relative velocity and the angle of attack are calculated from the DMS model and subsequently become the inputs into the BL DS model. Thus, the normal force coefficient and the chordwise force coefficient are corrected by including the dynamic stall effect. The lift coefficient and drag coefficient are obtained at each time step.
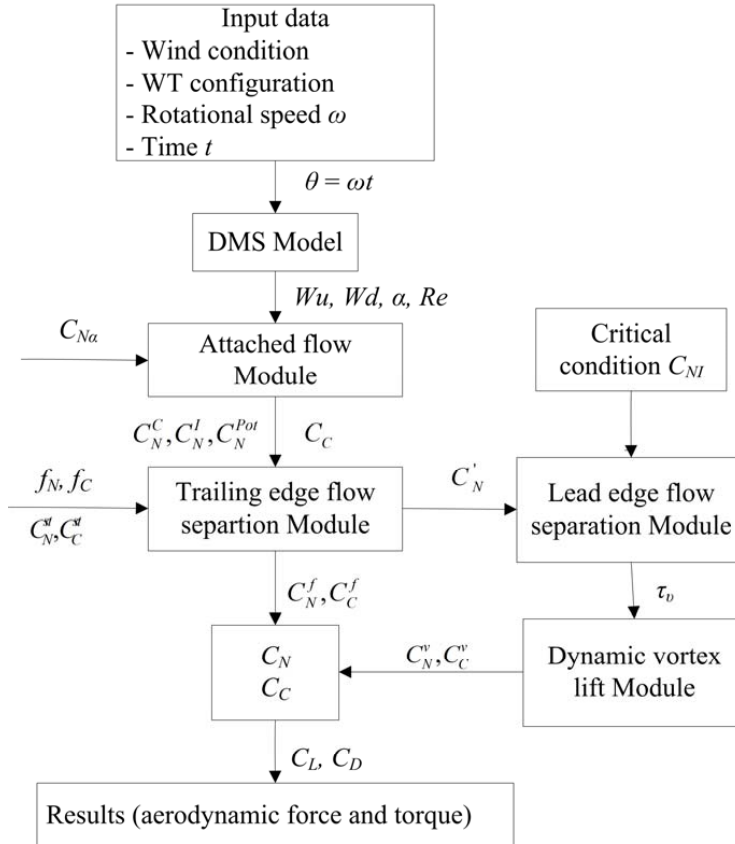

Figure 2.4: Flowchart of the integration of the DMS and the BL DS model in the time domain

2.4 Validation of the Present Model

In this section, the presented modified DMS model is validated against experimental results, demonstrating a high correlation between the theoretical and experimental results. The experimental results were first used by Mertens et al. [153] to validate his analytical model of an H-Darrieus vertical axis wind turbine in skewed flow, as shown in Figure 2.5. The H-Darrieus VAWTs are widely applied on roofs of high buildings where skewed flow is present. The effect of the skewed flow on the performance of an H-Darrieus VAWT was found to be significant and must thus be evaluated properly. Mertens adapted the single disk multiple streamtube model for the H-Darrieus VAWT in skewed flow and carried out the experimental tests for a two-bladed H-Darrieus VAWT of 0.755-m diameter, 0.5-m height and 0.08-m chord length at a wind tunnel velocity of 7 m/s in the open jet wind tunnel of the TU Delft Wind Energy Section. The measurements and calculations performed with the Mertens model for the tip speed ratio and power coefficient are reproduced as shown in Figures 2.6 and 2.7 as a function of the tilt angle ϕ. It is noted that the tip speed ratio in Figure 2.6 corresponds to the maximum power coefficient and the power coefficient in Figure 2.7 is the maximum value for every tilt angle.
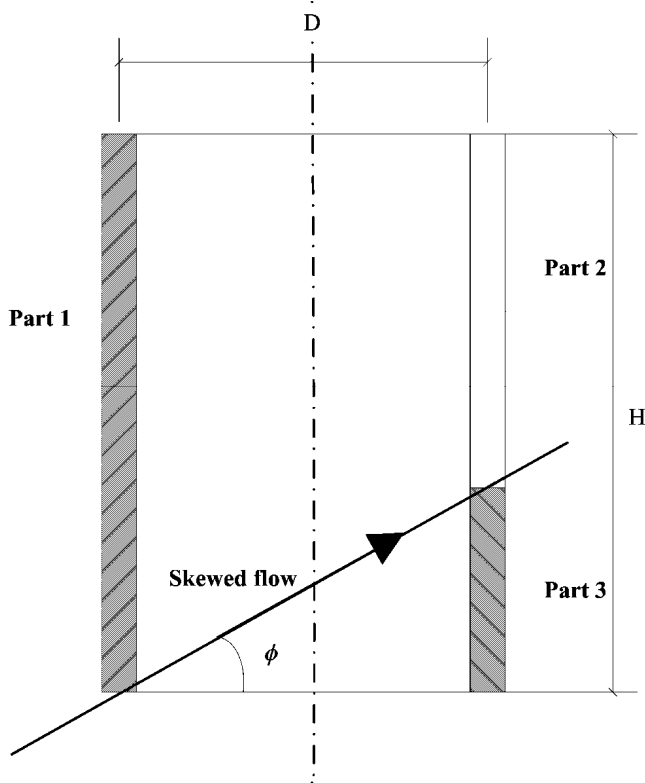

Figure 2.5: Schematic drawing of the H-Darriues partitions

In order to validate the present model using the existing experimental results, the H-Darrieus VAWT is split up into three parts, as shown in Figure 2.5; one part of the rotor is located within the upwind zone, one part of the rotor is located within the downwind zone through which the wake flow passes and one part of the rotor is located within the downwind zone through which the undisturbed flow passes. The effect of the skewed flow on the downwind rotor can thus be taken into account. When the present model is applied, the undisturbed wind speed of the skewed flow is considered for parts 1 and part 3, whereas the reduced wind speed of the wake flow from the upwind zone is calculated for part 2. The lengths of parts 2 and 3 are calculated according to the tilt angle of the flow and the azimuthal position. Furthermore, the dynamic stall model is switched off in this calculation because it was not included in the Mertens model. The calculated results from the present model are compared with the experimental results and the calculated results from Mertens, as shown in Figures 2.6 and 2.7. The comparison of the tip speed ratios shows that the mismatch between data and prediction for the tilt angle at which the tip speed ratio starts to decrease is not improved by the present model, but the predicted value becomes slightly closer to the experimental data, especially for a tilt angle larger than 30 degrees. Comparison of the power coefficient in Figure 2.7 demonstrates that the power coefficient in the skewed flow as predicted by the present model matches the experimental data quite well. However, when the tilt angle is larger than 40 degrees, the power coefficient is overestimated. This result can be primarily ascribed to the observation that the decreasing velocity perpendicular to the blade with the increase of the tilt angle results in a heavily loaded rotor, which causes a convergence failure in the numerical calculation of the momentum equations. However, it can be concluded that the present model works well for predicting the power coefficient when the tilt angle is less than 40 degrees.
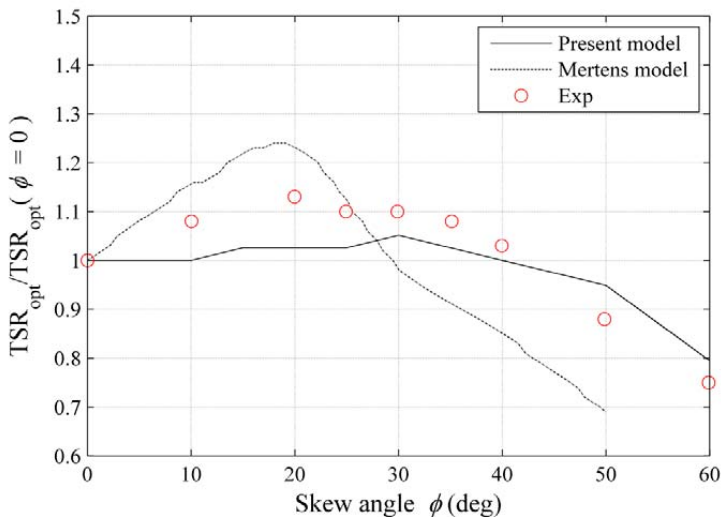
Figure 2.6: Measured and calculated tip speed ratio at maximum power coefficient in skewed flow with skew angle ϕ
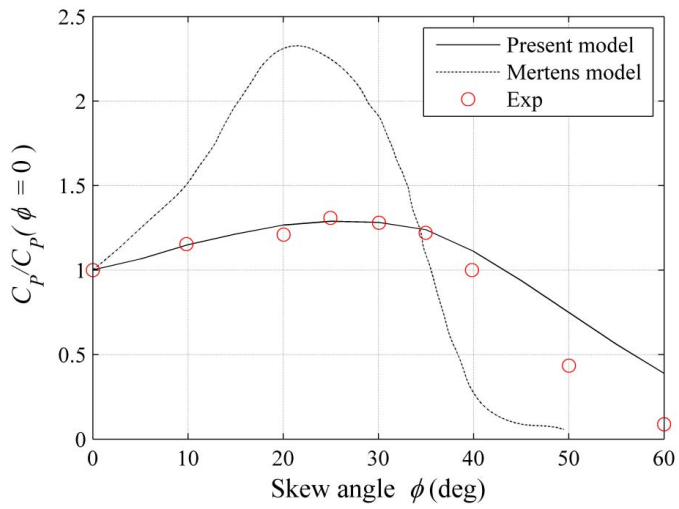
Figure 2.7: Measured and calculated maximum power coefficient in skewed flow with skew angle ϕ

3 Modelling of a Floating Vertical Axis Wind Turbine

Different concepts for floating vertical-axis wind turbines (FVAWTs) have been previously presented based on different combination of platforms and VAWTs in Section 1.2. Platforms used as the floating substructures to support the wind turbine primary include spar, semi-submersible and TLP types. Wind turbines can be one of H-type, Darrieus, helical-bladed and V-type rotors. This Chapter presents another novel FVAWT by combining the DeepWind 5MW rotor [57] and the DeepCwind floater from the OC4 project [155]. It is used as representative turbines in this thesis. A coupled non-linear aero-hydro-servo-elastic model to analyze this concept is described in Section 3.2.

3.1 Floating Vertical Axis Wind Turbine

A novel FVAWT is proposed by mounting a Darrieus-type VAWT on a semi-submersible floater. Thus, it includes a 5 MW Darrieus rotor, a semi-submersible and three catenary mooring lines, as shown in Figure 3.1(a). The Darrieus rotor is composed of two blades and one rotating shaft which spans from the top to the bottom where the generator is connected. The rotor are from the DeepWind project (2010-2014) which is a part of the FP7 European project [48]. The geometry and specification of the rotor are listed in Table 3.1.

Figure 3.1: (a) Floating vertical axis wind turbine   (b) Mooring line arrangement

Table 3.1: Specification of the vertical axis wind turbine

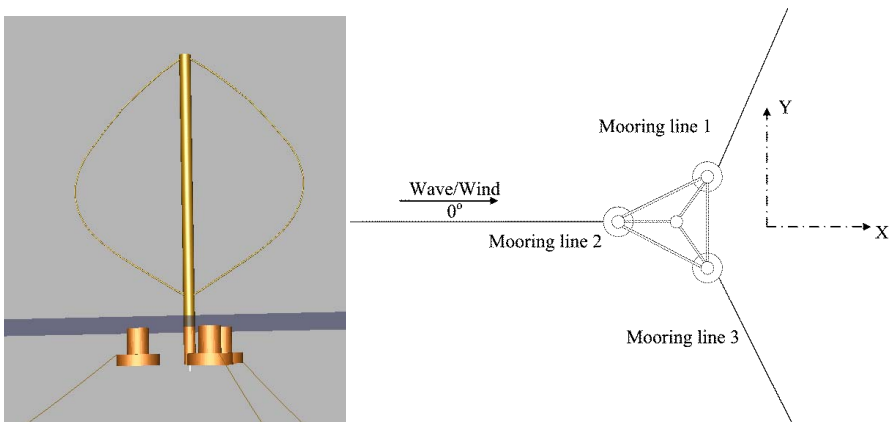| Rated power	5 MW
Configuration	2 blades
Rotor radius	63.74 m
Rotor height / Hub height	129.56 m
Airfoil type	NACA0018
Chord	7.45 m
Cut-in, Rated, Cut-out Wind Speed	5 m/s, 14 m/s, 25 m/s
Rated rotational speed	5.26 rpm
Nacelle Mass	0 kg
Rotor mass	305,044 kg
Shaft mass /Tower mass	449,182 kg
Coordinate Location of Overall CM	(0 m, 0 m, 75.6 m)

The semi-submersible floater is composed of three offset columns, three pontoons, a central column and braces. The offset columns and pontoons are around the central column where the rotor is located. All of the columns and pontoons are connected by braces to form an integrated body. Three catenary mooring lines are attached on the three offset columns to provide horizontal restoring stiffness, as arranged in Figure 3.1(b). Sufficient restoring stiffness is ensured by the large second moment of water line area to limit the mean pitch angle of the platform under various wave and wind conditions. The semi-submersible floater and the mooring line were originally developed for the DeepCwind project and are also used for supporting a 5 MW HAWT in Phase II of the Offshore Code Comparison Collaboration Continuation (OC4) project. DeepCwind is a U.S. - based project aimed at generating field-test data for use in validating floating offshore wind turbine modeling tools. The OC4 project is a continuation of the OC3 project and the Phase II of the OC4 project involved modeling of a semisubmersible floating offshore wind system [155]. When compared to the FHAWT in the OC4 project, the FVAWT uses the 5 MW Darrieus rotor instead of the NREL 5 MW reference HAWT turbine. To adapt the VAWT rotor on the mentioned semi-submersible, the floater had to be slightly modified since the VAWT rotor is heavier than the HAWT rotor. Thus, the ballast water of the FVAWT is slightly less than the ballast water of the FHAWT to ensure the same draft of the two wind turbines. In addition, a direct drive is assumed to be placed inside the central column of the platform, so the gearbox is not considered in the model and the mass of the generator is integrated into the total mass of the platform. The specification of the present FVAWT is listed in Table 3.2.

Table 3.2: Geometry, Structural and hydrodynamic properties of platform configuration

Floater	FVAWT
Depth of platform base below SWL (total draft)	20 m
Spacing between offset columns	50 m
Platform mass, including ballast and generator	13353.7 t
CM location of total concept below SWL	8.66 m
Buoyancy in undisplaced position	14267.41t
CB location below SWL	13.15 m
Hydrostatic restoring stiffness in heave C33	3.836E+06 N/m
Hydrostatic restoring stiffness in roll C44	-3.77E+08 N·m/rad
Hydrostatic restoring stiffness in pitch C55	-3.77E+08 N·m/rad
Moment of inertia in roll	9159733 t·m^2
Moment of inertia in pitch	9159733 t·m^2
Moment of inertia in yaw	12087187 t·m^2

3.2 Coupled Model of the FVAWT

A fully coupled simulation tool Simo-Riflex-DMS was developed for time domain simulation of the dynamic behaviour of a FVAWT. The dynamic responses of the FVAWT were calculated by integrating separate models for the wind inflow, aerodynamics, hydrodynamics, structural dynamics and controller dynamics. Three computer codes are coupled: Simo calculates the rigid body hydrodynamic forces and moments on the floater; Riflex models the blades, tower, shaft and mooring system as finite flexible elements, as well as provides the link to the DMS code and external controller; the DMS code provides the aerodynamic loads on the blades using an external aerodynamic module. The generator torque characteristic was written in Java. Simo implementation computes the hydrodynamic loads at the actually displaced position of the floater, DMS calculates the aerodynamic loads on the blades and Riflex carries out full equilibrium iteration at each time step. This combination produces a comprehensive aero-hydro-servo-elastic simulation tool with sophisticated hydrodynamics, stable non-linear finite element solver, well-known aerodynamics and user-defined controller. The implementation of the individual models was described from section 3.2.1 to section 3.2.4. The computation flow chart for this coupled model in Figure 3.2 illustrates how the developed Simo-Riflex-DMS simulation tool works on this coupled model. The Simo-Riflex wind turbine module has previously been verified [69, 70], and the Simo-Riflex-DMS was presented and verified [156] (see Paper 2).
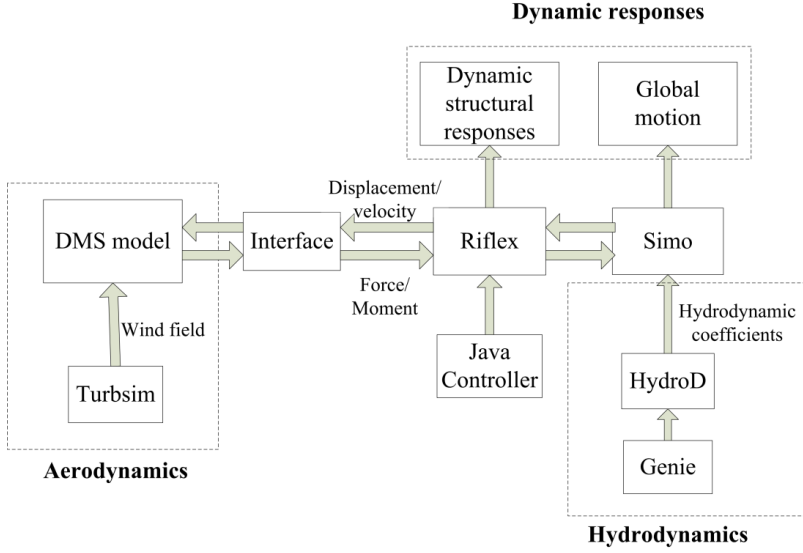
Figure 3.2: Computation flow chart for the coupled model

The equation of motion of the platform under wind and wave loads can be formulated by Equation (3.1):

$$((M+A_\infty)\ddot{x}(t)+\int_{-\infty}^{\infty}\kappa(t-\tau)\dot{x}(\tau)d\tau+(K_m(x(t))+K_h)x(t)=F_{exc}(t) \tag{3.1}$$

where M is the body mass matrix, A_∞ is the added mass at infinite frequencies, $x(t)$ is the displacement of motion, $\kappa(t-\tau)$ is retardation function accounting for frequency-dependent added mass and damping, $K_m(x(t))$ is the non-linear restoring matrix from the mooring system, $F_{exc}(t)$ is the excitation forces. In this study it includes the Froude-Krylov force F^{FK}, diffraction force F^{D}, aerodynamic force F^{Aero} and viscous drag F^{Drag}, shown in Equation (3.2):

$$F_{exc}(t)=F^{FK}+F^{D}+F^{Aero}+F^{Drag} \tag{3.2}$$

The aerodynamic force F^{Aero} is calculated from the aerodynamic model and transferred from the wind turbine to the generator. The applied viscous forces represent quadratic damping on the floater and mooring system. Finally, the equations are solved with aerodynamic loads and hydrodynamic loads included at each time step through Simo-Riflex-DMS simulation tool.

3.2.1 Aerodynamics

The aerodynamic loads for the FVAWT are calculated based on the DMS model including the effect of Reynolds number variations and the Beddoes-Leishman dynamic stall model, as described in Chapter 2. The Beddoes-Leishman dynamic stall model, representing the unsteady aerodynamics of the airfoils for three states: unsteady attached flow, unsteady separated flow and dynamic vortex lift, was applied in all simulations under normal operating conditions, except for the parked condition. Turbulent wind field is generated by Turbsim [157]. However, the global motion of the FVAWT platform poses several challenges to the DMS model. The translational and rotational velocity of the platform motion is to be taken into account in the relative velocity while the inflow velocity is interpolated based on the updated position of each blade element. When calculating the induced velocity in the downstream domain, it is impossible to track the wake velocity from the upstream at the updated position. This limit is due to the DMS model, unlike the vortex method. Therefore, when calculating the induced velocity for a blade located in the downstream, the induced velocity in the corresponding upstream is assumed to be calculated for an upstream blade at the same updated position. One more challenge is to consider the roll and pitch motion into the DMS model. These motions significantly change the direction of streamtube in the DMS model. Tower tilting occurs and the dynamic inflow model needs to be revised. More efforts are necessary on this topic. Otherwise, a more advanced model needs to be employed to include the effect of the platform motion on the aerodynamic model. However, an improved model to evaluate the effect of tower tilting on the aerodynamics of a VAWT was presented in Chapter 2 and it indicates that the effect of the pitch angle of the platform on the aerodynamic loads is almost insignificant up to 10 degrees [158] (*Paper 1*). Therefore, the aerodynamic loads are calculated by assuming that the tower is not tilted, but the blade element velocity from rotational motion of the platform has been taken into account. Additionally, a dynamic wake model for the induced velocity is not considered. Finally, the relative velocity seen at a blade section is the vector sum of the induced velocity, the free wind speed and subtracting the velocity due to the motion. The velocity of the motion is comprised by the blade rotation, the translational and rotational velocity from the platform and the elastic deformation of the blades.

3.2.2 Hydrodynamics

In the calculation of hydrodynamic loads, the floater was considered as a rigid body in Simo and the mooring lines were represented by finite beam elements in Riflex. The hydrodynamic loads on the floater include the first order wave forces and viscous forces. The former is handled by a linear potential flow model while the latter is expressed by the viscous term of the Morison formula. In addition, the hydrodynamic loads on the mooring lines are considered by Morison formula. The potential flow model produced the first order wave forces, as well as added mass and radiation

damping in Wadam [159]. Then the frequency-dependent added mass and radiation damping are used in the Cummins equation as formulated in time domain by Equation (3.1), which will be solved by introducing the retardation function. The retardation function involves a convolution term representing the component of the radiation forces associated with fluid memory effects. The applied viscous force acting a at strip along the length of the slender element is calculated approximately based on the drag coefficient C_d according to the Equation (3.3)

$$dF^{Drag} = \frac{1}{2}\rho_w C_d D |u - \dot{x}|(u - \dot{x})$$

(3.3)

Where ρ_w is the water density, D is the diameter of a column at the stip, u is the water velocity at the strip, $\dot{x}$ is the body velocity at the strip.

3.2.3   Structural dynamics

The structural dynamics of the rotor and mooring lines is calculated by the nonlinear finite element solver in Riflex while the platform is considered as rigid body. The rotor consists of a rotating shaft and two blades. A very short tower is assumed to connect with the rotating shaft and platform in this structural model. The properties as described in [48] are used to establish the structural model. The tower and shaft are modelled as flexible axisymmetric beam elements, while the blades are modelled as flexible beam elements with two symmetric planes to differ the stiffness in the direction along the chord and the direction perpendicular to the chord of blade. Thus, each blade with the length of 188.3 m is modelled by 75 elements with two symmetry axes and the gyroscopic effects and geometric stiffening effect are taken into account in the blade model.

The Newmark-β numerical integration (β = 0.256, γ = 0.505) is used to solve the dynamic equilibrium equations with a time step of 0.0025 s. To ensure the numerical stability, structural damping is included through global proportional Rayleigh damping terms for all beam elements. A global stiffness proportional damping factor is set to 0.003 for all the structures.

3.2.4   Control model

A PI generator controller for the rotational speed is applied in the coupled model. The objective of the control model is to enable variable speed operation maximizing power capture below rated operation point and maintaining generator speed above the rated operation point in the simulations, as show in Figure 3.3. Therefore, the generator torque is provided by the optimized curve of torque versus rotational speed calculated from the aerodynamic model when the rotor rotational speed is smaller than the rated rotational speed. When the rotor rotational speed reaches the rated rotational speed, the PI generator controller is activated to maintain the rotational speed at the rated value.

The generator torque is provided by the PI controller in Equation (3.4). However, the rotational speed oscillates around the specified rotational speed because of the periodically changing aerodynamic forces due to the cyclic variation of the angle of attack during one revolution. The detailed controller strategy and relevant controller parameters have been documented by Merz et al. [90, 91] and the application in this coupled model has been verified (*Paper 2*).

$$T_{gen} = K_P(\omega - \omega_{ref}) + \int_0^t K_I(\omega - \omega_{ref})dt \qquad (3.4)$$

where ω_{ref} is the rated rotational speed, K_P and K_I are the generator controller proportional and integral gains, respectively.
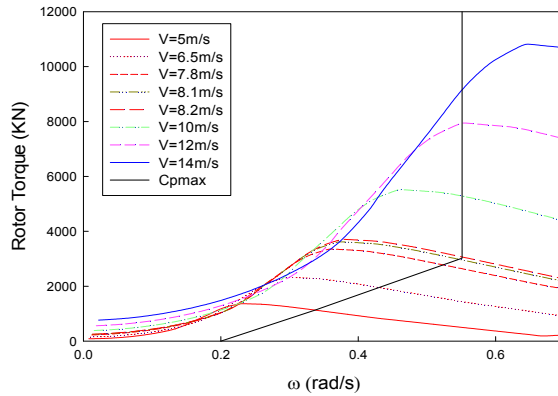
Figure 3.3: Optimized torque-speed curve

3.3 Characteristics of the FVAWT

To determine modal characteristics of the rotor configuration and investigate the structural dynamics of the VAWT rotor, eigenanalysis was performed to obtain natural frequencies and mode shapes of the VAWT rotor. Both Riflex and Abaqus were used to calculate the natural frequencies and corresponding eigen modes of the equivalent land-based VAWT excluding the transmission and generator components, as presented in *Paper 1*. Table 3.3 lists results for the first 10 natural frequencies and mode shapes. The agreement between Riflex and Abaqus is quite good. The flatwise modes are the motion perpendicular to the chord of the blade whereas the edgewise modes are the motion parallel to the chord of the blade. The edgewise modes can be divided in to butterfly modes and twist modes. The butterfly modes are associated with both blades moving in the same direction, like butterfly wings flapping while the twist modes involve motion of both blades in the opposite direction, like rotation of blades around tower.

The natural frequencies shift due to centrifugal stiffening and gyroscopic effects when the blades rotate. The effect of centrifugal stiffening is most prominent in flatwise bending because the increase in stiffness is a much greater percentage of the total

stiffness than in the edgewise case. The gyroscopic effects make significant frequency shifts on tower modes and edgewise modes. In addition, a significant amount of modal cross-talk may occur for dynamic responses.

Table 3.3: Natural frequencies of VAWT in Hertz

Mode Number	Mode type	Frequency (Hz)		
		Riflex	Abaqus	Diff
1	1st tower side-to-side	0.2043	0.2074	1.457 %
2	1st tower fore-aft	0.2195	0.2231	1.645 %
3	1st blade collective flatwise	0.2683	0.2698	0.556 %
4	1st blade asymmetric flatwise	0.2694	0.2719	0.910 %
5	1st blade twist	0.3516	0.3420	2.821 %
6	1st blade butterfly (Edgewise)	0.4276	0.4214	1.457 %
7	2nd blade asymmetric flatwise	0.4940	0.4912	0.556 %
8	2nd blade collective flatwise	0.4986	0.4979	0.139 %
9	3rd blade asymmetric flatwise	0.7641	0.7654	0.172 %
10	3rd blade collective flatwise	0.7724	0.7721	0.037 %

When considering the floating support structure, the natural periods of the global motion of the FVAWT were estimated through numerical simulations of the free-decay test based on the fully coupled simulation tool Simo-Riflex-DMS. In the decay tests, the wind turbines are parked and no aerodynamic loads are acting on the wind turbines. The natural periods of the FVAWT with a rigid rotor and a flexible rotor are both listed in Table 3.4 from *Paper 4* and *additional Paper 1*.

Table 3.4: Natural periods

DOF	Natural period (s) - FVAWT with rigid rotor	Natural period (s) - FVAWT with flexible rotor
Surge/Sway	114.2	114.0
Heave	17.1	17.1
Roll/Pitch	30.3	31
Yaw	79.7	79.7

3.4 Environmental Conditions

In order to design and evaluate a novel offshore concept, it is necessary to choose realistic environmental conditions. It is of great importance to consider combined wind and wave conditions for a FVAWT. Some other conditions such as current, ice and tidal conditions could be important at some offshore location. However, consideration on such conditions is outside the scope of the present work. In addition, the loading and response for the FVAWT should be considered from probabilistic perspective due to the randomness of wind and wave in nature.

The wind speed has spatial and temporal variation with longitudinal, lateral and vertical components. The longitudinal component is considered as primary wind direction at which the mean wind speed is described for periods 10 minutes or 1 hour. The sum of mean wind speed and fluctuating part represents an instantaneous wind speed at certain direction and a particular point in space. The mean lateral and vertical wind speed are assumed to be zero in the present thesis. The temporal variations in wind speed are quantified by turbulent intensity which is defined as the ratio between the standard deviation of the wind speed and the mean wind at a reference height. The normal turbulence model (NTM) was used in this thesis according to the IEC standard. A three-dimensional turbulent wind fields were generated using NREL's TurbSim program [157] based on the Kaimal turbulence model for IEC Class C. In addition to spatial coherence included in the model, variation of the mean wind speed with height above the ground is significant, and known as wind shear due to viscous boundary layer effects. For the normal wind profile model (NWP) proposed in IEC standard, the power law formulation of the wind shear is applied to calculate the wind profile $U(z)$ as a function of height z above the mean sea level, as in Equation (3.5)

$$U(z) = U_{ref}(z/z_{ref})^{\alpha} \qquad\qquad (3.5)$$

where U_{ref} is the reference wind speed, z_{ref} is the height of the reference wind speed and α is the power law exponent. For this study, the value of z_{ref} was set to 79.78 m (vertical center of blades) above mean sea level and the value of α was set to 0.14 for the floating turbine according to IEC 61400-3 [160].

Ocean waves are characterized by irregularity and randomness in shape, height, length and speed of propagation. A real sea state can be described by a linear random wave models or a non-linear random wave model. The former is a sum of many small linear wave components with different amplitude, frequency and direction. The simplest one is the linear long-crested wave model, as in Equation (3.6). The latter allows for sum and difference frequency wave component caused by non-linear interaction between the individual wave components. Several wave theories, such as linear wave theory, Stokes wave theory, cnoidal wave theory, solitary wave theory and stream function wave theory, have been developed to describe wave surface elevation at specific ranges. The ranges of validity for the different wave theories are determined by the wave height, the wave period and the water depth [161]. The linear wave theory as the simplest one is usually referred to Airy theory, and widely used when the wave height is much smaller than both the wave length and water depth. This linear wave theory can be improved by introducing higher-order terms in a consistent manner through the Stokes expansion [162]. Linear waves and Stokes wave provide directly wave kinematics below z=0 and wave kinematics between the wave crest and the still water level can be estimated by different mathematical models such as constant stretching and Wheeler stretching method. In contrast, the stream function provides wave kinematics all the way up to the free surface elevation.

In the present research, the linear wave theory is applied to simulate irregular wave as a summation of sinusoidal wave components, and the linear long-crested wave model is correspondingly given by [162]

$$\varsigma(t) = \sum_{j=1}^{N} A_j \sin(\omega_j t - k_j x + \varepsilon_j)$$ (3.6)

In Equation (3.6), $\varsigma(t)$ is the free surface elevation for long-crested waves travelling in the positive x-direction, A_j is the wave amplitude, ω_j is the k_j is the wave number and ε_j is the phase angle of component j. ω_j and k_j are related by the dispersion relation.

The wave elevation obtained by Equation (3.6) can be assumed to be Gaussian-distributed. If the wave elevation is further a narrow-banded process, the wave crests follow the Rayleigh distribution. Based on the Gaussian assumption, the wave elevation can be related to a wave spectrum which represents an offshore site, and then the wave time series are generated by using inverse fast Fourier transformation (IFFT). The amplitudes can be derived from the wave spectrum, while the phase angle is uniformly distributed within the interval [0 2π]. The JONSWAP (Joint North Sea Wave Project) spectrum has been used for generating the long-crested irregular waves in this thesis, given by

$$S(\omega) = \frac{\alpha g^2}{\omega^5} \exp(-\beta(\frac{\omega_p}{\omega})^4) \gamma^{\exp(-\frac{(\omega/\omega_p - 1)^2}{2\sigma^2})}$$ (3.7)

where

$$\alpha = 5.061 \frac{H_s^2}{T_p^4}(1 - 0.287\ln(\gamma))$$ (3.8)

$$\sigma = \begin{cases} 0.07 \, for \omega < \omega_p \\ 0.09 \, for \omega \geq \omega_p \end{cases}$$ (3.9)

In Equation (3.7), α is spectral parameter, γ is the peakedness parameter and a typical value of γ=3.3 represents a sea state that is not fully developed, β is the form parameter and ω_p is peak frequency ($\omega_p = 2\pi/T_p$) [163].

For the combined wind and wave conditions, the correlation between the wind and waves should be considered by using a joint distribution of the 1-hour mean wind speed at 10 m above sea water level, the significant wave height (H_s) and the spectral peak period (T_p). Based on wind and wave measurements from 1973-1999, Johannessen et al. [164] proposed a joint probability density distribution as a product of the marginal wind distribution $f_{U_{10}}(w)$, the conditional distribution of H_s given U_{10}, and the conditional distribution of T_p given H_s and U_{10}, as in Equation (3.10)

$$f_{U_{10}H_sT_p}(u,h,t) = f_{U_{10}}(w)f_{H_s|U_{10}}(h\,|\,u)f_{T_p|H_sU_{10}}(t\,|\,h,u)$$ (3.10)

This joint probabilistic model can be used to establish a contour surface and provide combinations of the weather parameters with a certain return period. In the present thesis, the joint distribution function has been used to calculate conditional mean values of H_s and T_p for a given U_{10} which is calculated from the wind speed U_w from cut-in to cut-out wind speeds at the reference height z_{ref}. A set of environmental conditions has been chosen for simulating FVAWT response based on calculated correlated wave and wind conditions at the Statfjord site in the North Sea. As shown in Table 3.5, the wind and waves are correlated and directionally aligned corresponding to normal operating condition. Furthermore, the parked condition for the FVAWT was also chosen to be a one-hour mean wind speed of 50 m/s, a significant wave height of 12.9 m and a spectral peak period of 14.1 s.

Table 3.5: Combined wind and wave environment for normal operating condition

Load case	U_w (m/s)	H_s (m)	T_p (s)	Turb. Model
LC 1	5	2.10	9.74	NTM
LC 2	10	2.88	9.98	NTM
LC 3	14	3.62	10.29	NTM
LC 4	18	4.44	10.66	NTM
LC 5	22	5.32	11.06	NTM
LC 6	25	6.02	11.38	NTM

4 Dynamic Response Analysis of the FVAWT

4.1 General

A variety of studies have been conducted on floating horizontal axis wind turbines FHAWTs to better understand the performance of different concepts and to provide the basis for a detailed structural design. Xing et al. [165] studied the drivetrain dynamics of a spar-type FHAWT. The loads and motions on the drivetrain calculated from HAWC2 were used as inputs for a multi-body drivetrain model in SIMPACK, and thus the main shaft loads and internal drivetrain responses were studied. Jiang et al. [166] analyzed the dynamic response of a 5 MW FHAWT under blade pitch system fault and emergency shutdown conditions. Stochastic dynamic response of a tension leg spar-type offshore wind turbine was analyzed by Karimirad and Moan [167]. The effect of hydrodynamic modeling and mooring line modeling on the motions and structural fatigue damage for a semi-submersible wind turbine have been investigated and a frequency versus time domain fatigue analysis of the same wind turbine has been conducted by Kvittem et al [80, 81, 168].

For FVAWTs, limited research has been performed, especially regarding dynamic response analysis based on a fully coupled model. Berthelsen et al. [169] presented a conceptual design of a floating support structure and mooring system for the DeepWind concept and conducted a feasibility study using efficient frequency-domain technique. A research group at the Technical University of Denmark (DTU) has performed a design optimization of the proposed DeepWind concept [58]. An improved design has been obtained with an optimized blade profile with less weight and higher stiffness than the 1st baseline design. However, the optimization of this design has not been published. Based on a developing simulation tool named as FloVAWT [99, 170], Borg et al. [171-174] presented a review of the dynamic modeling of FVAWTs, used a wave energy converter as a motion suppression device for floating wind turbines and further performed a comparison on the dynamics of FVAWTs with three different floating support structures. Furthermore, different simulation tools are being developed to investigate the behavior of FVAWTs. Hence it is of great interest to assess the effect of different models used in the simulation tools. Thus, a comparison of two coupled dynamic models for FVAWTs has been conducted by Borg et al. [175]. The comparison identified the importance of the dynamic modelling of the mooring lines and the control model, and it also

discussed the needs for further development. However, other aspects in modeling also need to be addressed. One of these aspects is the modeling of the flexibility of the blades and the rotating shaft which was not considered in the comparative study [175]. The rotor was assumed to be rigid for the code-to-code comparison, so the effect of structural flexibility should be further studied. Moreover, the comparative study focused on the mechanics. The stochastic nature of the response also needs to be properly addressed.

In this thesis, the stochastic dynamic response of the studied FVAWT has been calculated based on fully coupled nonlinear time domain simulations under different environmental conditions. The fully coupled nonlinear time domain simulations are conducted using the developed Simo-Riflex-DMS coupled solver as presented in Chapter 3. The dynamic response of the FVAWT includes global motions of the platform, structural responses of the rotor, and mooring line tension. Analysis for the FVAWT is focused on the turbulent effect and flexibility effect on the dynamics response under normal operating conditions in Section 4.2. In addition, the behavior of the FVAWT is also compared to an equivalent land-based wind turbine. In Section 4.3, the dynamic response is determined as a function of azimuthal angle in the parked condition, and in Section 4.4, the dynamic response of the FVAWT in misaligned wind and wave conditions is also analyzed. To study the FVAWT with consideration of fault, the dynamic response has been investigated under emergency shutdown condition based on the use of a novel hydrodynamic brake in Section 4.5. The last section of this chapter shows a comparative study between the FVAWT and a FHAWT.

4.2 Responses Under Normal Operating Condition

4.2.1   Turbulence effect

When FVAWTs operate in wave and wind conditions, the rotor experiences aerodynamic loads that vary continuously as a function of the azimuthal blade position, even in steady wind. Turbulent wind can magnify this variation and introduce additional excitation. To investigate these effects, it is of importance to study the response characteristics of the FVAWT under steady wind and turbulent wind conditions and make comparison between the dynamic responses of these two conditions. The irregular waves are used as the wave condition. At specific mean wind speed, identical time series of wave elevation are generated in combination with the steady wind and the turbulent wind.

Figure 4.1 compares the generator power output of the FVAWT under steady wind and turbulent wind conditions. The wind speed is used as the variable on the abscissa axis, the corresponding wave conditions are given in Table 3.3 in Chapter 3. The

power curve is based on the mean value of the simulated power for each 3600 s simulation after removing start-up transient for five different seeds. The variability in the power output is indicated by error bars showing the standard deviation from the mean values. Although the same control model is used for steady and turbulent wind conditions, the mean power is observed to differ above the rated wind speed of 14 m/s, and the difference increases as the wind speed increases. The mean value rather exceeds the rated power of 5 MW at the rated wind speed because the BL dynamic stall model is included in this model; the mean value just reaches 5 MW at the rated wind speed when the dynamic stall model is not included in the DMS model. This demonstrates that the dynamic stall model is important in the design of the DeepWind rotor. Additionally, it is observed that the variation in the power under turbulent wind conditions is greater than the variation under steady wind conditions.
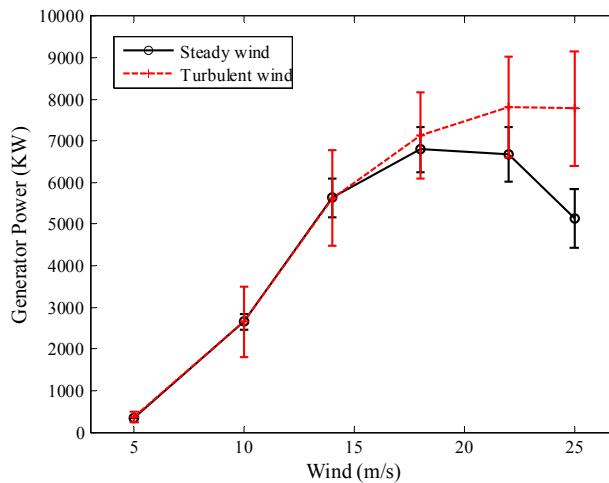

Figure 4.1: Power production under steady and turbulent wind conditions

In *Paper 5*, several measures of the dynamic response, including the global motion of the platform (i.e., surge ζ_1, sway ζ_2, heave ζ_3, roll ζ_4, pitch ζ_5 and yaw ζ_6), the tower base fore-aft bending moment (the FA bending moment), the tower base side-side bending moment (the SS bending moment) and the tension of the mooring lines, are used as the primary performance parameters. Figure 4.2 shows the time series and power spectrum for pitch motion of the platform from one realization in steady and turbulent wind for LC 4. Higher amplitude pitch motion is observed in the time history for the turbulent wind condition than for the steady wind condition, and this can be explained by comparing the power spectra to evaluate the effect of turbulent wind. The turbulent wind excites much larger pitch natural responses at the frequency of 0.2 rad/s and lower-frequency responses with energy contents in the range of the wind spectrum. Furthermore, a peak at the 2P frequency is also observed for both steady and turbulent wind conditions. It should be noted that the 2P frequency originates from the characteristics of vertical-axis wind turbines with two blades. Because the axis of rotation is not parallel to the wind direction and the angle of attack of the blades varies with the azimuthal position during operation, the

aerodynamic loads vary within one revolution. For a two-bladed wind turbine, the variation in the torque occurs twice per revolution, and the 2P variation leads to the 2P frequency. When the wind turbine rotates at the rated rotational speed of 0.551 rad/s, the 2P frequency is approximately 1.1 rad/s. However, the peak corresponding to the 2P frequency for turbulent wind is slightly lower than the peak for steady wind, which indicates that the 2P effect is reduced slightly by the turbulent wind. A similar result can be observed for the surge, sway, roll and yaw motions. The responses at the natural frequency of each motion, i.e., 0.055 rad/s for surge and sway motions, 0.2 rad/s for roll and pitch motions and 0.079 rad/s for yaw motion, are significantly magnified under turbulent wind conditions.
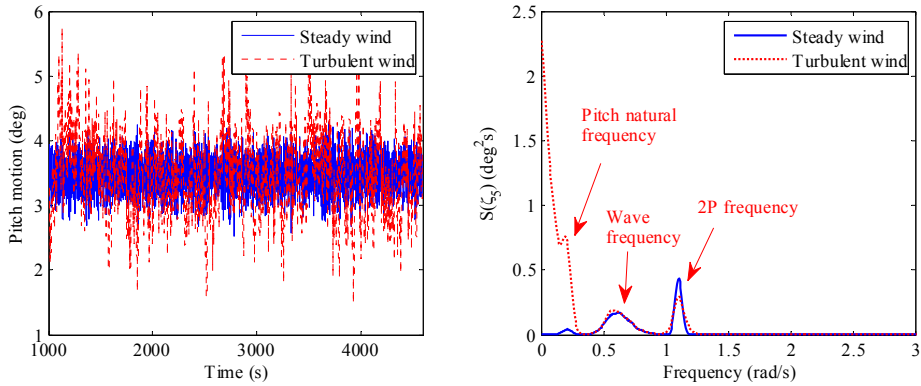

Figure 4.2: Time series and power spectrum of pitch motion for $V = 14$ m/s, $H_s = 3.62$ m and $T_p = 10.29$ s

In the mooring system, the low-frequency responses of the mooring line tension due to the turbulent wind are also excited significantly. The peak corresponding to the 2P frequency in the turbulent wind condition becomes higher than the peak in the steady wind condition as the wind speed increases, whereas the peak at the higher structural natural frequency becomes lower under the turbulent wind condition. Similar effects on the bending moments are observed at the 2P frequency and the structural natural frequency. The effects are only obvious at high wind speeds, such as 22 and 25 m/s. Additionally, the turbulent wind excites the low-frequency response in the fore-aft bending moment more than in the side-side bending moment.

In addition to the power spectral density, the statistics for the responses, such as mean values, standard deviations and maximum values, is also important for the comparison. Figure 4.3 shows the statistics for pitch motion, yaw motion, the tension of mooring line 2, the side-side bending moment and the fore-aft bending moment at the base of the tower for different wind conditions. The mean values for surge and yaw motion depend on the mooring system stiffness and the wind load while the mean values for roll and pitch motion depend primarily on the restoring moment of the platform and the moment due to the wind turbine thrust. The tension of the mooring system is related to the displacement due to surge, sway and yaw motion. The bending moments

also depend on the tower and blades displacement (gravitational loading) relative to the platform and the wind loads on the rotor. Therefore, the mean values are almost identical under steady and turbulent wind conditions. A slight difference is observed at the high wind speed of 25 m/s due to the small difference in the rotational speed produced by the control model under turbulent wind conditions. The effect of turbulent wind can be seen clearly by comparison with the steady wind results. Both the standard deviations and the maximum values of the selected responses are greater in the turbulent wind condition than in the steady wind condition. Moreover, the difference in the yaw motion is much greater because the restoring moment in the yaw motion from mooring system stiffness is small.
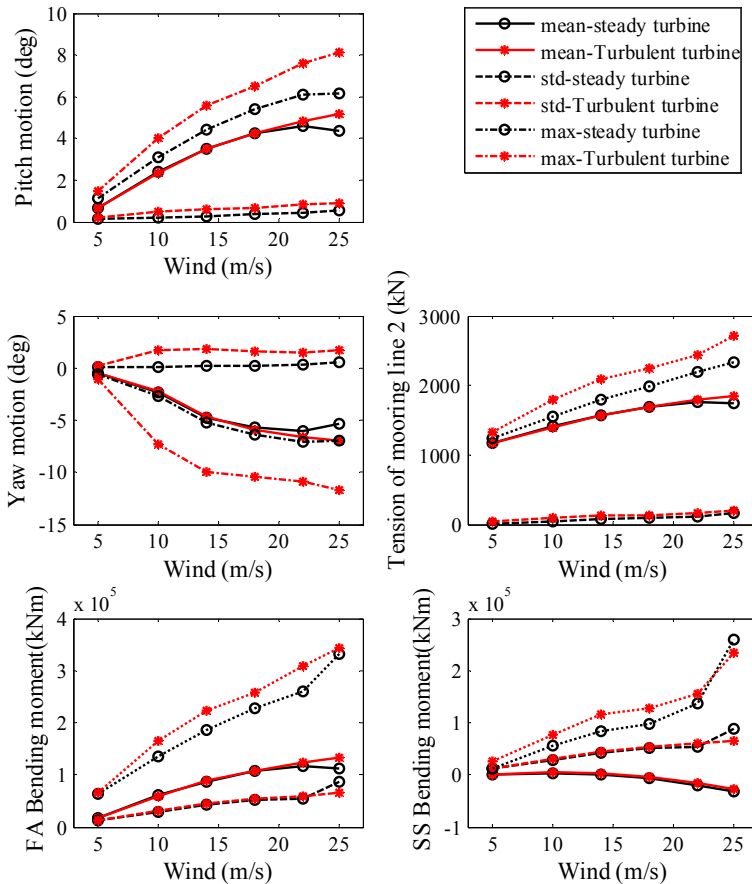

Figure 4.3: Comparison of selected response statistics: mean values, standard deviations and maximum values of pitch and yaw motion, mooring line tension and tower base bending moments

4.2.2   Effect of structural flexibility

When establishing a model for a floating wind turbine, the wind turbines can be modeled to be rigid so as to simplify the integrated system. Thus, the question is then what level of accuracy can be obtained when using this rigid model as compared to a model with representation of the structural flexibility. Based on the use of Statoil's implementation of Thrust-Dynamic-Horizontal-Mill (TDHMILL), Karimirad and Moan [68, 176] has showed that the global motion and structural response for floating wind turbines were dominated by rigid body motions rather than elastic deformations, except for the local response of the rotor, such as the blade structural responses. Moreover, Karimirad and Moan [71] further introduced a simplified method for the dynamic analysis of floating wind turbines based on the rigid body formulation to analyze the general motions and structural responses with acceptable accuracy. Although this finding has been observed for FHAWT, there is still a need for evaluating the effect of structural flexibility on the dynamic response of the FVAWT by comparing a rigid wind turbine to the flexible wind turbine under the same wave and turbulent wind conditions. A comparison between the modeling of an elastic wind turbine and the modeling of a rigid wind turbine is of importance, and therefore this comparison is performed in *Paper 5*.

The flexible wind turbine refers to the FVAWT studied in this thesis. To model the rigid wind turbine, the axial, bending and torsional stiffness are set sufficiently high to be regarded as rigid. All other properties and environmental conditions remain the same for the two wind turbines. To highlight the differences in the responses of the rigid wind turbine and the flexible wind turbine in the turbulent wind conditions, the comparison focuses on the normalized mean values, standard deviations and maximum values of the responses. The normalized values are defined as the ratio of the results for the FVAWT to the results for the rigid wind turbine.

Figure 4.4 shows the normalized mean values, standard deviations and maximum values for all responses under different turbulent wind and wave conditions. The normalized mean values are very close to 1 except for the pitch and the fore-aft bending moment, which are significantly larger than 1 at a wind speed of 5 m/s and slightly greater than 1 as the wind speed increases. However, the surge and yaw values are slightly less than 1 at wind speed greater than 5 m/s. In the normalized standard deviations, the effect of structural flexibility on the responses is obvious except for the surge motion. The flexible wind turbine has lower standard deviations for pitch motion than the rigid wind turbine, whereas the standard deviations for the fore-aft bending moment are much greater in the flexible wind turbine than in the rigid wind turbine as the wind speed increases. Additionally, the standard deviations for the tension of mooring line 1 and 3 vary more than the values of the tension of mooring line 2 because mooring lines 1 and 3 are less tensioned than the mooring line 2, and they consequently have lower mean values. Therefore, greater consideration should be given to the tower bending moment and the tension of mooring lines 1 and

3 when performing fatigue calculations in a simplified model to determine whether the rigid wind turbine is sufficient to replace the flexible wind turbine. For the normalized maximum values, the most apparent difference occurs in the fore-aft bending moment, which has a greater maximum in the flexible wind turbine than in the rigid wind turbine because the deformation of the wind turbine produces extra gravitational loading on the rotor, resulting in a larger bending moment. Unlike the mean values for pitch, the maximum pitch values are lower in the flexible wind turbine at lower wind speeds, whereas they are close to the values for the rigid wind turbine at higher wind speeds. The effect of structural flexibility on the maximum values of the other responses is not pronounced, except for the maximum surge value at a wind speed of 5 m/s.

Figure 4.4: Comparison of selected responses for the flexible FVAWT normalized by the values for the rigid FVAWT

The reason for the differences observed between the rigid wind turbine and the flexible wind turbine can be determined through the power spectra for different responses. For instance, at the low wind speed a larger mean pitch is observed for the flexible wind turbine while smaller standard deviation and maximum value of the pitch is observed. The reason is that the rigid wind turbine has a much larger peak corresponding to the pitch natural response than the flexible wind turbine at the low wind speed, as shown in Figure 4.5. This might be because the flexible rotor provides more aerodynamic damping than the rigid rotor, especially at low wind speeds. More observation and detailed explanation can be found in *Paper 5*.

It should be highlighted that the effect of structural flexibility on the natural frequencies of the global motion can be neglected, but the effect on the standard

deviations of the global motion and mooring lines should be considered when evaluating modeling of a FVAWT. The effect of the structural flexibility on the fore-aft bending moment of the tower base is the most apparent. Kvittem and Moan [81] found that the frequency-domain model with the rigid structure assumption gave a reasonable representation of the frequency content in the bending moment, but the amplitude were underestimated by 10-17% when compared to a time-domain model with the flexible structure. A similar result that the standard deviations of the fore-aft bending moment of the FVAWT with the rigid structure assumption are significantly underestimated is observed.
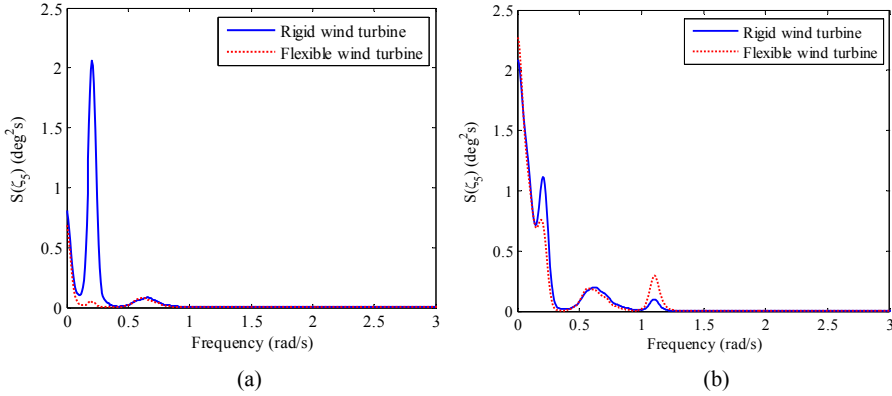

Figure 4.5: Comparison of the power spectra of pitch motion for the rigid FVAWT and the flexible FVAWT: (a) LC 1 V = 5 m/s, H_s = 2.1 m and T_p = 9.74 s and (b) LC 4 V = 14 m/s, H_s = 3.62 m and T_p = 10.29 s

4.2.3   Comparison of response in the FVAWT and a land-based VAWT

The floating support of a FVAWT makes the response characteristics of the wind turbine much different from those of an equivalent land-based wind turbine. Identifying the advantages and challenges of the use of VAWTs in offshore applications compared to equivalent land-based wind turbines is also of importance. The same rotor used in the FVAWT is installed on the ground to form a land-based vertical-axis wind turbine. However, no guy cables connecting the top of the tower with the ground are used, as would be common in VAWTs.

The generator power between the land-based wind turbine and the floating wind turbine is first compared, as shown in Figure 4.6. The FVAWT can produce a bit more power than the land-based wind turbine below the rated wind speed while it produces less power with increasing wind speed up to the cut-off wind speed. It indicates mounting a VAWT on a platform does not affect the ability of power generation significantly.
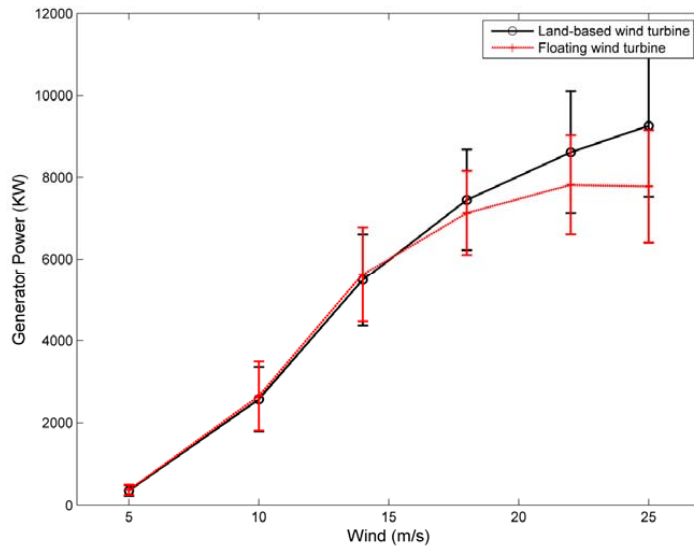
Figure 4.6: Power production of the land-based and the floating wind turbines
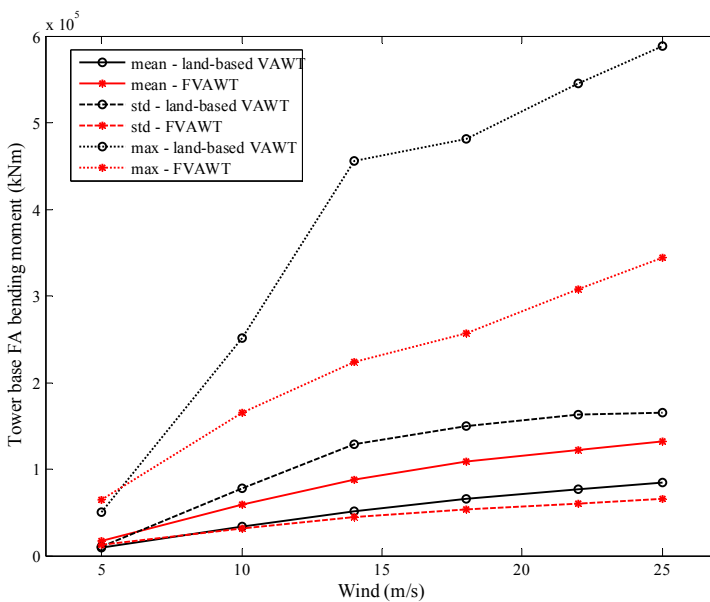
Figure 4.7: Comparison of the tower base fore-aft bending moment between the land-based VAWT and the FVAWT

The response of the FVAWT is also compared with the response of the land-based wind turbine. As observed in *Paper 5,* the 2P effect on the fore-aft bending moment and side-side bending moment is much larger in the land-based wind turbine than the FVAWT. This indicates that the floating support structure can mitigate the 2P excitation that is considered one of the most critical challenges for VAWTs. Therefore,

the standard deviations and maximum values for the fore-aft bending moment in the FVAWT are smaller than in the land-based wind turbine, as shown in Figure 4.7. The maximum response values for the land-based wind turbine are much larger than the maximum values for the FVAWT, and the difference increases with wind speed. Whereas, the mean values for the fore-aft bending moment in the FVAWT are larger than the land-based wind turbine due to large bending moment contribution from the non-zero tilt angle of the tower in the FVAWT.

It can be briefly concluded that the tower base bending moments in the FVAWT at the 2P frequency are found to be much reduced when compared to the tower base bending moments in an equivalent land-based VAWT. The 2P effect on the structural integrity and fatigue damage in the VAWTs is significant, but this result indicates that some of the 2P effects can be alleviated with a floating platform.

4.3 Effect of the Azimuth angle in Parked Condition

VAWTs with fixed-pitch blades experience large aerodynamic loads in high wind conditions or in stormy weather. The blades may be deformed or broken, and in the most severe cases, the tower could collapse because there is no blade pitch mechanism in VAWTs with Darrieus rotors. Thus, it is important to ensure the survival of the FVAWT in extreme conditions, by proper choice of the azimuthal position of the blades. Hence, the effect of the blade position on the dynamic response should be studied in the parked condition.

The rotor is assumed to be in a standstill configuration when the turbine is parked. The azimuthal position of the rotor is crucial to the global and structural responses of the FVAWT in the parked condition. Figure 4.8 illustrates the rotor at two azimuthal angles θ measured from the positive wind direction along the X axis of the global coordinates XOY. A series of simulations is performed at different azimuthal angles under aligned wave and wind conditions, and the results are analyzed using the statistical method. Figure 4.9 shows the mean values, standard deviations and maximum values of the global motion as a function of the azimuthal angle. The azimuthal angle has little effect on the standard deviations of the surge, sway and heave motions, but the difference in the standard deviations of the roll, pitch and yaw motions with different azimuthal angle is apparent. The difference in the standard deviations with the azimuthal angle depends on the different excitations contributing to the peaks in the power spectra as studied in *Paper 5*. The effect of the azimuthal angle on the standard deviations of the global motions is less significant than the effects on the mean values and maximum values. The mean values and maximum values of all global motions except the heave motion vary significantly as the azimuthal angle changes. The azimuthal angles corresponding to the highest and lowest mean values and maximum values can be obviously observed for the different

motions. An important result is that the optimal azimuthal angle is found to be 90 degrees based on the consideration of all motions. At the optimal azimuthal angle, the mean values, standard deviations and maximum values of the responses are smallest compared to the values at other azimuthal angles. On the contrary, the worst azimuthal angles, corresponding to the largest responses for each of the platform motions, can also be observed. These angles are important when evaluating the ultimate loads for structural design.

The statistical results for the bending moments as a function of the azimuthal angle were also studied. To reduce the amplitude of the bending moments and improve the safety of the wind turbine in the parked position, the azimuthal angle of the blade should be set to approximately 90 degrees, at which the chords of the blades are parallel to the direction of the wind. The standard deviations also depend on the azimuthal angle because the wind-induced loading in the low-frequency range dominates the dynamic response for the bending moments at the different azimuthal angles. A similar result can be observed for the mooring line tension, and the optimal azimuthal angle is also found for the dynamics of the mooring lines.

It can be briefly concluded that the azimuthal angle at which the responses in the parked condition are minimized occurs when the chords of the blades are aligned with the wind. This is important for the survivability of the FVAWT.
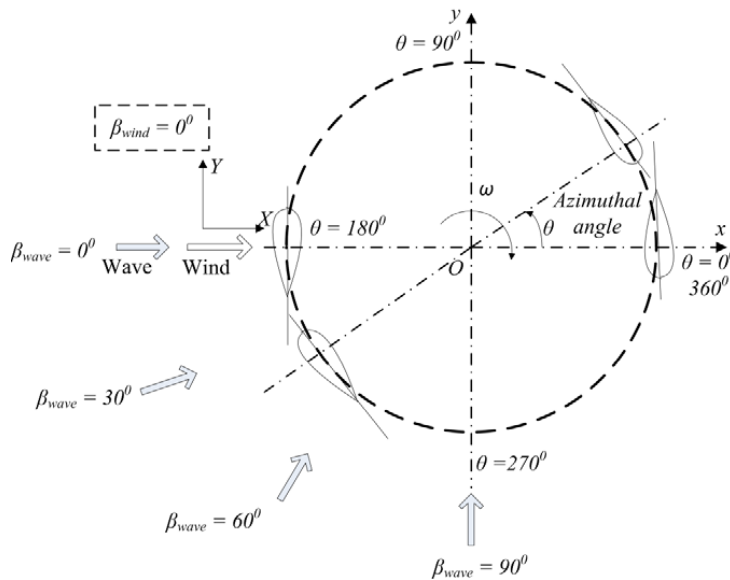

Figure 4.8: A horizontal cross section of the rotor showing the azimuthal angle in parked conditions and showing the wave direction distribution in wind-wave misalignment conditions
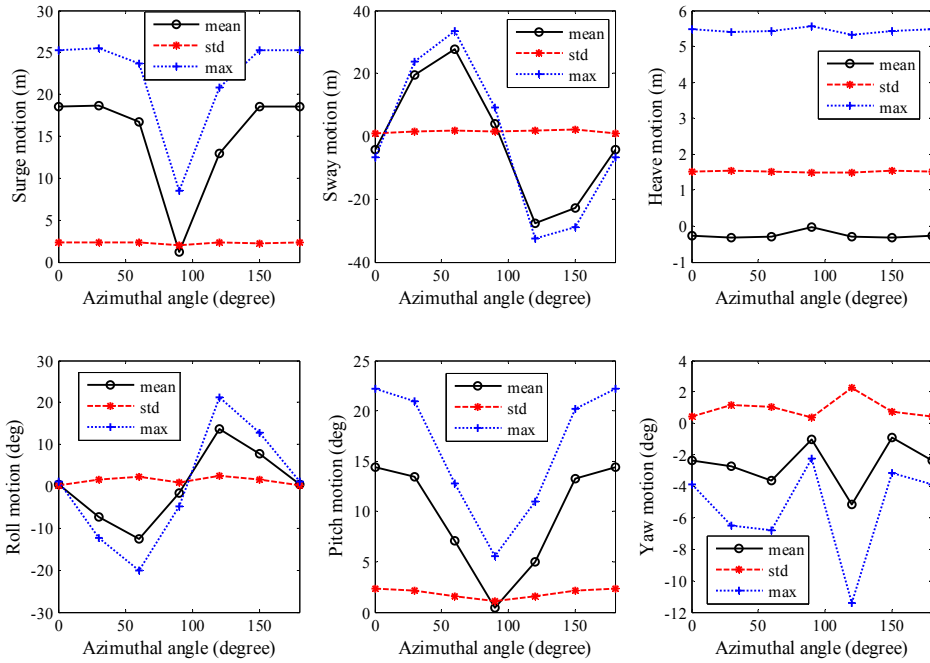
Figure 4.9: Statistical values of the global motion as a function of the azimuthal angle in the parked condition

4.4 Misaligned Wind and Wave Condition

When considering combined wind and wave conditions, the misalignment between the wind and wave should also be taken into account in the dynamic analysis of a FVAWT. In general, large misalignments occur at lower wind speeds while small misalignments occur at higher wind speeds [177]. Based on observations in the North Sea, it is common to reach 30 degrees of misalignment, but misalignments greater than 60 degrees occur less than 5% of the time [178]. Therefore, misalignment effects on four different FHAWTs were investigated in conditions of up to 90 degrees of misalignment between the wind and wave directions by Bachynski et al. [179], whereas Barj et al. [180] conducted a study on wind-wave misalignment in the loads analysis of a spar floating wind turbine for all angles between wind and wave directions.

To investigate the effect of wind-wave misalignment on the dynamic response of the FVAWT, numerical simulations are performed for a wind direction of 0 degrees and four wave directions (β_{wave}: 0, 30, 60 and 90 degrees). The configurations of the wave and wind directions are depicted in Figure 4.8. The mean values, standard deviations

and maximum values of the responses have been presented as functions of the wind-wave misalignment in *Paper 5*. The mean values of the global motions, except for the yaw motion, are not significantly affected by the wave direction, whereas the standard deviations of the global motions are sensitive to the wave directions, as shown in Figure 4.10. For example, in LC 1-3 it can be observed that the surge standard deviation increases with increasing β_{wave}. This is because the low-frequency response increases with increasing β_{wave}, while the wave-frequency response decreases. The pitch motion, which contributes significantly to the tower bending moment, is most affected by the response at the wave frequency when the wave direction changes. As with the surge motion, the wave-frequency pitch motion decreases with increasing β_{wave} while the low-frequency pitch motion and the pitch motion due to the 2P effect do not depend strongly on the wave direction. Consequently, the pitch motion decreases as β_{wave} increases, but only slightly. As for the maximum value, a decrease in the maximum value of the surge motion with increasing β_{wave} can be observed at high wind speeds in LC 4-6 because the decrease in the viscous hydrodynamic loads on the platform in the surge direction is greater under higher significant wave height conditions. For the sway, roll and pitch motions, the maximum values have a similar trend as the standard deviations for corresponding motions.
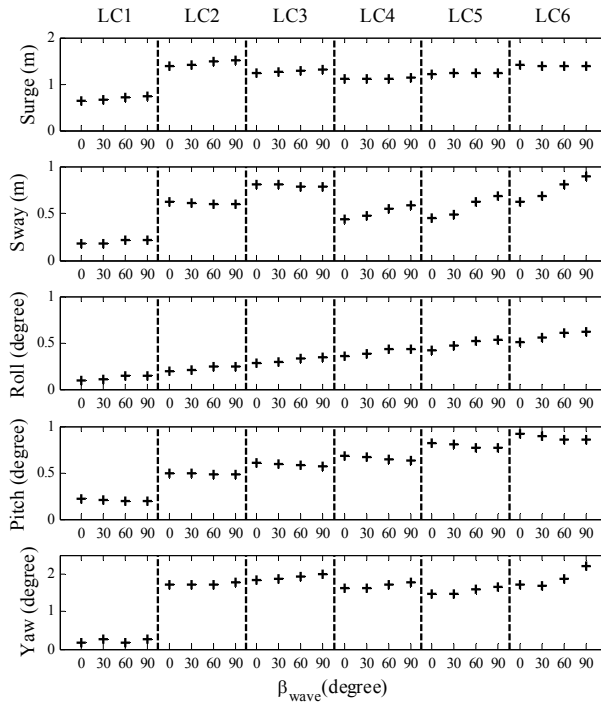

Figure 4.10: Standard deviations of the platform motion as a function of the wave direction β_{wave} for all load cases

The mean values of the bending moments and the mooring line tension remain almost the same when changing the wave direction because the mean values are primarily determined by the wind loads, and they are thus not affected by the wave direction. The effect of wind-wave misalignment on the standard deviations of the tower base bending moments and the mooring line tension does not depend strongly on the wave direction.

In summary, largest standard deviations of global motions in sway, roll and yaw are observed at the wave direction of 90 degrees, especially more apparently at high wind speeds, whereas, largest pitch motion is observed in the aligned wind and wave conditions. The tower base bending moments and the mooring line tension are found not to depend strongly on the wave directions due to the large contribution from the 2P load variation. Not only do the wind loads dominate the mean motions and structural responses, but the aerodynamic variation also affects the standard deviations of responses significantly. Therefore, the effect of the wind-wave misalignment on the responses of FVAWT is not as significant as compared to the amplitude of the wind loads.

4.5 Emergency Shutdown Condition

4.5.1   Novel hydrodynamic brake

Emergency shutdown is one of the most important concerns for VAWTs, and it poses a challenge for an operating VAWTs. When the FVAWT operates in high wind conditions or in stormy weather, the produced large aerodynamic loads acting on blades may lead to the large deformation or destruction of blades and collapse of the tower because there is no blade pitch mechanism in VAWTs with Darrieus rotors. Therefore, it is necessary to initiate the emergency shutdown to prevent the rotor from being destroyed. Experience has shown that aerobrakes also need to be installed to keep the rotational speed down in emergency situations when the generator torque is lost due to grid loss and the mechanical brake fails. The mechanical brake usually acts as a parking brake to stop the machine for maintenance purposes, therefore, aerodynamic braking is used to decelerate the rotor firstly and then the mechanical brake torque can be quite low. Although the mechanical brake is also used to bring the rotor to a standstill during high wind shutdowns for the majority of HAWTs, it is not easily applied for large scale VAWTs. As an efficient and simple type of aerobrakes, spoilers are plates used to increase aerodynamic drag. However, the spoilers are integrated with blades, and their efficiency should be determined by involving aerodynamic calculation of the blades together.

In *Paper* 3, a novel concept of hydrodynamic brake was proposed for the FVAWTs so as to utilize the advantages of the floating concept in the emergency shutdown event.

When generator failure happens, this brake should be applied to stop the acceleration of the rotor to prevent the rotor from overspeeding and subsequent disaster. This novel brake is composed of four plates and a centre column, and utilizes the drag force from water on the rotating plate, as shown in Figure 4.11a. The centre column of the brake provides enough buoyancy to balance the weight of the column itself and the four plates so that the brake does not affect the equilibrium condition of the floater. Under the normal operating conditions of the FVAWT, the centre column of the brake is connected to the floater. A device is assumed to activate the centre column to connect to the rotating shaft of the rotor during emergency shutdown. Two hydrodynamic brakes with different size have been preliminarily designed. Brake I has a small size. It does not create enough torque to stop the rotation, but it can prevent the overspeeding of the rotor. Furthermore, the rotational speed decreases to a lower value for most wind speeds. Brake II features a larger plate width than the brake I, so it can exert greater torque on the rotating shaft. After hydrodynamic brake II was applied in the FVAWT, the rotational speed in all load cases at different wind speeds could be rapidly reduced to a very low value.
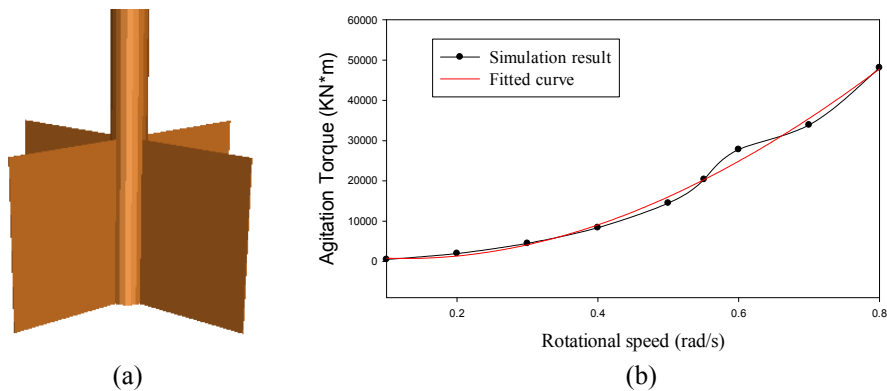
Figure 4.11: (a) Hydrodynamic brake (b) Relationship between rotational speed and torque

In the hydrodynamic load calculation for the hydrodynamic brake, the hydrodynamic coefficients of the column and the plates are included in the coupled model. Before the hydrodynamic brake is connected to the rotating shaft, it functions as a damping plate. The hydrodynamic loads on the brake can be calculated by the Morison formula. The added mass and drag coefficient for a cylinder and a thin plat can be determined from the DNV standard [181]. The friction drag of flat plate parallel to the flow was neglected. Thus, the plate provided a damping effect in the translational degrees of freedom of the floater. After the centre column of the hydrodynamic brake is connected to the rotating shaft, it rotates along with the shaft to decelerate the rotor to a lower speed. The added mass and drag force in the translational degrees of freedom remains the same as that in the previous stage, whereas the drag in a rotational degree of freedom is newly generated. This drag force was represented as additional torque

acting on the column. The torque on this rotating flat plate was first computed from a simplified Computational fluid dynamics (CFD) model by using the sliding mesh technique [182]. The relation between the estimated torque and the rotational speed was integrated into the model. In this manner, the effect of the hydrodynamic brake can be taken into account in the simulation. However, the damping effect in the yaw degree of freedom was neglected in the first stage because it is relatively small compared with that in the second stage. Furthermore, the interaction between the translational degrees of freedom and rotational degrees of freedom for the hydrodynamic brake was also neglected, thus, the complex model could be simplified and the main features maintained.

4.5.2   Torque estimation of the hydrodynamic brake

The concept of the hydrodynamic brake is analogous to stir mixer of different liquids, and the CFD model used to predict the dynamics of the stir process can be used to simulate the hydrodynamic brake. The commercial CFD software FLUENT was chosen and the sliding mesh approach, as an accurate model for simulating the flow rotation problem, was used in the simulation. When applying the sliding mesh approach, the computational domain is divided into an inner region containing the rotating plate and an outer region of stationary flow. Based on transient computation to produce a time accurate flow field, it allows the inner region to slide relative to the outer region in discrete time steps and carries out time-dependent computations using implicit or explicit interpolation of data at successive time steps. Because the length of the brake is long, a 2D model was established so as to reduce the computational cost and simplify the CFD model. For the discretization scheme, the first-order upwind was used because the choice of the discretization scheme has no effect on the mean velocities, as concluded by Aubin et al. [183]. Furthermore, the absolute velocity formulation and Renormalized Group (RNG) k-ε turbulence model with a standard wall function for near-wall treatment were used in the simulation because the effect of swirl on turbulence is included in the RNG model, enhancing the accuracy for swirling flows.

Through the CFD technique, the hydrodynamic characteristics of the hydrodynamic brake has been investigated and detailed information regarding the flow field, such as the pressure and velocity of the rotational flow, is obtained. One of the most important hydrodynamic parameters is the relationship between the torque on the brake from water and the rotational speed of the brake. By understanding this relationship, the relevant coefficients can be implemented in the coupled model. After a series of simulations for different rotational speeds, the agitation torques corresponding to each rotational speed could be determined. By multiplying the length of the plate, the relationship between the total torque and the rotational speed of hydrodynamic brake has been obtained, and a three order polynomial has been used to fit the relationship, as shown in Figure 11b for brake I (See *Paper 3*).

4.5.3 Effect of hydrodynamic brake

The addition of the hydrodynamic brake to the original FVAWT concept may change the properties of the platform and subsequently the dynamic responses of the global motion and structural responses of the wind turbine. To investigate the use of the hydrodynamic brake in normal operating conditions and emergency shutdown process, the fault configurations have been defined as follows:

A) The original FVAWT without hydrodynamic brake and no fault occurrence
B) The FVAWT with hydrodynamic brake I and no fault occurrence
C) The FVAWT with hydrodynamic brake I and fault occurrence, followed by free rotation
D) The FVAWT with hydrodynamic brake II and fault occurrence, followed by shutdown

The effect of the hydrodynamic brake on the platform motion and structural loads under normal operating conditions have been evaluated by comparing the response of FVAWT with brake I with that of the original FVAWT. In *Paper 3* it shows that the hydrodynamic brake has a less effect on the surge motion in the load case with lower wind speed. When the wind speed increases, the platform with the brake has much less response at the surge resonance frequency than the platform without the brake. The response near the wave frequency slightly decreases. The drag force from water on the brake actually introduces rather strong damping effect on the platform, and the damping increases with the relative velocity between the platform and wave velocity. A similar effect on the sway motion can be observed, but the difference is that the brake introduces a slightly stronger wave frequency response in sway motion. The brake hardly affects the heave motion of the platform because the drag force on the column associated with the heave motion is relatively small and the natural frequency of the heave motion lies outside the range of wave and wind frequencies.
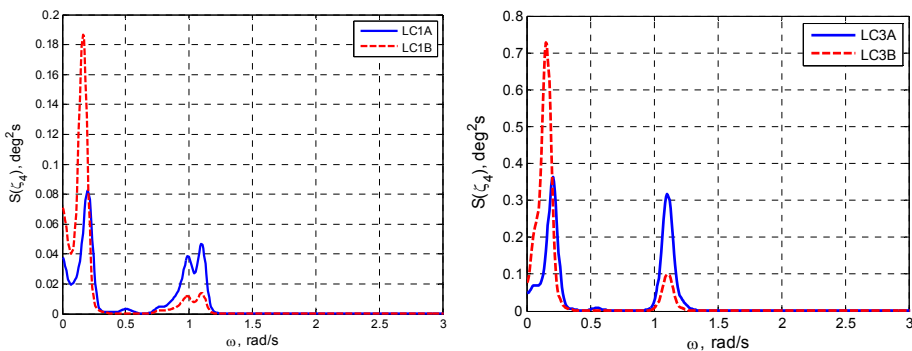

Figure 4.12: Power spectra for roll motion of the platform for load cases 1 and 3 with fault configurations A and B

Figure 4.12 compares the power spectra of the roll motion between the platform with the brake and the original platform under load cases 1 and 3. The brake can decrease

the natural frequency of the roll motion of the platform due to the mass change of integrated system and induce a larger peak at the roll resonance frequency when compared with the roll motion of the FVAWT without brake. On the other hand, the drag force on the brake can reduce the roll motion induced by the 2P frequency of approximately 1.1 rad/s. The 2P frequency originates from the characteristics of vertical axis wind turbines with two blades. Because the axis of rotation is not parallel to the wind direction and the angle of attack of the blades varies with the azimuthal position during operation, the aerodynamic loads vary within one revolution. However, the roll motion itself is relatively small under aligned wind and wave conditions, and the effect is not as significant. A similar effect can be observed for the pitch motion. As the wind increases, the effect becomes increasingly apparent.

The brake can significantly reduce the mooring tension response to the wind excitation, whereas it induces larger peaks at higher frequencies. In addition to the peak at the 2P frequency, another peak at a higher frequency is observed, which is believed to be induced by the eigenfrequency of the blade. With the increase in wind speed, the peak which is induced at the structural eigenfrequency of 1.7 rad/s becomes increasingly apparent. The effect of the brake on the bending moment of the tower base in the fore-aft (FA) and side-side (SS) directions was also investigated, and the main difference is the larger peak at the 2P frequency for the FVAWT with the brake. The reason for this finding is that the inclusion of the brake changes the mass distribution of the platform and introduces much more damping, and thus the bending moment induced by the 2P frequency increases.

4.5.4   Investigation of emergency shutdown process

A fault, such as grid loss, was assumed to occur at 1200 s, at which point the wind turbine entered a state of free rotation without any generator torque or other torque to balance the aerodynamic torque before the brake connected to the rotating shaft of the wind turbine. Due to the large inertia of the wind turbine and variation of the aerodynamic torque, the increase in the rotational speed of shaft was not distinct. Once the hydrodynamic brake takes effect to counter the aerodynamic torque, the rotational speed varies depending on the difference between the aerodynamic torque and hydrodynamic torque on the brake. Figure 4.13 shows a time series of the rotational speed of the rotor for different wind speeds after fault occurs when the Brake I is used in the fault configuration C. As mentioned previously, Brake I does not create enough torque to stop the rotation, but it can prevent the overspeeding of the rotor. Furthermore, the rotational speed decreases to a lower value for most wind speeds. The rotational speed after fault is determined by the balance of aerodynamic torque and hydrodynamic torque. The final rotational speed at a wind speed of 25 m/s is similar to the rotational speed before the occurrence of fault, as shown in Figure 4.13. A further investigation was also carried out for the global motion of the platform, mooring line tension and tower base bending moment when the brake was also rotating with the rotor.

Due to the decrease in the rotational speed after the activation of the hydrodynamic brake, the global motion of the platform shows better performance. Both the mean values and standard deviations of the global motion, mooring line tension and bending moments can be significantly reduced at different wind speeds, except for wind speed of 25 m/s. Figure 4.14 compares the global motion between fault configurations B and C for different wind speeds. It can be observed that the surge and pitch motions are greatly reduced, whereas the sway and roll motions experience both positive and negative effects under different load cases. However, the sway and roll motions are relatively small compared with the surge, pitch and yaw motions. Thus, the effect of the hydrodynamic brake on the sway and roll motions can be neglected. More results and detailed analyses can be found in *Paper 3*.
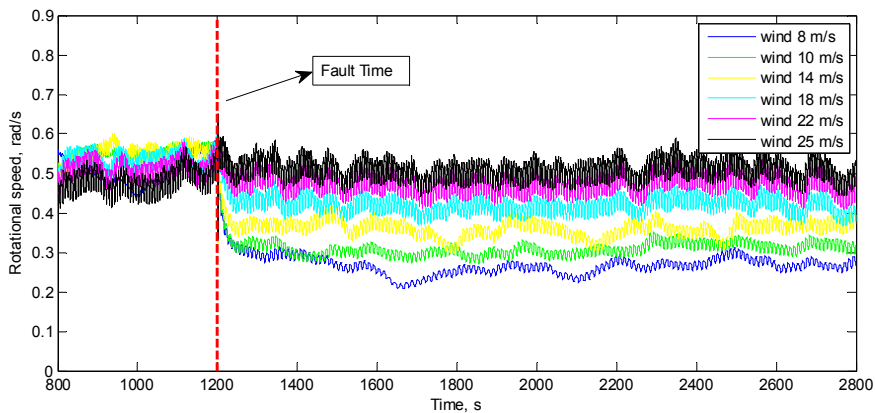

Figure 4.13: Rotational speed for different wind speed after fault occurs at TF=1200 s by using brake I
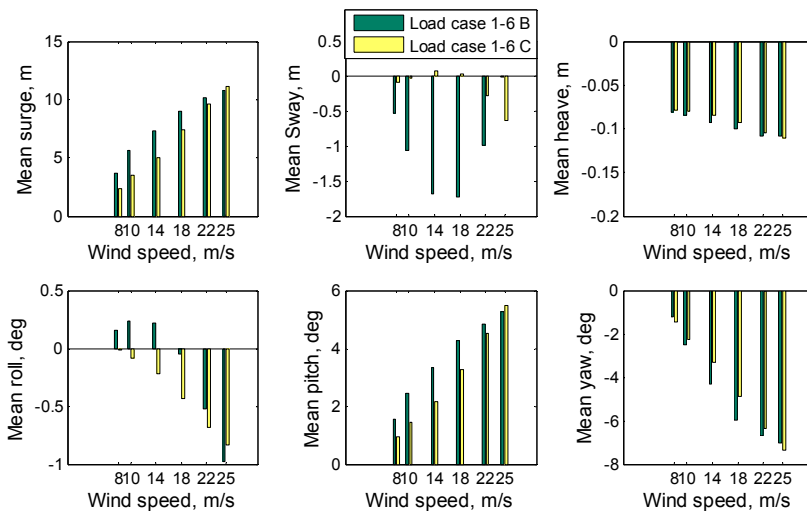
Figure 4.14: Mean values of the platform motions under the fault case B and fault case C for all wind speeds

To completely stop the rotation of the rotor of the FVAWT, hydrodynamic brake II and mechanical brake are both used for the emergency shutdown. Hydrodynamic brake II features a larger plate width than hydrodynamic brake I and can exert greater torque on the rotating shaft. After hydrodynamic brake II was applied in the FVAWT, the rotational speed in all load cases at different wind speeds could be rapidly reduced to a very low value. Then, the mechanical brake could be applied on the brake disk to stop the rotation of the wind turbine 200 s after the fault occurred. Until the wind turbine was completely shut down, the process remained transient, and the platform gradually moves toward its final equilibrium position with some delay after the rotational speed, as shown in Figure 4.15. The figure shows that the combination of the hydrodynamic brake and mechanical brake can effectively complete an emergency shutdown.
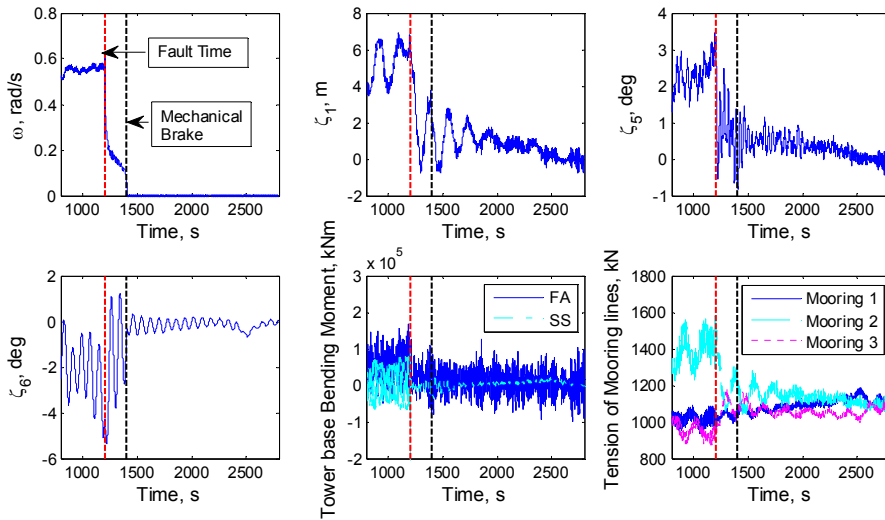
Figure 4.15: Time history of the rotational speed, surge, pitch, yaw, tower base bending moments (FA: fore-aft; SS: side-side) and mooring line tension for load case 2D

4.6 Comparison of a FVAWT and a FHAWT

To better understand the FVAWTs for further development, it is also of great interest to compare a FVAWT with a FHAWT, both for onshore and offshore use. In addition to the comparison mentioned in Section 1.2, more comparisons have been presented by other researchers. Paraschivoiu [15] compared the HAWTs and the VAWTs, by discussing the advantages and disadvantages of the HAWTs and the VAWTs, looking at the rotor performance (output power and torque) as a function of some design

parameters and the predicted foundation loads. In addition to some proposed new techniques to take advantage of the incremental improvement for the VAWTs, the potential application of the VAWTs in harsh northern climates was also presented in his book. An evaluation of three different turbine concepts for wind power has been carried out, including the HAWTs and two different concepts of the VAWTs [46], specifically, the Darrieus turbine and the H-rotor. The comparative study was mainly based on some important aspects such as structural dynamics, control systems, maintenance, manufacturing and electrical equipment. Furthermore, a case study and a blade area study were also presented, and the VAWTs appeared to be advantageous compared to the HAWTs in several aspects. Jamieson also presented a comparison between VAWT and HAWT from the point of view of power performance and energy capture in his recent book [12].

However, the aforementioned discussions and comparisons cover only the onshore VAWTs, and the comparison between floating concepts for horizontal type and vertical type turbines has not been presented. *Paper 4* presented a comparative study of the FVAWT and a FHAWT with the same rated power. The FHAWT used in the OC4 project is selected for this comparison. It is composed of the 5 MW NREL reference wind turbine and the original OC4 semi-submersible. The global motions, structural dynamic response and tensions of the mooring lines have been calculated for this comparison to allow for a detailed evaluation of these two wind turbines.

Table 4.1: Model description of the numerical model

FVAWT	FHAWT
Simulation Code	
Simo-Riflex-DMS	Simo-Riflex-Aerodyn
Aerodynamic	
DMS + DS	BEM or GDW) + DS
Hydrodynamics	
Airy + PF + ME	Airy + PF + ME
Structural Dynamics (Elastic)	
Turbine: FEM	Turbine: FEM
Mooring: FEM	Mooring: FEM
Control System (Servo)	
(Generator) DLL	(Generator + Blade Pitch) DLL
Airy - Airy wave theory ME - Morison's equation	
PF - Linear potential flow with radiation & diffraction	
DS - Dynamic stall FEM - Finite element method	
DLL - External dynamic link library	

Simo-Riflex-Aerodyn [78] is used for modeling and numerical simulation of the FHAWT, while Simo-Riflex-DMS is used for the FVAWT. The Simo-Riflex-Aerodyn couples three computer codes: Simo, Riflex and AeroDyn. The significant difference between the Simo-Riflex-DMS and the Simo-Riflex-Aerodyn is that the DMS model

is used to calculate the aerodynamic loads on the vertical axis wind turbine while AeroDyn calculates the forces and moments on the blades based on the Blade Element/Momentum (BEM) theory and Generalized Dynamic Wake (GDW) theory, including dynamic stall, tower shadow and skewed inflow correction. Additionally, the generator torque and blade pitch control system are both included in the Simo-Riflex-Aerodyn. Therefore, both of these two codes can model the wind turbine concepts in the time domain as a so-called aero-hydro-servo-elastic system. A brief summary of these two models is presented in Table 4.1.

A set of time domain simulations with different conditions, i.e., the decay tests, wave only conditions, wind only conditions and the combined wind and wave conditions, have been conducted for the FVAWT and FHAWT. The comparison have been performed based on statistical results and power spectra of the global motions in six DOFs, the mooring line tension and the internal loads at the base of the rotor of the FVAWT and at the base of the tower of the FHAWT.

Figure 4.16 compares the surge decay and pitch decay between the FHAWT and the FVAWT. In the decay tests, the wind turbines are parked and no aerodynamic loads are acting on the wind turbines. The natural periods are estimated through the free-decay test. The natural periods of the global motions of the FVAWT and the FHAWT are tabulated in Table 4.2. The comparison shows that the natural periods of the global motions of the FVAWT are close to the periods of the FHAWT, except for the natural periods of roll and pitch due to the difference between the inertia moments of the wind turbines.
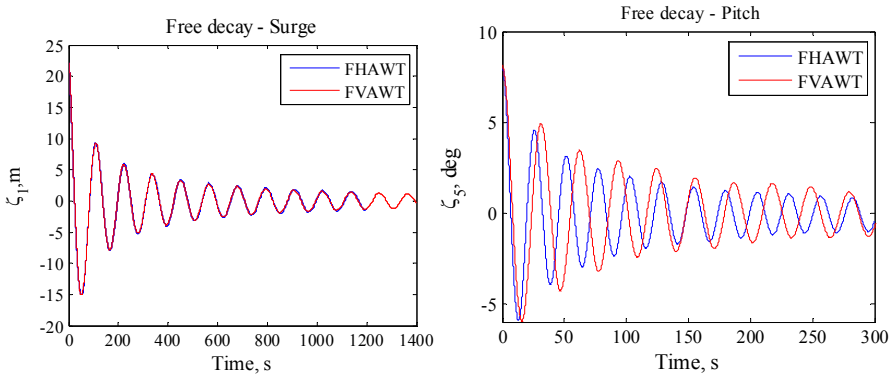

Figure 4.16: Free decay test of surge and pitch for the FHAWT and the FVAWT

Table 4.2: Natural periods of the FVAWT and the FHAWT

	Surge	Heave	Pitch	Yaw
FVAWT [s]	114.0	17.1	31.0	79.7
FHAWT [s]	112.0	17.1	25.8	80.2

Under the wave conditions only, the statistical results also show almost identical mean platform motions and mooring line tension for these two concepts, as shown in Table 4.3. Through the comparison under the wind conditions only, the effect of 2P frequency on the structural response has been identified for the FVAWT. The 2P effect could also be clearly observed in the platform motion, mooring line tension and the rotor base bending moment for the FVAWT in the combined wind and wave conditions, as shown in Figure 4.17. The importance of the 2P effect increases with the increase of the mean wind speed in the operational conditions. The peak corresponding to the pitch natural period for the FHAWT is larger than the peak for the FVAWT. As a result, the comparison of statistical results shows the pitch motion of the FVAWT has mean values and standard deviations very close to the values obtained for the FHAWT at low wind speeds. The surge motion of the FVAWT is also smaller than the surge motion of the FHAWT at low wind speed. However, due to the absence of a blade pitch controller, the FVAWT suffers larger platform motions, mooring line tensions and structural responses for the cases with above-rated wind speed. The structural responses such as the bending moment resulting from the 2P effect of aerodynamic loads have much larger variations for the FVAWT. This disadvantage of the FVAWT could be overcome by a novel rotor type such as helical blades, or at least an optimized structure design and adopting three blades could reduce this disadvantage. The global motion of the platform and the tensions of the mooring lines of the FVAWT at high wind speed also could be much alleviated using a different control strategy which reduces the rotational speed and keeps generated power constant when the wind speed exceeds the rated wind speed. Furthermore, a floater exclusively designed for the FVAWT with a different mooring lines design and arrangement could improve the performance of the FVAWT. Therefore, the FVAWT is still considered to be promising in the offshore application when the rotor, mooring lines and control system are further optimized.

Table 4.3: Mean values of the FVAWT and the FHAWT (U_w= 0 m/s, H_s = 6 m and T_p= 10 s, Jonswap spectrum)

Mean	Surge [m]	Sway [m]	Heave [m]	Pitch [deg]	Roll/ Yaw [deg]	M_1/ M_3 [KN]	M_2 [KN]
FVAWT	-0.011	0	-0.07	0.007	0	1095	1094
FHAWT	-0.037	0	0.002	-0.077	0	1096	1093

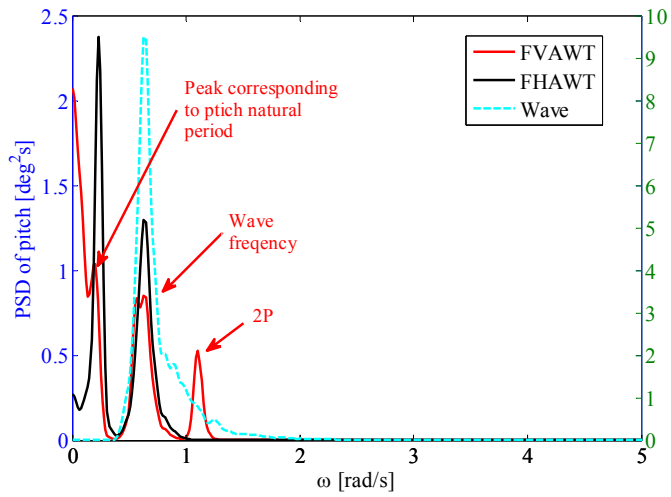Figure 4.17: Power spectra of pitch of the FVAWT and the FHAWT (U_w= 11.4 m/s, H_s = 6 m and T_p= 10 s, Jonswap spectrum)

5 Conclusions and Recommendations for Furture Work

This thesis focuses on the development, verification and application of a coupled model for dynamic analysis of FVAWTs. Based on coupled time domain simulations, dynamic response analysis of a FVAWT is performed in normal operating conditions, parked conditions and emergency shutdown conditions. In addition, the FVAWT is compared with a FHAWT to better understand difference between these two concepts. The final chapter presents the main conclusions, contributions and recommendations for future work.

5.1 Conclusions

The main conclusions of this thesis are described as follows.

- An improved Double Multiple-Streamtube (DMS) model based on the Glauert momentum theory and the blade element theory including the vertical component of wind velocity in the upwind zone was presented to calculate the aerodynamics of a vertical axis wind turbine when the tower is tilted. The model has been validated against experimental data from an H-Darrieus VAWT. Three different dynamic stall models were also integrated to assess the dynamic stall effect and improve the accuracy of the results. By comparing the results from the different dynamic stall models with the experimental data, this work has demonstrated that the BL DS model is superior to the other models tested for predicting the aerodynamic characteristics of a Darrieus-type VAWT.

- Analysis of the computed results of VAWTs for different tilt angles applied under steady condition. The analysis shows that the effect of tower tilting on the power coefficient is insignificant for the Sandia 17-m wind turbine up to a 15-degree tilt angle, whereas pitching the tower has a larger effect on the maximum values of rotor torque when the tilt angle exceeds 10 degrees. Moreover, the effect on the local tangential force coefficient is more evident than that on the local normal tangential force coefficient, especially at certain

azimuthal positions. For the DeepWind 5 MW wind turbine, the results presents a conclusion similar to that for the Sandia 17-m wind turbine but with a lesser effect on the power coefficient and local normal coefficient. The tangential force coefficient is much more sensitive to tilt angle than the normal force coefficient.

- The development of a coupled method for modeling of the dynamics of a floating vertical axis wind turbine has been presented by taking into account the wind inflow, aerodynamics, hydrodynamics, structural dynamics and a generator control. Verification of this coupled method has been carried out through model-to-model comparison. The aerodynamic model imbedded in the integrated system is well verified by comparing with the stand-alone aerodynamic code which was already verified by experimental data. The results of the bottom fixed wind turbine and floating wind turbine are all very close to the results from stand-alone aerodynamic code. The structural modeling of the wind turbine in Riflex was verified by comparing the eigen frequencies from Riflex with those calculated using the commercial software Abaqus. The power curve, aerodynamic torque, generator torque and generator speed have been presented to prove the effectiveness of the controller. Furthermore, the results from frequency domain simulation have been computed for the linear rigid boy motion of the platform with vertical axis wind turbine included. Then the results from the coupled method in time domain simulation were compared with the results from frequency domain simulation, showing a good agreement. The 2p response and first natural pitch motion from wind can be observed when the wind is combined with wave.

- The effect of the hydrodynamic brake on the FVAWT has been evaluated by comparing the results obtained for the FVAWT with a hydrodynamic brake with the results obtained for the original FVAWT under normal operating conditions. The addition of the hydrodynamic brake does not affect the surge motion as long as the wind speed is not too high. Otherwise, the surge motion induced by the wind can be greatly reduced by the drag force on the hydrodynamic brake. It was observed that the sway motion could be affected by the drag force on the brake when the yaw degree of freedom was presented. The effects on the roll and pitch motions also depend on the wind speed and are slightly complex because both the natural frequency and 2P frequency affect the responses. From a structural point of view, the brake has a greater positive effect on the mooring lines, but it could enlarge the 2P effect on the tower base bending moment. This finding indicates that a better hydrodynamic brake design is critical to reducing the 2P effect on the tower base bending moment by avoiding the stiffening of the platform.

- By investigating the shutdown process following the activation of the hydrodynamic brake to decelerate the wind turbine, a series of promising

results revealed the merits of the hydrodynamic brake for the emergency shutdown. As long as rotational speed can be reduced to relatively lower values, the global motion and structural responses can both be reduced. Furthermore, by combing a mechanical brake with a larger hydrodynamic brake, the shutdown process could be successfully completed. Application of a hydrodynamic brake is expected to be efficient for rotor shutdown and for reducing the platform motion and structural loads.

- The dynamic response of a FVAWT and a FHAWT have been compared, considering global motions in six DOFs, the mooring line tension and the internal loads at the base of the rotor of the FVAWT and at the base of the tower of the FHAWT. Comparing natural periods of the FVAWT and FHAWT through decay tests has ensured the similar platform properties. The statistical results corresponding to the wave conditions only also show almost identical mean platform motions and mooring line tension for these two concepts. Through the simulation in the wind conditions only, the effect of 2P frequency on the structural response was identified for the FVAWT. The 2P effect resulting from the rotation of the shaft of the FVAWT leads to a large fluctuation of the aerodynamic loads on the rotor and the internal loads in the rotor even in steady wind conditions. The 2P effect could also be clearly observed in the platform motion, mooring line tension and the tower base bending moment for the FVAWT in the combined wind and wave conditions. The importance of the 2P effect increases with the increase of the mean wind speed in the operational conditions. The comparison shows that the pitch motion of the FVAWT has mean values and standard deviations very close to the values obtained for the FHAWT at low wind speeds. The surge motion of the FVAWT is also smaller than the surge motion of the FHAWT. Due to the absence of a blade pitch controller, the FVAWT suffers larger platform motions, mooring line tensions and structural responses for the cases with above-rated wind speed. However, the FVAWT studied can generate much more electrical power than the FHAWT at high wind speeds. Moreover, the presented controller can be further improved to enhance the performance of the FVAWT. Further considering the optimization of the rotor and exclusive design of the platform and mooring system for the FVAWTs, the FVAWTs are still considered to be promising in the offshore application.

- Based on comparisons between the mean values, standard deviations and maximum values of selected response parameters under steady wind conditions and turbulent wind conditions, the effect of turbulent wind on the global motions and structural responses have been evaluated. The mean values remain almost the same in the steady and turbulent wind conditions, but the standard deviations and the maximum values increase in the turbulent wind conditions. The contributions to the differences in the standard deviations are identified at different frequencies by comparing the power spectra of the

selected response, showing that the low-frequency responses are significantly excited by the turbulent wind and that the increase in the low-frequency responses is much greater than the decrease in the 2P response.

- The 2P effect on the structural integrity and fatigue damage in the VAWTs is significant. The results shows that the tower base bending moments in the FVAWT at the 2P frequency are found to be much reduced when compared to the tower base bending moments in an equivalent land-based VAWT. This indicates that some of the 2P effects can be alleviated with a floating platform. It should be noted, however, that most land-based VAWTs are supported by a tower with guy cables. Therefore, a further comparison between prototypes of a land-based VAWT and a FVAWT is recommended.

- By comparing the global motions and structural response of the FVAWT with the equivalent rigid wind turbine, the differences between the investigated responses have been analyzed to determine the effect of structural flexibility in the FVAWT on the response and loads. The structural flexibility does not significantly affect the mean values of the global motions or the tower base bending moments. However, the standard deviations and maximum values of the responses are found to be different for the flexible wind turbine and the rigid wind turbine. The most evident difference is that much larger standard deviations are observed for the tower base fore-aft bending moment in the flexible wind turbine. That is, the standard deviations of the fore-aft bending moment of the FVAWT with the rigid structure assumption are significantly underestimated. This indicates that fatigue calculation should be given some considerations if a rigid model of a FVAWT is used. The responses of the flexible wind turbine and the rigid wind turbine in the frequency domain have also been investigated, and the contributions of the different excitations to the responses at different frequencies have also been analyzed.

- The FVAWT has also been investigated in the parked condition with respect to global motions and structural responses as a function of the azimuthal angle of the rotor. It is found that the azimuthal angle at which the responses in the parked condition are minimized occurs when the chords of the blades are aligned with the wind. This is important for the survivability of the FVAWT.

- The effect of wind-wave misalignment on the global motions and structural responses in selected operational conditions has also been investigated. Increased global motions, except for the pitch motions, are observed in the misaligned wind and wave conditions. The tower base bending moments and the mooring line tension are found not to depend strongly on the wave directions due to the large contribution from the 2P load variation. The effect of the wind-wave misalignment is not significant when compared to the amplitude of the wind loads. Not only do the wind loads dominate the mean

motions and structural responses, but the aerodynamic variation also affects the standard deviations of responses significantly.

5.2 Original Contributions

This thesis includes original contributions to the development, verification and application of the coupled model for FVAWTs as well as several systematic investigations. First, in order to be able to study FVAWT concept, the following items address the development of the simulation tool:

- *Integration of the DMS model and different dynamic stall models*: the DMS model was implemented with different dynamic stall models by the programming language Fortran for aerodynamic loads on a VAWT, and different combination of the DMS model and dynamic stall model were compared with experimental data

- *Model improvement with consideration of the tower tilting*: an improvement in the DMS mode was made to be able to evaluate the effect of the tower tilting on the aerodynamics of a VAWT, and validated by comparing with experimental data. Furthermore, the improved model was applied to study two VAWTs with different size.

- *Development of a coupled model for FVAWTs*: the Fortran DLL for computation between Riflex and DMS was written in a coupled manner; the control system for generator torque both in normal operating conditions and fault conditions was implemented in Java and coupled with Riflex; integration of the aerodynamic model in DMS, the hydrodynamic model in Simo, the structural dynamic model in Riflex and the generator control model in Java forms the coupled model to simulate dynamic behavior of FVAWTs, and the interaction between the rotor dynamics, platform motion and mooring dynamics were taken into account.

- *Verification of the coupled model for FVAWTs*: the verification of this method was made through model-to-model comparisons; a code-to-code comparison was also carried out by comparing the presented simulation tool Simo-Riflex-DMS with another simulation code FloVAWT developed by Cranfield University

Using the developed simulation tool, several investigations of a proposed novel FVAWT in different aspects were performed:

- *Proposal of a novel FVAWT concept*: a novel FVAWT was presented by installing the DeepWind 5 MW rotor on the DeepCwind floater from the OC4 project.

- *Preliminary design of a novel hydrodynamic brake*: a novel hydrodynamic brake is installed at the end of the extended shaft of the FVAWT through the centre column of the floater. The torque provided by the brake on the rotor was estimated by CFD technique. The motivation is to initiate an emergency shutdown of the FVAWT when the generator torque is lost due to grid loss and the mechanical brake fails.

- *Evaluation of the hydrodynamic brake*: the hydrodynamic brake was modeled to integrate with the original FVAWT, and the effect of this brake on the dynamic response of the FVAWT was evaluated by comparing the dynamic response of the FVAWT with brake I with the original FVAWT without any brake under normal operating conditions.

- *Investigation of the emergency shutdown process*: emergency shutdown processes for the FVAWT using the hydrodynamic brake were investigated based on the integrated model. The dynamic response was studied with different fault configurations. Furthermore, shutdown processes by using the hydrodynamic Brake II and mechanical brake were also demonstrated to prove the effectiveness of the hydrodynamic brake concept.

- *Dynamic analysis of the FVAWT*: the response characteristics under steady wind and turbulent wind condition was studied; the effect of structural flexibility was evaluated; difference between the FVAWT and an equivalent land-based wind turbine was identified; the dynamic response as a function of azimuthal angle in parked condition was investigated.

- *The effect of misalignment between wind and wave*: the dynamic response analysis of the FVAWT in selected misaligned wind and wave conditions was performed, and the effect of misalignment between the mean wind direction and the long-crested waves were investigated. Increased global motions are observed in the misaligned conditions, whereas the tower base bending moments and the mooring line tension are found not to depend strongly on the wave directions due to the large contribution from the 2P load variation.

- *Comparative study of a FVAWT and a FHAWT*: the FVAWT was compared with a FHAWT based on selected dynamic response in a series of load cases. The results gave more insights into the advantages and disadvantages of the FVAWT as well as several suggestions for improvement.

5.3 Recommendations for Future Work

Higher-fidelity aerodynamic model for offshore application
The DMS model used in this thesis has limitations for a high solidity turbine and at higher tip speed ratio. When it is used for the floating offshore wind turbine, this aerodynamic model encounters other limitations such as tracking the wake velocity from the upstream for calculating induced velocity in the downstream, considering the interaction between each of the turbine blades and either their own wakes, and accurately taking into account the effect of the platform pitch and roll motion on the aerodynamics. To overcome these limitations, a higher-fidelity aerodynamic model should be further formulated into the coupled model. The vortex model or panel model could be a promising choice, but the accuracy needs to be assessed in view of the computational time.

Considering second order effect in hydrodynamic modelling
The mean wave drift force and the slowly varying drift force are usually interest for a semi-submersible having natural periods in heave and pitch well above peak period of the wave spectrum. The second order wave drift forces were not applied to the semi-submersible in this thesis. Therefore, including the mean drift force and the slowly varying drift force in further studies would be expected to increase the effect of wind-wave misalignment on the low-frequency platform responses, and it could also provide additional information for the fatigue calculation of mooring lines.

Investigating different control model
A PI generator controller was applied in the presented coupled model. The PI generator controls the rotational speed corresponding to different wind speeds based on the optimized curve of torque versus rotational speed below the rated wind speed, and maintains the generator speed at rated rotational speed above the rated wind speed. Thus, it leads to larger thrust force and generator power at high wind speed. An improved control strategy could be designed to keep constant power by reduce rotational speed of the rotor in high wind speed. Subsequently, the wind loads will be reduced and better performance of this vertical floating concept will be achieved.

Model validation by comparison against model tests
Model verification has been performed by model-to-model comparison and code-to-code comparison in this thesis. However, the conducted code-to-code comparison has some limitations, such as different capabilities of the simulation codes, different damping models, different structural modelling and mooring line modelling. Therefore, further code-to-code comparison should be made so as to better investigate the effect of different modelling on the response. Furthermore, it is also necessary to carry out model testing on prototype wind turbines to validate current numerical simulation tool in the future.

Fatigue loads evaluation

This thesis has not considered fatigue problem for structural components such as blades, tower and mooring lines. For FVAWTs, the continuously varying aerodynamic loads on the rotor lead to considerably higher load level of the fatigue loads and number of load cycles. Therefore, it is of significant importance to evaluate fatigue damage based on the time history of calculated response. The rainflow counting technique, considered as the best method for fatigue damage estimation, can be used for further short-term and long-term fatigue analysis.

Investigating other promising rotor types

The structural responses such as the bending moment at the bottom of the shaft have much large variations for the FVAWT due to the 2P effect of aerodynamic loads. This disadvantage of the FVAWT could be overcome by using a rotor with helical blades. Based on evenly distributed aerodynamic loads, the dynamic performance of global motion of the platform, bending moment of the structures as well as tensions of the mooring lines of the FVAWT could be much improved. Furthermore, the fatigue problem will be much alleviated. Therefore, it is of interest to investigate this promising concept for further development of FVAWTs.

Comparative study of different floating concepts

Comparison between a FVAWT and a FHAWT has been performed and a semi-submersible type floater is used as a floating support in this thesis. However, the spar type FHAWT has been widely investigated based on numerical models, model tests and prototypes. It is also interesting to compare a FVAWT and a FHAWT with a spar type floater. Additionally, FVAWTs using different floaters, such as spar, semi-submersible and TLP, need to be compared to determine the performance of the floaters used for the VAWT based on the presented coupled simulation tool. Lastly, FVAWTs with different type of rotor, such as H-type, V-type, curved blades and helical blades, are also interesting to be compared to give further insight into characteristics of different concepts.

References

[1]   Global Wind Energy Council (GWEC), Global Wind Report - Annual Market Update, 2013.

[2]   European Wind Energy Association, Wind energy scenarios for 2020, July, 2014.

[3]   European Wind Energy Association, Wind in power: 2013 European Statistics, February 2014.

[4]   European Wind Energy Association, Building a stable future - Annual report 2013, June, 2014.

[5]   Twidell J and Gaudiosi G. *Offshore wind power*. Multi-Science Publishing Company, 2009. ISBN: 0906522633.

[6]   European Wind Energy Association, Deep water - The next step for offshore wind energy, July 2013.

[7]   Jonkman JM. Dynamics modeling and loads analysis of an offshore floating wind turbine, Technical Report NREL/TP-500-41958, NREL November 2007.

[8]   Musial W, Butterfield S, and Boone A. Feasibility of Floating Platform Systems for Wind Turbines. Presentation at the 23rd ASME Wind Energy Symposium, NREL/CP-500-34874 [WWW Document] URL http://www.nrel.gov/docs/fy04osti/34874.pdf, 2004.

[9]   Statoil. Hywind brochure. Available from http://www.statoil.com. 2012.

[10]   D.Roddier AP, A.Aubault, J,Weinstein. A Generic 5MW Wind Float For Numerical Tool Validation and Comparison against a Generic Spar, *Proceedings of the ASME 2011 30th Internatil Conference on Ocean, Offshore, and Arctic Engineering*, Rotterdam, The Netherlands, June 19-24, 2011.

[11]   Edenhofer O, Pichs-Madruga R, Sokona Y, Seyboth K, et al. IPCC Special Report on Renewable Energy Sources and Climate Change Mitigation, Cambridge University Press, Cambridge, United Kingdom; New York, NY, USA, 2012.

[12]   Jamieson P. (2011) HAWT or VAWT?, in *Innovation in Wind Turbine Design*. John Wiley & Sons, Ltd, Chichester, UK. DOI: 10.1002/9781119975441.ch13. p. 211-222.

[13]   Blackwell BF, Sheldahl RE, and Feltz LV. Wind Tunnel Performance Data for Two- and Three Savonius Rotors, SAND76-0131, July 1977.

[14]   Bhutta MMA, Hayat N, Farooq AU, Ali Z, et al. Vertical axis wind turbine – A review of various configurations and design techniques. *Renewable and Sustainable Energy Reviews*, 2012; **16**: p. 1926-1939.

[15]   Paraschivoiu I. *Wind turbine design: with emphasis on Darrieus concept*. Polytechnic International Press, 2002: Montreal. ISBN: 2553009313.

[16]   Penna PJ. Wind tunnel tests of the Quiet Revolution Ltd. QR5 vertical axis wind turbine, Institute for Aerospace Research, National Research Council Canada, Canada, LTR-AL-2008-0004, 2008.

[17]   Armstrong S and Tullis S. Power performance of canted blades for a vertical

axis wind turbine. *Journal of Renewable and Sustainable Energy*, 2011; **3**(1): p. 013106.

[18]   Scheurich F, Fletcher TM, and Brown RE. Effect of blade geometry on the aerodynamic loads produced by vertical-axis wind turbines. *Proceedings of the Institution of Mechanical Engineers, Part A: Journal of Power and Energy*, 2011; **225**(3): p. 327-341.

[19]   McIntosh SC and Babinsky H. Aerodynamic Modeling of Swept-Bladed Vertical Axis Wind Turbines. *Journal of Propulsion and Power*, 2012; **29**(1): p. 227-237.

[20]   Castelli MR, De Betta S, and Benini E. Three-Dimensional Modeling of a Twisted-Blade Darrieus Vertical-Axis Wind Turbine, *World Academy of Science, Engineering and Technology*, 2013.

[21]   Brahimi M, Allet A, and Paraschivoiu I. Aerodynamic analysis models for vertical-axis wind turbines. *International Journal of Rotating Machinery*, 1995; **2**(1): p. 15-21.

[22]   Deglaire P, Engblom S, Ågren O, and Bernhoff H. Analytical solutions for a single blade in vertical axis turbine motion in two-dimensions. *European Journal of Mechanics-B/Fluids*, 2009; **28**(4): p. 506-520.

[23]   McIntosh S, Babinsky H, and Bertényi T. Convergence failure and stall hysteresis in actuator-disk momentum models applied to vertical axis wind turbines. *Journal of Solar Energy Engineering*, 2009; **131**(3): p. 034502.

[24]   Deglaire P. Analytical aerodynamic simulation tools for vertical axis wind turbines. PhD thesis, Acta University Upsaliensis, Uppsala, Sweden. *Digital Comprehensive Summaries of Uppsala Dissertations from the Faculty of Science and Technolog 774*, 2010.

[25]   Scheurich F, Fletcher TM, and Brown RE. Simulating the aerodynamic performance and wake dynamics of a vertical-axis wind turbine. *Wind Energy*, 2011; **14**(2): p. 159-177.

[26]   Ferrari GM. Development of an aeroelastic simulation for the analysis of vertical-axis wind turbines. PhD thesis, University of Auckland. 2012.

[27]   Zanon A, Giannattasio P, and Simão Ferreira CJ. A vortex panel model for the simulation of the wake flow past a vertical axis wind turbine in dynamic stall. *Wind Energy*, 2013; **16**(5): p. 661-680.

[28]   Scheurich F and Brown RE. Modelling the aerodynamics of vertical-axis wind turbines in unsteady wind conditions. *Wind Energy*, 2013; **16**(1): p. 91-107.

[29]   Simão Ferreira C, van Bussel G, and van Kuik G. 2D CFD simulation of dynamic stall on a Vertical Axis Wind Turbine: verification and validation with PIV measurements. *45th AIAA Aerospace Sciences Meeting and Exhibit/ASME Wind Energy Symposium*, 2007.

[30]   Raciti Castelli M, Englaro A, and Benini E. The Darrieus wind turbine: Proposal for a new performance prediction model based on CFD. *Energy*, 2011; **36**(8): p. 4919-4934.

[31]   McLaren K, Tullis S, and Ziada S. Computational fluid dynamics simulation of the aerodynamics of a high solidity, small-scale vertical axis wind turbine.

Wind Energy, 2012; **15**(3): p. 349-361.

[32]   Edwards JM, Danao LA, and Howell RJ. PIV measurements and CFD simulation of the performance and flow physics and of a small-scale vertical axis wind turbine. *Wind Energy*, 2015; **18**(2).

[33]   Ferreira CJS, van Bussel GJW, and van Kuik GAM. Wind tunnel hotwire measurements, flow visualization and thrust measurement of a VAWT in skew. *Journal of Solar Energy Engineering*, 2006; **128**: p. 487.

[34]   Simao Ferreira C, Hofemann C, Van Kuik G, and Van Bussel G. Experimental and numerical investigation of the 3D VAWT wake. 2009.

[35]   Howell R, Qin N, Edwards J, and Durrani N. Wind tunnel and numerical study of a small vertical axis wind turbine. *Renewable Energy*, 2010; **35**(2): p. 412-422.

[36]   McLaren K, Tullis S, and Ziada S. Measurement of high solidity vertical axis wind turbine aerodynamic loads under high vibration response conditions. *Journal of Fluids and Structures*, 2012; **32**: p. 12-26.

[37]   El-Sayed A, Hirsch C, and Derdelinckx R. Dynamics of vertical axis wind turbines (darrieus type). *International Journal of Rotating Machinery*, 1995; **2**(1): p. 33-41.

[38]   Ottermo F and Bernhoff H. An upper size of vertical axis wind turbines. *Wind Energy*, 2014; **17**(10): p. 1623-1629.

[39]   ERIKSSON S. Direct Driven Generators for Vertical Axis Wind Turbines. PhD thesis, Uppsala University. 2008.

[40]   Dabiri JO. Potential order-of-magnitude enhancement of wind farm power density via counter-rotating vertical-axis wind turbine arrays. *Journal of Renewable and Sustainable Energy*, 2011; **3**(4): p. 043104.

[41]   Kinzel M, Mulligan Q, and Dabiri JO. Energy exchange in an array of vertical-axis wind turbines. *Journal of Turbulence*, 2012; **13**(1).

[42]   Sutherland HJ, Berg DE, and Ashwill TD. A Retrospective of VAWT Technology, Sandia National Laboratories, SAND2012-0304, January 2012.

[43]   Worstell MH. Aerodynamic performance of the DOE/Sandia 17-m-diameter Vertical-axis wind turbine. *AIAA Journal of Energy*, 1981; **5**.

[44]   Maydew RC and Klimas PC. Aerodynamic performance of Vertical and Horizontal-Axis Wind Turbine. *AIAA Journal of Energy*, May 1981; **5**.

[45]   Dessaint L, Nakra H, and Mukhedkar D. Propagation and elimination of torque ripple in a wind energy conversion system. *Energy Conversion, IEEE Transactions on*, 1986(2): p. 104-112.

[46]   Eriksson S, Bernhoff H, and Leijon M. Evaluation of different turbine concepts for wind power. *Renewable and Sustainable Energy Reviews*, 2008; **12**(5): p. 1419-1434.

[47]   Paquette J and Barone M. Innovative offshore vertical-axis wind turbine rotor project. *EWEA 2012 Annual Event, Copenhagen, Denmark*, 2012.

[48]   Vita L. Offshore Floating Vertical Axis Wind Turbines with Rotating Platform, *Risø-PhD-80(EN)*, National Laboratory for Sustainable Energy, DTU, 2011.

[49]   Cahay M, Luquiau E, Smadja C, and SILVERT FCC. Use of a Vertical Wind

Turbine in an Offshore Floating Wind Farm, *Offshore Technology Conference* Houston, Texas, USA, 2-5 May 2011.

[50]   10MW Aerogenerator X © Wind Power Limited & Grimshaw at http://vimeo.com/13654447.

[51]   Akimoto H, Tanaka K, and Uzawa K. Floating axis wind turbines for offshore power generation—a conceptual study. *Environmental Research Letters*, 2011; **6**(4): p. 044017.

[52]   http://www.gwind.no/ (accessed on 2014-10-19).

[53]   http://www.modec.com/fps/skwid/pdf/skwid.pdf (accessed on 2014-10-19).

[54]   Paulsen US, Pedersen TF, Madsen HA, Enevoldsen K, et al. Deepwind - An innovative wind turbine concept for offshore, *European Wind Energy Association (EWEA) Annual Event*, Brussels, 2011.

[55]   Vita L, Paulsen US, and Pedersen TF. A novel floating offshore wind turbine concept: new developments, *European Wind Energy Conference and Exhibition*, Poland, 2010.

[56]   Vita L, Paulsen US, Pedersen TF, Madsen HA, et al. A novel floating offshore wind turbine concept, *European Wind Energy Conference and Exhibition*, Marseille, France, 16-19 March, 2009.

[57]   Paulsen US, Vita L, Madsen HA, Hattel J, et al. 1st DeepWind 5 MW Baseline design. *Energy Procedia*, 2012; **24**: p. 27-35.

[58]   Paulsen US, Madsen HA, Hattel JH, Baran I, et al. Design optimization of a 5 MW floating offshore vertical-axis wind turbine. *Energy Procedia*, 2013; **35**: p. 22-32.

[59]   Vita L, Zhale F, Paulsen US, Pedersen TF, et al. A novel concept for floating offshore wind turbines: recent developments in the concept and investigation on fluid interaction with the rotating foundation, *ASME 2010 29th International Conference on Ocean, Offshore and Arctic Engineering*, 2010: p. 389-396.

[60]   Collu M, Brennan F, and Patel M. Conceptual design of a floating support structure for an offshore vertical axis wind turbine: the lessons learnt. *Ships and Offshore Structures*, 2014; **9**(1): p. 3-21.

[61]   Wayman E, Sclavounos P, Butterfield S, Jonkman J, et al. Coupled dynamic modeling of floating wind turbine systems, *2006 Offshore Technology Conference*, Houston, 1-4 May 2006.

[62]   Wayman EN. Coupled dynamics and economic analysis of floating wind turbine systems. M.S. Dissertation, Department of Mechanical Engineering, Massachusetts Institute of Technology, Cambridge, MA, USA, June, 2006.

[63]   Vijfhuizen W. Design of a Wind and Wave Power Barge. MS Dissertation, Department of Naval Architecture and Mechanical Engineering, Universities of Glasgow and Strathclyde, Glasgow, Scotland. 2006.

[64]   Lee KH. Responses of floating wind turbines to wind and wave excitation. Master of Science Thesis, Massachusetts Institute of Technology. 2005.

[65]   Bulder B, van Hees MT, Henderson A, Huijsmans R, et al. Study to feasibility of and boundary conditions for floating offshore wind turbines, Novem

2002-CMC-R43, ECN, MARIN, Lagerway the Windmaster, TNO, TUD, MSC, December, 2002.

[66] Skaare B, Hanson, TD, Nielsen, FG, Yttervik, R, Hansen, AM, Thomsen, K, and Larsen, T,. Integrated dynamic analysis of floating offshore wind turbines, *European Wind Energy Conference and Exhibition*, Milano, Italy, 2007.

[67] Jonkman JM. Dynamics of offshore floating wind turbines - model development and verification. *Wind Energy*, 2009; **12**(5): p. 459-492.

[68] Karimirad M and Moan T. Extreme dynamic structural response analysis of catenary moored spar wind turbine in harsh environmental conditions. *Journal of offshore mechanics and Arctic engineering*, 2011; **133**(4).

[69] Luxcey N, Ormberg H, and Passano E. Global analysis of a floating wind turbine using an aero-hydro-elastic numerical model. Part 2: Benchmark study, *Offshore Mechanics and Arctic Engineering Conference*, Rotterdam, The Netherlands, 2011.

[70] Ormberg H, Passano E, and Luxcey N. Global analysis of a floating wind turbine using an aero-hydroelastic model. Part 1: Code development and case study, *Offshore Mechanics and Arctic Engineering Conference*, Rotterdam, The Netherlands, 2011.

[71] Karimirad M and Moan T. A simplified method for coupled analysis of floating offshore wind turbines. *Marine Structures*, 2012; **27**(1): p. 45-63.

[72] Jonkman JM and Buhl Jr ML. FAST user's guide. *Golden, CO: National Renewable Energy Laboratory*, 2005.

[73] Moriarty PJ and Hansen AC. Aerodyn Theory Manual, National Renewable Energy Laboratory, Golden, Colorado, NREL/TP-500-36881, 2005.

[74] NWTC Information Portal (*HydroDyn*). https://nwtc.nrel.gov/HydroDyn, Last modified 06-October-2014; Accessed 03-November-2014.

[75] Larsen TJ. How 2 HAWC2, the user's manual, Tech. Rep. Risø-R-1597(ver. 3-9). 2009.

[76] MARINTEK, RIFLEX User's Manual, 2009.

[77] MARINTEK, SIMO User's Manual, 2011.

[78] Ormberg H and Bachynski EE. Global Analysis of Floating Wind Turbines: Code Development, Model Sensitivity and Benchmark Study, *Proceedings of the Twenty-second (2012) International Offshore and Polar Engineering Conference*, Rhodes, Greece, 2012.

[79] Bachynski EE and Moan T. Design considerations for tension leg platform wind turbines. *Marine Structures*, 2012; **29**(1): p. 89-114.

[80] Kvittem MI, Bachynski EE, and Moan T. Effects of Hydrodynamic Modelling in Fully Coupled Simulations of a Semi-submersible Wind Turbine. *Energy Procedia*, 2012; **24**: p. 351-362.

[81] Kvittem MI and Moan T. Frequency versus time domain fatigue analysis of a semi-submersible wind turbine tower, *ASME 2014 33rd International Conference on Ocean, Offshore and Arctic Engineering*, 2014: p. V09AT09A021; 12 pages.

[82] Luan C, Gao Z, and Moan T. Modelling and analysis of a semi-submersible

wind turbine with a central tower with emphasis on the brace system, *Proceedings of the 32nd International Conference on Ocean, Offshore and Arctic Engineering*, Nantes, France, June, 2013.

[83]   Myhr A and Nygard TA. Load Reductions and Optimizations on Tension-Leg-Buoy offshore wind turbines platforms, *Proceedings of the Twenty-Second International Offshore and Polar Engineering Conference*, Rhodes, Greece, 2012: p. 232-239.

[84]   Bossanyi EA. Gh Bladed Theory Manual Version 4.3, Garrad Hassan and Partners ltd.:Bristol, England, 2011.

[85]   Hansen MOL, Holmas T, Aas-Jakobsen K, and Amdahl J. VpOne – a new FEM based servo hydro- and aeroelastic code for wind turbines, *European Offshore wind 2009 Conference and Exhibition*, Stockholm, 14-16 September 2009.

[86]   J.Jonkman WM. Offshore Code Comparison Collaboration (OC3) for IEA Task 23 Offshore Wind Technology and Deployment, *Tech. Rep. NREL/TP-5000-48191*, National Renewable Energy Laboratory, 2010.

[87]   Vorpahl F, Strobel M, Jonkman JM, Larsen TJ, et al. Verification of aero-elastic offshore wind turbine design codes under IEA Wind Task XXIII. *Wind Energy*, 2014; **17**(4): p. 519-547.

[88]   Robertson A, Jonkman J, Vorpahl F, Popko W, et al. Offshore Code Comparison Collaboration Continuation Within IEA Wind Task 30: Phase II Results Regarding a Floating Semisubmersible Wind System, *ASME 2014 33rd International Conference on Ocean, Offshore and Arctic Engineering*, 2014.

[89]   Merz KO. A Method for Analysis of VAWT Aerodynamic Loads under Turbulent Wind and Platform Motion. *Energy Procedia*, 2012; **24**: p. 44-51.

[90]   Svendsen HG, Merz KO, and Endegnanew AG. Control of floating vertical axis wind turbine, *European Wind Energy Conference and Exhibition*, Copenhagen, Denmark, 2012.

[91]   Merz K and Svendsen H. A control algorithm for the deepwind floating vertical-axis wind turbine. *Journal of Renewable and Sustainable Energy*, 2013; **5**(6): p. 063136.

[92]   Svendsen HG and Merz KO. Control System for Start-up and Shut-down of a Floating Vertical Axis Wind Turbine. *Energy Procedia*, 2013; **35**: p. 33-42.

[93]   Owens B, Hurtado J, Barone M, and Paquette J. An energy preserving time integration method for gyric systems: development of the offshore wind energy simulation toolkit, *Proceedings of the European Wind Energy Association Conference & Exhibition*, EWEA Vienna, Austria, 2013.

[94]   Owens BC, Hurtado JE, Paquette JA, Griffith DT, et al. Aeroelastic Modeling of Large Offshore Vertical-axis Wind Turbines: Development of the Offshore Wind Energy Simulation Toolkit, *54th AIAA/ASME/ASCE/AHS/ASC Structures, Structural Dynamics, and Materials Conference*, 2013.

[95]   Murray JC and Barone M. The development of CACTUS, a Wind and Marine Turbine Performance Simulation Code, *Proceedings of the 49th AIAA*

Aerospace Sciences Meeting, AIAA, Orlando, FL, 2011.

[96]   Fowler MJ, Owens B, Bull D, Goupee AJ, et al. Hydrodynamic Module Coupling in the Offshore Wind Energy Simulation (OWENS) Toolkit, *ASME 2014 33rd International Conference on Ocean, Offshore and Arctic Engineering*, 2014.

[97]   Helge M, Torben L, Luca V, and Uwe P. Implementation of the Actuator Cylinder flow model in the HAWC2 code for aeroelastic simulations on Vertical Axis Wind Turbines, in *51st AIAA Aerospace Sciences Meeting including the New Horizons Forum and Aerospace Exposition.* 2013, American Institute of Aeronautics and Astronautics. DOI: 10.2514/6.2013-913

[98]   Collu M, Borg M, Shires A, and Brennan FP. FLOVAWT: Progress on the development of a coupled model of dynamics for floating offshore vertical axis wind turbines, *Proceedings of the 32nd International Conference on Ocean, Offshore and Arctic Engineering*, Nantes, France, June, 2013.

[99]   Collu M, Borg M, Shires A, Rizzo FN, et al. FloVAWT: Further Progresses on the Development of a Coupled Model of Dynamics for Floating Offshore VAWTS, *ASME 2014 33rd International Conference on Ocean, Offshore and Arctic Engineering*, 2014.

[100]   MSS, Marine Systems Simulator (2010). Viewed 02.11.2014, http://www.marinecontrol.org.

[101]   Darrieus G, Turbine having its rotating shaft transverse to the flow of the current, December 1931.

[102]   Klimas PC. Darrieus rotor aerodynamics. *Transactions of the ASME. Journal of Solar Energy Engineering*, 1982; **104**: p. 102-105.

[103]   Templin RJ. Aerodynamic performance theory for the NRC vertical-axis wind turbine, *Technical Report LTR-LA-160*, National Aeronautical Establishment, Ottawa, Ontario (Canada), 1974.

[104]   Strickland JH. The Darrieus Turbine: A Performance Prediction Model Using Multiple Streamtubes, *SAND75-0430*, Sandia National Laboratories, Albuquerque, N.M., October 1975.

[105]   Paraschivoiu I and Delclaux F. Double multiple streamtube model with recent improvements. *AIAA Journal of Energy*, 1983; **7**: p. 250-255.

[106]   Paraschivoiu I. Double-multiple streamtube model for Darrieus Wind Turbines, *Second DOE/NASA Wind Turbines Dynamics Workshop, NASA CP-2185*, Cleveland, Ohio, February 1981.

[107]   Paraschivoiu I. Double-multiple streamtube model for studying vertical-axis wind turbines. *AIAA Journal of Propulsion and Power*, 1988; **4**: p. 370-378.

[108]   Madsen H. The Actuator Cylinder – a flow model for vertical axis wind turbines. PhD thesis, Part 1,2 and 3 Aalborg University Centre. 1982.

[109]   Ponta FL and Jacovkis PM. A vortex model for Darrieus turbine using finite element techniques. *Renewable Energy*, 2001; **24**(1): p. 1-18.

[110]   Strickland JH, Webster BT, and Nguyen T. A vortex model of the Darrieus turbine: An analytical and experimental study. *Journal of Fluid Engineering*, December 1979; **101**: p. 500-505.

[111] Hirsch H and C MA. A cascade theory for the aerodynamic performance of Darrieus wind turbines. *Wind Engineering*, 1987; **11**: p. 164-175.

[112] Dixon K. The near wake structure of a vertical axis wind turbine. TU Delft, Netherlands. 2009.

[113] Simão Ferreira C. The near wake of the VAWT: 2D and 3D views of the VAWT aerodynamics. PhD thesis, Delft University of Technology, Faculty of Aerospace Engineering. 2009.

[114] Simão Ferreira C and Scheurich F. Demonstrating that power and instantaneous loads are decoupled in a vertical-axis wind turbine. *Wind Energy*, 2014; **17**(3): p. 385-396.

[115] Dixon K, Ferreira CS, Hofemann C, van Bussel G, et al. A 3d unsteady panel method for vertical axis wind turbines. *The proceedings of the European Wind Energy Conference & Exhibiti on EWEC Brussels*, 2008: p. 1-10.

[116] Madsen HA. Application of actuator surface theory on wind turbines, *Proceedings of IEA meeting on Joint Actions on Aerodynamics of Wind Turbines, 2. Symposium held in Lyngby*, 21.-22. November 1988, Department of Fluid Mechanics, Technical University of Denmark.

[117] Aagaard Madsen H, Schmidt Paulsen U, and Vita L. Analysis of VAWT aerodynamics and design using the Actuator Cylinder flow model. *The science of Making Torque from Wind 2012*.

[118] Larsen HC. Summary of a vortex theory for the cyclogiro, *Proceedings of the second US national conferences on wind engineering research*, Colorado state university, 1975: p. V8-1-3.

[119] Fanucci JB and Walter RE. Innovative wind machines: the theoretical performace of a vertical-axis wind turbine, *Proceedings of the vertical-axis wind turbine technology workshop*, Sandia Laboratories, SAND76-5586, iii-61-95, USA, 1976.

[120] Holme OA. Contribution to the aerodynamic theory of the vertical axis wind turbine, *International symposium on wind energy system*, Cambridge, England, 1976: p. C4-55-71.

[121] Wilson RE. Wind-turbine aerodynamics. *Journal of Wind Engineering and Industrial Aerodynamics*, May 1980; **5**(3-4): p. 357-372.

[122] Strickland JH, Webster B, and Nguyen T. Vortex model of the Darrieus turbine: An analytical and experimental study, *Technical report SAND81-7017*, Sandia National Laboratory, 1981.

[123] Cardona JL. Flow curvature and dynamic stall stimulated with an aerodynamic free-vortex model for vawt. *Wind Engineering*, 1984; **8**(3): p. 135-143.

[124] Vandenberghe D and Dick E. A free vortex simulation method for the straight bladed vertical axis wind turbine. *Journal of Wind Engineering and Industrial Aerodynamics*, 1987; **26**(3): p. 307-324.

[125] Brown RE. Rotor wake modeling for flight dynamic simulation of helicopters. *AIAA journal*, 2000; **38**(1): p. 57-63.

[126] Schuerich F and Brown RE. Effect of dynamic stall on the aerodynamics of vertical-axis wind turbines. *AIAA journal*, 2011; **49**(11): p. 2511-2521.

[127] Scholz N. *Aerodynamics of cascades*. Translated and revised by A. Kline. AGARD-AG-220, 1965.

[128] Hirsch IH and Mandal AC. A cascade theory for the aerodynamic performance of Darrieus wind turbines. *Wind Engineering*, 1987; **11**(3): p. 164-175.

[129] Islam M, Ting DS-K, and Fartaj A. Aerodynamic models for Darrieus-type straight-bladed vertical axis wind turbines. *Renewable and Sustainable Energy Reviews*, 2008; **12**(4): p. 1087-1109.

[130] Wang L, Zhang L, and Zeng N. A potential flow 2-D vortex panel model: Applications to vertical axis straight blade tidal turbine. *Energy conversion and management*, 2007; **48**(2): p. 454-461.

[131] Katz J and Plotkin A. *Low Speed Aerodynamics, 2nd ed.* Cambridge University Press: Cambridge, UK, 2001. ISBN: ISBN-13:978-0521665520.

[132] Erickson LL. Panel Methods - An Introduction, NASA, California, NASA TP-2995, 1990.

[133] Hansen M.O.L and Sørensen DN. CFD model for vertical axis wind turbine., *Wind Energy for the New Millennium - Proceedings of the European Wind Energy Conference*, Copenhagen, 2001: p. 485-488.

[134] Horiuchi K, I U, and K S. Straight wind vertical axis wind turbines: a flow analysis. *Wind Engineering*, 2005; **29**: p. 243-252.

[135] Simão Ferreira CJ, van Zuijlen A, Bijl H, van Bussel G, et al. Simulating dynamic stall in a two-dimensional vertical-axis wind turbine: verification and validation with particle image velocimetry data. *Wind Energy*, 2009; **13**(1): p. 1-17.

[136] Leishman JG. *Principles of helicopter aerodynamics*. 2nd ed. Cambridge Aerospace Series, Cambridge University Press, 2006: Cambridge. ISBN: 0521858607.

[137] Gormont RE. A mathematical model of unsteady aerodynamics and radial flow for application to helicopter rotors, *USAMRDL Technical Report 72-67*, Boeing Co., Vertol Div., Philadelphia, PA, 1973.

[138] Johnson W. Comparison of three methods for calculation of helicopter rotor blade loading and stresses due to stall, *NASA TN D-7833*, National Aeronautics and Space Administration, 1974.

[139] Beddoes T. A synthesis of unsteady aerodynamic effects including stall hysteresis. *Vertica*, 1976; **1**(2): p. 113-123.

[140] Beddoes T. Onset of leading edge separation effects under dynamic conditions and low Mach number, *34th Annual Forum of the American Helicopter Society*, Washington, D. C., May 15-17, 1978.

[141] Gangwani ST. Synthesized airfoil data method for prediction of dynamic stall and unsteady airloads, *American Helicopter Society, Annual Forum, 39 th, St. Louis, MO*, 1984: p. 15-33.

[142] Truong VK. Prediction of helicopter rotor airloads based on physical modelling of 3D unsteady aerodynamics, *22nd European Rotorcraft Forum*, Brighton, UK, 1996.

[143] Carr LW. Progress in analysis and prediction of dynamic stall. *Journal of*

Aircraft, 1988; **25**(1): p. 6-17.

[144]   Rapin M and Ortun B. 3D rotational correction in ONERA aeroelastic predictions of NREL wind turbine, *45th AIAA Aerospace Sciences Meeting and Exhibit*, Reno, Nevada, 2007.

[145]   Brouwer HH. The adaptation of the ONERA model for dynamic stall, for application in the wind-turbine analysis programme PHATAS, *In Contract Report NLR CR 90104 L*, National Aerospace Laboratory NLR, The Netherlands, In Contract Report NLR CR 90104L, 1990.

[146]   Øye S. Dynamic stall simulated as time lag of separation, *Proceedings of the 4th IEA Symposium on the Aerodynamics of Wind Turbines, McAnulty, KF (Ed)*, Rome, Italy, 1991.

[147]   Snel H. Application of a modified Theodorsen model to the estimation of aerodynamic forces and aeroelastic stability, *European Wind Energy Conference*, London, 22-25 November 2004.

[148]   Gupta S and Leishman J. Dynamic stall modelling of the S809 aerofoil and comparison with experiments. *Wind Energy*, 2006; **9**(6): p. 521-547.

[149]   Larsen JW, Nielsen SRK, and Krenk S. Dynamic stall model for wind turbine airfoils. *Journal of Fluids and Structures*, 2007; **23**(7): p. 959-982.

[150]   Sheng W, Galbraith RAM, and Coton F. A modified dynamic stall model for low mach numbers. *Journal of Solar Energy Engineering*, 2008; **130**: p. 031013.1-031013.10.

[151]   Berg DE. An Improved Double-Multiple Streamtube Model for the Darrieus Type Vertical-Axis Wind Turbine, *Preceedings of the Sixth Biennial Wind Energy Conference and Workshop,Minneapolis,MN*, June 1983: p. 231-238.

[152]   Leishman J and Beddoes T. A semi-empirical model for dynamic stall. *Journal of the American Helicopter Society*, 1989; **34**(3): p. 3-17.

[153]   Mertens S, van Kuik G, and van Bussel G. Performance of an H-Darrieus in the skewed flow on a roof. *Journal of Solar Energy Engineering*, 2003; **125**(4): p. 433-440.

[154]   Burton T, Jenkins N, Sharpe D, and Bossanyi E. *Wind Energy Handbook*. John Wiley & Sons Ltd, 2011: England. ISBN: 0470699752.

[155]   Robertson A, Jonkman J, Masciola M, Song H, et al. Definition of the Semisubmersible Floating System for Phase II of OC4, 2012.

[156]   Wang K, Moan T, and Hansen MOL. A method for modeling of floating vertical axis wind turbine, *Proceedings of the 32nd International Conference on Ocean, Offshore and Arctic Engineering*, Nantes, France, June, 2013.

[157]   Jonkman B. TurbSim user's guide: version 1.50, *Tech. rep. NREL/TP-500-46198.*, National Renewable Energy Laboratory, 2009.

[158]   Wang K, Hansen MOL, and Moan T. Model improvements for evaluating the effect of tower tilting on the aerodynamics of a vertical axis wind turbine. *Wind Energy*, 2015; **18**(1): p. 91-110.

[159]   Det Norske Veritas. Sesam user manual:Wadam, 2008.

[160]   International Electrotechnical Commission (2009). *IEC61400-3 Wind turbines - Part 3: Design requirement for offshore wind turbines.*

[161] Det Norske Veritas, 2010. Environmental conditions and environmental loads. DNV-RP-C205.

[162] Faltinsen OM. *Sea Loads on Ships and Offshore Structures.*, Cambridge University Press, UK, 1995.

[163] MARINTEK, SIMO - Theory Manual Version 3.7, 2009.

[164] Johannessen K, Meling TS, and Haver S. Joint distribution for wind and waves in the northern north sea. *International Journal of Offshore and Polar Engineering*, 2002; **12**(1).

[165] Xing Y, Karimirad M, and Moan T. Modelling and analysis of floating spar-type wind turbine drivetrain. *Wind Energy*, 2014; **17**(4): p. 565-587.

[166] Jiang Z, Karimirad M, and Moan T. Dynamic response analysis of wind turbines under blade pitch system fault, grid loss, and shutdown events. *Wind Energy*, 2014; **17**(9): p. 1385-1409.

[167] Karimirad M and Moan T. Stochastic dynamic response analysis of a tension leg spar-type offshore wind turbine. *Wind Energy*, 2013; **16**(6): p. 953-973.

[168] Kvittem MI and Moan T. Effect of Mooring Line Modelling on Motions and Structural Fatigue Damage for a Semisubmersible Wind Turbine, *Proceedings of the Twenty-second International Offshore and Polar Engineering Conference.*, Rhodes, Greece, 2012.

[169] Berthelsen PA, Fylling I, Vita L, and Paulsen US. Conceptual Design of a Floating Support Structure and Mooring System for a Vertical Axis Wind Turbine, *Proceedings of the 31st International Conference on Ocean, Offshore and Arctic Engineering*, Rio de Janeiro, Brazil, June, 2012: p. 259-268.

[170] Collu M, Borg M, Shires A, and Brennan F. Progress on the development of a coupled model of dynamics for floating offshore vertical axis wind turbines, *Proceedings of the ASME 2013 32nd International Conference on Ocean, Offshore and Arctic Engineering*, 2013: p. 9-14.

[171] Borg M, Collu M, and Brennan FP. Use of a wave energy converter as a motion suppression device for floating wind turbines. *Energy Procedia*, 2013; **35**: p. 223-233.

[172] Borg M and Collu M. A Comparison on the Dynamics of a Floating Vertical Axis Wind Turbine on Three Different Floating Support Structures. *Energy Procedia*, 2014; **53**: p. 268-279.

[173] Borg M, Collu M, and Kolios A. Offshore floating vertical axis wind turbines, dynamics modelling state of the art. Part II: Mooring line and structural dynamics. *Renewable and Sustainable Energy Reviews*, 2014; **39**: p. 1226-1234.

[174] Borg M, Shires A, and Collu M. Offshore floating vertical axis wind turbines, dynamics modelling state of the art. part I: Aerodynamics. *Renewable and Sustainable Energy Reviews*, 2014; **39**: p. 1214-1225.

[175] Borg M, Wang K, Collu M, and Moan T. A comparison of two coupled model of dynamics for offshore floating vertical axis wind turbines(VAWT), *Proceedings of the ASME 2014 33nd International Conference on Ocean, Offshore and Arctic Engineering*, San Francisco, California, USA, June, 2014.

[176] Karimirad M and Moan T. Wave-and wind-induced dynamic response of a spar-type offshore wind turbine. *Journal of waterway, port, coastal, and ocean engineering*, 2012; **138**(1): p. 9-20.

[177] Fischer T, Rainey P, Bossanyi E, and Kühn M. Study on control concepts suitable for mitigation of loads from misaligned wind and waves on offshore wind turbines supported on monopiles. *Wind Engineering*, 2011; **35**(5): p. 561-574.

[178] Kuhn M. Dynamics and design optimization of offshore wind energy conversions systems. PhD thesis, Civil Engineering and Geosciences, Delft University of Technology. 2001.

[179] Bachynski EE, Kvittem MI, Luan C, and Moan T. Wind-wave misalignment effects on floating wind turbines: motions and tower load effects. *Journal of Offshore Mechanics and Arctic Engineering*, 2014; **136**(4): p. 12.

[180] Barj L, Stewart S, Lackner M, Jonkman J, et al. Wind/wave misalignment in the loads analysis of a floating offshore wind turbine, *AIAA SciTech 2014*, National Harbor, Maryland 13-17 January 2014.

[181] Det Norske Veritas, ENVIRONMENTAL CONDITIONS AND ENVIRONMENTAL LOADS, Tech. Rep., DNV-RP-C205 (2007),

[182] ANSYS, Inc. ANSYS FLUENT Tutorial Guide - Release 13.0, November 2010,

[183] Aubin J, Fletcher DF, and Xuereb C. Modeling turbulent flow in stirred tanks with CFD: the influence of the modeling approach, turbulence model and numerical scheme. *Experimental Thermal and Fluid Science*, 2004; **28**(5): p. 431-445.

Appendix A

A.1   Paper 1

A method for modeling of floating vertical axis wind turbine

Kai Wang, Torgeir Moan and Martin O.L. Hansen

Published in Proceedings of the 32nd International Conference on Ocean, Offshore and Arctic Engineering, Nantes, France. June 2013

A.2   Paper 2

Model improvements for evaluating the effect of tower tilting on the aerodynamics of a vertical axis wind turbine

Kai Wang, Martin O.L. Hansen and Torgeir Moan

RESEARCH ARTICLE

Model improvements for evaluating the effect of tower tilting on the aerodynamics of a vertical axis wind turbine

K. Wang[1,2], M. O. L. Hansen[2,3] and T. Moan[2]

[1] NOWITECH, Norwegian University of Science and Technology, 7491 Trondheim, Norway
[2] Centre for Ships and Ocean Structures, Norwegian University of Science and Technology, 7491 Trondheim, Norway
[3] DTU Wind Energy, Department of Mechanical Engineering, Technical University of Denmark, Lyngby, Denmark

ABSTRACT

If a vertical axis wind turbine is mounted offshore on a semi-submersible, the pitch motion of the platform will dominate the static pitch and dynamic motion of the platform and wind turbine such that the effect of tower tilting on the aerodynamics of the vertical axis wind turbine should be investigated to more accurately predict the aerodynamic loads. This paper proposes certain modifications to the double multiple-streamtube (DMS) model to include the component of wind speed parallel to the rotating shaft. The model is validated against experimental data collected on an H-Darrieus wind turbine in skewed flow conditions. Three different dynamic stall models are also integrated into the DMS model: Gormont's model with the adaptation of Strickland, Gormont's model with the modification of Berg and the Beddoes–Leishman dynamic stall model. Both the small Sandia 17 m wind turbine and the large DeepWind 5 MW are modelled. According to the experimental data, the DMS model with the inclusion of the dynamic stall model is also well validated. On the basis of the assumption that the velocity component parallel to the rotor shaft is small in the downstream part of the rotor, the effect of tower tilting is quantified with respect to power, rotor torque, thrust force and the normal force and tangential force coefficients on the blades. Additionally, applications of Glauert momentum theory and pure axial momentum theory are compared to evaluate the effect of the velocity component parallel to the rotor shaft on the accuracy of the model. Copyright © 2013 John Wiley & Sons, Ltd.

NOMENCLATURE

U_∞	Wind velocity at the equator level
U	Local upwind wind velocity
Z_{EQ}	Elevation of the equatorial level
Z	Elevation of the streamtube with respect to the ground
γ	Atmospheric wind shear exponent
ρ	Air density
a_u	Induction factor at the upwind rotor
a_d	Induction factor at the downwind rotor
ϕ	Tilt angle
θ	Azimuthal angle
δ	Angle between the blade normal and the equatorial plane
$\Delta I_u, \Delta I_d$	Rate of change of momentum for upwind and downwind streamtubes
U_u	Upwind horizontal velocity at the rotor
V_u	Upwind vertical velocity at the rotor
U_e	Equilibrium velocity in the middle plane between the upstream and downstream zone
U_d	Downwind induced velocity at the rotor

W_{Disk}	Local relative velocity at any azimuthal position
W_u, W_d	Upwind and downwind local relative velocity
A_s	Cross sectional area of the streamtube
ω	Rotational angular speed of rotor
r	Local rotor radius
Δh	Height of a single streamtube
c	Blade chord
N_b	Number of blades
C_L	Blade section lift coefficient
C_D	Blade section drag coefficient
C_t	Blade section normal force coefficient including viscous drag
C_n	Blade section tangential force coefficient including viscous drag
C_x	Blade section thrust force coefficient
C_y	Blade section lateral force coefficient
R_e	Reynolds number
C_{NI}	Critical normal force coefficient
$C_{N\alpha}$	Normal force coefficient curve slope
C_N^{st}, C_C^{st}	Static normal force coefficient and chordwise force coefficient
f_N, f_C	Effective flow separation point for static normal force coefficient and chordwise force coefficient
f''_C	Flow separation point including unsteady effects for chordwise force coefficient
C_N^I	Impulsive normal force coefficient
C_N^C	Circulatory normal force coefficient
C_N^{Pot}	Normal force coefficient under potential flow conditions
C'_N	Normal force coefficient including pressure lag response
C_N^f, C_C^f	Normal force coefficient and chordwise force coefficient including trailing edge separation
C_N^v, C_C^v	Vortex-induced normal force coefficient and chordwise force coefficient
C_N	Blade section normal force coefficient without viscous drag
C_C	Blade section chord-wise force coefficient without viscous drag
τ_v	Non-dimensional vortex time

1. INTRODUCTION

The exploitation of offshore wind energy offers great potential and requires a wide range of technologies, but offshore wind technology is still at its early stage. Hence, more research is still required, especially for floating wind turbines in deep water. Floating wind turbines can be classified as floating horizontal axis wind turbines (FHAWTs) and floating vertical axis wind turbines (FVAWTs). Although the research on the former type of turbines prevails, it is also of great interest to investigate FVAWTs to evaluate their economic potential. Examples of recent concepts include the DeepWind concept,[1–3] the VertiWind concept[4] and the Aerogenerator X concept.[5]

For the VAWT, the angle of attack of a fixed position on a blade varies with its azimuthal position during operation, and furthermore, the blades within the downwind zone experience a lower wind speed from the wake of the upwind part of the rotor. The aerodynamics of the VAWT is much more complicated than that of the HAWT for a single wind turbine. The double multiple-streamtube (DMS) model,[6] proposed by Paraschivoiu, is based on a combination of momentum theory and blade element theory and has been further improved.[7] This advanced model produces better correlation between the calculated results and experimental data compared with other earlier prediction models for VAWT, such as the single streamtube model by Templin[8] and the multiple-streamtube model by Strickland.[9] Although a great assortment of vortex models[10–13] and computational fluid dynamics (CFD) models[14] have been comprehensively applied and offer more detailed flow field information, application to the coupled dynamic analysis of floating wind turbines under both wind and wave conditions remains limited due to the more expensive computational cost.

A dynamic stall model must be included to simulate the effect of unsteady aerodynamics on the rotor blades during starting-up, stopping or operating at a low tip speed ratio. Several empirical methods exist for predicting dynamic stall, such as the earlier models that are primarily based on numerical correction of the dynamic stall delay, e.g. Gormont's model[15] or a model from the Massachusetts Institute of Technology.[16] Gormont's model was first developed for blades on helicopter rotors, and several adaptations have been proposed for VAWTs, including those by Strickland,[13] Paraschivoiu[16] and Berg.[17] Among others,[18–23] one of the most recent and advanced dynamic stall models is the Beddoes–Leishman dynamic stall (BL DS) model,[24,25] which includes trailing edge and leading edge or shock-induced separation together with vortex shedding and offers simplicity and low computational cost.

The aforementioned aerodynamic and dynamic stall models are all tailored for onshore wind turbines. If the VAWT is mounted on a floating support structure, the pitch motion of the floating support occurs, and the resulting effect of tower

tilting on the aerodynamics should be considered to more accurately calculate the performance and aerodynamic loads. Previous research on FVAWTs is limited because this concept was first proposed in recent years. A similar effect has recently been found to be significant in VAWTs operating on buildings where skewed inflow is occasionally present. The effect of the skewed flow on the performance of an H-Darrieus designed for installation on roofs of high buildings was modelled using a single actuator disk multiple streamtube model and was measured in a wind tunnel by Mertens.[26] The conclusion of this work shows that the skewed flow causes an effective increase of the energy extraction area and subsequently leads to an increase in the power output. Ferreira[27] further conducted a wind tunnel hotwire measurement to determine the effect of skewed inflow on the thrust variation.

In this paper, the DMS model is reformulated to account for the effect of tower tilting for the curved-blade Darrieus VAWTs, including a dynamic stall model. However, the effect of tower tilting is evaluated with respect to the case of steady tilt. The dynamic stall modeling includes Gormont's model with the adaptation of Strickland, Gormont's model with the modification of Berg and the BL DS model. In order to validate the DMS model with different dynamic stall models, the aerodynamic performance and aerodynamic loads at zero tower tilt angle are first calculated and compared with the experimental data; comparative studies of different dynamic stall models are also carried out. The results from different tower tilt angles are compared with those at zero tilt angle of the tower.

2. THE INVESTIGATED WIND TURBINE

Two different VAWTs are chosen for aerodynamic calculation in the present study: the Sandia 17 m wind turbine[28,29] and the DeepWind 5 MW rotor.[30] Since the 1970s, Sandia National Laboratory has put great efforts into research and engineering development of VAWTs, especially the curved-blade Darrieus type. Among them, the Sandia 17 m wind turbine was designed and tested correspondingly with four configurations; one of these is selected as representative of a small wind turbine primarily due to its more easily available experimental data. In contrast, a large VAWT known as the DeepWind 5 MW wind turbine is also presented in this work and represents a new preliminary design used as a baseline model of a floating VAWT from Technical University of Denmark (DTU) and is a part of the FP7 European project DeepWind (2010–2014). Table I summarizes selected important parameters for the two wind turbines.

3. THEORY AND METHODOLOGY

Similar to the BEM model for the aerodynamic calculation of a HAWT, the aerodynamic streamtube model for a VAWT combines momentum theory and blade element theory. This model is based on the conservation-of-momentum principle in a quasi-steady flow by equating the forces on the rotor blades to the change in the streamwise momentum through the turbine. As previously mentioned, this combination can be classified using three different types of models: single streamtube model, assuming that the entire rotor represented by an actuator disk is enclosed in one streamtube; multiple-streamtube model, in which the volume swept by the rotor is divided into a series of adjacent streamtubes; and DMS model, which assumes that the VAWT can be represented by a pair of actuator disks in tandem at each level of the rotor, as shown in Figure 1. The DMS model is described in great detail in the work of Parasschivoiu.[16] The pitch motion of a floating VAWT leads to tower tilt expressed by the tilt angle ϕ. The freestream velocity can be decomposed into a component parallel to the tilted tower and a component perpendicular to the tilted tower. This decomposition is equivalent to the case of having both a horizontal velocity component $U \cos \phi$ and a vertical component $U \sin \phi$ acting on a wind turbine with a non-tilted tower. The general procedure for modifying the DMS model and its subsequent description and analysis are all based on this equivalence, as shown in Figure 1.

Table I. Configuration of VAWT.

Wind turbine	Sandia 17 m	DeepWind 5 MW
Rotor height (m)	16.7	129.56
Rotor diameter (m)	17	127.48
Blade number	2	2
Base height (m)	4.88	15
Chord (m)	0.61	7.45
Airfoil type	NACA0015	NACA0018

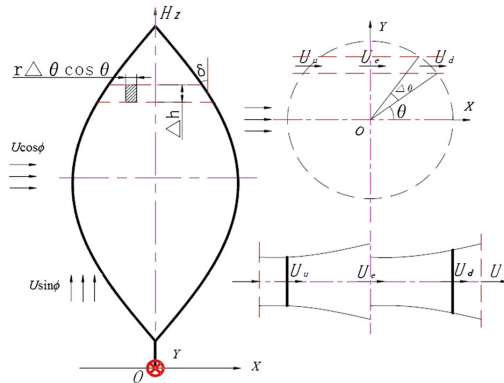NACA = National Advisory Committee for Aeronautics.

Figure 1. DMS model for a Darrieus wind turbine with two actuator disks in tandem with horizontal and vertical inflows.

The wind shear effect is modelled using an exponential wind shear exponent γ given as

$$U/U_\infty = (Z/Z_{EQ})^\gamma \tag{1}$$

where the subscript EQ refers to the equatorial level and Z is the elevation of the streamtube with respect to the ground.

3.1. Adaptation of the Glauert momentum theory for VAWT

The flow through the rotor is subdivided into a sufficiently large number of aerodynamically independent streamtubes. Next, the flow in each streamtube is considered to be acted upon by two actuator disks: the first one representing the upwind half of the surface swept by the rotor blades ($\pi/2 \leq \theta \leq 3\pi/2$) and the second one representing the downwind half of the rotor ($-\pi/2 < \theta < \pi/2$), where the azimuthal angle θ is measured as shown in Figure 1. The variation of the induced velocities as a function of the azimuthal angle is considered in each streamtube to distinguish between the loads in the upwind and downwind part of the rotor.

If tower tilting is present, the induction factor a_u is calculated along the direction normal to the tilted tower, and the wind velocity at the upwind rotor is decomposed into a horizontal velocity U_u and a vertical velocity V_u. The vertical velocity within the downwind zone is mingled with the turbulent wake from the upwind zone and assumed negligible compared with the complex wake. Then, the Glauert momentum theory for yawed flow (according to the Wind Energy Handbook[31]) is applied in the horizontal direction for both the upwind and downwind zones and is coupled with the blade element theory. The contribution from the vertical velocity is considered only for the upwind part of the rotor when calculating the momentum and elemental force. The assumption that the vertical velocity in the downstream zone is negligible is undoubtedly applied for small tilt angles. The extent to which the neglect of the vertical velocity in the downstream zone will affect the calculated result at large tilt angles is an open question. Therefore, pure axial momentum theory will be applied to evaluate the effect of the vertical velocity on the power coefficient by comparing the calculated results with the so-called Glauert momentum theory, which includes the vertical velocity. The difference between these two momentum theories is that the vertical velocity in the upwind zone is included in the mass flow when calculating the momentum in equation (6) and in the velocity triangle when calculating the angle of attack for the Glauert momentum theory, whereas it is neglected in the axial momentum theory. However, both the momentum and the induced velocity are assumed to be normal to the rotating shaft. The upwind horizontal velocity U_u, the upwind vertical velocity V_u, the equilibrium velocity U_e and the downwind horizontal velocity U_d along any given streamtube can be formulated by equations (2–5), respectively:

$$U_u = (\cos\phi - a_u)U \tag{2}$$

$$V_u = U\sin\phi \tag{3}$$

$$U_e = (\cos\phi - 2a_u)U \tag{4}$$

$$U_d = (1 - a_d)U_e = (1 - a_d)(\cos\phi - 2a_u)U \tag{5}$$

On the basis of the aforementioned velocities, the rate of change of momentum for the upwind streamtube and the downwind streamtube are obtained from equations (6) and (7), respectively:

$$\Delta I_u = \rho A_s U^2 \sqrt{(\cos\phi - a_u)^2 + \sin^2\phi} \, 2a_u \tag{6}$$

$$\Delta I_d = \rho A_s U_e^2 (1 - a_d) 2a_d \tag{7}$$

where A_s is the cross sectional area of the streamtube denoted as $r\Delta\theta|\cos\theta|\Delta h$.

3.2. Blade element theory

When the flow passes over the airfoil, lift force is produced perpendicular to the direction of the relative velocity, and drag force acts in the direction of the relative velocity. The normal and tangential forces can be obtained from projection of the lift and drag force according to the azimuthal position. The relative velocity, the angle of attack and the section forces are shown in Figure 2. The lift force L and drag force D_r per length are represented by equations (8) and (9), respectively:

$$L = C_L \frac{1}{2} \rho W_{\text{Disk}}^2 c \tag{8}$$

$$D_r = C_D \frac{1}{2} \rho W_{\text{Disk}}^2 c \tag{9}$$

The non-dimensional airfoil characteristics, C_L and C_D, as a function of angle of attack for the local blade element are obtained from experiments with the appropriate wind turbine blade Reynolds number and airfoil shape. The relative velocity and angle of attack are the foremost parameters that must be determined for evaluating the amplitude and direction of force. Because a difference exists in the velocity distribution between the upwind half of the rotor and downwind half of the rotor, the relative velocity and angle of attack should be treated separately. The W_{Disk} is represented by the local relative velocity at the upwind zone W_u and the local relative velocity at the downwind zone W_d.

The local relative velocity W_u and the local angle of attack α for the upstream half-cycle of the rotor, $\pi/2 \leq \theta \leq 3\pi/2$, are related by

$$W_u \cos\alpha = \omega r + U_u \sin\theta \tag{10}$$

$$W_u \sin\alpha = U_u \cos\delta\cos\theta + V_u \sin\delta \tag{11}$$

$$\alpha = \tan^{-1}\left(\frac{U_u \cos\delta\cos\theta + V_u \sin\delta}{\omega r + U_u \sin\theta}\right) \tag{12}$$

where δ is the angle between the blade normal and the equatorial plane. The second term on the right-hand side in equation (11) stems from the vertical component of the wind speed. When the tilt angle ϕ becomes zero, this component will disappear and the equations coincide with their original form in the DMS model.
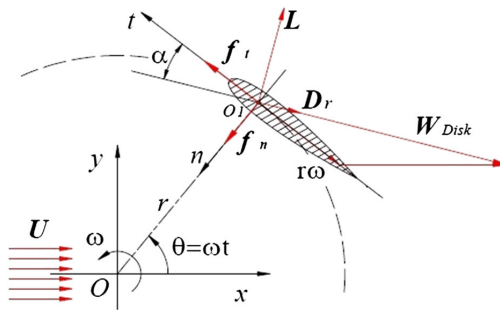

Figure 2. Velocity and force of blade section.

The local relative velocity W_d and the local angle of attack α for the downstream half-cycle of the rotor, $-\pi/2 < \theta < \pi/2$, are related by

$$W_d \cos \alpha = \omega r + U_d \sin \theta \tag{13}$$

$$W_d \sin \alpha = U_d \cos \delta \cos \theta \tag{14}$$

$$\alpha = \tan^{-1} \left(\frac{U_d \cos \delta \cos \theta}{\omega r + U_d \sin \theta} \right) \tag{15}$$

As stated previously, the vertical component of the wind speed is assumed to be small in the downwind zone such that the formulation for the relationship between the relative velocity and induced velocity is identical to that of the original DMS model.

In order to calculate the power performance and evaluate the influence of the dynamic stall correction, it is convenient to resolve the lift and drag coefficients into a normal force coefficient C_n and a tangential force coefficient C_t, as shown in equations (16) and (17):

$$C_t = C_L \sin \alpha - C_D \cos \alpha \tag{16}$$

$$C_n = -C_L \cos \alpha - C_D \sin \alpha \tag{17}$$

The combination of momentum theory and blade element theory requires projection of the normal force and the tangential force coefficients into a thrust force coefficient C_x and a lateral force coefficient C_y, as shown in equations (18) and (19), to calculate the induction factor.

$$C_x = -C_t \sin \theta - C_n \cos \delta \cos \theta \tag{18}$$

$$C_y = C_t \cos \theta - C_n \cos \delta \sin \theta \tag{19}$$

The average thrust force in the streamtube corresponds to the streamwise force f_x produced by an individual blade element as it passes through the streamtube in which each of N_b blade elements spends $\Delta\theta/2\pi$ percent of their time. Therefore, the average thrust force in the direction of the streamtube at a certain azimuthal position from the blade element theory can be expressed as

$$f_{\text{xave}} = \frac{N_b \Delta \theta}{2\pi} \cdot \frac{1}{2} \rho W_{\text{Disk}}^2 \frac{c \Delta h}{\cos \delta} (-C_t \sin \theta - C_n \cos \delta \cos \theta) \tag{20}$$

By equating equation (20) to equations (6) and (7) separately, the induction factor can be calculated from equations (21) and (22):

$$a_u \sqrt{(\cos\phi - a_u)^2 + \sin^2\phi} = \frac{N_b c}{8\pi \cdot r \cdot |\cos\theta|} \cdot \left(\frac{W_u}{U_\infty}\right)^2 \left(-C_{tu} \frac{\sin\theta}{\cos\delta} - C_{nu} \cos\theta\right) \tag{21}$$

$$a_d(1 - a_d) = \frac{N_b c}{8\pi \cdot r \cdot |\cos\theta|} \cdot \left(\frac{W_d}{U_e}\right)^2 \left(-C_{td} \frac{\sin\theta}{\cos\delta} - C_{nd} \cos\theta\right) \tag{22}$$

The power coefficient is given as

$$C_P = \frac{\overline{T}\omega}{0.5\rho U_\infty^3 S_{\text{wind}}} \tag{23}$$

where $\overline{T}$ is the average rotor torque and S_{wind} is the rotor swept area.

3.3. Dynamic stall model

Dynamic stall is a complex unsteady phenomenon related to the time response of the viscous boundary layer and thus to the chordwise pressure and skin friction distribution for the rapid variation of the angle of attack as well. The mechanism of dynamic stall was first identified on helicopters with the physics of the stall developments being fundamentally different from the static stall mechanism for the same airfoil. This mechanism produces a delay in stall onset, i.e. the stall occurs

at a higher angle of attack than for the static stall case and is characterized by shedding and passage over the upper lifting surface of a vortex-like structure. The process begins with a rapid increase in lift and ends with full flow separation and catastrophic loss of lift as the vortex disturbance is convected past the trailing edge of the airfoil.[32] Subsequently, hysteresis loops occur in the force coefficients and produce cyclic pressure loading that is not predicted using conventional aerodynamics.

A variety of computationally efficient engineering models were originally developed to predict the dynamic stall effects in helicopters[15,33–38] and a subset of these were adapted for use in wind turbine aerodynamics, e.g. the ONERA method.[39,40] However, under normal operating conditions, the Mach number and rotational frequency for wind turbines are significantly lower than those for helicopters, and thus, specific dynamic stall models tuned for wind turbines have been developed by several researchers, such as Øye,[22] Snel,[18] Gupta,[24] Larsen[21] and Sheng.[23] These semi-empirical models contain a re-synthesis of the measured unsteady airfoil data to represent the essential physics using sets of linear and non-linear equations for the lift, drag and pitching moment coefficients of airfoils under dynamic conditions. The empirical parameters must be deduced for these equations from unsteady airfoil measurements.

To model the dynamic stall effect for VAWTs, various adaptations of Gormont's model[15] were first proposed. In this paper, Gormont's model with the adaptation of Strickland[13] and with the adaptation of Berg[17] are used to predict the unsteady aerodynamics of VAWTs at a low tip speed ratio. The assumptions that the lift curve and zero-lift angle remain unchanged and that the dynamics effects only modify the angle of attack at which stall occurs are upheld for the former model, denoted as 'Gormont DS' in the following analysis. Thus, a modified angle of attack α_M is used to derive the two-dimensional force coefficient data as a function of $c\dot{\alpha}_e/(2W)$ and other parameters (α_e, γ and K_1), as shown in equation (24)

$$\alpha_M = \alpha_e - \gamma K_1 \left(\left| \frac{c\dot{\alpha}_e}{2W} \right| \right)^{1/2} S_{\dot{\alpha}} \tag{24}$$

where W represents the relative inflow velocity, α_e is the effective blade angle of attack, γ and K_1 are empirical constants, $\dot{\alpha}_e$ represents the instantaneous rate of change of α_e and $S_{\dot{\alpha}}$ is the sign of $\dot{\alpha}$. The latter model, which was intended to avoid the drawback of Gormont's model, was proposed to compute the modified dynamic coefficients using linear interpolation between the dynamic coefficient predicted by Gormont's model and the static coefficient. This model will be denoted as 'Berg DS' in the following analysis.

The BL DS model is also used to calculate the VAWTs' aerodynamics in this work. This approach is quite different from those of the aforementioned methods and represents the physical phenomenon to a certain extent through a superposition of separate indicial functions. The original BL DS model[25] is capable of simulating the dynamic stall effect on helicopters, and the adaptation of this model has been validated for wind turbines by Gupta and Leishman.[24] The model consists of three components: unsteady attached flow, unsteady separated flow and dynamic vortex lift. The loads in the unsteady attached flow regime are obtained by treating the aerodynamic forces on the airfoil as the sum of a circulatory component related to the change of the angle of attack and an impulsive component generated by the change rate of the angle of attack and pitch movement. Next, the total normal force coefficient C_N^{Pot} under attached flow condition is given by

$$C_N^{Pot} = C_N^C + C_N^I \tag{25}$$

where C_N^C is the circulatory normal force coefficient and C_N^I is the impulsive normal force coefficient. The unsteady chordwise force coefficient, C_C, which is identical to the tangential force coefficient in this case, is obtained using the effective angle of attack α_e

$$C_C = C_N^C \alpha_e \tag{26}$$

The unsteady separate flow together with the non-linear effects usually includes leading edge separation and trailing edge separation, both of which must be predicted correctly to accurately estimate the influence on the aerodynamic coefficients. The normal force coefficient and the chordwise force coefficient are related to the dynamic separation point on the basis of the static condition according to the Kirchhoff theory and the history of the angle of attack. Finally, a vortex may detach from the surface at a certain critical point and move downstream along the chord after it is formed near the leading edge. This vortex does not significantly change the pressure distribution until it detaches from the airfoil. The vortex lift contribution is modeled as the difference between the attached flow C_N^C and the unsteady non-linear value from the Kirchhoff relationship. These three components are connected in an open loop system, in which the input for one component comes from the output of the previous component. Thus, the total loading on the airfoil is obtained by summing all of the aforementioned components.

In order to adapt the BL DS model for VAWT applications, certain modifications are implemented according to the AeroDyn theory manual of National Renewable Energy Laboratory.[41] This model is capable of producing aerodynamic force coefficients over the entire range of possible angles of attack. Two different effective separation point tables

(f_N and f_C) are calculated for the normal force coefficient and the chordwise force coefficient, respectively. The chordwise force coefficient is obtained by adding one additional term from the vortex lift, similar to the normal force coefficient. It is written as

$$C_C = C_{N\alpha}(\alpha_e - \alpha_0)\alpha_e\sqrt{f_C^{"}} + C_N^v\alpha_e(1 - \tau_v) \tag{27}$$

where the $C_{N\alpha}$ is the normal force coefficient curve slope, $f_C^{"}$ is the dynamic separation point function taking into account the temporal effects for chordwise force coefficient, C_N^v is the normal force coefficient from the vortex lift contribution and τ_v is a non-dimensional parameter to track the position of the vortex across the airfoil. Finally, the lift coefficient and drag coefficient are calculated from C_N and C_C by force resolution as

$$C_L = C_N \cos\alpha + C_C \sin\alpha \tag{28}$$

$$C_D = C_N \sin\alpha - C_C \cos\alpha + C_{d0} \tag{29}$$

where C_{d0} is the minimum drag coefficient corresponding to the zero angle of attack.

The integration of the DMS model and the BL DS model in the time domain is represented by a flowchart, as shown in Figure 3. At a given time, the relative velocity and the angle of attack are calculated from the DMS model and subsequently become the inputs into the BL DS model. Thus, the normal force coefficient and the chordwise force coefficient are corrected by including the dynamic stall effect. The lift coefficient and drag coefficient are obtained at each time step.

4. VALIDATION OF THE PRESENT MODEL

In this section, the presented modified DMS model is validated against experimental results, demonstrating a high correlation between the theoretical and experimental results. The experimental results were first used by Mertens[26] to validate his analytical model of an H-Darrieus VAWT in skewed flow, as shown in Figure 4. The H-Darrieus VAWTs are widely applied on roofs of high buildings where skewed flow is present. The effect of the skewed flow on the performance of an H-Darrieus VAWT was found to be significant and thus must be evaluated properly. Mertens adapted the single disk multiple streamtube model for the H-Darrieus VAWT in skewed flow and carried out the experimental tests for a two-
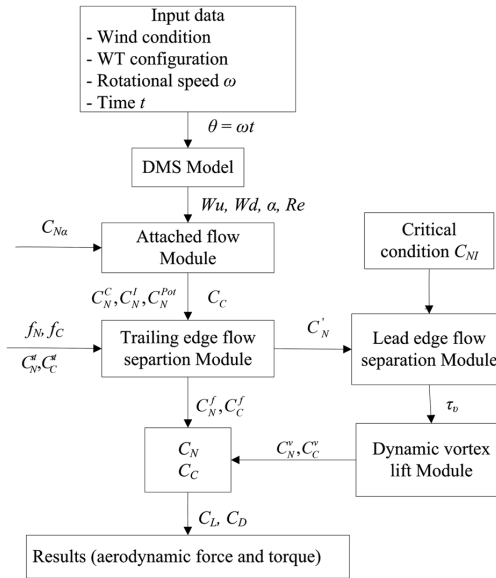

Figure 3. Flowchart of the integration of the DMS and the BL DS model in the time domain.

bladed H-Darrieus VAWT of 0.755 m diameter, 0.5 m height and 0.08 m chord length at a wind tunnel velocity of $7 \, \text{m s}^{-1}$ in the open jet wind tunnel of the TU Delft Wind Energy Section. The measurements and calculations performed with the Mertens model for the tip speed ratio and power coefficient are reproduced as shown in Figures 5 and 6 as a function of the tilt angle ϕ. It is noted that the tip speed ratio in Figure 5 corresponds to the maximum power coefficient, and the power coefficient in Figure 6 is the maximum value for every tilt angle.

In order to validate the present model using the existing experimental results, the H-Darrieus VAWT is split up into three parts, as shown in Figure 4; one part of the rotor is located within the upwind zone, one part of the rotor is located within the downwind zone through which the wake flow passes and one part of the rotor is located within the downwind zone through which the undisturbed flow passes. The effect of the skewed flow on the downwind rotor can thus be taken into account. When the present model is applied, the undisturbed wind speed of the skewed flow is considered for part 1 and part 3, whereas the reduced wind speed of the wake flow from the upwind zone is calculated for part 2. The lengths of parts 2 and 3 are calculated according to the tilt angle of the flow and the azimuthal position. Furthermore, the dynamic stall model is switched off in this calculation because it was not included in the Mertens model. The calculated results from the present
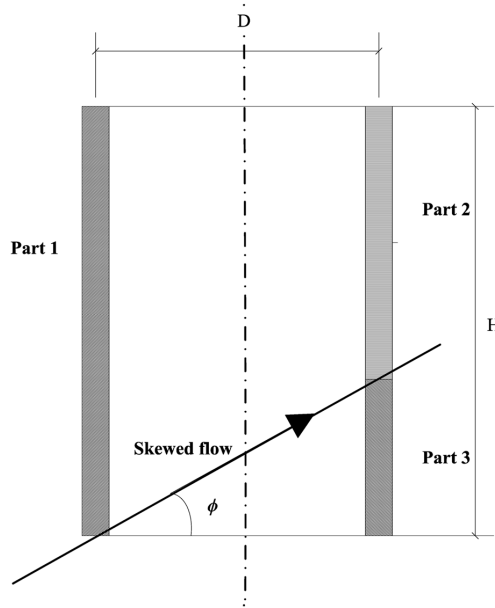
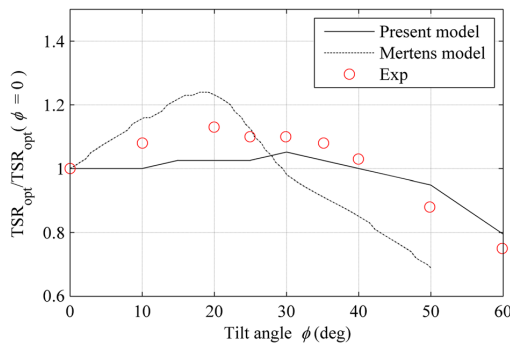

Figure 4. Schematic drawing of the H-Darrieus partitions.

Figure 5. Measured and calculated tip speed ratio at maximum power coefficient in skewed flow with tilt angle ϕ.
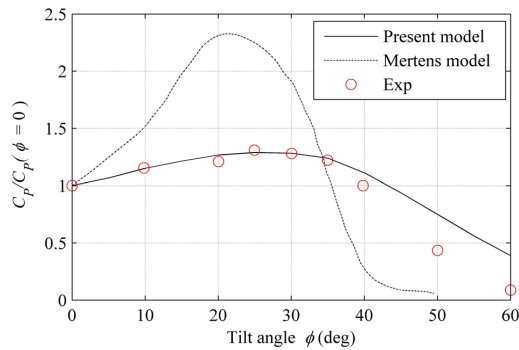
Figure 6. Measured and calculated maximum power coefficient in skewed flow with tilt angle ϕ.

model are compared with the experimental results and the calculated results from Mertens, as shown in Figures 5 and 6. The comparison of the tip speed ratios shows that the mismatch between data and prediction for the tilt angle at which the tip speed ratio starts to decrease is not improved by the present model, but the amplitude becomes slightly closer to the experimental data, especially for a tilt angle larger than 30°. A comparison of the power coefficient in Figure 6 demonstrates that the power coefficient in the skewed flow as predicted by the present model matches the experimental data quite well. However, when the tilt angle is larger than 40°, the power coefficient is overestimated. This result can be primarily ascribed to the observation that the decreasing velocity perpendicular to the blade with the increase of the tilt angle results in a heavily loaded rotor, which causes a convergence failure in the numerical calculation of the momentum equations. However, it can be concluded that the present model works well for predicting the power coefficient when the tilt angle is less than 40°.

5. RESULTS AND DISCUSSIONS

This section discusses the effect of the tilt angle and the various dynamic stall models on the aerodynamics of VAWTs. A selection of results is presented, including the global performance, and the local aerodynamic coefficients obtained by the DMS model both without the dynamic stall model and with three different dynamic stall models. The calculated results for the Sandia 17 m wind turbine are compared with the experimental data from the prototype of the wind turbine.[42,43] The thrust force for the DeepWind 5 MW wind turbine design is compared with computations from Risø DTU.[44]

5.1. Global performance of the Sandia 17 m wind turbine

The global performance includes power and rotor torque. First, the Sandia 17 m wind turbine is chosen in this study because the experimental test results are available. The power coefficient and rotor torque are evaluated when the turbine operates at 42.2 and 50.6 rpm, respectively. Figure 7 presents the aerodynamic performance of the wind turbine at zero tilt. The power coefficient C_P is calculated as a function of the tip speed ratio X_{eq}, both in the absence of the dynamic stall model and in the presence of the three dynamic stall models, and it is compared with the experimental data. The comparison shows that the result is not improved significantly using the Gormont DS model and the Berg DS model except at a low tip speed ratio, where the dynamic stall effect is more significant. The dynamic stall model generally plays a role in the accuracy of the results at a low tip speed ratio, where the wind speed is high compared with the rotational speed. When applying the BL DS model, the calculated results match the experimental data much better, not only at low tip speed ratios but also at large tip speed ratios. However, the BL DS model slightly underestimates the maximum value of the power coefficient, whereas other models overestimate not only the maximum value but also most of the values, especially at high tip speed ratios. Therefore, the BL DS model performance is retained for use in the subsequent calculations because it is one of the most recent dynamic stall models and offers better prediction ability for wind turbine performance.

The power coefficient C_P for different tilt angles is calculated using the BL DS model and plotted in Figure 8. The figure shows that the power decreases with the increase in the tilt angle of the rotor shaft, which is more apparent at the middle tip speed ratios ($4 < X_{eq} < 7$). The power coefficient C_P reaches a maximum at $X_{eq} = 5.2$. The percentage differences of the maximum C_P between the 0° tilt angle and others (i.e. 5, 10, 15 and 20°) are 1.0%, 2.6%, 4.6% and 6.7%, respectively. Moreover, the band of the power coefficient curve becomes slightly broader. When the dynamic stall model is switched off, the similar results can be observed and the percentage differences of the maximum C_P between the 0° tilt angle and
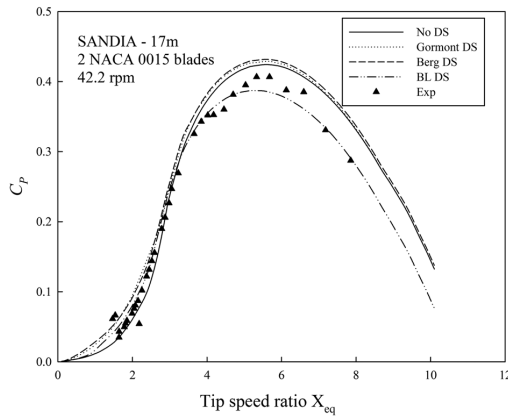
Figure 7. Comparison of C_P between different models and experimental data, the Sandia 17 m rotor for zero tilt angle.
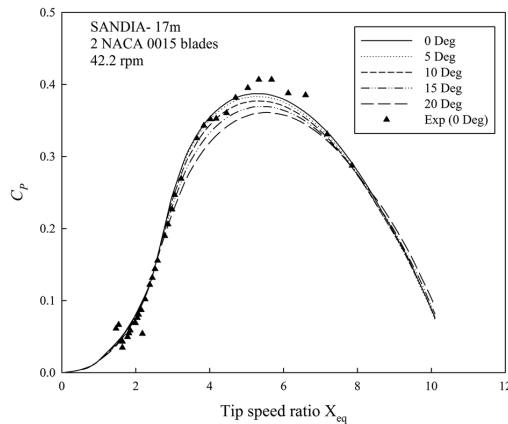

Figure 8. Power coefficient C_P as a function of tilt angle by using the BL DS model, Sandia 17 m rotor.

others are 0.9%, 2.4%, 4.6% and 7.1%, respectively. On the basis of the aforementioned comparison, the effect of tilt angle on the power coefficient can be considered insignificant when the tilt angle is less than 15°.

The elemental tangential force multiplied by corresponding radius can be integrated along the length of the two blades to calculate the total rotor torque and its variation with the azimuthal angle θ. The rotor torque is shown in Figure 9 as a function of the azimuthal angle θ within the upwind zone at a tip speed ratio of $X_{eq} = 2.0$ for the two-bladed Sandia 17 m wind turbine from the pure DMS model and with use of different dynamic stall models. The experimental data are also plotted with comparison of the numerical results. The plot shows that the results in the absence of any dynamic stall model underestimate the rotor torque from 140 to 200° and overestimate from 200 to 240° within the upwind zone. The absence of a dynamic stall model leads to a large difference between the numerical results and the experimental data. When the Gormont DS and Berg DS models are applied, the dynamic delay phenomenon is well predicted but the results are overestimated, especially for the values near the two peak areas. If the BL DS model is used, moderate results are obtained for amplitude and dynamic delay. To remedy this deficiency, the various parameters of the BL DS model could be optimized,[45,46] especially the time constant T_p for the leading edge pressure lag. Alternatively, a revised DS model could be used to predict the stall-onset more accurately as proposed by Sheng.[23] The DMS model with the BL DS model is used to investigate the effect of different tilt angles on the rotor torque, and the results are shown in Figure 10. The main difference is found near the maximum torque zone between the 130° azimuthal angle and the 170° azimuthal angle. There is little difference in the results between the 0° tilt angle and the 5° tilt angle. However, the percentage differences compared with 0° tilt angle at the azimuthal angle of 145° reach 5.2%, 10.7% and 18.7% for 10, 15 and 20° tilt angles, respectively.
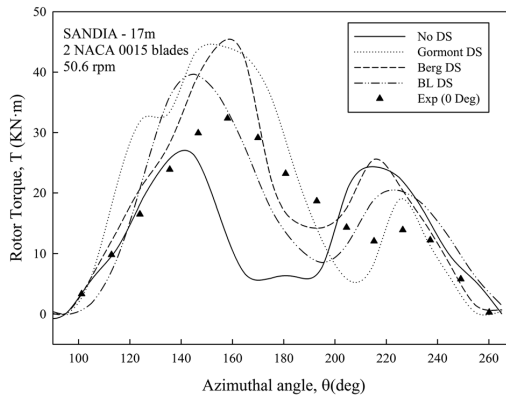
Figure 9. Rotor torque as a function of the azimuthal angle by using the DMS with different dynamic stall models at $X_{eq} = 2.0$.
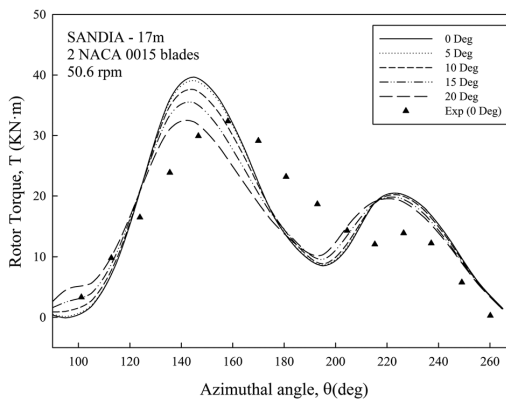

Figure 10. Rotor torque as a function of the azimuthal angle by using the BL DS model for different tilt angles at $X_{eq} = 2.0$.

The main reason for the large difference is that the presence of the tilt angle changes the angle of attack and subsequently affects the aerodynamic loads. In particular, the changes are larger when the aerodynamic loads become sensitive at large angles of attack.

5.2. Local aerodynamic coefficients of the Sandia 17 m wind turbine

Normal force and tangential force coefficients are two important parameters when evaluating aerodynamic loads on a blade section. The computed azimuthal distribution of the local normal force coefficient C_n at the equator level using different dynamic stall models at the tip speed ratio of 3.09 for the Sanida 17 m wind turbine operating at 38.7 rpm is plotted together with the experimental data in Figure 11. All of the models predict the normal force coefficient quite accurately, except at the stall regions, i.e. the azimuthal angle θ from -50 to $20°$ within the downwind zone and from 150 to $250°$ within the upwind zone. Because the angles of attack at this tip speed ratio remains below $20°$, the effect of the dynamic stall does not play a major role on the coefficients for most of the azimuthal angles. The DMS results coupled with the Gormont DS model and Berg DS model overestimate the maximum values and underestimate the values after the stall point, and these results are not better than the result from the DMS model without any dynamic stall. However, the DMS model coupled with the BL DS model produces more pertinent results than other models, again indicating that this model is much better for this type of flow.

If the tilt angle is considered, the normal force coefficient C_n at the equator level using BL DS model is plotted as a function of the azimuthal angle in Figure 12. A noticeable difference between different tilt angles is observed at the azimuthal angle $-35°$ within the downwind zone. The reason for this result is that the corresponding angle of attack at this azimuthal
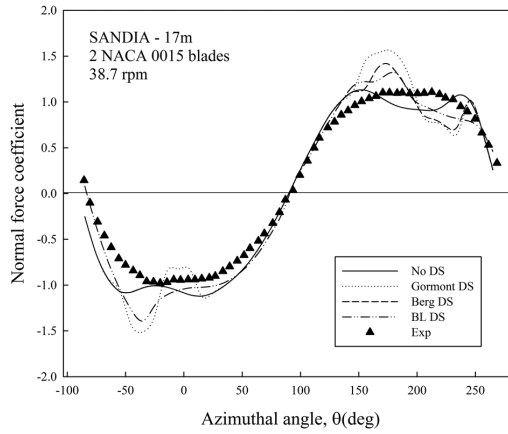
Figure 11. Normal force coefficient versus azimuthal angle at 38.7 rpm and $X_{eq} = 3.09$.
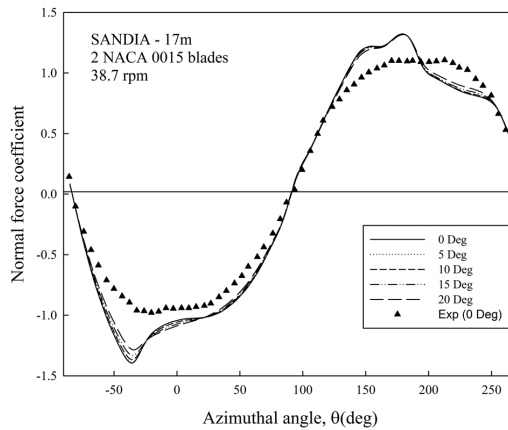

Figure 12. Normal force coefficient versus azimuthal angle for different tilt angles at 38.7 rpm and $X_{eq} = 3.09$.

position is close to the stall point, at which the lift coefficient is much more sensitive. However, the differences between different tilt angles can be considered negligible in general.

Given the same operating condition and tip speed ratio as for the local normal force coefficient C_n, the values of local tangential force coefficient C_t predicted by DMS with and without dynamic stall modeling are presented as a function of the azimuthal angle in Figure 13. Apparently, the DMS model without a dynamic stall model reproduces the experimental values of the tangential force coefficient C_t quite well, except near $\theta = 200°$ in the upwind zone, where the predicted values are slightly underestimated and near $\theta = 0°$ in the downwind zone, where the predicted values are slightly overestimated. When the Gormont DS model and Berg DS model are coupled with the DMS model, the results tend to produce an irregular stall phenomenon in the curves of the tangential force coefficient near $\theta = 200°$, and these results look quite different compared with the experimental data. The result from the BL DS model is improved compared with that of other models, although the part defined by $\theta < -50°$ in the downwind zone and $\theta > 250°$ in the upwind zone still underestimates the tangential force coefficient.

When the tilt angle is taken into account, the tangential force coefficient C_t at the equator level using the BL DS model is plotted as a function of the azimuthal angle in Figure 14. The difference in the results from 0 to 10° is not easily identified, whereas certain differences for larger tilt angles can be observed for the azimuthal angle between 200 and 225° in the upwind zone and the azimuthal angle near the peak in the downwind zone. The maximum values of the tangential force coefficient C_t decrease as the tilt angle changes from 0 to 20° because the horizontal wind velocity decreases, especially in the downwind zone. However, the tangential force coefficient C_t increases slightly near the near 210° in the upwind zone.
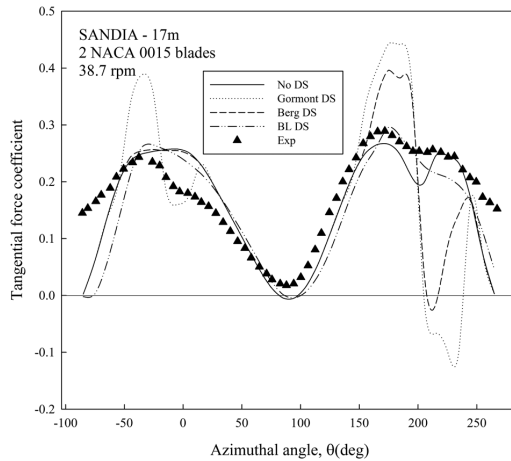
Figure 13. Tangential force coefficient versus azimuthal angle at 38.7 rpm and $X_{eq} = 3.09$.
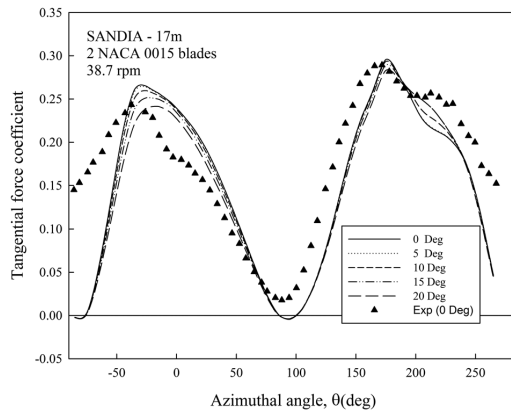

Figure 14. Tangential force coefficient versus azimuthal angle for different tilt angles at 38.7 rpm and $X_{eq} = 3.09$.

5.3. Global performance of the DeepWind 5 MW wind turbine

This section presents the computed global power coefficient C_P and thrust force for the DeepWind 5 MW wind turbine operating at the rated rotor speed of 5.26 rpm. The cut-in wind speed is $5 \, \text{m s}^{-1}$ and the cut-out wind speed is $25 \, \text{m s}^{-1}$, such that the tip speed ratio varies from 1.4 to 7. Experimental test results are not available for this model, and therefore, the calculated thrust force is compared with the computed values from Risø DTU.[44] Figure 15 represents the power coefficient C_P of the wind turbine as a function of the tip speed ratio X_{eq} and tilt angles using the DMS model together with the BL DS model. The percentage differences of the maximum C_P between 0° tilt angle and others (i.e., 5, 10, 15 and 20°) are 1.0%, 2.0%, 2.8% and 3.7%, respectively, which are smaller than those of the Sandia 17 m wind turbine. When the wind speed is greater than $12 \, \text{m s}^{-1}$ corresponding to a tip speed ratio of 2.93, the results are nearly identical. The effect of tower tilting on the power coefficient C_P can be considered negligible at least up to 10° for all ranges of tip speed ratios.

The thrust force is the integrated aerodynamic load normal to the rotating shaft in the horizontal direction of the wind. A comparison between the thrust forces from the DMS model for various tilt angles is shown in Figure 16, and the computed results from DTU are also displayed. DTU also uses the DMS model without a dynamic stall model, and the effect of tower tilting is not included. Therefore, the data from Risø DTU refer to the thrust force corresponding to a tilt angle of 0°. The calculated results of the non-tilting wind turbine from the present model show good agreement with those from DTU,
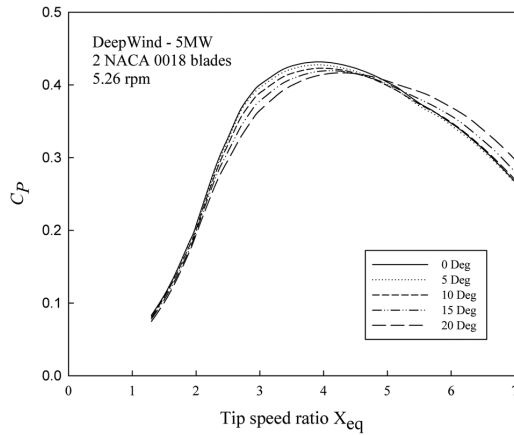
Figure 15. Power coefficient C_P as a function of tip speed ratio by using the BL DS model.
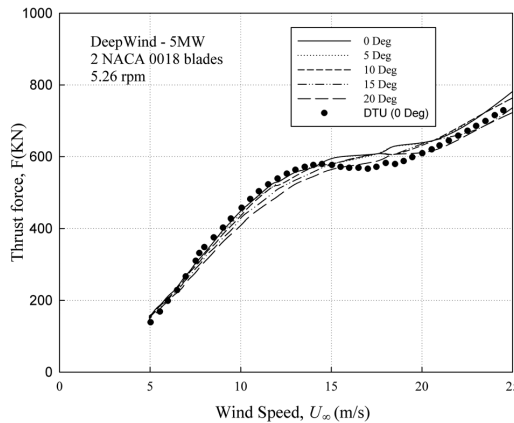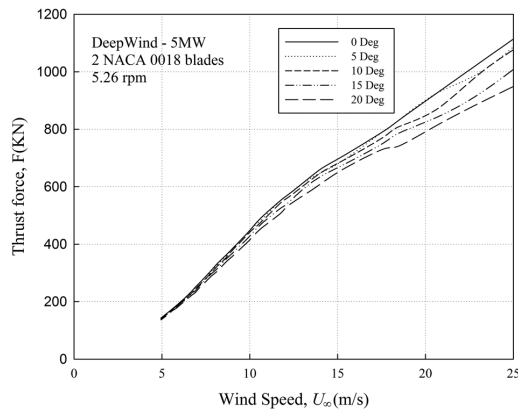

Figure 16. Thrust force as a function of wind speed for different tilt angles at 5.26 rpm; the tip speed ratio varies from 1.4 to 7.

except for a small difference after stall for wind speed greater than $14 \, \mathrm{m \, s}^{-1}$. The percentage differences of the thrust force between the 0° tilt angle and others (i.e. 5, 10, 15 and 20°) are 0 %, 0%, 2.3% and 4.6%, respectively, at the rated wind speed of $14 \, \mathrm{m \, s}^{-1}$. Therefore, the effect of tilt angle on the thrust force can be neglected at least within the 10° tilt angle. When the BL DS model is integrated into the DMS model, the thrust forces corresponding to different tilt angles are plotted as a function of wind speed in Figure 17. The percentage differences of the thrust force between the 0° tilt angle and others are 2.0 %, 2.0%, 3.9% and 7.8%, respectively, at the rated wind speed of $14 \, \mathrm{m \, s}^{-1}$, which are a bit larger than those only using a DMS model. When the wind speed increases to $25 \, \mathrm{m \, s}^{-1}$, the decreases in the thrust force for tilt angles of 5 and 10° are still small, whereas the decrease for larger tilt angles becomes noticeable.

5.4. Local aerodynamic coefficients of the DeepWind 5 MW wind turbine

The distribution of the local normal force coefficient C_n at the equator level using the BL DS model is plotted in Figure 18 for different tilt angles as a function of the azimuthal angle at the tip speed ratio of $X_{eq} = 2.5$ for the DeepWind 5 MW wind turbine operating at 5.26 rpm. The visible difference is only limited to a narrow range of minimum values of the normal force coefficient in the downwind zone and maximum values of the normal force coefficient in the upwind zone. However, this difference is considered negligible at least up to a tilt angle of 10°. In other words, the effect of tower tilting on the normal force coefficient is quite small.

Figure 17. Thrust force as a function of wind speed for different tilt angles by using the BL DS model at 5.26 rpm; the tip speed ratio varies from 1.4 to 7.
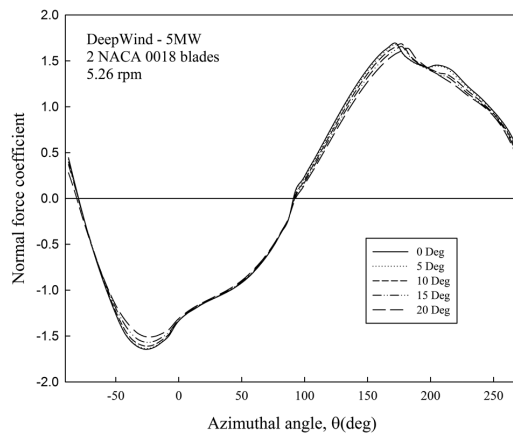
Figure 18. Normal force coefficient versus azimuth angle at 5.26 rpm and $X_{eq} = 2.5$.

The local tangential force coefficient C_t corresponding to different tilt angles is plotted as a function of azimuthal angle in Figure 19. A pronounced difference is observed near the maximum values of the tangential force coefficient C_t in the downwind zone, and noticeable differences occur after the stall point in the upwind zone, especially for the tilt angles of 15 and 20° compared with that of the small tilt angles. Therefore, the effect of tower tilting on the tangential force coefficient C_t is negligible up to a 10° tilt angle and should be considered for larger tilt angles. In other words, this result implies that the aerodynamic calculation of a floating VAWT can be simplified by neglecting the tower tilting effect as long as the steady tilt angle is less than 10°. For a spar type VAWT in still water, the tilt angle can reach up to 6° when the wind speed varies from 5 to 25 m s^{-1}.[44] For a semi-submersible type VAWT in the conditions of 3 m wave height and 8 s wave peak period, the tilt angle is only approximately 3° when the wind speed is given at the rated speed of 14 m s^{-1}.[47]

5.5. Investigation on the application of the axial momentum theory

Investigation of the aerodynamic performance when the axial momentum theory is applied to the case of tower tilting is also of interest. The vertical velocity in the upwind zone is removed when using the axial momentum theory for comparison
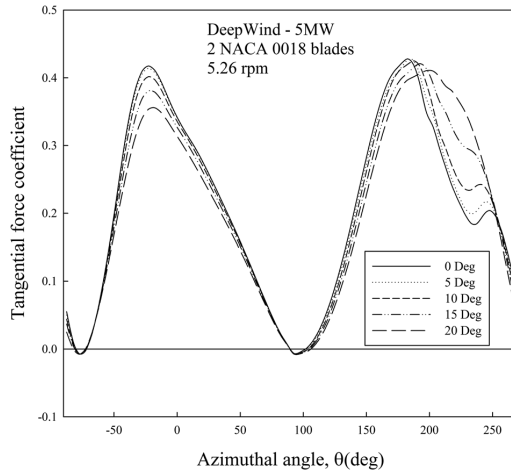
Figure 19. Tangential force coefficient versus azimuth angle at 5.26 rpm and $X_{eq} = 2.5$.
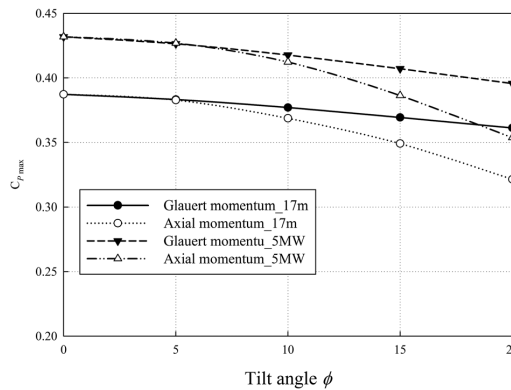
Figure 20. Maximum power coefficient variation with tilt angle; comparison between the Glauert momentum theory and the axial momentum theory.

with the case of including the vertical velocity in the upwind zone when the Glauert momentum theory is applied. Neglecting the vertical wind speed component in the upstream zone, equation (6) simplifies to

$$\Delta I_u = \rho A_s U^2 (\cos\phi - a_u) 2 a_u \tag{30}$$

The vertical component of the wind velocity is also disregarded during the implementation of blade element theory, and therefore, the second term on the right-hand side of equation (11) that quantifies the effect of vertical wind velocity on the aerodynamics is neglected. Consequently, equation (21) is modified to

$$a_u (\cos\phi - a_u) = \frac{N_b c}{8\pi \cdot r \cdot | \cos\theta |} \cdot \left(\frac{W_u}{U_\infty} \right)^2 \left(-C_{tu} \frac{\sin\theta}{\cos\delta} - C_{nu} \cos\theta \right) \tag{31}$$

In a manner similar to that of the Glauert momentum theory used in the previous calculation, the effect of tilt angle on the power performance can be investigated on the basis of the axial momentum theory.[31] The maximum power coefficient of the Sandia 17 m wind turbine operating at 42.2 rpm and the DeepWind 5 MW wind turbine operating at 5.26 rpm for different tilt

angles are both plotted in Figure 20. Although the large VAWT has a higher power coefficient compared with that of the small one, they both display the same trend in the change of power coefficient, showing a decrease as the tilt angle is increased for both momentum theories. When the tilt angle is less than 10°, the difference between the power coefficients from the Glauert momentum theory and from the axial momentum theory is quite small. When the tilt angle becomes larger, the latter theory predicts a much more evident decrease of the power coefficient than the former theory. This difference is reasonable because the vertical component of the wind velocity in the upwind zone is also neglected when using the axial momentum theory. The difference in the maximum power coefficient between the two different models can reach 10% at a tilt angle of 15° and 17% at a tilt angle of 20° for both the small and large wind turbines. Taking into account characteristics of the wake flow, the effect of neglecting vertical velocity in the downwind zone will be smaller than that in the upwind zone. Consequently, implementing the proposed model is acceptable up to a tilt angle of 20°, that is, neglecting the vertical velocity in the downwind zone does not affect the analysis of the calculated results in the given tilt angle range, and the conclusion is conservative.

6. CONCLUSIONS

This work provides certain specific insights into the effect of tower tilting on the aerodynamics of a Darrieus VAWT with curved blades, which have not yet been explored in the literature. However, the effect must be evaluated when the VAWT is applied to a floating structure in which the platform pitch motion has a rather large amplitude. A modified DMS model based on the Glauert momentum theory and the blade element theory including the vertical component of wind velocity in the upwind zone is proposed to calculate the aerodynamics of a VAWT when the tower is tilted. The model has been validated against experimental data from an H-Darrieus VAWT. Three different dynamic stall models are also integrated to assess the dynamic stall effect and improve the accuracy of the results. By comparing the results from the different dynamic stall models with the experimental data, this work has demonstrated that the BL DS model is superior to the other models tested for predicting the aerodynamic characteristics of a Darrieus-type VAWT.

Analysis of the computed results is based on different tilt angles applied under steady condition. The analysis shows that the effect of tower tilting on the power coefficient is insignificant for the Sandia 17 m wind turbine up to a 15° tilt angle, whereas pitching the tower has a larger effect on the maximum values of rotor torque when the tilt angle exceeds 10°. Moreover, the effect on the local tangential force coefficient is more evident than that on the local normal tangential force coefficient, especially at certain azimuthal positions. For the DeepWind 5 MW wind turbine, the results present a conclusion similar to that for the Sandia 17 m wind turbine but with a lesser effect on the power coefficient and local normal coefficient. The tangential force coefficient is much more sensitive to tilt angle than the normal force coefficient.

Finally, comparing the results from the Glauert momentum theory and the axial momentum theory, a similar trend is observed for the effect of a non-zero tilt angle on the aerodynamics, which shows that the axial momentum theory predicts a larger decrease of the power coefficient because it neglects the vertical velocity in the upwind zone. Neglecting the vertical velocity does not affect the power coefficient at small tilt angles. Thus, the effect of the vertical velocity is evaluated using different momentum theories, and the assumption of neglecting the vertical velocity in the downwind zone is proved acceptable in the presented model over the given range of tilt angles. However, a specific experimental test for a curved-blade Darrieus VAWT with different tilt angles is expected to be a component of a more detailed investigation in the future.

ACKNOWLEDGEMENTS

REFERENCES

1. Paulsen US, Pedersen FT, Madsen HA, Enevoldsen K, Nielsen PH, Hattel J, Zanne L, Battisti L, Brighenti A, Lacaze M, Lim V, Heinen JW, Berthelsen PA, Carstensen S, de Ridder EJ, vanBussel G, Tescione G. Deepwind—an innovative wind turbine concept for offshore. *European Wind Energy Association (EWEA) Annual Event*. Brussels, 2011.
2. Vita L, Paulsen US, Pedersen TF. A novel floating offshore wind turbine concept: new developments. *European Wind Energy Conference and Exhibition*. Poland, 2010.
3. Vita L, Paulsen US, Pedersen TF, Madsen HA, Rasmussen F. A novel floating offshore wind turbine concept. *European Wind Energy Conference and Exhibition*. Marseille, France, 16–19 March, 2009.

4. Cahay M, Luquiau E, Smadja C, Silvert FCC. Use of a vertical wind turbine in an offshore floating wind farm. *Offshore Technology Conference* Houston, Texas, USA, 2-5 May 2011.

5. 10MW Aerogenerator X © Wind Power Limited & Grimshaw at http://vimeo.com/13654447.

6. Paraschivoiu I. Double-multiple streamtube model for Darrieus wind turbines. Second DOE/NASA Wind Turbines Dynamics Workshop, NASA CP-2185. Cleveland, Ohio, February 1981.

7. Paraschivoiu I, Delclaux F. Double multiple streamtube model with recent improvements. *AIAA Journal of Energy* 1983; **7**: 250–255.

8. Templin RJ. Aerodynamic performance theory for the NRC vertical-axis wind turbine. *Technical Report LTR-LA-160*, National Aeronautical Establishment, Ottawa, Ontario (Canada), 1974.

9. Strickland JH. The Darrieus turbine: a performance prediction model using multiple streamtubes. *SAND75-0430*, Sandia National Laboratories, Albuquerque, N.M., October 1975.

10. Ponta FL, Jacovkis PM. A vortex model for Darrieus turbine using finite element techniques. *Renewable Energy* 2001; **24**: 1–18.

11. Scheurich F, Fletcher TM, Brown RE. Simulating the aerodynamic performance and wake dynamics of a vertical-axis wind turbine. *Wind Energy* 2011; **14**: 159–177. DOI: 10.1002/we.409.

12. Zanon A, Giannattasio P, Simão Ferreira CJ. A vortex panel model for the simulation of the wake flow past a vertical axis wind turbine in dynamic stall. *Wind Energy* 2012. DOI: 10.1002/we.1515.

13. Strickland JH, Webster BT, Nguyen T. A vortex model of the Darrieus turbine: an analytical and experimental study. *Journal of Fluid Engineering* 1979; **101**: 500–505.

14. Simão Ferreira CJ, van Zuijlen A, Bijl H, van Bussel G, vanKuik G. Simulating dynamic stall in a two-dimensional vertical-axis wind turbine: verification and validation with particle image velocimetry data. *Wind Energy* 2009; **13**: 1–17. DOI: 10.1002/we.330.

15. Gormont RE. A mathematical model of unsteady aerodynamics and radial flow for application to helicopter rotors. *USAMRDL Technical Report 72-67*, Boeing Co., Vertol Div., Philadelphia, PA, 1973.

16. Paraschivoiu I. *Wind Turbine Design: with Emphasis on Darrieus Concept*. Polytechnic International Press: Montreal, 2002.

17. Berg DE. An improved double-multiple streamtube model for the Darrieus type vertical-axis wind turbine. *Preceedings of the Sixth Biennial Wind Energy Conference and Workshop,Minneapolis,MN*, June 1983.

18. Snel H. Application of a modified Theodorsen model to the estimation of aerodynamic forces and aeroelastic stability. *European Wind Energy Conference*, London, 22–25 November 2004.

19. Tran C, Falchero D. Application of the ONERA dynamic-stall model to a helicopter blade in forward flight. *Vertica* 1982; **6**: 219–239.

20. Hansen MH, Gaunaa M, Madsen HA. A Beddoes–Leishman type dynamic stall model in state-space and indicial formulations. *Technical Report Risø-R-1354 (en)*, Risø National Laboratory, Roskilde, Denmark, 2004.

21. Larsen JW, Nielsen SRK, Krenk S. Dynamic stall model for wind turbine airfoils. *Journal of Fluids and Structures* 2007; **23**: 959–982.

22. Øye S. Dynamic stall simulated as time lag of separation. *Proceedings of the 4th IEA Symposium on the Aerodynamics of Wind Turbines*, IEA, Rome, ETSU-N-118, November 1991.

23. Sheng W, Galbraith RAM, Coton F. A modified dynamic stall model for low Mach numbers. *Journal of Solar Energy Engineering* 2008; **130**: 031013.1–031013.10. DOI: 10.1115/1.2931509.

24. Gupta S, Leishman J. Dynamic stall modelling of the S809 aerofoil and comparison with experiments. *Wind Energy* 2006; **9**: 521–547.

25. Leishman J, Beddoes T. A semi-empirical model for dynamic stall. *Journal of the American Helicopter Society* 1989; **34**: 3–17.

26. Mertens S, van Kuik G, van Bussel G. Performance of an H-Darrieus in the skewed flow on a roof. *Journal of Solar Energy Engineering* 2003; **125**: 433–440.

27. Ferreira CJS, van Bussel GJW, van Kuik GAM. Wind tunnel hotwire measurements, flow visualization and thrust measurement of a VAWT in skew. *Journal of Solar Energy Engineering* 2006; **128**: 487.

28. Worstell MH. Aerodynamic performance of the 17-metre-diameter Darrieus wind turbine. *Technical Report SAND-78-1737*, Department of Energy, Sandia Laboratories, Albuquerque, N.M., 1979.

29. Worstell MH. Measured aerodynamics and systems performance of the 17-m research machine. *Proceedings of the Vertical-Axis Wind Turbine Design Technology Seminar for Industry*, Albuquerque, N.M., April 1980.

30. Paulsen US, Vita L, Madsen HA, Hattel J, Ritchie E, Leban KM, Berthelsen PA, Carstensen S. 1st DeepWind 5 MW base-line design. *Energy Procedia* 2012; **24**: 27–35.

31. Burton T, Jenkins N, Sharpe D, Bossanyi E. *Wind Energy Handbook*. John Wiley & Sons Ltd: England, 2011.

32. Leishman JG. *Principles of Helicopter Aerodynamics* (2nd edn). Cambridge Aerospace Series. Cambridge University Press: Cambridge, 2006.

33. Johnson W. Comparison of three methods for calculation of helicopter rotor blade loading and stresses due to stall. *NASA TN D-7833*, National Aeronautics and Space Administration, 1974.

34. Beddoes T. A synthesis of unsteady aerodynamic effects including stall hysteresis. *Vertica* 1976; **1**: 113–123.

35. Beddoes T. Onset of leading edge separation effects under dynamic conditions and low Mach number. *34th Annual Forum of the American Helicopter Society*, Washington, D. C., May 15-17, 1978.

36. Gangwani ST. Synthesized airfoil data method for prediction of dynamic stall and unsteady airloads. *American Helicopter Society, Annual Forum, 39th, St. Louis, MO*, 1984.

37. Truong VK. Prediction of helicopter rotor airloads based on physical modelling of 3D unsteady aerodynamics. *22nd European Rotorcraft Forum*. Brighton, UK, 1996.

38. Carr LW. Progress in analysis and prediction of dynamic stall. *Journal of Aircraft* 1988; **25**: 6–17.

39. Rapin M, Ortun B. 3D rotational correction in ONERA aeroelastic predictions of NREL wind turbine. *45th AIAA Aerospace Sciences Meeting and Exhibit*, Reno, Nevada, 2007.

40. Brouwer HH. The adaptation of the ONERA model for dynamic stall, for application in the wind-turbine analysis programme PHATAS. In *Contract Report NLR CR 90104 L*. National Aerospace Laboratory NLR: The Netherlands, 1990.

41. Moriarty PJ, Hansen AC. Aerodyn theory manual. *NREL/TP-500-36881*, National Renewable Energy Laboratory, Golden, Colorado, 2005.

42. Allet A, Paraschivoiu I. Viscous flow and dynamic stall effects on vertical-axis wind turbines. *International Journal of Rotating Machinery* 1995; **2**: 1–14.

43. Akins RE. Measurements of surface pressures on an operating vertical-axis wind turbine. *Contractor Report SAND89-7051*, Sandia National Laboratories, November 1989.

44. Vita L. Offshore floating vertical axis wind turbines with rotating platform. *Risø-PhD-80(EN)*, National Laboratory for Sustainable Energy, DTU, August 2011.

45. Mert M. Optimization of semi-empirical parameters in the FFA-Beddoes dynamic stall model. *FFA TN 1999-37*, 1999.

46. Pereira R, Schepers G, Pavel MD. Validation of the Beddoes–Leishman dynamic stall model for horizontal axis wind turbines using MEXICO data. *Wind Energy* 2013; **16**: 207–219. DOI: 10.1002/we.541.

47. Wang K, Hansen MOL, Moan T. A method for modeling of floating vertical axis wind turbine. *Proceedings of the 32nd International Conference on Ocean, Offshore and Arctic Engineering*, Nantes, France, June 9–14, 2013.

A.3   Paper 3

Dynamic analysis of a floating vertical axis wind turbine under emergency shutdown using hydrodynamic brake

Kai Wang, Martin O.L. Hansen and Torgeir Moan

EERA DeepWind'2014, 11th Deep Sea Offshore Wind R&D Conference

Dynamic analysis of a floating vertical axis wind turbine under emergency shutdown using hydrodynamic brake

K. Wang[1,2], M.O.L. Hansen[2,3] and T. Moan[1,2]

[1] *NOWITECH, Norwegian University of Science and Technology, 7491 Trondheim, Norway*
[2] *Centre for Ships and Ocean Structures, Norwegian University of Science and Technology, 7491 Trondheim, Norway*
[3] *DTU Wind Energy, Department of Mechanical Engineering, Technical University of Denmark, Lyngby, Denmark*

Abstract

Emergency shutdown is always a challenge for an operating vertical axis wind turbine. A 5-MW vertical axis wind turbine with a Darrieus rotor mounted on a semi-submersible support structure was examined in this study. Coupled non-linear aero-hydro-servo-elastic simulations of the floating vertical axis wind turbine were carried out for emergency shutdown cases over a range of environmental conditions based on correlated wind and wave data. When generator failure happens, a brake should be applied to stop the acceleration of the rotor to prevent the rotor from overspeeding and subsequent disaster. In addition to the traditional mechanical brake, a novel hydrodynamic brake was presented to apply to the shutdown case. The effects of the hydrodynamic brake on the platform motions and structural loads under normal operating conditions and during the emergency shutdown events were evaluated. The use of both the hydrodynamic brake and mechanical brake was also investigated. The application of the hydrodynamic brake is expected to be efficient for rotor shutdown and for reducing the platform motions and structural loads.

Keywords: Emergency shutdown; Floating vertical axis wind turbine; Platform motion; Hydrodynamic brake

1. Introduction

As wind turbines continue to extend to deep waters, different platforms are used as the floating support structures, such as spar, semi-submersible and TLP. Most studies in this field have focused on the design, structural integrity, platform motion and installation of floating horizontal axis wind turbines (FHAWTs) to better understand the performance of different concepts and provide a basis for detailed structural design. However, different concepts for floating vertical axis wind turbines (FVAWTs) have also been presented, including the DeepWind [1-3], VertiWind [4] and Aerogenerator X concepts [5], to evaluate their economic potential and technical feasibility. A novel concept combining the DeepWind 5-MW rotor [6] and DeepCwind floater of the OC4 project [7] has also been proposed, and a coupled non-linear aero-hydro-servo-elastic model for analyzing this concept has been established and accordingly verified [8].

Many different challenges arise when FVAWTs operate under various wave and wind environmental conditions. Under normal operating conditions, the rotor can experience aerodynamic loads with continuous variation contributed by the azimuthal position and turbulent wind. Considerable forces acting on the rotor with fixed blades can be produced in stormy weather at increased rotational speed. The blades may also be deformed or broken, and the tower could collapse in more severe cases. Thus, determining how to initiate the emergency shutdown of a wind turbine is one of the most important concerns. The blade pitch mechanism is not applied in VAWTs with a Darrieus rotor, unlike in HAWTs, and the mechanical brake is installed in a standard manner. Experience has shown that aerobrakes also need to be installed to keep the rotational speed down in emergency situations when the generator torque is lost due to grid loss and the mechanical brake fails. The mechanical brake usually acts as a parking brake to stop the machine for maintenance purposes, therefore, aerodynamic braking is used to decelerate the rotor firstly and then the mechanical brake torque can be quite low. Although the mechanical brake is also used to bring the rotor to a standstill during high wind shutdowns for the majority of HAWTs, it is not easily applied for large scale VAWTs. Spoilers, an efficient and simple type of aerobrakes, are plates used to increase aerodynamic drag. However, the spoilers are integrated with blades, and their efficiency is determined by involving aerodynamic calculation of the blades together.

The current work presents a novel concept for a hydrodynamic brake that is installed at the end of the extended shaft of a vertical axis wind turbine through the centre column of the floater. The studied FVAWT has a 5-MW Darrieus rotor mounted on a semi-submersible support structure. The global motion and dynamic structural response of the FVAWT are calculated for the case in which the hydrodynamic brake is activated during emergency shutdown.

2. Methodology

2.1. Floating Wind Turbine Model

The FVAWT considered in this study is composed of a 5-MW Darrieus rotor, a semi-submersible and three catenary mooring lines. The rotor is located on a main column as shown in Fig. 1a. There are three offset columns with pontoons around the main column. Each catenary mooring is attached to an offset column to provide horizontal restoring stiffness. All of the columns are connected by braces to form an integrated body. Good stability and stiffness are ensured by a large waterplane area moment of inertia to limit the platform pitch angle under wave and wind conditions. Both of the mooring lines and the floating support structure were originally developed for the DeepCwind project and also used for supporting a 5-MW HAWT in Phase II of the Offshore Code Comparison Collaboration Continuation (OC4) project. DeepCwind is a U.S. - based project aimed at generating field-test data for use in validating floating offshore wind turbine modeling tools. The OC4 project is a continuation of the OC3 project, and Phase II of the OC4 project involved modeling a semisubmersible floating offshore wind system [7]. Among various numerical codes, the FAST semi-submersible floating wind turbine numerical model was also validated by comparing with DeepCwind test data [9]. The Darrieus rotor was originally developed for the DeepWind project (2010-2014), which is a part of the FP7 European project [10]. Compared to the FHAWT of the OC4 project, the FVAWT uses the 5-MW Darrieus rotor instead of the NREL 5-MW reference turbine. The slight difference between the two floating concepts indicates that the floater must be slightly modified to adapt for the VAWT rotor, which is heavier than the HAWT rotor. The specification of the present FVAWT are detailed in [8].
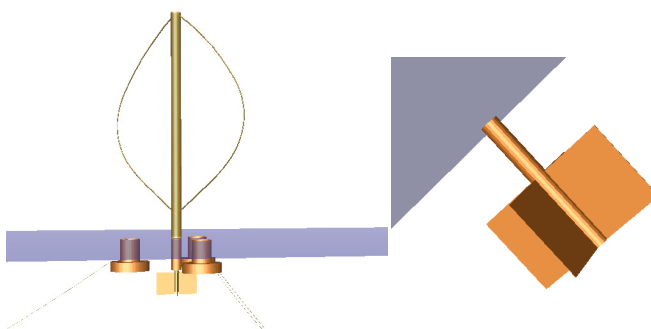
Fig. 1: (a) Floating vertical axis wind turbine; (b) Hydrodynamic brake

2.2. Coupled Time-Domain Analysis

The developed fully coupled simulation tool Simo-Riflex-DMS has the capability to carry out simulations of the dynamic motion of FVAWTs in the time domain. Thereby, the dynamic responses of a FVAWT can be calculated by integrating separate models of the wind inflow, aerodynamics, hydrodynamics, structural dynamics and controller dynamics. The tool couples three computer codes: Simo calculates the rigid body hydrodynamic forces and moments acting on the floater; Riflex modeles the blades, tower, shaft and mooring system as finite flexible elements, and provides the link to the DMS code and external controller; the DMS code calculates the forces on the blades based on an external aerodynamic module. The generator torque is written in Java. The Simo implementation computes the hydrodynamic loads at the actually displaced position of the floater, the DMS code calculates the aerodynamic loads on the blades and Riflex carries out full equilibrium iterations at each time step. This combination produces a comprehensive aero-hydro-servo-elastic simulation tool with sophisticated hydrodynamics, a stable non-linear finite element solver, well-known aerodynamics and a user-defined controller. The Simo-Riflex wind turbine module has been previously verified [11, 12], and the Simo-Riflex-DMS was presented and verified in [8].

In the aerodynamic load computation, the aerodynamic module is based on the Double Multiple Streamtube (DMS) model, which includes the effects of Reynolds number variations and incorporates the Beddoes-Leishman dynamic stall model. The turbulent wind field is generated by Turbsim. The code has been validated by comparison with existing experimental data [13]. The relative velocity sums up the incoming wind velocity at a certain point and the blade element velocity induced by platform motion and blade elastic deformation.

In the calculation of hydrodynamic loads carried out in this study, the floater was considered as a rigid body in Simo and the mooring line was represented as slender elements in Riflex. The hydrodynamic loads on the floater were handled by a linear potential flow model and the viscous term of the Morison formula, whereas the hydrodynamic loads on the mooring lines were represented using the Morison formula. The potential flow model produced added mass, radiation damping and first order wave forces in Wadam. The viscous forces were applied to represent the quadratic damping on the floater and mooring system. However, second order wave forces were not included in this model.

The structural dynamics of the rotor and mooring lines was calculated using the nonlinear finite element solver in Riflex. The rotor consisted of a tower and two blades, and their properties described in [10] were used to establish the structural model. Each blade, measuring 188.3 m in length, was modeled by 75 elements with two symmetry axes. The gyroscopic effects and the geometric stiffening effect were also considered.

A PI generator controller was employed in the control model. The objective of the control model was to enable variable speed operation maximizing power capture below the rated operation point and maintaining the generator speed above the rated operation point. The detailed controller strategy and relevant controller parameters are documented in [14], and their application in the integrated model used in this study has been verified in [8]. The notch filter used to reduce the effect of 2P variations was switched off in the present model.

2.3. Hydrodynamic Brake Model

Due to a lack of the blade pitch mechanism, the VAWT requires an additional device to stop the rotor under the emergency condition. In this study, a novel brake utilizing the drag force from water on the rotating plate was developed. The brake is composed of four plates and a centre column as shown in Fig. 2. The centre column of the brake provides enough buoyancy to balance the weight of the column itself and the four plates so that the brake does not affect the equilibrium condition of the floater. Under the normal operating conditions of the FVAWT, the centre column of the brake is connected to the floater. A device is assumed to enable the centre column to connect to the rotating shaft of the rotor during emergency shutdown. In this study, two hydrodynamic brakes were preliminarily designed. The dimensions of the centre column and the flat plate are detailed in Table 1.

In the hydrodynamic load calculation for the hydrodynamic brake, the hydrodynamic coefficients of the column and the plates are included in the model. Before the hydrodynamic brake is connected to the rotating shaft, it functions as a damping plate. The hydrodynamic loads on the break can be calculated by the Morison formula. The brake can be divided into an upper part and a lower part. The upper part of the brake is the upper part of the centre column, which is a cylinder. Thus, the Morison formula for a cylinder is directly applied to the upper part. The added mass and drag coefficient for the upper part can be determined from the DNV standard [15]. The lower part is composed of the centre column and four flat

plates. The dimensional added mass in the Morison model is computed as indicated in Eq. 1 for horizontal forces acting on the combined column and flat plates and as indicated in Eq. 2 for vertical forces acting on the components. The drag force on the combined column and flat plates was considered to be equivalent to that on a thin plate, as in the DNV standard, thus, a drag coefficient of 1.9 was used in the model. The friction drag of flat plate parallel to the flow was neglected. The plate was modeled as a slender line on which the equivalent drag acted. Thus, the plate provided a damping effect in the translational degrees of freedom of the floater. After the centre column of the hydrodynamic brake is connected to the rotating shaft, it rotates along with the shaft to decelerate the rotor to a lower speed. The added mass and drag force in the translational degrees of freedom remains the same as that in the previous stage, whereas the drag in a rotational degree of freedom is newly generated. This drag force was represented as an additional torque acting on the column. The torque on this rotating flat plate was first computed from a simplified CFD model by using the sliding mesh technique. The relation between the estimated torque and the rotational speed was integrated into the model. In this manner, the effect of the hydrodynamic brake can be taken into account in the simulation. However, the damping effect in the yaw degree of freedom was neglected in the first stage because it is relatively small compared with that in the second stage. Furthermore, the interaction between the translational degrees of freedom and rotational degrees of freedom for the hydrodynamic brake was also neglected, thus, the complex model could be simplified and the main features maintained.

$$m_A^{hor} = \rho(1-(r/b)^2+(r/b)^4)\pi b^2 l_2 \tag{1}$$

$$m_A^{ver} = \rho C_A^{ver} \pi r^2 l_2 \tag{2}$$

Table 1: Hydrodynamic brake model

	Hydrobrake I		Hydrobrake II	
	Column	Plate	Column	Plate
Radius/Width (m)	1.5	11	2	16
Length (m)	38.494	36	30.494	28
Thickness (m)	0.02	0.083[a]	0.02	0.083[b]
Weight (N)	551509.2	3506517.8	583500.1	4765248.1
Bouyancy (N)	2736013.9	1321983.8	3853160.8	1495577.7

[a] Sum of the hollow thickness and plate thickness of 0.014 m

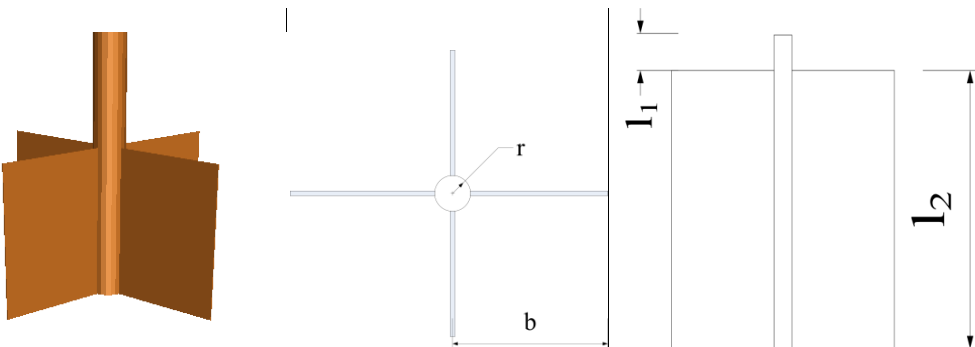[b] Sum of the hollow thickness and plate thickness of 0.017 m

Fig. 2: Hydrodynamic brake

2.4. Environmental and Shutdown Conditions

A set of environmental conditions were prescribed for the FVAWT in the simulations. Six conditions with correlated and directionally aligned wind and waves were applied as listed in Table 2. For the wind conditions, both the normal wind profile model (NWP) and the normal turbulence model (NTM) were used in all of the cases. For the NWP conditions, the wind profile U(z) is the average wind speed, as a function of height z above the free water level, given by the power law

$$U(z) = U_{ref}\left(z/z_{ref}\right)^{\alpha} \tag{3}$$

where U_{ref} is the reference wind speed, z_{ref} is the height of the reference wind speed and α is the power law exponent. For this study the value of z_{ref} was set to 79.78 m (vertical center of blades) above mean sea level and the value of α was set to 0.14 for the floating turbine according to IEC 61400-3 [16]. For the NTM conditions, three-dimensional turbulent wind fields were generated using NREL's TurbSim program [5] based on the Kaimal turbulence model for IEC Class C. For the wave conditions, the significant wave height (Hs) and peak period (Ts) were set based on the correlation with wind speed for the Statfjord site in the North Sea [17]. Then, wave time series were generated from JONSWAP spectra in the Simo program [18].

Table 2: Combined wind and wave conditions

	Uw (m/s)	Hs (m)	Tp (s)	Turb. Model	Fault Configuration	Sim. Length
LC 1	8	2.55	9.86	NTM	A, B, C, D	2800
LC 2	10	2.88	9.98	NTM	A, B, C, D	2800
LC 3	14	3.62	10.29	NTM	A, B, C, D	2800
LC 4	18	4.44	10.66	NTM	A, B, C, D	2800
LC 5	22	5.32	11.06	NTM	A, B, C, D	2800
LC 6	25	6.02	11.38	NTM	A, B, C, D	2800

A) The original FVAWT without hydrodynamic brake and no fault occurrence
B) The FVAWT with hydrodynamic brake I and no fault occurrence
C) The FVAWT with hydrodynamic brake I and fault occurrence, followed by free rotation
D) The FVAWT with hydrodynamic brake II and fault occurrence, followed by shutdown

Emergency shutdown is required to prevent the rotor from overspeeding after grid loss occurs. Accidental grid loss was assumed to occur at time TF = 1200 s, and the hydrodynamic brake was connected to the rotating shaft to initiate the shutdown process with a short time delay TD = 1 s. It should be noted that the TD was assumed based on the use of 0.1-s time delay between the moment of fault occurrence and the initiation of shutdown for a floating horizontal wind turbine [19]. To ensure the reaction process is conservative, a value 10 times the 0.1-s time delay was used in the simulation.

3. Torque estimation of the hydrodynamic brake

3.1. CFD Model of Hydrodynamic Brake

The concept of the hydrodynamic brake originated from the process of stir mixing of different liquids [20-23] and the high shear powder mixers used in the chemical industry [24, 25]. In addition to the flow features, turbulent kinetic energy and particle motion, the agitation torque is also calculated by numerical simulation and investigated by experiment. Although a wide variety of agitators are used for different mixing and agitation applications and although the researchers have postulated that an impeller with more baffles exhibit better performance in terms of power consumption, the simplest flat plates were proposed as a hydrodynamic brake in this work. Computational fluid dynamics (CFD) has already been used in many studies to predict the dynamics of the stir process. Therefore, the commercial CFD software FLUENT was used to simulate the hydrodynamic brake proposed in this study.

   Two commonly used models the capability of computing the flow field for the rotating flow problem are the multiple reference frame (MRF) and the sliding mesh approach. When applying these models, the computational domain is divided into an inner region containing the rotating plate and an outer region of stationary flow. For the MRF model, the steady state computation, producing a time average flow field, is conducted with a rotating reference frame in the inner region and a stationary reference in the outer region, whereas the sliding mesh approach, based on transient computation to produce a time accurate flow field, allows the inner region to slide relative to the outer region in discrete time steps and carries out time-dependent computations using implicit or explicit interpolation of data at successive time steps. Therefore, the sliding mesh approach, as the more accurate model for simulating the flow rotation problem, was used in the simulation.

   Because the length of the brake is long, a 2D model was established so as to reduce the computational cost and simplify the CFD model. The difference between the hydrodynamic brake model and the agitation model in the stirred tank is the definition of the boundary conditions according to the physical background. The infinite region in this model replaces a defined tank, so a sufficiently large outer region was built to eliminate the wall effect. The resolution of the computational grid is a key factor in any CFD simulation because it is related to the simulation accuracy and computational cost. Based on a preliminary convergence study, a grid mesh with 135900 cells for the inner region and 24640 cells for the outer region was established, as shown in Fig. 3a. For the discretization scheme, the first-order upwind was used because the choice of the discretization scheme has no effect on the mean velocities, as concluded by Aubin [23]. Furthermore, the absolute velocity formulation and Renormalized Group (RNG) *k-ε* turbulence model with a standard wall function for near-wall treatment were used in the simulation because the effect of swirl on turbulence is included in the RNG model, enhancing the accuracy for swirling flows. The size of the time step plays a significant role on the simulation accuracy in this model, and thus, the results could vary largely. Therefore, the time step was set to 0.1 s, providing an acceptable level of accuracy and an acceptable computational cost.

3.2. Estimation of Torque

   The hydrodynamic character of the hydrodynamic brake was investigated and detailed information regarding the flow field, such as the pressure and velocity of the rotational flow, could be obtained. Fig. 3b shows an example of the velocity distribution around the brake. One of the most important hydrodynamic parameters is the relationship between the torque on the brake from water and the rotational speed of the brake, by understanding this relationship, the relevant coefficients can be implemented in the coupled model. After a series of simulations were performed with different rotational speeds, the agitation torques corresponding to each rotational speed could be determined. By multiplying the length of the plate, the relationship between the total torque and the rotational speed of hydrodynamic brake I was plotted, as shown in Fig. 4. A three order polynomial with unit of kNm was used to fit the relationship:

$$T_q = -20229\omega^3 + 125338\omega^2 - 30925\omega + 2680.2 \qquad (4)$$
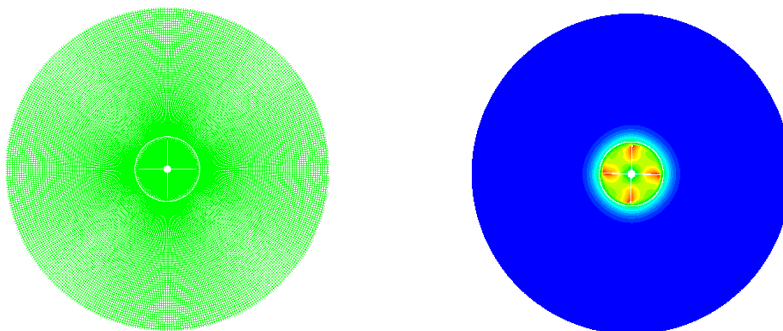
Fig. 3: (a) 2D mesh of hydrodynamic brake; (b) An example of velocity distribution at a rotational speed of 0.5 rad/s
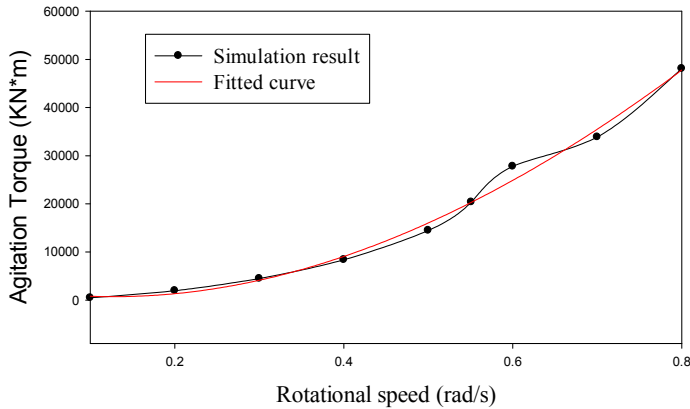
Fig 4: Relationship between rotational speed and torque

A similar method was used to determine the relationship between the torque and rotational speed for hydrodynamic brake II:

$$T_q = 123523\omega^3 + 21286\omega^2 + 9917.4\omega + 19.624 \tag{5}$$

4. Results

4.1. Effect of Hydrodynamic Brake I

The addition of the hydrodynamic brake to the original FVAWT concept may change the properties of the platform and subsequently the dynamic responses of the global motion and structural responses of the wind turbine. To evaluate the effect of the hydrodynamic brake, numerical simulations of the FVAWT with brake I and the original FVAWT without any brake installed were carried out to obtain the responses of the global motion of the platform, bending moment of the tower base and the mooring line tension. Then, the responses of these two structures were investigated.

The results of the comparison are summarized as follows:

1) In the load case with lower wind speed, the hydrodynamic brake has a less effect on the surge motion, as shown in Fig. 5. When the wind speed increases, the platform with the brake has much less response at the surge resonance frequency than the platform without the brake. The response near the wave frequency slightly decreases. The drag force from water on the brake actually introduces rather strong damping effect on the platform, and the damping increases with the relative velocity between the platform and wave velocity. A similar effect on the sway motion can be observed, but the difference is that the brake introduces a slightly stronger wave frequency response in sway motion. The brake hardly affects the heave motion of the platform because the drag force on the column associated with the heave motion is relatively small and the natural frequency of the heave motion lies outside the range of wave and wind frequencies.

2) Fig. 6 compares the power spectra of the roll motion between the platform with the brake and the original platform under load cases 1 and 3. The brake can decrease the natural period of the roll motion of the platform and induce a larger peak at the roll resonance frequency when compared with the roll motion of the FVAWT without brake. On the other hand, the drag force on the brake can reduce the roll motion induced by the 2P frequency of approximately 1.1 rad/s. The 2P frequency originates from the characteristics of vertical axis wind turbines with two blades. Because the axis of rotation is not parallel to the wind direction and the angle of attack of the blades varies with the azimuthal position during operation, the aerodynamic loads vary within one revolution. For a two-blade wind turbine, the variation of the torque occurs twice per revolution and the 2P

variations lead to the 2P frequency. Not only are the generator torque and gird affected significantly but the structures are also subject to severer fatigue problems. However, the roll motion itself is relatively small under aligned wind and wave conditions, and the effect is not as significant. A similar effect can be observed for the pitch motion, as shown in Fig. 7. As the wind increases, the effect becomes increasingly apparent.

3) The brake can significantly reduce the mooring tension response to the wind excitation as shown in Fig. 8, whereas it induces larger peaks at higher frequencies. In addition to the peak at the 2P frequency, another peak at a higher frequency is observed, which should be induced by the eigenfrequency of the blade. With the increase in wind speed, the peak induced by the structural eigenfrequency becomes increasingly apparent.

4) The effect of the brake on the bending moment of the tower base in the fore-aft (FA) and side-side (SS) directions was also investigated, and the main difference is the larger peak at the 2P frequency for the FVAWT with the brake. The reason for this finding could be that the brake makes the platform much stiffer, and thus, the bending moment induced by the 2P frequency increases.
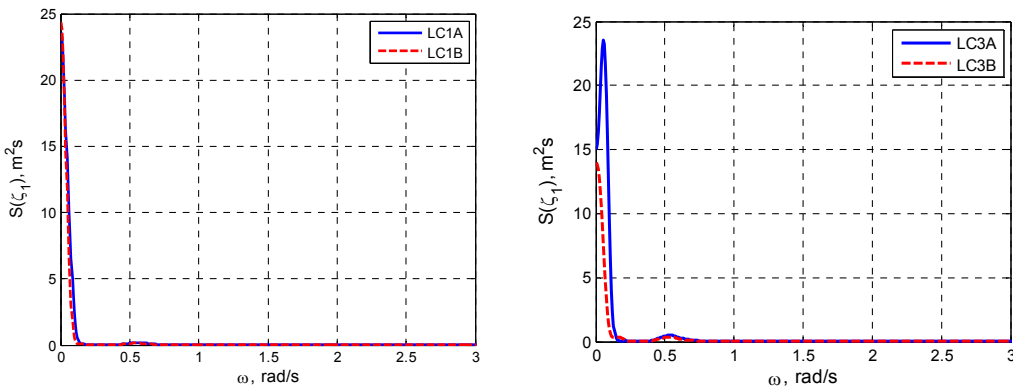

Fig. 5: Power spectra for surge motion of the platform for load cases 1 and 3 with fault configurations A and B

Fig. 6: Power spectra for roll motion of the platform for load cases 1 and 3 with fault configurations A and B

Fig. 7: Power spectra for pitch motion of the platform for load cases 1 and 3 with fault configurations A and B
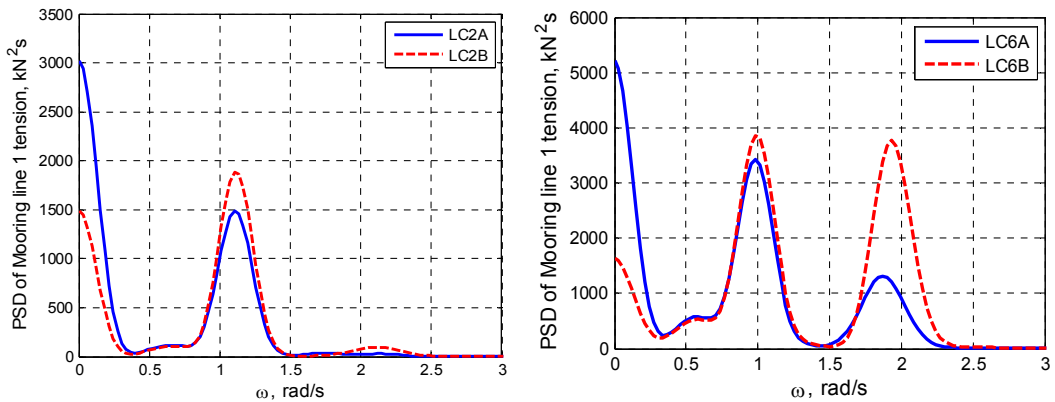
Fig. 8: Power spectra for mooring line tension for load cases 2 and 6 with fault configurations A and B

4.2. Analysis of Emergency Shutdown by Using Hydrodynamic Brake I

A fault, such as grid loss, was assumed to occur at 1200 s, at which point the wind turbine entered a state of free rotation without any generator torque or other torque to balance the aerodynamic torque before the brake connected to the rotating shaft of the wind turbine. Due to the large inertia of the wind turbine and variation of the aerodynamic torque, the increase in the rotational speed of shaft was not distinct. Once the hydrodynamic brake takes effect to counter the aerodynamic torque, the rotational speed varies depending on the difference between the aerodynamic torque and hydrodynamic torque on the brake. Fig. 9 shows a time series of the rotational speed of the rotor for different wind speeds. Brake I does not create enough torque to stop the rotation, but it can prevent the overspeeding of the rotor. Furthermore, the rotational speed decreases to a lower value for most wind speeds. If a mechanical brake is also applied at the same time, the shutdown of the wind turbine can be expected. However, the effect of the mechanical brake was not considered in this section. A further investigation was carried out for the global motion of the platform, mooring line tension and tower base bending moment when the brake was also rotating with the rotor.
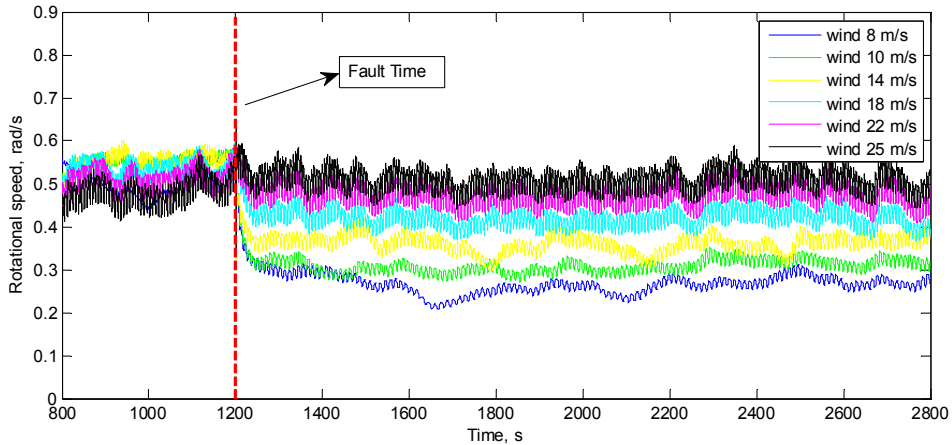
Fig. 9: Rotational speed for different wind speed after fault occurs at TF=1200 s by using brake I

Due to the decrease in the rotational speed after the activation of the hydrodynamic brake, the global motion of the platform shows better performance. Fig. 10 compares the global motion between fault configuration B and fault configuration C for different wind speeds. It can be observed that the surge and pitch motions are greatly enhanced, whereas the sway and roll motions experience both positive and negative effects under different load cases. However, the sway and roll motions are relatively small compared with the surge, pitch and yaw motions. Thus, the effect of the hydrodynamic brake on the sway and roll motions can be neglected. When the pitch motion was investigated using the power spectra shown in Fig. 11, it could also be observed that the decrease in the pitch motion mainly depended on the wind speed. The lower the wind speed was, the more the pitch motion was reduced. The peak at the 2P frequency still appeared, but the 2P frequency was reduced to a lower value corresponding to a lower rotational speed. A similar result was also observed for the roll motion, which decreased at the natural roll frequency and with a shift of 2P frequency. Furthermore, the peak of the roll response at higher structural frequency observed in the high wind case could be eliminated.

The mean tension of the three mooring lines was not significantly affected during the shutdown process by the hydrodynamic brake. The mean tension of mooring line 2 connected to the left column of the platform decreased slightly due to the decrease in the mean surge, whereas the mean tension of mooring line 3 connected to the right column of the platform increased slightly toward the mean tension of the mooring line 1 because of the decreased yaw motion. The standard deviations of the mooring lines were significantly reduced in most cases because the responses to the excitations due to the 2P frequency and the higher structural eigenfrequency were strongly weakened. The exceptions are the cases examined under high wind speeds. The 2P effect was reduced as the peak corresponding to the blade mode at its eigenfrequency was magnified at a wind speed of 22 m/s; On the other hand, the 2P effect was magnified as the peak at the structural eigenfrequency was reduced at a wind speed of 25 m/s. Therefore, the mooring line tension is sensitive to the rotational speed, which should be well configured to avoid exciting a 2P effect on the mooring line and inducing the structural eigenmodes.

Regarding the structural response, the bending moment of the tower base, which is one of the most important concerns under fault conditions, was also investigated. Both the mean values and standard deviations of the FA and SS tower base bending moments were significantly reduced, with the exception of the mean value of the FA tower base bending moment, at a high wind speed of 25 m/s. Because the rotational speed in load case 6C was not reduced, the thrust force due to the wind could still produce a large FA tower base bending moment. The activation of the brake together with the rotating shaft of the wind turbine could eliminate the 2P effect, thus allowing the wave frequency excitation to dominate the response of the FA tower base bending moment, as shown in the comparison between load cases 3B and 3C in Fig.12.

Fig.10: Mean values of the platform motions under the fault-free case and fault case C for all wind speeds
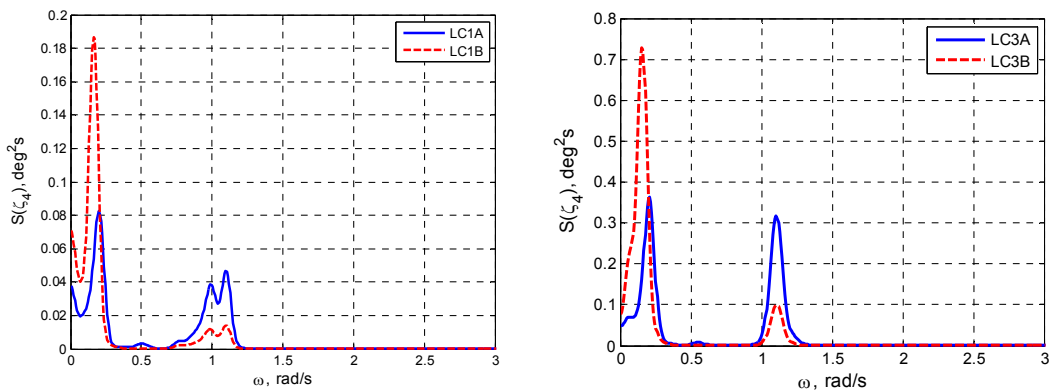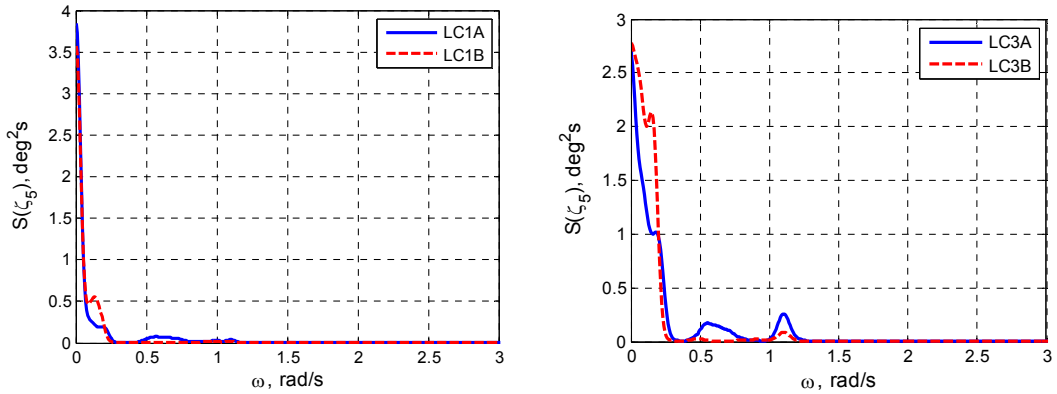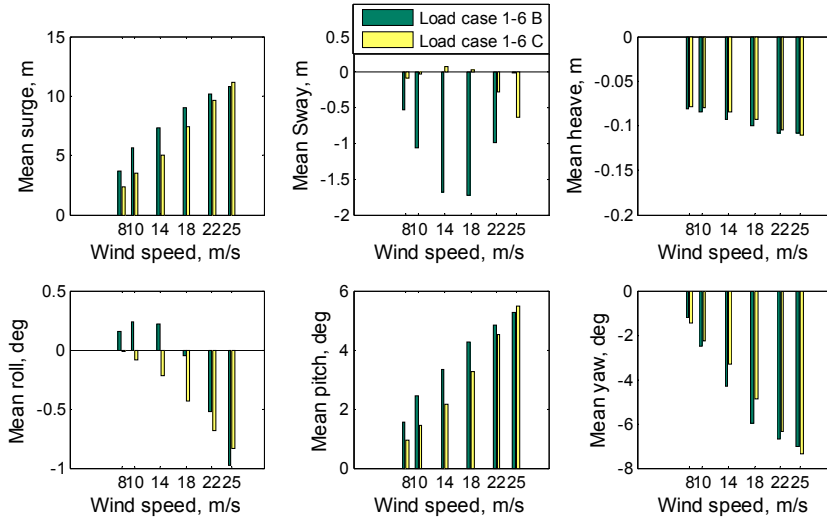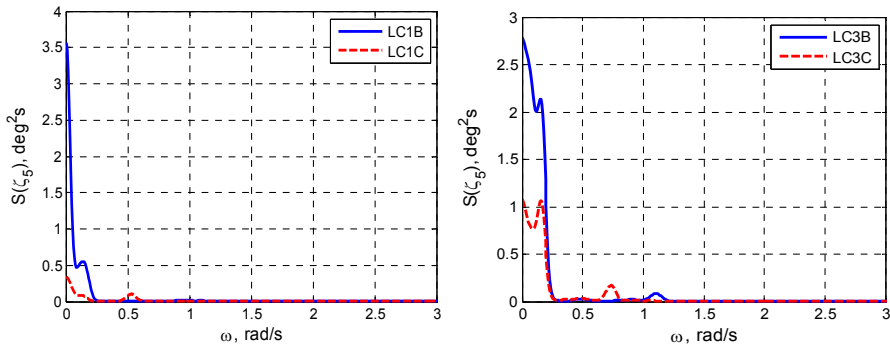

Fig. 11: Power spectra for pitch motion of the platform for load cases 1 and 3 with fault configurations B and C
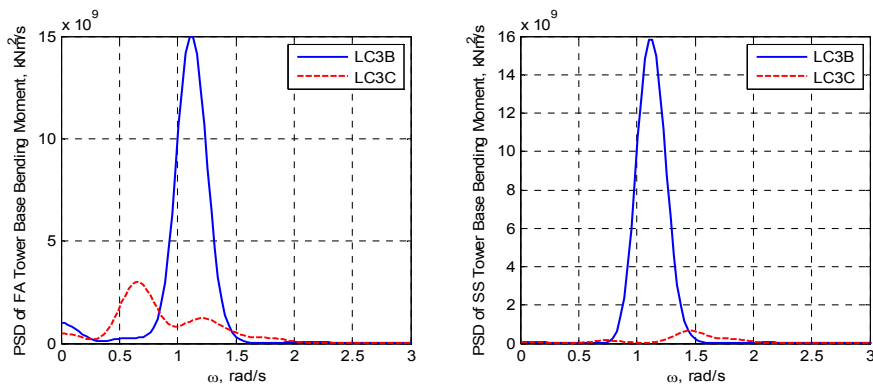

Fig. 12: Power spectra for FA and SS tower base moment for load case 3 with fault configurations B and C

4.3. Investigation of the Shutdown Process by Using Hydrodynamic Brake II and Mechanical Brake

Hydrodynamic brake II features a larger plate width than hydrodynamic brake I and can exert greater torque on the rotating shaft. After hydrodynamic brake II was applied in the FVAWT, the rotational speed in all load cases at different wind speeds could be rapidly reduced to a very low value. Then, the mechanical brake could be applied on the brake disk to stop the rotation of the wind turbine 200 s after the fault occurred. The value of the mechanical brake torque was assumed to be twice the value used in the NREL reference wind turbine and was set to 5454.5 kNm for a low speed shaft. Until the wind turbine was completely shut down, the process remained transient, and the platform gradually moves toward its final equilibrium position with some delay after the rotational speed, as shown in Fig. 13. The figure shows that the combination of the hydrodynamic brake and mechanical brake can effectively complete an emergency shutdown. It should be noted that the global motion, bending moment and tension of the mooring lines after the shutdown of the wind turbine can also vary under several factors, such as wind speed, wave condition and control strategy, because the aerodynamic loads depend on the azimuthal angle of the blades in the equilibrium position.
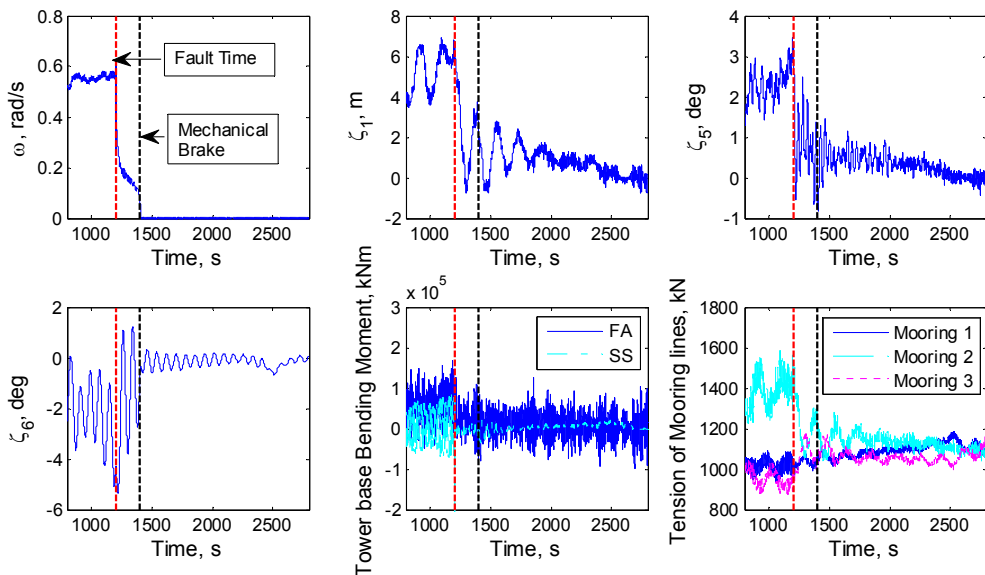
Fig. 13: Time history of the rotational speed, surge, pitch, yaw, tower base bending moments and mooring line tension for load case 2D

5. Conclusions

In the present work, a coupled non-linear time domain code was used to carry out numerical simulations for a floating vertical axis wind turbine with a hydrodynamic brake. To integrate the hydrodynamic brake into the original FVAWT, the hydrodynamic brake was modeled by a slender line, whose the hydrodynamic coefficient includes the added mass and drag coefficient. Furthermore, the torque of the hydrodynamic brake from the water was also calculated by a CFD model for different rotational speeds. Based on the integrated model, a series of load cases were selected to investigate the effect of the hydrodynamic brake and shutdown process for the wind turbine under normal operating conditions. The dynamic analysis focused on the comparison of global motions, tower base bending moments and the tensions of mooring lines for different load cases with different fault configurations.

The effect of the hydrodynamic brake on the FVAWT was evaluated by comparing the results obtained for the FVAWT with hydrodynamic brake I with the results obtained for the original FVAWT under normal operating conditions.

The addition of the hydrodynamic brake does not affect the surge motion as long as the wind speed is not too high. Otherwise, the surge motion induced by the wind can be greatly reduced by the drag force on the hydrodynamic brake. It was observed that the sway motion could be affected by the drag force on the brake when the yaw degree of freedom was presented. The effect on the roll and pitch motions also depends on the wind speed and is slightly complex because both the natural frequency and 2P frequency both affect the responses. From a structural point of view, the brake has a greater positive effect on the mooring lines, but it could enlarge the 2P effect on the tower base bending moment. This finding indicates that a better hydrodynamic brake design is critical to reducing the 2P effect on the tower base bending moment by avoiding the stiffening of the platform.

By investigating the shutdown process following the activation of the hydrodynamic brake to decelerate the wind turbine, a series of promising results revealed the merits of the hydrodynamic brake for the emergency shutdown. As long as the rotational speed can be reduced to relatively lower values, the global motion and structural responses can both be reduced. Although the same wave and wind conditions were applied to compare the results of different fault configurations and one realization of each load case could lead to certain uncertainties in the mean values and standard deviations of the global motions and structural responses, the results obtained from the comparison of the different fault configurations for each load case are still sufficient for evaluating the effect of the hydrodynamic brake on the FAVWT during the shutdown process.

By combing a mechanical brake with a larger hydrodynamic brake, the shutdown process could be successfully completed. The application of a hydrodynamic brake is expected to be efficient for rotor shutdown and for reducing the platform motion and structural loads.

Acknowledgments

References

[1] Paulsen, U.S., et al. Deepwind - An innovative wind turbine concept for offshore. in *European Wind Energy Association (EWEA) Annual Event*. 2011. Brussels.
[2] Vita, L., Paulsen, U.S., and Pedersen, T.F. A novel floating offshore wind turbine concept: new developments. in *European Wind Energy Conference and Exhibition*. 2010. Poland: EWEA.
[3] Vita, L., et al. A novel floating wind turbine concept. in *European Wind Energy Conference and Exhibition*. 16-19 March, 2009. Marseille, France: EWEC.
[4] Cahay, M., et al. Use of a Vertical Wind Turbine in an Offshore Floating Wind Farm. in *Offshore Technology Conference* 2-5 May 2011. Houston, Texas, USA: Offshore Technology Conference.
[5] 10MW Aerogenerator X © Wind Power Limited & Grimshaw at http://vimeo.com/13654447.
[6] Paulsen, U.S., et al., 1st DeepWind 5 MW Baseline design. *Energy Procedia*, 2012. **24**: p. 27-35.
[7] Robertson, A., et al., Definition of the Semisubmersible Floating System for Phase II of OC4, 2012.
[8] Wang, K., Moan, T., and Hansen, M.O.L. A method for modeling of floating vertical axis wind turbine. in *Proceedings of the 32th International Conference on Ocean, Offshore and Arctic Engineering*. 2013. Nantes, France: paper no: OMAE2013-10289.
[9] Coulling, A.J., et al., Validation of a FAST semi-submersible floating wind turbine numerical model with DeepCwind test data. *Journal of Renewable and Sustainable Energy*, 2013. **5**: p. 023116.
[10] Vita, L., Offshore Floating Vertical Axis Wind Turbines with Rotating Platform, in *Risø-PhD-80(EN)*2011, National Laboratory for Sustainable Energy, DTU.
[11] Ormberg, H., Passano, E., and Luxcey, N. Global analysis of a floating wind turbine using an aero-hydroelastic model. Part 1: Code development and case study. in *Offshore Mechanics and Arctic Engineering Conference*. 2011. Rotterdam, The Netherlands.
[12] Luxcey, N., Ormberg, H., and Passano, E., Global analysis of a floating wind turbine using an aero-hydro-elastic numerical model. Part 2: Benchmark study, in *Offshore Mechanics and Arctic Engineering Conference*2011: Rotterdam, The Netherlands.
[13] Wang, K., Hansen, M.O.L., and Moan, T., Model improvements for evaluating the effect of tower tilting on the aerodynamics of a vertical axis wind turbine. *Wind Energy*, 2013.
[14] Svendsen, H.G., Merz, K.O., and Endegnanew, A.G. Control of floating vertical axis wind turbine. in *European Wind Energy Conference and Exhibition* 2012. Copenhagen, Denmark: EWEA.
[15] Det Norske Veritas, ENVIRONMENTAL CONDITIONS AND ENVIRONMENTAL LOADS, Tech. Rep., DNV-RP-C205 (2007).
[16] International Electrotechnical Commission (2009). *IEC61400-3 Wind turbines - Part 3: Design requirement for offshore wind turbines.*

[17] Johannessen, K., Meling, T.S., and Haver, S., Joint distribution for wind and waves in the northern north sea. *International Journal of Offshore and Polar Engineering*, 2002. **12**(1).

[18] MARINTEK, SIMO User's Manual, 2011.

[19] Jiang, Z., Karimirad, M., and Moan, T., Dynamic response analysis of wind turbines under blade pitch system fault, grid loss, and shutdown events. *Wind Energy*, 2013.

[20] Vakili, M. and Esfahany, M.N., CFD analysis of turbulence in a baffled stirred tank, a three-compartment model. *Chemical Engineering Science*, 2009. **64**(2): p. 351-362.

[21] Deglon, D. and Meyer, C., CFD modelling of stirred tanks: Numerical considerations. *Minerals Engineering*, 2006. **19**(10): p. 1059-1068.

[22] Ankamma Rao, D. and Sivashanmugam, P., Experimental and CFD simulation studies on power consumption in mixing using energy saving turbine agitator. *Journal of Industrial and Engineering Chemistry*, 2010. **16**(1): p. 157-161.

[23] Aubin, J., Fletcher, D.F., and Xuereb, C., Modeling turbulent flow in stirred tanks with CFD: the influence of the modeling approach, turbulence model and numerical scheme. *Experimental Thermal and Fluid Science*, 2004. **28**(5): p. 431-445.

[24] Sato, Y., Nakamura, H., and Watano, S., Numerical analysis of agitation torque and particle motion in a high shear mixer. *Powder Technology*, 2008. **186**(2): p. 130-136.

[25] Knight, P., et al., Prediction of impeller torque in high shear powder mixers. *Chemical Engineering Science*, 2001. **56**(15): p. 4457-4471.

A.4   Paper 4

Comparative study of a FVAWT and a FHAWT with a
semi-submersible floater

Kai Wang, Luan Chenyu, Torgeir Moan and Martin O.L. Hansen

Proceedings of the Twenty-fouth (2014) International Offshore and Polar Engineering Conference, Busan, Korea. June 15-20, 2014.

Comparative Study of a FVAWT and a FHAWT with a Semi-submersible Floater

Kai Wang
NOWITECH/CeSOS, NTNU
Trondheim, Norway

Chenyu Luan
NOWITECH/CeSOS, NTNU
Trondheim, Norway

Torgeir Moan
NOWITECH/CeSOS, NTNU
Trondheim, Norway

Martin Otto Laver Hansen
DTU Wind Energy/CeSOS
Lyngby, Denmark

ABSTRACT

As the application of wind energy moves forward to deep water, different concepts have been put forward. This paper presents a floating vertical axis wind turbine (FVAWT) with a 5 MW Darrieus rotor and a floating horizontal axis wind turbine (FHAWT) with the 5 MW NREL reference wind turbine, both mounted on a semi-submersible. Fully coupled nonlinear time domain simulation tools allow these two different wind turbines to be compared. In the present paper, the FVAWT is modeled by the Simo-Riflex-DMS code while the FHAWT is modeled by Simo-Riflex-Aerodyn, which is a state-of-the-art time domain code for FHAWTs.

The present paper focuses on the comparison between the FVAWT and the FHAWT based on numerical simulations. A series of load cases with combined wave and wind conditions are selected to calculate dynamic responses of the FVAWT and the FHAWT, such as the global motions of the floater in six DOFs, the bending moment of the bottom of the tower and the tension at the fairleads of the mooring lines. Statistical analysis and power spectra are used to analyze the time domain results for this comparison study.

The results give more insight into the difference between the FVAWT and the FHAWT. The disadvantages of the FVAWT have been identified by comparing it with the FHAWT. The comparison provides valuable information for the further study of floating concepts with a vertical axis wind turbine.

KEY WORDS: Floating vertical axis wind turbine; floating horizontal axis wind turbine; dynamic analysis; comparison study; time domain simulation.

INTRODUCTION

Wind turbines are mainly classified into horizontal axis wind turbines (HAWTs) and vertical axis wind turbines (VAWTs) based on different orientation of their axis of rotation. HAWTs are commercially successful, and the applications of HAWTs in deep water by using different floating support structures have led to ever-increasing and versatile researches, such as Spar type (Karimirad and Moan, 2011; Jiang, Karimirad and Moan, 2013), TLP type (Bachynski and Moan, 2012) and Semi-submersible type (Kvittem, Bachynski and Moan, 2012; Luan, Gao and Moan, 2013). However, VAWTs seem to be well fitted for offshore floating applications because these turbines have several advantages when compared with HAWTs, such as lower center of gravity, absence of a yaw control system as well as economical installation and maintenance. Therefore, more and more efforts have been invested in developing floating vertical axis wind turbines (FVAWTs) for application in deepwater areas. Among others, such as DeepWind concept (Vita, 2011) and VertiWind concept (Cahay, Luquiau, Smadja and SILVERT, 2011), a recently established concept is a 5 MW Darrieus rotor mounted on a semi-submersible and a modeling method for this floating concept was developed (Wang, Moan and Hansen, 2013). The further development of FVAWTs has encountered some challenges such as high fatigue loads on the blades, shaft and gearbox produced by aerodynamic torque ripple. Emergency shutdown procedures for the wind turbine are also one of the most critical challenges. In addition to the aerobrakes in the VAWT, a novel hydrodynamic brake used in the FVAWT was studied in an emergency situation (Wang, Hansen and Moan, 2014).

When the development of the FVAWT is mentioned above, it is also really necessary to recall a paper titled "HAWTs and VAWTs – Myths and Facts" by a known expert in the R&D of wind turbines, Carl Brothers (Paraschivoiu, 2002). It stated that the HAWTs were commercially successful due to enormous investment rather than due to their inherent technical superiority, while the VAWTs had little commercial success because the technical potential has not yet discovered rather than they had little commercial potential. It is also a myth that the VAWTs have too many inherent deficiencies to be technically viable, but the fact is that the HAWTs have at least as many deficiencies and have merely benefited from the resources needed to overcome them. It concluded that a small investment for the VAWTs may offer enormous paybacks. Both kind of wind turbines, the HAWTs and the VAWTs, seems to have their place in the developing wind energy industry, producing electricity to compete with traditional power such as thermal power and hydropower. Therefore, comparison

between these two types of turbines is of great interest all the time, especially for different researchers and industries focusing on FHAWT and FVAWT respectively.

Paraschivoiu (2002) compared the HAWTs and the VAWTs, by discussing the advantages and disadvantages of the HAWTs and the VAWTs, looking at the rotor performance (output power and torque) as a function of some design parameters and the predicted foundation loads. In addition to some proposed new techniques to take advantage of the incremental improvement for the VAWTs, the potential application of the VAWTs in harsh northern climates was also presented in his book. An evaluation of three different turbine concepts for wind power has been carried out, including the HAWTs and two different concepts of the VAWTs (Eriksson, Bernhoff and Leijon, 2008), specifically, the Darrieus turbine and the H-rotor. The comparative study was mainly based on some important aspects such as structural dynamics, control systems, maintenance, manufacturing and electrical equipment. Furthermore, a case study and a blade area study were also presented, and the VAWTs appeared to be advantageous compared to the HAWTs in several aspects.

However, the aforementioned discussions and comparisons are limited to the descriptive overview for onshore wind turbines and lack details in the dynamic analysis. Furthermore, the comparison between floating concepts for horizontal type and vertical type turbines has not been presented. In the present paper, a comparative study of a FVAWT with a 5 MW Darrieus rotor mounted on a semi-submersible and a FHAWT with the 5 MW NREL reference wind turbine mounted on the same semi-submersible except for the inside ballast water has been rearranged. Nonlinear fully coupled models for these two concepts are established to carry out simulations for global motions, structural dynamic response and tensions of the mooring lines. The comparison between the calculated results allows a detailed evaluation of these two wind turbines.
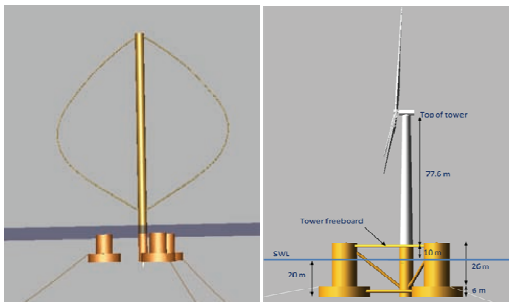

Fig. 1: FVAWT and FHAWT

FLOATING WIND TURBINE MODEL

FVAWT versus FHAWT

The FVAWT in this study includes a 5 MW Darrieus rotor, a semi-submersible and three catenary mooring lines, as shown in Fig. 1. The Darrieus rotor is composed of two blades and one rotating shaft which spans from the top to the bottom which is connected to the generator. The geometry and specification of the rotor are from the DeepWind project (2010-2014) which is a part of the FP7 European project (Vita, 2011). The semi-submersible floater is composed of three offset columns, three pontoons, a central column and braces. The offset columns and pontoons are around the central column. The rotor is located on the central column. All of the columns and pontoons are connected by braces to form an integrated body. Three catenary mooring lines are attached on the three offset columns to provide horizontal restoring stiffness. Sufficient restoring stiffness is ensured by the large second moment of water line area to limit the mean pitch angle of the platform under various wave and wind conditions. The semi-submersible floater and the mooring line were originally developed for the DeepCwind project and are used for supporting a 5 MW HAWT in Phase II of the Offshore Code Comparison Collaboration Continuation (OC4) project. DeepCwind is a U.S. - based project aimed at generating field-test data for use in validating floating offshore wind turbine modeling tools. The OC4 project is a continuation of the OC3 project and Phase II of the OC4 project involved modeling a semisubmersible floating offshore wind system (Robertson, Jonkman, Masciola, Song, Goupee, Coulling et al., 2012). The FHAWT in the OC4 project is compared with the FVAWT in the present paper. The FHAWT is composed of a 5 MW NREL reference wind turbine, a semi-submersible floater and three catenary mooring lines. The specifications of the Darrieus rotor and the rotor of the 5 MW NREL reference wind turbine are tabulated in Table 1. The rotor mass of the FVAWT only refers to the two blades, whereas the rotor mass of the FHAWT includes the mass of the three blades and the hub mass. The semi-submersible floater and the mooring lines of the FVAWT are the same design as the FHAWT except for the ballast water inside the semi-submersibles. To ensure the same draft of the two wind turbines, the ballast water of the FVAWT is slightly less than the ballast water of the FHAWT. An overview of the platform configurations of these two floating concepts is summarized in Table 2. A description of the design of the semi-submersible floater and the mooring lines of the FHAWT is available at (Robertson, Jonkman, Masciola, Song, Goupee, Coulling et al., 2012). The hydrostatic restoring stiffness ($C44$ and $C55$) in Table 2 includes the hydrostatic contribution solely from the water-plane area and the COB of the platform to remain consistent with the information provided by Robertson (2012). However, the hydrostatic contribution from the COG of the platform and the wind turbine has been included in the numerical models of the FVAWT and the FHAWT.

Table 1. Specification of these two wind turbines

Turbines	FVAWT	FHAWT
Rated power	5 MW	5 MW
Rotor radius	63.74 m	63 m
Rotor height / Hub height	129.56 m	90 m
Chord	7.45 m	1.419-4.652 m
Cut-in, Rated, Cut-out Wind Speed	5 m/s, 14 m/s, 25 m/s	3 m/s, 11.4 m/s, 25 m/s
Rated rotational speed	5.26 rpm	12.1 rpm
Nacelle Mass	0 kg	240,000 kg
Rotor mass	305,044 kg	110,000 kg
Shaft mass /Tower mass	449,182 kg	249,718 kg
Coordinate Location of Overall CM	(0 m, 0 m, 75.6 m)	(-0.2 m, 0 m, 70.6 m)

Table 2. Geometry, Structural and hydrodynamic properties of platform configurations

Floater	FVAWT	FHAWT
Depth of platform base below SWL (total draft)	20 m	20 m
Spacing between offset columns	50 m	50 m
Platform mass, including ballast	13353.7 t	13473 t
CM location of total concept below SWL	8.66 m	9.88 m
Buoyancy in undisplaced position	14267.41t	14267.41t
CB location below SWL	13.15 m	13.15 m
Hydrostatic restoring stiffness in heave C33	3.836E+06 N/m	3.836E+06 N/m
Hydrostatic restoring stiffness in roll C44	-3.77E+08 N·m/rad	-3.77E+08 N·m/rad
Hydrostatic restoring stiffness in pitch C55	-3.77E+08 N·m/rad	-3.77E+08 N·m/rad
Moment of inertia in roll	9159733 t·m^2	9220000 t·m^2
Moment of inertia in pitch	9159733 t·m^2	9220000 t·m^2
Moment of inertia in yaw	12087187 t·m^2	12200000 t·m^2

Nonlinear Fully Coupled Model

Calculating the dynamic response of a floating wind turbine requires the application of comprehensive aero-hydro-servo-elastic simulation tools that incorporate integrated models of the wind inflow, aerodynamics, hydrodynamics, structural dynamics and controller dynamics in the time domain through a nonlinear fully coupled simulation. Simo-Riflex-Aerodyn (Ormberg and Bachynski, 2012) is a non-linear simulation tool for modeling the FHAWTs. It is a state-of-the-art code and has been verified by comparison with the NREL-developed FAST servo-elastic tool and other comprehensive codes (Luxcey, Ormberg and Passano, 2011; Ormberg, Passano and Luxcey, 2011). Simo-Riflex-Aerodyn couples three computer codes to model the FHAWT in the time domain: Simo calculates the rigid body hydrodynamic forces and moments on the floater; Riflex models the blades, tower, shaft and mooring system as finite flexible elements, as well as provides the link to AeroDyn and external controller; AeroDyn calculates the forces and moments on the blades based on the Blade Element/Momentum (BEM) theory and Generalized Dynamic Wake (GDW) theory, including dynamic stall, tower shadow and skewed inflow correction. The generator torque and blade pitch control system was written in Java.

The FVAWT is modeled by the recently developed code, Simo-Riflex-DMS (Wang, Hansen and Moan, 2013; Wang, Moan and Hansen, 2013). The significant difference between this new code and Simo-Riflex-Aerodyn is that the Double Multiple-StreamTube (DMS) model is used to calculate the aerodynamic loads on the vertical axis wind turbine instead of BEM or GDW as in AeroDyn. The DMS model, including the effects of variations in the Reynolds number and incorporating the Beddoes-Leishman dynamic stall model, has been validated by comparison with existing experimental data (Wang, Hansen and Moan, 2013; Wang, Moan and Hansen, 2013). A PI generator controller is employed to keep the rotational speed constant

when the rated rotational speed is reached in the model. A notch filter illustrated in the control diagram is designed to reduce the 2P variations of the generator torque from the variations of rotor torque occurring twice per revolution subjected to the aerodynamic loads. However, the notch filter is switched off in the present model to simplify the simulation and ensure stability of the controller.

In both models, the structural model of the tower, blades and mooring line is based on the nonlinear FEM solver in Riflex. The hydrodynamic loads on the mooring lines are calculated by Morison formula. For the FVAWT, the semi-submersible floater is treated as a rigid body in Simo. The hydrodynamic loads on the semi-submersible floater are handled by first order potential theory and the viscous term of the Morison formula. The potential flow model produces added mass, radiation damping and first order wave forces in Wadam. Additional viscous forces are applied to represent the quadratic damping on the floater and mooring system. For the FHAWT, the semi-submersible floater is modeled as a multi-body system with a brace system. The modeling method for the semi-submersible floater has been introduced by Luan at al., 2013. Therefore, both of these two codes can model the wind turbine concepts in the time domain as a so-called aero-hydro-servo-elastic system. A brief summary of these two models is presented in Table 3.

Table 3. Model description of the numerical model

FVAWT	FHAWT
Simulation Code	
Simo-Riflex-DMS	Simo-Riflex-Aerodyn
Aerodynamic	
DMS + DS	BEM or GDW) + DS
Hydrodynamics	
Airy + PF + ME	Airy + PF + ME
Structural Dynamics (Elastic)	
Turbine: FEM Mooring: FEM	Turbine: FEM Mooring: FEM
Control System (Servo)	
(Generator) DLL	(Generator + Blade Pitch) DLL
Airy - Airy wave theory ME - Morison's equation	
PF - Linear potential flow with radiation & diffraction	
DS - Dynamic stall FEM - Finite element method	
DLL - External dynamic link library	

LOAD CASE

The comparison of these two different floating wind turbines is carried out using a selection of load cases (LCs), most of which were taken from the OC4 study. The LCs are summarized in Table 4, where LC 2.3 and 3.1 are additionally defined LCs. LC 1.3 consists of four decay tests for each DOF of the surge, heave, pitch and yaw in still water conditions without wind. The platform is displaced to an initial position from its equilibrium position in the corresponding DOF and then is released to settle down freely. LC 2.1 and 2.2 correspond to the wave only conditions and test the stochastic dynamic response of the system in irregular waves with a JONSWAP spectrum and no wind. LC 2.3 corresponds to the steady wind only conditions to investigate the aerodynamic effects. LC 3.1, 3.2, 3.3 and 3.4 test the stochastic response of the system under the combined irregular wave and turbulent wind conditions. The wind turbines are parked under the extreme condition for LC 3.4 with the peakedness factor of 1.05 while the wind turbines are operating under normal conditions for LCs 3.1 through 3.3 with the peakedness factor of 2.87. In all the cases, the wind and wave directions are aligned, in the positive x direction, and

all the DOFs of platform motion are enabled. The simulations last 4600 s in duration and discard the first 1000 s of start-up transients from the analysis.

Based on these load cases, the comparison between these two concepts can be studied for a range of different conditions: in still water, in irregular waves, in steady and turbulent winds, and in situations where the wind turbines are operating below the rated wind speed and over the rated wind speed. Furthermore, the FHAWT has one more situation that is operating at the rated wind speed of 11.4 m/s.

Table 4. Load cases

Load Case	Response	Aero	Wind	Waves
LC 1.3	Decay	Off	-	Still water
LC 2.1	Stochastic	Off	-	6 m, 10 s, JONSWAP
LC 2.2	Stochastic	Off	-	15 m, 19.2s, JONSWAP
LC 2.3	Steady	On	11.4 m/s	Off
LC 3.1	Stochastic	On	8 m/s	6 m, 10 s, JONSWAP
LC 3.2	Stochastic	On	11.4 m/s	6 m, 10 s, JONSWAP
LC 3.3	Stochastic	On	18 m/s	6 m, 10 s, JONSWAP
LC 3.4	Stochastic	On	47.5 m/s	15 m, 19.2s, JONSWAP

RESULTS AND DISCUSSIONS

In this section, the dynamic responses of the FVAWT and the FHAWT are compared done step by step, based on the numerical models and defined load cases introduced in the above sections. The focus is on the power spectrum and time series of the global motions of the platform in all six DOFs, and the mooring line tensions at the fairlead of the FVAWT and the FHAWT, the internal loads at the tower bottom of the FHAWT and the internal loads at the shaft of the rotor of the FVAWT. The statistical method and the power spectra are used to address the time domain results and carry out the comparison.

Free-decay Test

The semi-submersible floater and the three catenary mooring lines of the FVAWT are the same as the one of the FHAWT except for a slight difference between the ballast water inside the floater of each concept. The difference between the ballast water and the difference between the mass of the wind turbine of each concept results in a difference of the natural periods of the global motions in some DOFs. The natural periods of the global motions of the FVAWT and the FHAWT are tabulated in Table 5. The natural periods are estimated through numerical simulations of the free-decay test. In the decay tests, the wind turbines are parked and no aerodynamic loads are acting on the wind turbines. Table 5 shows that the natural periods of the global motions of the FVAWT are close to the periods of the FHAWT, except for the natural periods of roll and pitch due to the difference between the inertia moments of the wind turbines.

Table 5. Natural periods of the FVAWT and the FHAWT.

	Surge	Heave	Pitch	Yaw
FVAWT [s]	114.0	17.1	31.0	79.7
FHAWT [s]	112.0	17.1	25.8	80.2

Simulations with Wave Only Conditions

Two Jonswap spectra are selected to study the performance of the floating wind turbines in wave only conditions. The LC 2.1 represents the wave condition during the normal operational situation, whereas the LC 2.2 represents the wave condition during the extreme situation. One-hour time domain simulations with the same random seed have been carried out for each wave condition. In these simulations, the focus is on the wave loads only. As in the decay test, the wind turbines are parked and no aerodynamic loads on are the wind turbines. The statistical results of the responses of the global motions and the mooring line tensions of the FVAWT are very close to the results of the FHAWT, as shown in Table 6. In Table 6, M_1 represents the tension at the fairlead of the mooring line 1, M_2 represents the tension at the fairlead of the mooring line 2 and M_3 represents the tension at the fairlead of the mooring line 3. Mooring lines 1 and 3 are attached to the columns separately in the rear, while mooring 2 is attached to the front column along the wind direction, so the tensions in moorings 1 and 3 should be the same as long as the floater has no yaw motion.

Table 6. Mean values of the FVAWT and the FHAWT in LC2.1

Mean	Surge [m]	Sway [m]	Heave [m]	Pitch [deg]	Roll/ Yaw [deg]	M_1/ M_3 [KN]	M_2 [KN]
FVAWT	-0.011	0	-0.07	0.007	0	1095	1094
FHAWT	-0.037	0	0.002	-0.077	0	1096	1093

For the wave only simulations, the shapes of the wave spectra dominate the shapes of the power spectra of the global motions because the potential loads on the hull of the semi-submersible floaters are dominating. However, some peaks corresponding to the eigenvalues of the rotor of the FVAWT can be observed in the power spectra of the mooring line tensions.
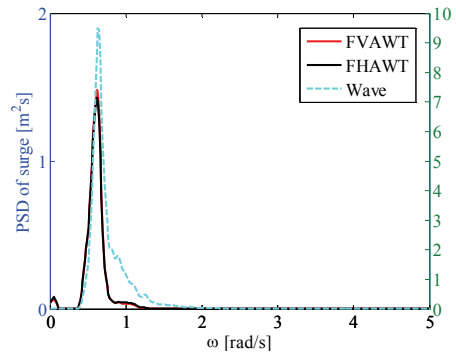
Fig. 2: Power spectra of surge of the FVAWT and the FHAWT in LC 2.1. The red line and the black line are described by the left ordinate, while the blue dot line is described by the right ordinate.

In Fig. 3, four peaks can be observed. "Peak A" corresponds to the peak period of the Jonswap spectrum of LC 2.1. "Peak B" represents the local dynamic responses of the mooring system excited by incident waves. This peak is also observed and reported by the OC4 project (Roberstson, Jonkman, vorphal, Popko, Qvist, Frøyd et al., 2014). The work performed in the OC4 project shows that "Peak B" is captured by the codes that enable dynamic modeling of the mooring system. "Peak C" and "Peak D" are related to the eigen modes of the rotor of the FVAWT. The first 10 eigen modes have been discussed in (Wang,

Moan and Hansen, 2013), where the results show that the eigenvalues of the first five eigen modes are in the range from 3 s to 5 s. As a result, incident waves with small periods may result in large responses of the rotor of the FVAWT.

Fig. 3: Power spectra of the tension of mooring line 3 of the FVAWT and the FHAWT in LC 2.1.

Simulations with Steady Wind Only Conditions

In addition to wave loads, the effect of aerodynamic loads should also be evaluated. The aerodynamic loads on the rotor of the FVAWT are complex. Fig. 4 shows the top view of a horizontal cross section of the rotor of the FVAWT. Three different coordinate systems are established in this section. One is the global co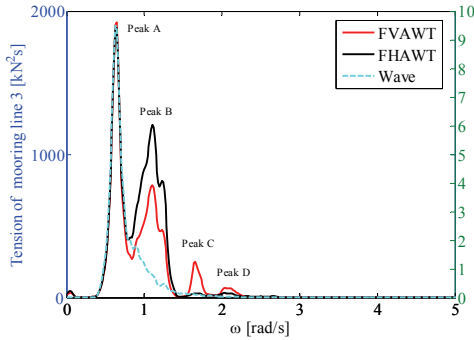ordinate system (XYZ), the second one is the local coordinate system (xyz) and the third coordinate system is the shaft fixed coordinate system (mnl). The global coordinate system is used as an absolute coordinate system for the wind and wave directions and the positions of the two wind turbines. O is the origin of the xyz and the mnl systems. The origin is located on the still water line at the point (0, 0, 0) in the global coordinate system when the floater is floating in calm water without aerodynamic loads, while the vertical axes (z and l) are in line with the central line of the central column of the semi-submersible floater. The position of the origin O and the directions of the axse move together with the global motions of the semi-submersible floater. The local coordinate system xyz is used to describe the positions of the tower, shaft and blades as well as the loads on the blades for both of the wind turbines. The coordinate system mnl is exclusively used for the FVAWT with the m and n rotating with the shaft. The aerodynamic loads on the cross section of each blade shown in Fig. 4 could be decomposed into a normal force F_N and a tangential force F_T. If we do not consider the flexibility of the shaft and the blades, we can assume that the cross section of the blades rotates circularly about the axis of the shaft. Consequently, F_N will always vary along the axis of m, while F_T will always vary along the axis of n. At each time step, the values of F_N and F_T are related to induced velocity of wind speed (V_u and V_d), the rotational speed (ω), the azimuth angle of the shaft (θ), the distance between the shaft and the blade cross section (R) and the lift and drag coefficients. When we look at the F_N and F_T in the xyz coordinates, not only the values of F_N and F_T but also the directions of F_N and F_T will change with the variation of θ. The variation of θ depends on ω. When the velocity of the incident wind is above 8 m/s, the control system of the FVAWT will try to keep the ω value at 0.551 rad/s. We denote this frequency as the 1P of the FVAWT. The internal loads in the cross section of the base of the shaft of the rotor for the FVAWT and in the cross section of the base of the tower for the FHAWT are described in

the xyz coordinates. F_x denotes the internal shear force in the direction of the x-axis in the xyz coordinates. M_x denotes the internal bending moment about the x-axis. Similarly, the internal loads about the y-axis can be described by F_y, M_y. The internal loads in the cross section of the base of the shaft of the rotor for the FVAWT are also denoted by F_m, M_m, F_n, M_n in the mnl coordinates. One-hour time domain simulations of the FVAWT and the FHAWT in calm water with steady wind are carried out. In LC 2.3, the mean wind speed is equal to 11.4 m/s, which is the rated wind speed for the 5 MW FHAWT. The time series of the internal loads between the FVAWT and the FHAWT are compared in the xyz coordinates in Fig. 5, while the power spectra of the internal loads only for the FVAWT are also compared between the xyz and mnl coordinates in Fig. 6. The comparison indicates that even in steady wind only conditions the variations of F_m, M_m, F_n, M_n with 1P frequency and the variations of F_x, M_x, F_y, M_y with 2P frequency are observed. The variations, which are quite large when compared to the corresponding values of the FHAWT, result from the rotation of the shaft of the FVAWT. For example, in the 11.4 m/s steady wind, the M_y of the FHAWT is equal to 78000 kNm, however, the M_y of the FVAWT varies from 31250 kNm to 144000 kNm with the frequency of 2P.

In addition to the 1P and 2P effects, some frequencies that correspond to the eigenvalues of the rotor can also be observed. However, the values of the power spectrum density at these frequencies are much smaller than the values at the 1P and 2P frequencies.
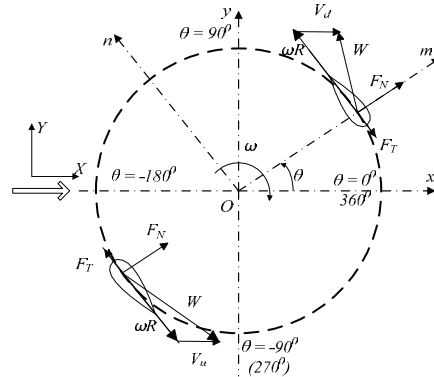

Fig. 4: A plot of a horizontal cross section of the rotor of the FVAWT with blade 1 and blade 2.
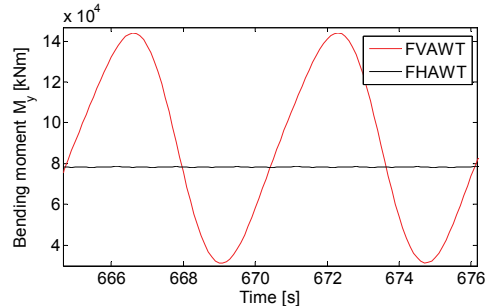

Fig. 5: Time series of the internal bending moment M_y of the FVAWT and the FHAWT in LC 2.3.
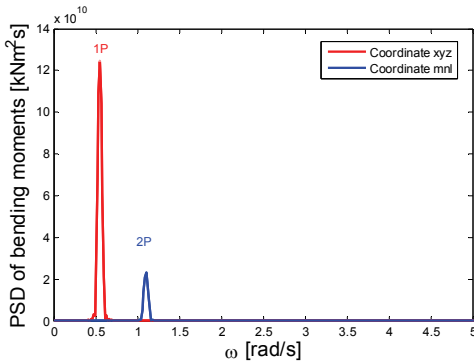
Fig. 6: Power spectra of M_n and M_y of the FVAWT in LC 2.3.

Fully Coupled Simulations with Combined Turbulent Wind and Irregular Wave Conditions

A floating wind turbine should be considered as an aero-hydro-servo-elastic system. Thus, the numerical models of the FVAWT and the FHAWT need to be checked and compared in the cases that combine turbulent winds and irregular waves. Four wind conditions have been selected based on the thrust curve of the 5 MW horizontal wind turbine. The IEC Kaimal wind spectrum is used to generate turbulent wind with the mean wind speed at 90 m above sea level by the NREL's TurbSim program. The IEC class C and normal turbulence model are assumed in this simulation according to IEC standard (2009). By combining the wave conditions, LC 3.1 through 3.4 are used for the dynamic simulations of the wind turbines in the combined turbulent wind and irregular wave conditions. For each case of each model, a one-hour simulation with the same random seed is carried out.
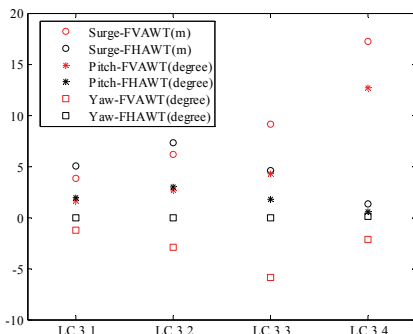

Fig. 7: Mean value of surge, pitch and yaw of the FVAWT and the FHAWT in combined turbulent wind and irregular wave conditions.

Because the linear potential theory is employed for considering the hydrodynamic loads on the floating wind turbines, the mean wave drift force is not presented and thus the mean values of surge and pitch result only from the mean thrust force and moment on the rotor. For the 5 MW NREL horizontal axis wind turbine, the mean thrust force on the rotor increases with the increase of the incident wind speed up to the rated wind speed. When the wind speed is above the rated speed, the

generator torque is kept constant and the imbalance between the aerodynamic torque and the generator torque will change the angular velocity. Thus, the pitch control system of the wind turbine is used to keep the rotational speed constant by increasing the pitch angle of the blades. As a result, the generator power is kept constant as well as the thrust force on the rotor is reduced. For the FVAWT, the stall regulation is employed to control the maximum generated power because the pitch angle of the blades of the FVAWT is fixed. However, with the inclusion of a dynamic stall model in the DMS, the calculated aerodynamic loads on the FVAWT continue to increase with the increase of the wind speed when the wind speed is above the rated speed, which is 14 m/s for the FVAWT. Once the rated rotational speed is reached, the rotational speed of the shaft is kept constant so that the thrust force and generator power still keep increasing. Consequently, the mean value of the surge and the pitch of the FVAWT continue to increase from LC 3.2 to LC 3.3, while in LC 3.3 the mean value of the surge and the pitch of the FHAWT is approximately only half of the corresponding value of the FVAWT. The mean values of the surge of the FVAWT in LC 3.1 and LC 3.2 are smaller than values of the FHAWT. However, the mean values of the pitch for these two models for LC 3.1 and LC 3.2 are close. Because the generator shaft torque is transferred to the submersible floater and balanced by the mooring system, the FVAWT has mean values for the yaw motion in LC 3.1, LC 3.2 and LC 3.3, representative of the operational conditions. In LC 3.3, the mean value of the yaw motion of the FVAWT is -5.86 degrees. LC 3.4 represents the extreme condition where both the FHAWT and the FVAWT are parked. The blades of the FVAWT are parked along the direction of the x-axis shown in Fig. 4. The simulation results show that the FVAWT has a very large mean thrust force, which results in a very large mean offset in the surge and pitch motion. The mean value of the surge of the FVAWT in LC 3.4 is 17.22 m, while the mean value of the pitch of the FVAWT in LC 3.4 is 12.65 degrees. Because the rotor is parked, the attack angles of the blades depend on the direction of the incident turbulent wind. This result may explain the mean values of the yaw and the sway of the FVAWT observed in LC 3.4.
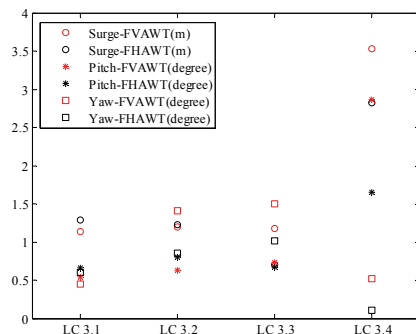
Fig. 8: Standard deviation of surge, pitch and yaw of the FVAWT and the FHAWT in combined turbulent wind and irregular wave conditions.

Regarding the standard deviations (std) of dynamic responses of both models, the simulation results for each case except LC 3.1 indicate that the FVAWT gives larger std for the global motions than the values for the FHAWT. The power spectra of the surge for the FHAWT and the FVAWT show that the spectra are dominated by the low frequency excitation loads from the wind, the resonance corresponding to the surge natural period and the wave frequency. The power spectra of the sway and yaw are similar to the surge except that the resonance corresponds to the natural periods of the sway and the yaw, and the

wave frequency cannot be observed. An exception from this observation is the FVAWT in LC 3.4. Due to the large mean offset in the surge, sway and yaw in LC 3.4 the power spectra of the roll and yaw are dominated by a frequency that equals to 0.117 rad/s. For each case, the spectrum of the heave is dominated by the spectrum of the wave. As a result, the std of the heave motion for these two models are very close. The power spectra for the pitch motion and roll motion are different from the rest of the power spectra for the global motions. A peak corresponding to the 2P effect can be observed in the power spectrum of the pitch motion for the FVAWT. This peak increases with the increase of the wind speed. Meanwhile, the thrust force on the rotor of the FVAWT keeps increasing with wind speed. The FVAWT does not suffer negative aerodynamic damping (Skaare, 2007), but has consistently positive aerodynamic damping. As a result, in Fig. 9, the peak corresponding to the pitch natural period for the FHAWT is larger than the peak for the FVAWT. As mentioned previously, the simulation results indicate that stall regulation does not work for the FVAWT designed in this paper when the dynamic stall model is included in the calculation of aerodynamics. If stall occurs above the rated wind speed, the thrust force on the rotor of the FVAWT is expected to also decrease with an increase of the wind speed until the turbine is parked. As a result, the FVAWT may suffer negative aerodynamic damping. This situation should be checked in the future when the power generated above the rated wind speed behaves more benignly through a different control strategy.
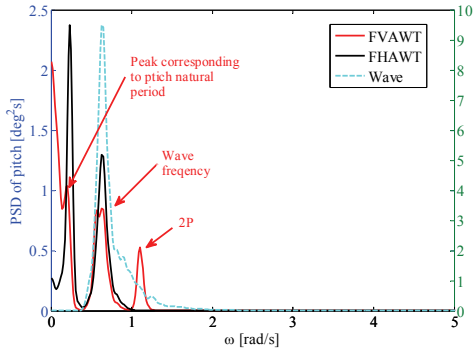

Fig. 9: Power spectra of pitch of the FVAWT and the FHAWT in LC 3.3.
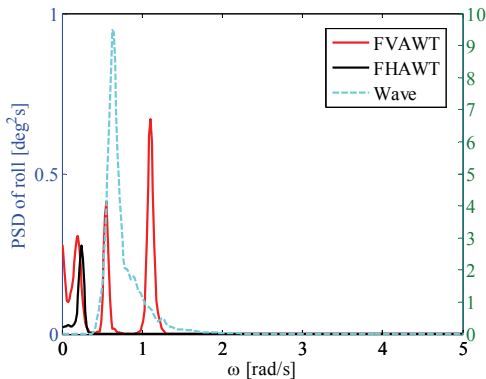

Fig. 10: Power spectra of roll of the FVAWT and the FHAWT in LC 3.3.

For the power spectrum of the roll motion, both the 1P and 2P effects can be observed for the FVAWT. However, the mean value and the std of the roll motion for the FVAWT in all the cases are relatively smaller than the values of the pitch motion. Simulations with misaligned wind and wave conditions are of interest to this work in the future.

The mooring systems of the FVAWT and the FHAWT are the same as those used in the OC4 project. In this paper, the directions of the specified incident winds and waves are the same as the direction of the "wind direction" shown in Fig. 4. Consequently, for each mooring system, the mooring line which is directed along the negative X-axis of the global coordinate system is the critical mooring line, which is denoted by "mooring line 2". The mean tension of the mooring lines is related to the mean position of the semi-submersible floater. The mean positions of the FVAWT and the FHAWT in different cases have been presented in Fig. 7. For LC 3.1 and LC 3.2, the power spectra of the mooring line tension are similar to the spectrum for the wave only condition as shown in Fig. 3, except that the spectra include values in the low frequency area corresponding to the effect of the surge motion due to the aerodynamic loads. Table 7 lists the std of the mooring line 2 tension for both of the floating concepts. In LC 3.3, the std of the tension of mooring line 2 of the FVAWT is equal to 2.34 times the value of the std of the FHAWT. The 2P effect can be clearly observed in the power spectrum of mooring line 2 for the FVAWT in LC 3.3, shown in Fig. 11. The 2P effect increases with the increase of the wind speed. "Peak B" shown in Fig. 11 is not due to the 2P effect. This observation has been explained in Fig. 3. In LC 3.4, the std of the tension of mooring line 2 of the FVAWT is equal to 4.18 times the value of the std of the FHAWT. For both models in LC 3.4, the variation of the mooring line tension is dominated by wave frequency. The large variation of the mooring line tension for the FVAWT in LC 3.3 and LC 3.4 indicates that the catenary mooring system with three mooring lines cannot effectively maintain the position of the FVAWT when the wind speed is above the rated speed. However, in LC 3.1 and LC 3.2 the std of the tension of mooring line 2 of the FVAWT is very close to the std of the FHAWT while the spectra of the mooring line tension are very similar.

Table 7. Std of the mooring line 2 tension for FVAWT and FHAWT in different load cases

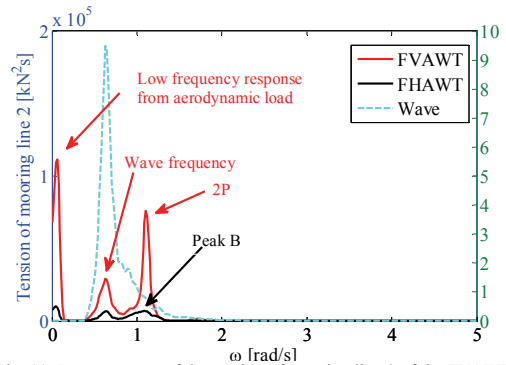| Std	LC 3.1	LC 3.2	LC 3.3	LC 3.4
FVAWT [kN]	83	110	157	1504
FHAWT [kN]	99	114	67	360

Fig. 11: Power spectra of the tension of mooring line 2 of the FVAWT and the FHAWT in LC 3.3.

The internal forces and moments at the base of the rotor of the FVAWT and at the base of the tower of the FHAWT have been checked. The results are denoted by $F_x, F_y, F_z, M_x, M_y, M_z$ in the xyz coordinates. The highlight of the results is that in all the cases the std of the F_x, F_y, M_x, M_y of the FVAWT are much larger than the std of the FHAWT. For example, in LC 3.1 and LC 3.2 the mean value and the std of the global motions and mooring line tensions of the FVAWT are very close to the values of the FHAWT, whereas the std of the M_y of the FVAWT are equal to 32379 kNm and 41768 kNm, respectively, while the M_y of the FHAWT are equal to 17804 kNm and 16936 kNm, respectively, which are approximately 50% of the corresponding value of the FVAWT. The power spectra show that the 2P effect is critical to the fluctuation of the internal loads at the base of the rotor of the FVAWT. However, the 2P effect is not dominating the global motions such as the surge and pitch, especially in LC 3.1 and LC 3.2. To achieve a better design of the FVAWT, on one hand, the designer should put effort in reducing the fluctuation of the environmental loads due to the rotation of the shaft of the FVAWT, such as the use of helical blades; on the other hand, a survey of novel designs of the supporting floaters that could limit the fluctuation of the internal loads through the inertial loads could be interesting.
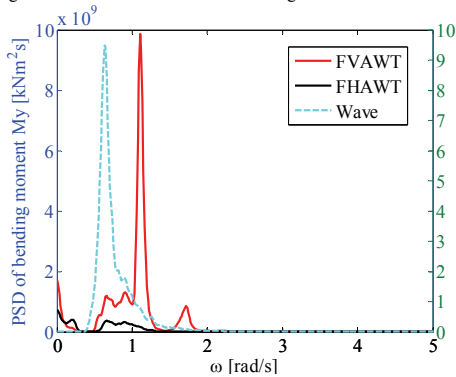

Fig. 12: Power spectra of M_y of the FVAWT and the FHAWT in LC 3.2.

CONCLUSIONS

This paper addresses the global analysis of a floating vertical axis wind turbine and a floating horizontal axis wind turbine on a similar semi-submersible platform. Time domain numerical models of the FVAWT and the FHAWT have been developed based on the codes Simo-Riflex-DMS and Simo-Riflex-Aerodyn, respectively. These numerical models account for the aero-hydro-servo-elastic behavior. An assortment of time domain simulations with different conditions, i.e., the decay tests, wave only conditions, wind only conditions and the combined wind and wave conditions, have been conducted. The FVAWT and FHAWT have been checked and compared through statistical analysis of the time series and power spectra of the global motions in six DOFs, the mooring line tension and the internal loads at the base of the rotor of the FVAWT and at the base of the tower of the FHAWT.

Comparing natural periods of the FVAWT and FHAWT through decay tests has ensured the similar platform properties. The statistical results corresponding to the wave only conditions also show almost identical mean platform motions and mooring line tension for these two concepts. For the spectra of the mooring line tension of the FVAWT, the peaks corresponding to the structural eigen modes such as the tower bending modes, blade flatwise modes and blade edgewise modes are more obvious than the eigen modes for the FHAWT. Through the simulation in the wind only conditions, the effect of 2P frequency on the structural response was identified for the FVAWT. The 2P effect resulting from the rotation of the shaft of the FVAWT leads to a large fluctuation of the aerodynamic loads on the rotor and the internal loads in the rotor even in steady wind conditions. The 2P effect could also be clearly observed in the platform motion, mooring line tension and the rotor base bending moment for the FVAWT in the combined wind and wave conditions. The importance of the 2P effect increases with the increase of the mean wind speed in the operational conditions. The comparison shows that the pitch motion of the FVAWT has mean values and standard deviations very close to the values obtained for the FHAWT at low wind speeds. The surge motion of the FVAWT is also smaller than the surge motion of the FHAWT. Due to the absence of a blade pitch controller, the FVAWT suffers larger platform motions, mooring line tensions and structural responses for the cases with above-rated wind speed.

Based on this comparative study, the different characteristics of the FVAWT and the FHAWT have been captured and more insights into the further development of both these two concepts have been provided. The results shows that the global motion of the platform motion and the tensions of the mooring lines of the FVAWT have similar or even smaller dynamic responses than these values of the FHAWT at low wind speeds. The structural responses such as the bending moment at the bottom of the shaft resulting from the 2P effect of aerodynamic loads have much larger variations for the FVAWT. This disadvantage of the FVAWT could be overcome by a novel rotor type such as helical blades, or at least an optimized structure design and adopting three blades could reduce this disadvantage. The global motion of the platform and the tensions of the mooring lines of the FVAWT at high wind speed also could be much alleviated using a different control strategy which reduces the rotational speed and keeps generated power constant when the wind speed exceeds the rated wind speed. Furthermore, a floater exclusively designed for the FVAWT with a different mooring lines design and arrangement could improve the performance of the FVAWT. Therefore, the FVAWT is still considered to be promising in the offshore application when the rotor, mooring lines and control system are further optimized.

REFERENCES

International Electrotechnical Commission (2009). *IEC61400-3 Wind turbines - Part 3: Design requirement for offshore wind turbines.*

Bachynski, EE, and Moan, T (2012). "Design considerations for tension leg platform wind turbines." *Marine Structures*, Vol 29(1), pp 89-114, DOI: http://dx.doi.org/10.1016/j.marstruc.2012.09.001.

Cahay, M, Luquiau, E, Smadja, C, and SILVERT, FCC (2011). "Use of a Vertical Wind Turbine in an Offshore Floating Wind Farm". *Offshore Technology Conference* Houston, Texas, USA, Offshore Technology Conference.

Eriksson, S, Bernhoff, H, and Leijon, M (2008). "Evaluation of different turbine concepts for wind power." *Renewable and Sustainable Energy Reviews*, Vol 12(5), pp 1419-1434.

Jiang, Z, Karimirad, M, and Moan, T (2013). "Dynamic response analysis of wind turbines under blade pitch system fault, grid loss, and shutdown events." *Wind Energy*, DOI: 10.1002/we.1639.

Karimirad, M, and Moan, T (2011). "Wave-and wind-induced dynamic response of a spar-type offshore wind turbine." *Journal of waterway, port, coastal, and ocean engineering*, Vol 138(1), pp 9-20.

Kvittem, MI, Bachynski, EE, and Moan, T (2012). "Effects of Hydrodynamic Modelling in Fully Coupled Simulations of a Semi-submersible Wind Turbine." *Energy Procedia*, Vol 24, pp 351-362, DOI: http://dx.doi.org/10.1016/j.egypro.2012.06.118.

Luan, C, Gao, Z, and Moan, T (2013). "Modelling and analysis of a semi-submersible wind turbine with a central tower with emphasis on the brace system". *Proc of ASME 32nd Int Conf on Ocean, Offshore and Arctic Eng*, Nantes, France, OMAE2013-10408.

Luxcey, N, Ormberg, H, and Passano, E (2011). "Global analysis of a floating wind turbine using an aero-hydro-elastic numerical model. Part 2: Benchmark study". *Offshore Mechanics and Arctic Engineering Conference*, Rotterdam, The Netherlands.

Ormberg, H, and Bachynski, EE (2012). "Global Analysis of Floating Wind Turbines: Code Development, Model Sensitivity and Benchmark Study". *Proceedings of the Twenty-second (2012) International Offshore and Polar Engineering Conference*, Rhodes, Greece.

Ormberg, H, Passano, E, and Luxcey, N (2011). "Global analysis of a floating wind turbine using an aero-hydroelastic model. Part 1: Code development and case study". *Offshore Mechanics and Arctic Engineering Conference*, Rotterdam, The Netherlands.

Paraschivoiu, I (2002). *Wind turbine design: with emphasis on Darrieus concept*. Montreal, Polytechnic International Press.

Roberstson, A, Jonkman, J, vorphal, F, Popko, W, Qvist, J, Frøyd, L, et al. (2014). "Offshore code comparison collaboration, continuation within IEA wind taks 30: Phase II results regarding in a floating semisubmersible wind system". *Proceedings of the 33th International Conference on Ocean, Offshore and Arctic Engineering*, San Francisco, California, USA.

Robertson, A, Jonkman, J, Masciola, M, Song, H, Goupee, A, Coulling, A, et al. (2012). "Definition of the Semisubmersible Floating System for Phase II of OC4."

Skaare, B, Hanson, TD, Nielsen, FG, Yttervik, R, Hansen, AM, Thomsen, K, and Larsen, T, (2007). "Integrated dynamic analysis of floating offshore wind turbines". *European Wind Energy Conference and Exhibition*, Milano, Italy.

Vita, L (2011). "Offshore Floating Vertical Axis Wind Turbines with Rotating Platform." *Risø-PhD-80(EN)*

Wang, K, Hansen, MOL, and Moan, T (2013). "Model improvements for evaluating the effect of tower tilting on the aerodynamics of a vertical axis wind turbine." *Wind Energy*, DOI: 10.1002/we.1685.

Wang, K, Hansen, MOL, and Moan, T (2014). "Dynamic analysis of a floating vertical axis wind turbine under emergency shutdown using hydrodynamic brake". *EERA DeepWind'2014, 11th Deep Sea Offshore Wind R&D Conference*, Trondheim.

Wang, K, Moan, T, and Hansen, MOL (2013). "A method for modeling of floating vertical axis wind turbine". *Proceedings of the 32th International Conference on Ocean, Offshore and Arctic Engineering*, Nantes, France, paper no: OMAE2013-10289.

A.5   Paper 5

Stochastic dynamic response analysis of a floating vertical axis wind turbine with a semi-submersible floater

Kai Wang, Torgeir Moan and Martin O.L. Hansen

Stochastic dynamic response analysis of a floating vertical-axis wind turbine with a semi-submersible floater

K. Wang[1,2], T. Moan[1,2,3] and M.O.L. Hansen[2,4]

[1] NOWITECH, Norwegian University of Science and Technology, 7491 Trondheim, Norway
[2] Centre for Ships and Ocean Structures, Norwegian University of Science and Technology, 7491 Trondheim, Norway
[3] AMOS, Norwegian University of Science and Technology, 7491 Trondheim, Norway
[4] DTU Wind Energy, Technical University of Denmark, 2800 Lyngby, Denmark

ABSTRACT

Floating vertical-axis wind turbines (FVAWTs) provide the potential for utilizing offshore wind resources in moderate and deep water due to their economical installation and maintenance. Therefore, it is important to assess the performance of the FVAWT concept. This paper presents a stochastic dynamic response analysis of a 5 MW FVAWT based on fully coupled nonlinear time domain simulations. The studied FVAWT, which is composed of a Darrieus rotor and a semi-submersible floater, is subjected to various wind and wave conditions. The global motion, structural response and mooring line tension of the FVAWT are calculated using time domain simulations and studied based on statistical analysis and frequency-domain analysis. The response of the FVAWT is compared under steady and turbulent wind conditions to investigate the effects of turbulent wind. The advantage of the FVAWT in reducing the 2P effect on the response is demonstrated by comparing the floating wind turbine with the equivalent land-based wind turbine. Additionally, by comparing the behavior of FVAWTs with flexible and rigid rotors, the effect of rotor flexibility is evaluated. Furthermore, the FVAWT is also investigated in the parked condition. The global motions and structural responses as a function of the azimuthal angle are studied. Finally, the dynamic response of the FVAWT in selected misaligned wind and wave conditions is analyzed to determine the effects of wind-wave misalignment on the dynamic response.

Correspondence
K. Wang, Centre for Ships and Ocean Structures, Norwegian University of Science and Technology, 7491 Trondheim, Norway
E-mail: kai.wang@ntnu.no

1. INTRODUCTION

The main focus of research on the production of wind power in deep water has been on horizontal-axis wind turbines due to their commercial success in onshore applications. Different platforms have been used as the floating substructures to support the wind turbine, including spar[1], semi-submersible[2,3] and TLP types.[4] Research has focused on the design, structural integrity, platform motion and installation of floating horizontal-axis wind turbines (FHAWTs) to better understand the performance of different concepts and to provide the basis for detailed structural designs. A variety of studies have been conducted on FHAWTs.[2,5-9] However, the application of vertical-axis wind turbines is also of interest in the offshore wind industry, and consequently, different concepts for floating vertical-axis wind turbines (FVAWTs) have been presented, such as the DeepWind concept,[10-12] the VertiWind concept[13] and the Aerogenerator X concept,[14] and studies have described their conceptual designs and evaluated their technical feasibility. Another novel concept was proposed combining the DeepWind 5MW rotor[15] and the DeepCwind floater from the OC4 project,[16] and a coupled non-linear aero-hydro-servo-elastic model to analyze this concept was established.[17]

A conceptual design of a floating support structure and mooring system for the DeepWind concept was presented, and a feasibility study was conducted using efficient frequency-domain technique.[18] A research group at the Technical University of Denmark (DTU) has performed a design optimization of the proposed DeepWind concept.[19] An improved design has been obtained with an optimized blade profile with less weight and higher stiffness than the 1st baseline design. However, the optimization of this design has not been published. Furthermore, different modeling methods and corresponding simulation tools have been developed.[17, 20, 21] To determine the effect of using different simulation codes on the dynamic responses of a FVAWT, a code-to-code comparison of the dynamic models has been conducted.[22] The comparison identified the importance of the dynamic model of the mooring lines and the control model. However, additional aspects of modeling still need to be addressed. One of these aspects is the modeling of the structural dynamics for the blades and the rotating shaft. In the comparison, the rotor was assumed to be rigid, and the effect of structural flexibility was not studied. Although an analysis performed by Karimirad showed the global motion and structural response were dominated by rigid body motions rather than elastic deformations, except for the local response of the rotor for a FHAWT, there is still a need for more study on the FVAWTs with an elastic and a rigid rotors, and therefore this comparison is performed in this paper.

When FVAWTs operate under wave and wind environmental conditions, the rotor experiences aerodynamic loads that vary continuously as a function of the azimuthal blade position, even in steady wind. Turbulent wind can magnify this variation and introduce additional excitation. To investigate these effects, the response characteristics of a FVAWT under steady wind and turbulent wind conditions are studied and compared in this paper. Additionally, the floating support of a FVAWT makes the response characteristics of the wind turbine much different from those of an equivalent land-based wind turbine. Identifying the advantages and challenges of the use of VAWTs in offshore applications relative to equivalent land-based wind turbines is also one of the focuses of this study.

VAWTs with fixed-pitch blades experience large aerodynamic loads in high wind conditions or in stormy weather. The blades may be deformed or broken, and in the most severe cases, the tower could collapse because there is no blade pitch mechanism in VAWTs with Darrieus rotors. Thus, it is important to ensure the survival of the FVAWT in extreme conditions. Unlike a FHAWT, a FVAWT is not suitable to run in an idling condition. Therefore the effect of the azimuthal position of the blades on the dynamic response is studied in the parked condition where the wind turbine is halted.

When considering combined wind and wave conditions, the misalignment between the wind and wave should also be taken into account in the dynamic analysis of a FVAWT. In general, large misalignments occur at lower wind speeds while small misalignments occur at higher wind speeds.[23] Based on observations in the North Sea, it is common to reach 30 degrees of misalignment, but misalignments greater than 60 degrees occur less than 5% of the time.[24] Therefore, misalignment effects on four different FHAWTs were investigated in conditions of up to 90 degrees of misalignment between the wind and wave directions by Bachynski et al[25], whereas Barj et al[26] conducted a study on wind-wave misalignment in the loads analysis of a spar floating wind turbine for all angles between wind and wave directions.

In this paper, the dynamic response of a 5 MW FVAWT is analyzed by investigating the response of the FVAWT under steady wind and turbulent wind conditions, by comparing an elastic FVAWT and a rigid FVAWT, by studying the behavior of the FVAWT compared to an equivalent land-based wind turbine, by determining the dynamic response as a function of azimuthal angle in the parked condition and by analyzing dynamic response of the FVAWT in misaligned wind and wave conditions. Fully coupled nonlinear time domain simulations are conducted using the Simo-Riflex-DMS coupled solver, an aero-hydro-servo-elastic computational tool for FVAWTs.[17] The dynamic response of the FVAWT, including global motions, structural responses and mooring line tension, is studied based on statistical methods and frequency-domain analysis.

2. FLOATING VERTICAL-AXIS WIND TURBINE

The study uses a FVAWT, which includes a 5 MW Darrieus rotor, a semi-submersible floater and three catenary mooring lines, as shown in Figure 1(a). The Darrieus rotor is composed of two blades and one rotating shaft which spans from the top to the bottom where the generator is connected. The geometry and specifications of the rotor are derived from the DeepWind project (2010-2014), which is part of the European FP7 project.[27] The semi-submersible floater is composed of three offset columns, three pontoons, a central column and braces. The offset columns and pontoons surround the central column where the rotor is located. All of the columns and pontoons are connected by braces to form an integrated body. Three catenary mooring lines are attached to the three offset columns to provide horizontal restoring stiffness, arranged as shown in Figure 1(b). The semi-

submersible floater and the mooring line were originally developed for the DeepCwind project and are also used to support a 5 MW HAWT in Phase II of the Offshore Code Comparison Collaboration Continuation (OC4) project. The DeepCwind project is a U.S. based project aimed at generating field test data for use in validating floating offshore wind turbine modeling tools. The OC4 project is a continuation of the OC3 project, and the Phase II of the OC4 project involves the modeling of a semi-submersible floating offshore wind system.[16] Compared to the FHAWT developed in the OC4 project, the FVAWT uses a 5 MW Darrieus rotor instead of the NREL 5MW reference HAWT turbine. To use the VAWT rotor on the semi-submersible floater, the floater had to be modified slightly because the VAWT rotor is heavier than the HAWT rotor. Therefore, slightly less ballast water is used for the FVAWT than for the FHAWT to ensure the same draft for the two wind turbines. The specifications for the current FVAWT has been presented.[17]
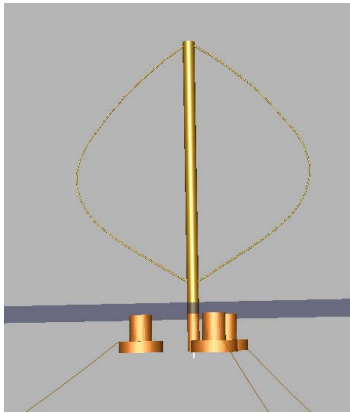
Figure 1. (a) Floating vertical-axis wind turbine;   (b) Mooring line arrangement.
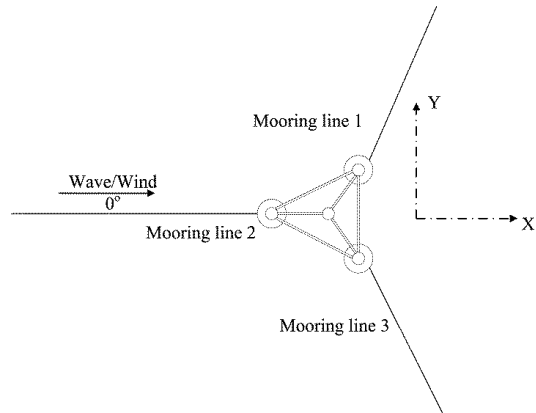
3. THEORY AND METHODOLOGY

A fully coupled simulation tool, Simo-Riflex-DMS, was developed for time domain simulation of the dynamic behavior of FVAWTs. The dynamic response of the FVAWT is calculated by integrating separate models for the wind inflow, aerodynamics, hydrodynamics, structural dynamics and controller dynamics. Three computer codes are coupled: Simo calculates the rigid body hydrodynamic forces and moments on the floater; Riflex models the blades, tower, shaft and mooring system as finite flexible elements, and provides a link to the DMS code and external controller; and the DMS provides the aerodynamic loads on the blades using an external aerodynamic module. The generator torque code was written in Java. Simo computes the hydrodynamic loads at the actually displaced position of the floater, DMS code calculates the aerodynamic loads on the blades, and Riflex performs full equilibrium iteration at each time step. This combination produces a comprehensive aero-hydro-servo-elastic simulation tool with sophisticated hydrodynamics, stable non-linear finite element solver, well-known aerodynamics and user-defined controller, as illustrated in Figure 2. The Simo-Riflex wind turbine module has been previously verified [28, 29], and the Simo-Riflex-DMS tool was presented and verified by Wang et al.[17, 22]

3.1. Aerodynamic modeling

The aerodynamic loads in the FVAWT are calculated based on the Double Multiple-Streamtube (DMS) model including the effect of Reynolds number variations and the Beddoes-Leishman dynamic stall model. The DMS model is described in detail in the work of Paraschivoiu.[30] The Beddoes-Leishman (BL) dynamic stall model is used to represent the unsteady aerodynamics of the airfoils, including three states: unsteady attached flow, unsteady separated flow and dynamic vortex lift. The dynamic stall model is applied in the simulations for all normal operating conditions except the parked condition. A turbulent wind field is generated by Turbsim.[31] This code has been validated by comparison with existing experimental data.[32]

3

However, the global motion of the FVAWT platform poses several challenges to the DMS model. The translational and rotational velocity of the platform must be taken into account in the relative velocity while the inflow velocity is interpolated based on the updated position of each blade element. When calculating the induced velocity in the downstream domain, it is impossible to track the wake velocity from upstream at the updated position. This is a limitation of the DMS model that does not occur in the vortex method. Therefore, when calculating the induced velocity for a blade located downstream, the induced velocity in the corresponding upstream domain is assumed to be calculated for an upstream blade at the same updated position. An additional challenge is including roll and pitch motion in the DMS model. These motions significantly change the direction of the streamtube in the DMS model. Tilting of tower occurs, and the dynamic inflow model needs to be revised. More effort is necessary on this topic. A more advanced model needs to be employed to include the effect of the platform motion on the aerodynamic model. However, an improved model to evaluate the effect of tower tilting on the aerodynamics of a VAWT was presented by Wang et al[32] and the model indicated that the effect of the pitch angle of the platform on the aerodynamic loads was almost insignificant up to 10 degrees. Therefore, in the present paper, the aerodynamic loads are calculated by assuming that the tower is not tilted, but the blade element velocity from rotational motion of the platform has been taken into account. Additionally, a dynamic wake model for the induced velocity is not considered. Finally, the relative velocity seen at a blade section is the vector sum of the induced velocity, the free wind speed and subtracting the velocity due to the motion. The velocity of the motion is comprised by the blade rotation, the translational and rotational velocity from the platform and the elastic deformation of the blades.
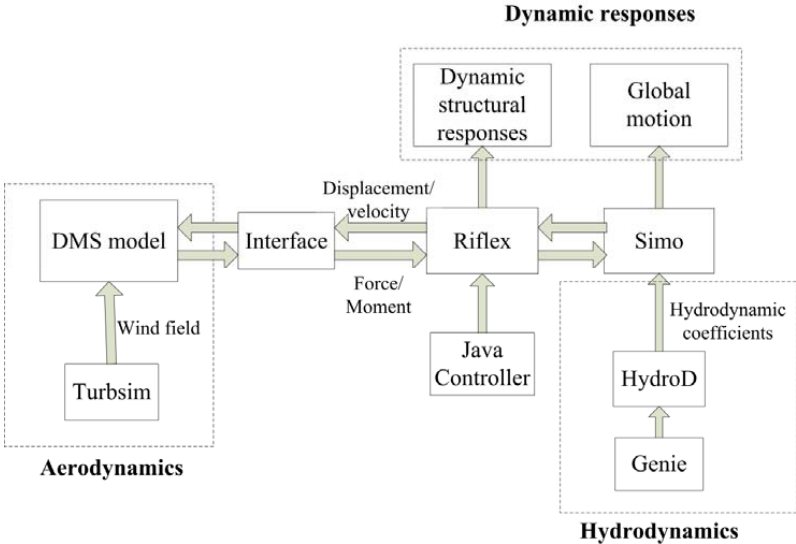
Figure 2. Computation flow chart for the coupled model.

3.2. Hydrodynamic modeling

In the calculation of hydrodynamic loads, the floater is considered as a rigid body in Simo, and the mooring lines are represented by finite beam elements in Riflex. The hydrodynamic loads on the floater include the first order wave forces and viscous forces. The former are handled by a linear potential flow model, and the latter are expressed by the viscous term of the Morison equation. Additionally, the hydrodynamic loads on the mooring lines are modelled by Morison equation. The potential flow model produced the first order wave force transfer function as well as the added mass and radiation damping in Wadam.[33] The frequency-dependent added mass and radiation damping are then included in the Cummins equation as formulated in the time domain in equation 1, which is solved by introducing the retardation function. The retardation function involves a convolution term representing the component of the radiation forces associated with fluid memory effects. The applied viscous forces represent quadratic damping on the floater and mooring system.

4

$$((M+A_\infty)\ddot{x}(t)+\int_{-\infty}^{\infty}\kappa(t-\tau)\ddot{x}(\tau)d\tau+(K_m(x(t))+K_h)x(t)=F_{exc}(t) \tag{1}$$

where M is the body mass matrix, A_∞ is the added mass at high frequencies, $x(t)$ is the displacement of motion, $\kappa(t-\tau)$ is the retardation function accounting for the frequency-dependent added mass and damping, $K_m(x(t))$ is the non-linear restoring matrix for the mooring system, and $F_{exc}(t)$ is the excitation force. In this study, excitation force includes the Froude-Krylov force, the diffraction force, aerodynamic forces and viscous drag.

3.3. Structural modeling

The structural dynamics of the rotor and mooring lines is calculated using nonlinear finite element solver in Riflex while the platform is considered as a rigid body. The rotor consists of a rotating shaft and two blades. A very short tower is assumed to connect with the rotating shaft and platform in this structural model. The properties described in the thesis of Vita[27] are used to establish the structural model. The tower and shaft are modeled as flexible axisymmetric beam elements, and the blades are modeled as flexible beam elements with two symmetric planes to differentiate the stiffness in the direction along the chord and the direction perpendicular to the chord of blade. Therefore, each blade with the length of 188.3 m is modeled by 75 elements with two symmetry axes, as well as gyroscopic effects and the geometric stiffening effect are included in the blade model.

The Newmark-β numerical integration (β = 0.256, γ = 0.505) is used to solve the dynamic equilibrium equations with a time step of 0.0025 s. To ensure numerical stability, structural damping is included through global proportional Rayleigh damping terms for all beam elements. A global stiffness proportional damping factor of 0.003 is used for all structures.

3.4. Control system modeling

A PI generator controller is used in this study. The objective of the control model is to enable variable speed operation maximizing the power capture below the rated operating point and maintaining the generator speed above the rated operating point in the simulations. Therefore, the PI generator controls the rotational speed corresponding to different wind speeds based on the optimized curve of torque versus rotational speed calculated from the aerodynamic model. However, the rotational speed oscillates around the specified rotational speed because of the periodically changing aerodynamic forces caused by the cyclic variation of the angle of attack during each revolution. The detailed controller strategy and relevant controller parameters are documented by Merz et al[34, 35] and the application in this integrated model has been verified by Wang.[17]

3.5. Environmental conditions

A set of environmental conditions is defined for the FVAWT in the simulations. Six conditions of correlated and directionally aligned wind and waves are applied as load cases, as shown in Table 1. For the wind conditions, both the normal wind profile model (NWP) and the normal turbulence model (NTM) are used in all cases. In the NWP conditions, the wind profile $U(z)$ is the average wind speed as a function of the height z above the free water level, given by the power law

$$U(z) = U_{ref}\left(z/z_{ref}\right)^\alpha \tag{2}$$

where U_{ref} is the reference wind speed, z_{ref} is the height of the reference wind speed and α is the power law exponent. For this study the value of z_{ref} was set to 79.78 m (the height of the vertical center of the blades) above mean sea level, and the value of α for the floating wind turbine is set to 0.14 in accordance with IEC 61400-3.[36] For the NTM conditions, three-dimensional turbulent wind fields are generated using NREL's TurbSim program,[31] based on the Kaimal turbulence model for IEC Class C. For the wave conditions, the significant wave height (H_s) and peak period (T_p) are set based on their correlation with the wind speed for the Statfjord site in the North Sea.[37] The wave time series are generated from JONSWAP spectra in the Simo program.[38] Aligned wind and wave directions are used in all the following sections except for the last section, in which the effect of wave-wind misalignment is investigated. Additionally, to simulate the FVAWT in the parked condition, an extreme environmental condition is used of a one-hour mean wind speed of 50 m/s, a significant wave height of 12.9 m and a spectral peak period of 14.1 s.

5

Table 1: Combined wind and wave environment for normal operating condition

| Load case	Uw (m/s)	Hs (m)	Tp (s)	Turb. Model
LC 1	5	2.10	9.74	NTM
LC 2	10	2.88	9.98	NTM
LC 3	14	3.62	10.29	NTM
LC 4	18	4.44	10.66	NTM
LC 5	22	5.32	11.06	NTM
LC 6	25	6.02	11.38	NTM

Each simulation lasts 4600 s, but the first 1000 s of start-up transients is removed, for a one-hour dynamic analysis. To reduce the stochastic variability in the simulation results, each of the LCs with turbulent winds or irregular waves is run with 5 different seeds for the randomized wind and wave processes.

4. Results and Discussion

4.1. Response characteristics of the FVAWT

In this section, the response of the FVAWT under combined wave and wind conditions is calculated using the Simo-Riflex-DMS coupled solver. Steady and turbulent wind conditions are compared in this section, but irregular wave conditions are used for all simulations. The turbulent wind and irregular wave conditions are defined as in Table 1. For the steady wind conditions, the same wind speed and NWP model are used as for turbulent wind, but the NTM model is not used. The analysis of the response focuses on assessing the effect of turbulent wind on the dynamic response by comparing the simulated results under steady wind conditions with turbulent wind conditions. Several dynamic measures, including the platform motion (i.e., surge ζ_1, sway ζ_2, heave ζ_3, roll ζ_4, pitch ζ_5 and yaw ζ_6), the tower base fore-aft (FA) bending moment, the tower base side-side (SS) bending moment and the tension of the mooring lines, are used as the primary performance parameters for comparisons. The behavior of the FVAWT differs from the FHAWT in that not only does the FA bending moment vary with the azimuthal angle of the blades but the SS bending moment also has greater variation in the FVAWT, consequently, both of the two bending moments are investigated.

Figure 3 shows the time series and power spectrum for pitch motion of the platform from one realization in steady and turbulent wind for LC 4. Higher amplitude pitch motion is observed in the time history for the turbulent wind condition than for the steady wind condition, and this can be explained by comparing the power spectra to evaluate the effect of turbulent wind. The turbulent wind excites the pitch natural responses and the wind-induced responses. Furthermore, a peak at the 2P frequency is also observed for both steady and turbulent wind conditions. It should be noted that the 2P frequency originates from the characteristics of VAWTs with two blades. Because the axis of rotation is not parallel to the wind direction and the angle of attack of the blades varies with the azimuthal position during operation, the aerodynamic loads vary within one revolution. For a two-blade wind turbine, the variation in the torque occurs twice per revolution, and the 2P variation leads to the 2P frequency. When the wind turbine rotates at the rated rotational speed of 0.551 rad/s, the 2P frequency is approximately 1.1 rad/s. However, the peak corresponding to the 2P frequency for turbulent wind is slightly lower than the peak for steady wind, which indicates that the 2P effect is reduced slightly by the turbulent wind. A similar result can be observed for the surge, sway, roll and yaw motions. The responses at the natural frequency of each motion, i.e., 0.055 rad/s for surge and sway motions, 0.2 rad/s for roll and pitch motions and 0.079 rad/s for yaw motion, are significantly magnified under turbulent wind conditions. In addition to the difference in the magnitude of the response peak at the 2P frequency under steady versus turbulent wind conditions, the value of 2P frequency also changes when the wind speed increases to 25 m/s, as shown in Figure 4. This is because different rotational speeds are generated in steady and turbulent wind conditions due to the effect of turbulent wind on the controller. Moreover, a peak near a frequency of 1.7 rad/s is only observed in the steady wind condition rather than in the turbulent wind. This peak corresponds to the natural frequency of the first blade flatwise mode and can be identified in the surge, sway, roll and pitch motions. The calculated natural frequencies of the rotor have been listed by Wang.[17]
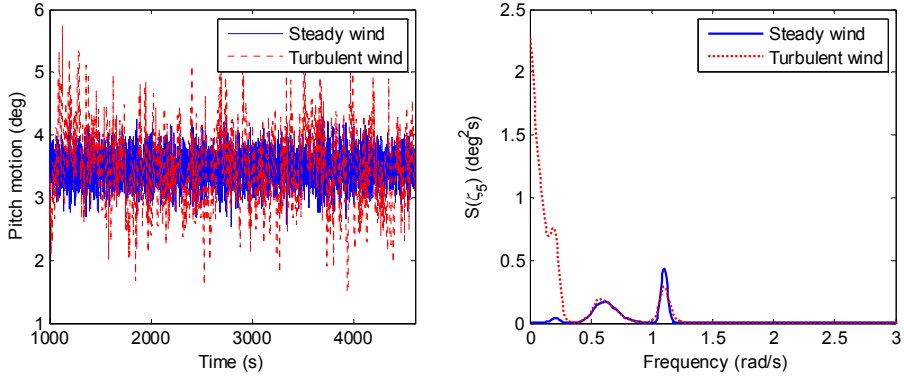
Figure 3. Time series and power spectrum of pitch motion for $V = 14$ m/s, $H_s = 3.62$ m and $T_p = 10.29$ s (LC 4).
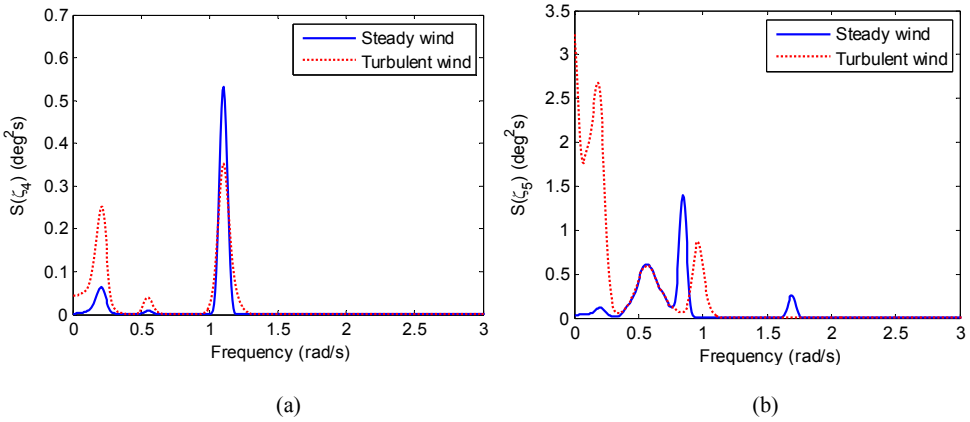
Figure 4. Power spectra: (a) roll motion for $V = 14$ m/s, $H_s = 3.62$ m and $T_p = 10.29$ s (LC 4); (b) pitch motion for $V = 25$ m/s, $H_s = 6.02$ m and $T_p = 12.38$ s (LC 6).

In the mooring system, the low-frequency responses of the mooring line tension due to the turbulent wind are also excited significantly. The peak corresponding to the 2P frequency in the turbulent wind condition becomes higher than the peak in the steady wind condition as the wind speed increases, whereas the peak at the higher structural natural frequency becomes lower under the turbulent wind condition. Similar effects on the bending moments are observed at the 2P frequency and the structural natural frequency. The effects are only obvious at high wind speeds, such as 22 and 25 m/s. Additionally, the turbulent wind excites the low-frequency response in the fore-aft bending moment more than in the side-side bending moment.

The statistics for the responses, such as mean values, standard deviations and maximum values, can also be compared. Figure 5 shows the statistics for pitch motion, yaw motion, the tension of mooring line 2, the SS bending moment and the FA bending moment at the base of the tower for different wind conditions. The mean values for surge and yaw motion depend on the mooring system stiffness and the wind load while the mean values for roll and pitch motion depend primarily on the restoring moment of the platform and the moment due to the wind turbine thrust. The tension of the mooring system is related to the displacement due to surge, sway and yaw motion. The bending moments also depend on the tower and blades displacement (gravitational loading) relative to the platform and the wind loads on the rotor. Therefore, the mean values are almost identical under steady and turbulent wind conditions. A slight difference is observed at the high wind speed of 25 m/s due to the small difference in the rotational speed produced by the control model under turbulent wind conditions. The effect of turbulent wind can be seen clearly by comparison with the steady wind results. Both the standard deviations and the maximum values of the selected responses are greater in the turbulent wind condition than in

the steady wind condition. Moreover, the difference in the yaw motion is much greater because the restoring moment in the yaw motion from mooring system stiffness is small.

Figure 5. Comparison of selected response statistics: mean values, standard deviations and maximum values of pitch and yaw motion, mooring line tension and tower base bending moments.

4.2. Comparison of the FVAWT with a land-based wind turbine

In this section, the response of the FVAWT is compared with the response of an equivalent bottom-fixed land-based wind turbine. The same rotor used in the FVAWT is installed in a bottom-fixed structure to form a land-based vertical-axis wind turbine. However, no guy cables connecting the top of the tower with the ground are used, as would be common in VAWTs. The same turbulent wind field files are generated for the simulations of the two wind turbines, whereas the wave conditions are only applied to the FVAWT.

The characteristics of the FVAWT are compared to the land-based wind turbine to provide insight that might be used in the development of FVAWTs. Figure 6 compares the power spectra of the fore-aft bending moment for the two wind turbines as well as the power spectra of the side-side bending moment under LC 4. The turbulent wind excites the low-frequency responses of the fore-aft bending moment for both the FVAWT and the land-based wind turbine, but the wind-induced response is much less than the response excited at the 2P frequency. Moreover, the 2P effect on the fore-aft bending moment and side-side bending moment is much larger in the land-based wind turbine than the FVAWT. This indicates that the floating support structure can mitigate the 2P excitation that is considered one of the most critical challenges for VAWTs. Consequently, the standard deviations and maximum values for the fore-aft bending moment in the FVAWT are smaller than in the land-based wind turbine, as shown in Figure 7. The maximum response values for the land-based wind turbine are much larger than the maximum values for the FVAWT, and the difference increases with wind speed.

8

Whereas, the mean values for the fore-aft bending moment in the FVAWT are smaller than for in the land-based wind turbine due to large bending moment contribution from the non-zero tilt angle of the tower in the FVAWT. A similar effect is also observed for the side-side bending moment.
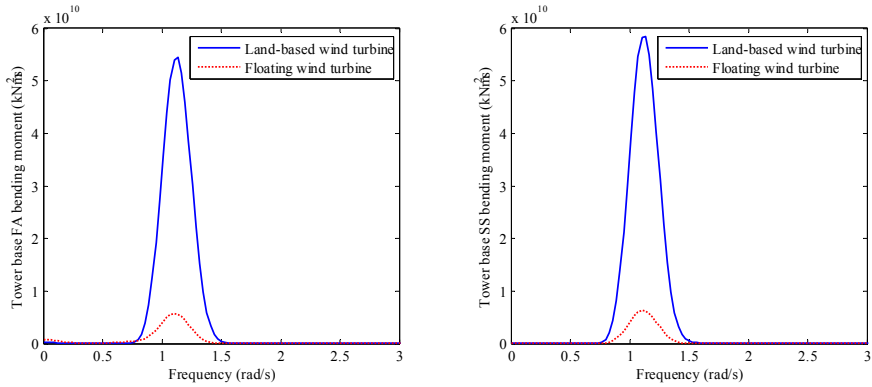
Figure 6. Comparison of the tower base bending moments between the land-based VAWT and the FVAWT (LC 4): power spectral of the fore-aft bending moment and the side-side bending moment.
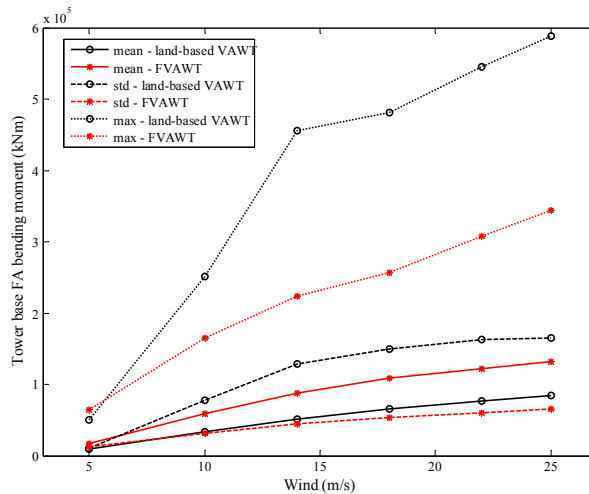
Figure 7. Comparison of the tower base fore-aft bending moment between the land-based VAWT and the FVAWT.

4.3. Effect of structural flexibility on the dynamic response

The effect of structural flexibility on the dynamic response is evaluated by comparing a rigid wind turbine to the flexible wind turbine under the same wave and turbulent wind conditions listed in Table 1. The flexible wind turbine refers to the FVAWT studied in the paper. To model the rigid wind turbine, the axial, bending and torsional stiffness are set sufficiently high to be regarded as rigid. All other properties and environmental conditions remain the same for the two wind turbines. To highlight the differences in the responses of the rigid wind turbine and the flexible wind turbine in the turbulent wind conditions, the comparison focuses on the normalized mean values, standard deviations and maximum values of the responses. The normalized values are defined as the ratio of the results for the FVAWT to the results for the rigid wind turbine. The responses for the sway and roll motion as well as the side-side bending moment are not presented in this comparison. The mean

9

values of statistics of these measures are very small and small difference could lead to large normalized values; therefore, their evaluation would not be representative of the effects of structural flexibility.

Figure 8 shows the normalized mean values, standard deviations and maximum values for all responses under different turbulent wind and wave conditions. The normalized mean values are very close to 1 except for the pitch and the fore-aft bending moment, which are significantly larger than 1 at a wind speed of 5 m/s and slightly greater than 1 as the wind speed increases. However, the surge and yaw values are slightly less than 1 at wind speed greater than 5 m/s. In the normalized standard deviations, the effect of structural flexibility on the responses is obvious except for the surge motion. The flexible wind turbine has lower standard deviations for pitch motion than the rigid wind turbine, whereas the standard deviations for the fore-aft bending moment are much greater in the flexible wind turbine than in the rigid wind turbine as the wind speed increases. Additionally, the standard deviations for the tension of mooring line 1 and 3 vary more than the values of the tension of mooring line 2 because mooring lines 1 and 3 are less tensioned than the mooring line 2, and they consequently have lower mean values. Therefore, greater consideration should be given to the tower bending moment and the tension of mooring lines 1 and 3 when performing fatigue calculations in a simplified model to determine whether the rigid wind turbine is sufficient to replace the flexible wind turbine. For the normalized maximum values, the most apparent difference occurs in the fore-aft bending moment, which has a greater maximum in the flexible wind turbine than in the rigid wind turbine because the deformation of the wind turbine produces extra gravitational loading on the rotor, resulting in a larger bending moment. Unlike the mean values for pitch, the maximum pitch values are lower in the flexible wind turbine at lower wind speeds, whereas they are close to the values for the rigid wind turbine at higher wind speeds. The effect of structural flexibility on the maximum values of the other responses is not pronounced, except for the maximum surge value at a wind speed of 5 m/s.

Figure 8. Comparison of selected responses for the flexible FVAWT normalized by the values for the rigid FVAWT

To determine the reason for the differences observed between the rigid and the flexible wind turbines, the power spectra for different responses are plotted. Figure 9 compares the power spectra of the pitch motion of the rigid wind turbine and the flexible wind turbine at wind speeds of 5 m/s and 14 m/s. At the lower wind speed, three main peaks can be identified in three frequency ranges: in the low-frequency range (wind-induced), at the pitch natural frequency and in the wave-frequency range (wave-induced approximately from 0.5 rad/s to 1 rad/s). At the higher wind speed, a peak at the 2P frequency is also observed for both the two wind turbines. The peak at the 2P frequency and the wave-induced peak in the flexible wind turbine become more evident and larger than

the peaks in the rigid wind turbine as the wind speed increases. However, the rigid wind turbine has a much larger peak corresponding to the pitch natural response than the flexible wind turbine at the low wind speed. This might be because the flexible rotor provides more aerodynamic damping than the rigid rotor, especially at low wind speeds. Additionally, the low-frequency response excited by the wind is dominant, and the difference in the peak of the pitch natural response decreases as the wind speed increases. Therefore, the difference in the mean values of the pitch motion reduced, and the wind-induced response and the pitch natural response dominate as the wind speed increases. A similar result is observed for other motions such as the surge, sway, roll and yaw. A slight difference is that the 2P effect dominates the response in the roll motion, and the peak in the flexible wind turbine is significantly larger than the peak in the rigid wind turbine. However, in the surge, sway and yaw motions, the corresponding natural response is dominant, and the difference in the response of the rigid and the flexible wind turbines depends primarily on the peak at the resonant frequency of the platform motion.
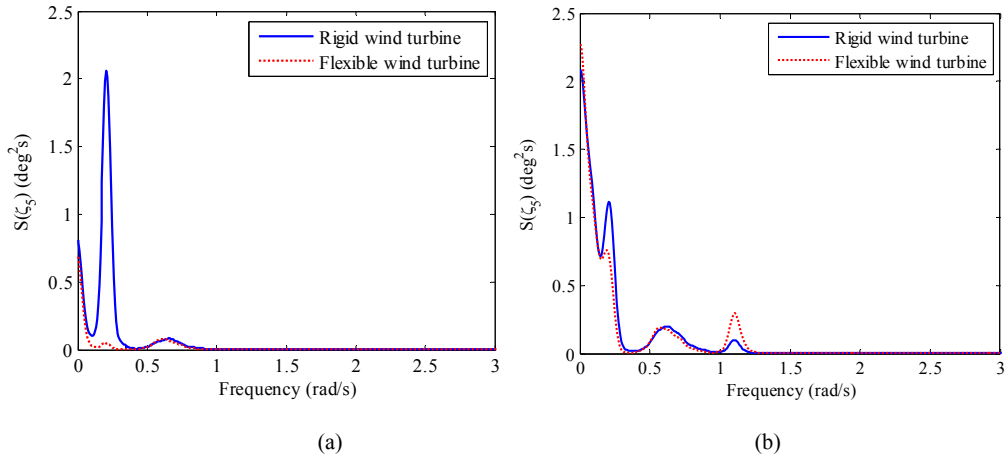
Figure 9. Comparison of the power spectra of pitch motion for the rigid FVAWT and the flexible FVAWT: (a) LC 1 and (b) LC 4

The standard deviations of the bending moments and the mooring line tension, which are important to consider when evaluating the fatigue life of the tower and the fairlead of the mooring lines, are significantly affected by the 2P frequency, as shown in Figure 10. A large difference can be identified in the spectral peak of the bending moment at the 2P frequency in the flexible wind turbine and the rigid wind turbine. This results in large increase in the standard deviations of the bending moment for the flexible wind turbine when compared to the rigid wind turbine. However, the peak in the tension of the mooring line at the 2P frequency is slightly smaller in the flexible wind turbine than in the rigid wind turbine at a wind speed of 5 m/s. As the wind speed increases, the peak in the tension of the mooring line at the 2P frequency becomes larger in the flexible wind turbine than in the rigid wind turbine. Additionally, a peak at the structural natural frequency can also indicate larger standard deviations in the bending moment and the mooring line tension in the flexible wind turbine. The contribution from the structural natural frequency becomes more apparent as the wind speed increases.

4.4. Evaluating the effect of the azimuthal angle

In this section, the effect of the azimuthal angle of the rotor on the different responses when the wind turbine is parked under extreme wind speeds and corresponding wave conditions is evaluated. The rotor is assumed to be in a standstill configuration when the turbine is parked. The azimuthal position of the rotor is crucial to the global and structural responses of the FVAWT in the parked condition. Figure 11 illustrates the rotor at two azimuthal angles θ measured from the positive wind direction along the X axis of the global coordinates XOY. A series of simulations is performed at different azimuthal angles under aligned wave and wind conditions, and the results are analyzed using the statistical method. Figure 12 shows the mean values, standard deviations and maximum values of the global motion as a function of the azimuthal angle. The azimuthal angle has little effect on the standard deviations of the surge, sway and heave motions, but the difference in the standard deviations of the roll, pitch and yaw motions with different azimuthal angle is apparent. The difference in the standard

11

deviations with the azimuthal angle depends on the different excitations contributing to the peaks in the power spectra, as shown in Figure 13. The main contribution to the standard deviations of the sway and yaw are related to the spectral peak at the natural frequency of the sway and yaw motions, respectively. However, both the peaks at the natural frequency and in the wave-induced range could contribute to the surge and pitch motions. Additionally, the wind-induced loading affects the pitch motion significantly as a function of the azimuthal angle. However, the effect of the azimuthal angle on the standard deviations of the global motions is less significant than the effects on the mean values and maximum values. The mean values and maximum values of all global motions except the heave motion vary significantly as the azimuthal angle changes. The azimuthal angles corresponding to the highest and lowest mean values and maximum values can be obviously observed for the different motions. An important result is that the optimal azimuthal angle is found to be 90 degrees based on the consideration of all motions. At the optimal azimuthal angle, the mean values, standard deviations and maximum values of the responses are smallest compared to the values at other azimuthal angles. On the contrary, the worst azimuthal angles, corresponding to the largest responses for each of the platform motions, can also be observed. These angles are important when evaluating the ultimate loads for structural design.

Figure 10. Comparison of the power spectra of the fore-aft bending moment and the tension of mooring line 2 for the rigid FVAWT and the flexible FVAWT under LC 4
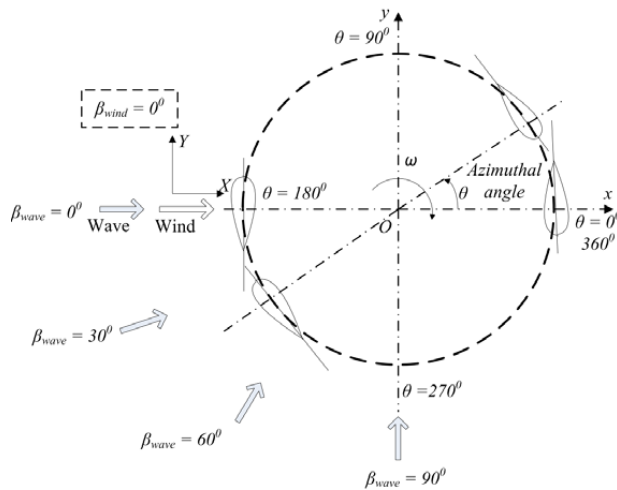
Figure 11. A horizontal cross section of the rotor showing the azimuthal angle in parked conditions and showing the wave direction distribution in wind-wave misalignment conditions.
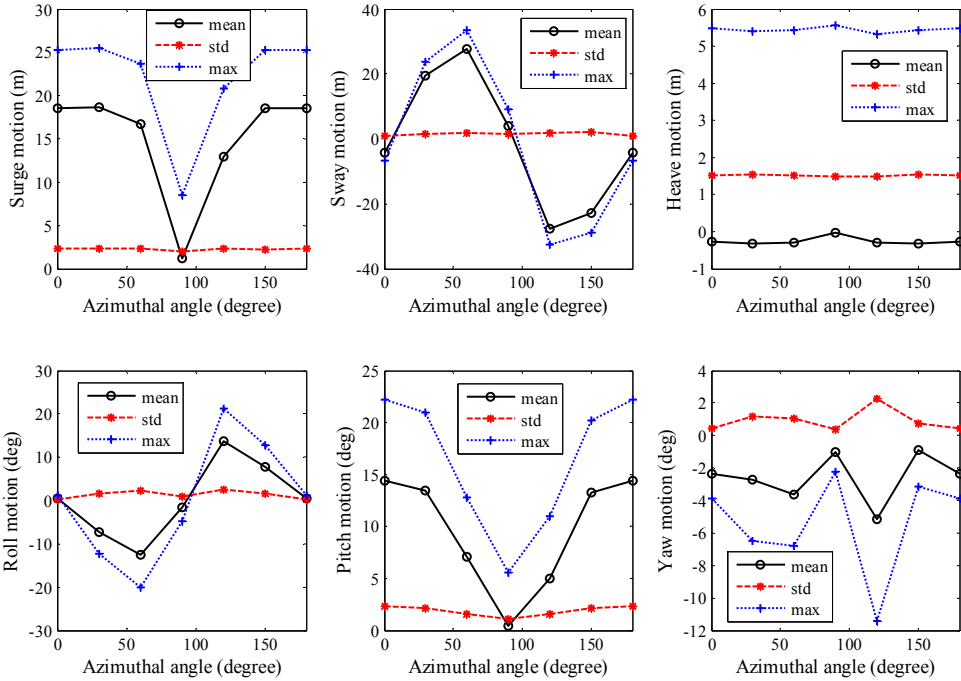
Figure 12. Statistical values of the global motion as a function of the azimuthal angle in the parked condition.
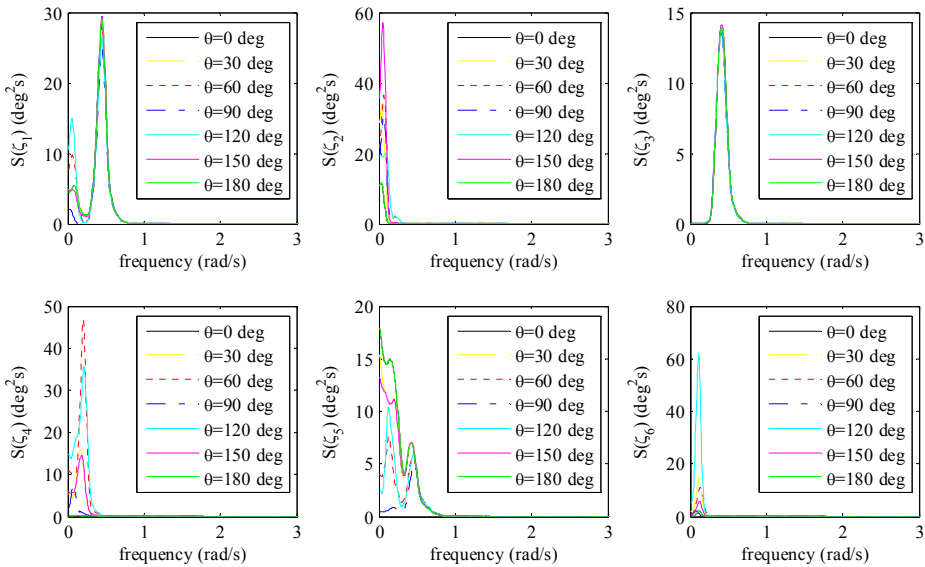
Figure13. Power spectral of the global motion as a function of the azimuthal angle in the parked condition.

The statistical results for the bending moments as a function of the azimuthal angle are shown in Figure 14. The azimuthal angles corresponding to the maximum fore-aft bending moments are approximately 0 and 180 degrees while the azimuthal angles corresponding to the maximum side-side bending moments are approximately 60 and 120 degrees. The mean values have a similar trend to the maximum values. The azimuthal

13

angle with the lowest values for both the bending moments is approximately 90 degrees. To reduce the amplitude of the bending moments and improve the safety of the wind turbine in the parked position, the azimuthal angle of the blade should be set to approximately 90 degrees, at which the chords of the blades are parallel to the direction of the wind. The standard deviations also depend on the azimuthal angle because the wind-induced loading in the low-frequency range dominates the dynamic response for the bending moments at the different azimuthal angles. A similar result can be observed for the mooring line tension, and the optimal azimuthal angle is also found for the dynamics of the mooring lines.
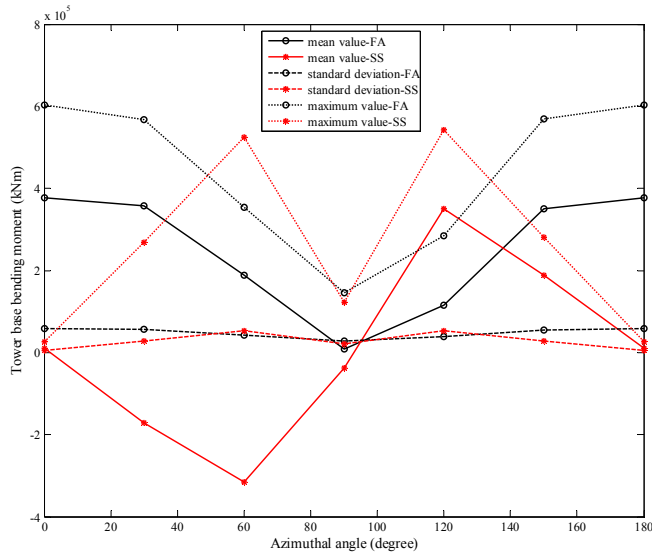
Figure 14. Statistical values of the tower base bending moments as a function of the azimuthal angle in the parked condition.

4.5. Effect of wind-wave misalignment

To investigate the effect of wind-wave misalignment, numerical simulations are performed to study the dynamic response of the FVAWT for a wind direction of 0 degrees and four wave directions (β_{wave}: 0, 30, 60 and 90 degrees). The configurations of the wave and wind directions are depicted in Figure 11. The mean values, standard deviations and maximum values of the responses are presented as functions of the wind-wave misalignment.

The mean values of the global motions, except for the yaw motion, are not significantly affected by the wave direction. The yaw motion depends on the aerodynamic torque on the rotor, the hydrodynamic loads on the platform and the mooring line tension on the fairlead of the platform. Greater mean values for the yaw motion are observed at β_{wave} = 30 and 90 degrees, due to the change in the hydrodynamic loads on the mooring line and the viscous hydrodynamic loads on the braces and columns of the platform with changing wave direction.

Unlike the mean values, the standard deviations of the global motions are sensitive to the wave directions, as shown in Figure 15. The surge standard deviation increases with increasing β_{wave}, as can be observed in LC 1-3. A similar result has been found in evaluating the effect of the wind-wave misalignment on the FHAWT.[25] This is because the low-frequency response increases with increasing β_{wave}, while the wave-frequency response decreases. A decrease in the maximum value of the surge motion with increasing β_{wave} can be observed at high wind speeds in LC 4-6 because the decrease in the viscous hydrodynamic loads on the platform in the surge direction is greater under higher significant wave height conditions.

The standard deviation of the sway motion increases as β_{wave} increases, although this can only be clearly observed in LC 4-6, because as β_{wave} increases, the wave excitation causes increased wave-frequency sway motion, whereas the low-frequency sway motion decreases. The decreased low-frequency sway motions cancel out the increased wave-frequency sway motions for LC 1-3; therefore increased sway motions can only be observed in LC 4-6, in which the increased wave-frequency sway motions are more significant due to the larger

14

significant wave height and wave period. Although the sway motions are present at the 2P frequency, it is negligible compared to the sway motions at the wave frequency and the natural frequency. The maximum values of the sway motions have a similar trend to the standard deviations.

The standard deviation of the roll motions also increases with increasing β_{wave}. Although three components of the roll responses, i.e., at the low frequency, wave frequency and 2P frequency, contribute to the roll motion, the wave-frequency roll motion clearly increases with increasing β_{wave} while the low-frequency roll motion and the roll motion at the 2P frequency only change slightly, and do not depend strongly on the wave direction. The maximum values show a clear trend of increasing with β_{wave}.

The pitch motion, which contributes significantly to the tower bending moment, is most affected by the response at the wave frequency as the wave direction changes. As with the surge motion, the wave-frequency pitch motion decreases with increasing β_{wave} while the low-frequency pitch motion and the pitch motion due to the 2P effect do not depend strongly on the wave direction. Consequently, the pitch motion decreases as β_{wave} increases, but only slightly. The maximum values of the pitch motion show a similar trend to the standard deviations.

The standard deviation of the yaw motion depends primarily on the response at the yaw natural frequency, and the relationship with the wave direction is not obvious. However, larger yaw motions at high wind speeds occurs at β_{wave} = 60 and 90 degrees, whereas larger yaw motions at the 5 m/s wind speed occur at β_{wave} = 30 and 90 degrees. In addition to the wind-induced contribution to the yaw motion, yaw motion can also been observed at the roll frequency and at the wave frequency. The contribution of the wave-frequency response to the yaw motion at a wind speed of 5 m/s is larger than the contribution at high wind speeds because here the wind-induced yaw motion dominates. Therefore, larger yaw motions at β_{wave} = 30 and 90 degrees at the 5 m/s wind speed due to wave-induced yaw motion while larger yaw motions at β_{wave} = 60 and 90 degrees at high wind speeds is due to the wind-induced yaw motion.
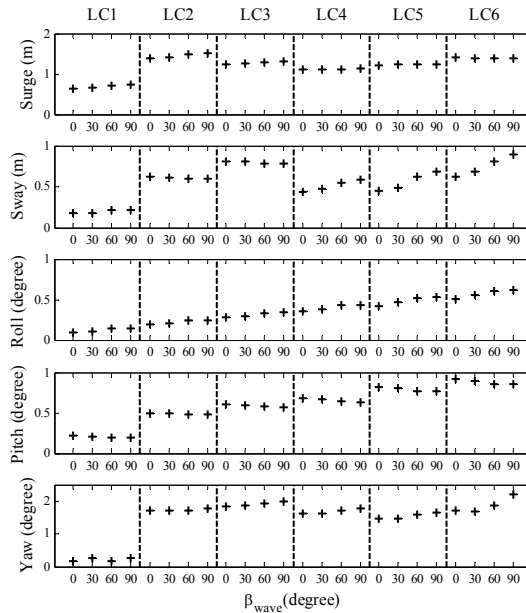
Figure 15. Standard deviations of the platform motion as a function of the wave direction β_{wave} for all load cases.

The mean values of the bending moments and the mooring line tension remain almost the same when changing the wave direction because the mean values are primarily determined by the wind loads, and they are thus not affected by the wave direction. The effect of wind-wave misalignment on the standard deviations of the tower base bending moments and the mooring line tension does not depend strongly on the wave direction, but variation in the standard deviations can nevertheless be observed in Figure 17. Slightly decreased standard deviations of fore-aft bending moment are present for β_{wave} larger than 30 degrees while the standard deviations of side-side bending moment slightly increase for β_{wave} larger than 30 degrees. The response component at the 2P

15

frequency primarily contributes to the bending moments, and the 2P component does not depend on the wave direction; therefore the bending moments are nearly independent of β_{wave}. A similar result is observed for the standard deviations of the mooring line tensions. Larger tension of mooring line 1 is found at β_{wave} = 60 degrees at all wind speeds, but the change in the tension of mooring line 3 is negligible. The largest tension of mooring line 2 is found at β_{wave} = 0 degrees for LC 4-6, but for LC 1-3, larger tension of mooring line 2 is found at β_{wave} = 60 and 90 degrees. The changes in the mooring line tension with β_{wave} are due to the change in the three main frequency components, i.e., the wind-induced response, wave-induced response and 2P response, contributing to the tension of mooring lines.
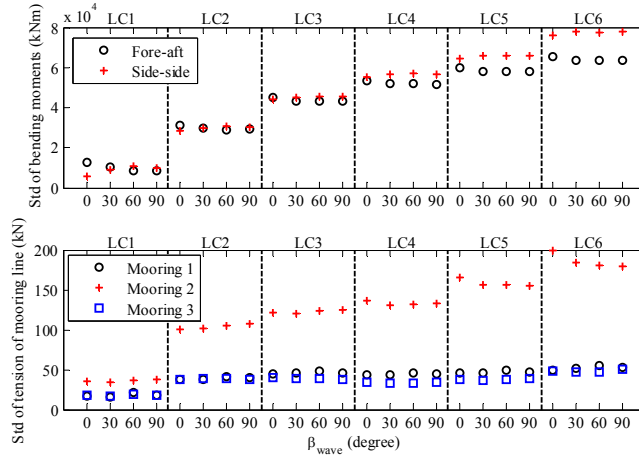
Figure 16. Standard deviations of the tower base bending moments and mooring line tension as a function of the wave direction β_{wave} for all load cases.

5. CONCLUSIONS

A comprehensive investigation of the dynamic response of a FVAWT is performed based on time domain simulations conducted using the Simo-Riflex-DMS coupled solver under different environmental conditions. The focus of the paper is on analyzing the response characteristics of the FVAWT, comparing it to a land-based wind turbine, evaluating the effect of structural flexibility on the dynamic response by comparing a rigid wind turbine and the flexible wind turbine, evaluating the effect of the azimuthal angle in the parked condition and determining the effect of wind-wave misalignment on the dynamic response.

Based on comparisons between the mean values, standard deviations and maximum values of selected response parameters under steady and turbulent wind conditions, the effect of turbulent wind on the global motions and structural responses have been evaluated. The mean values remain almost the same in the steady and turbulent wind conditions, but the standard deviations and the maximum values increase in the turbulent wind conditions. The contributions to the differences in the standard deviations are identified at different frequencies by comparing the power spectra of the selected response, showing that the low-frequency responses are significantly excited by the turbulent wind and that the increase in the low-frequency responses is much greater than the decrease in the 2P response.

The 2P effect on the structural integrity and fatigue damage in the VAWTs is significant. The results shows that the tower base bending moments in the FVAWT at the 2P frequency are found to be much reduced when compared to the tower base bending moments in an equivalent land-based VAWT. This indicates that some of the 2P effects can be alleviated with a floating platform. It should be noted, however, that most land-based VAWTs are supported by a tower with guy cables. Therefore, a further comparison between prototypes of a land-based VAWT and a FVAWT is recommended.

By comparing the global motions and structural response of the FVAWT with the equivalent rigid wind turbine, the differences between the investigated responses have been analyzed to determine the effect of structural flexibility in the FVAWT on the response and loads. The structural flexibility does not significantly

16

affect the mean values of the global motions or the tower base bending moments. However, the standard deviations and maximum values of the responses are found to differ for the flexible wind turbine and the rigid wind turbine. The most evident difference is that much larger standard deviations are observed for the tower base fore-aft bending moment in the flexible wind turbine. This indicates that fatigue calculation should be given some considerations if a rigid model of a FVAWT is used. The responses of the flexible wind turbine and the rigid wind turbine in the frequency domain have also been investigated, and the contributions of the different excitations to the responses at different frequencies have also been analyzed.

The FVAWT has also been investigated in the parked condition with respect to global motions and structural responses as a function of the azimuthal angle of the rotor. It is found that the azimuthal angle at which the responses in the parked condition are minimized occurs when the chords of the blades are aligned with the wind. This is important for the survivability of the FVAWT.

Finally, the effect of wind-wave misalignment on the global motions and structural responses in selected operational conditions has also been investigated. Increased global motions, except for the pitch motions, are observed in the misaligned conditions. The tower base bending moments and the mooring line tension are found not to depend strongly on the wave directions due to the large contribution from the 2P load variation. The effect of the wind-wave misalignment is not significant when compared to the amplitude of the wind loads. Not only do the wind loads dominate the mean motions and structural responses, but the aerodynamic variation also affects the standard deviations of responses significantly. No second order wave drift forces were applied to the semi-submersible in this study. Therefore, including the mean drift and difference-frequency forces in further studies would be expected to increase the effect of wind-wave misalignment on the low-frequency platform responses, and it could also provide additional information for the fatigue calculation of mooring lines.

Acknowledgments

References

1. Karimirad M, Moan T. Wave-and wind-induced dynamic response of a spar-type offshore wind turbine. *Journal of waterway, port, coastal, and ocean engineering* 2012; **138**: 9-20.
2. Kvittem MI, Bachynski EE, Moan T. Effects of Hydrodynamic Modelling in Fully Coupled Simulations of a Semi-submersible Wind Turbine. *Energy Procedia* 2012; **24**: 351-362. DOI: http://dx.doi.org/10.1016/j.egypro.2012.06.118
3. Luan C, Gao Z, Moan T. Modelling and analysis of a semi-submersible wind turbine with a central tower with emphasis on the brace system, *Proceedings of the 32nd International Conference on Ocean, Offshore and Arctic Engineering*, Nantes, France, June, 2013.
4. Bachynski EE, Moan T. Design considerations for tension leg platform wind turbines. *Marine Structures* 2012; **29**: 89-114. DOI: http://dx.doi.org/10.1016/j.marstruc.2012.09.001
5. Kvittem MI, Moan T. Effect of Mooring Line Modelling on Motions and Structural Fatigue Damage for a Semisubmersible Wind Turbine, *Proceedings of the Twenty-second International Offshore and Polar Engineering Conference.*, Rhodes, Greece, 2012.
6. Karimirad M, Moan T. Stochastic dynamic response analysis of a tension leg spar-type offshore wind turbine. *Wind Energy* 2013; **16**: 953-973. DOI: 10.1002/we.1537
7. Jiang Z, Karimirad M, Moan T. Dynamic response analysis of wind turbines under blade pitch system fault, grid loss, and shutdown events. *Wind Energy* 2014; **17**: 1385-1409. DOI: 10.1002/we.1639
8. Kvittem MI, Moan T. Frequency versus time domain fatigue analysis of a semi-submersible wind turbine tower, *ASME 2014 33rd International Conference on Ocean, Offshore and Arctic Engineering*, 2014.
9. Xing Y, Karimirad M, Moan T. Modelling and analysis of floating spar-type wind turbine drivetrain. *Wind Energy* 2014; **17**: 565-587. DOI: 10.1002/we.1590
10. Paulsen US, Pedersen TF, Madsen HA, Enevoldsen K, Nielsen PH, Hattel J, Zanne L, Battisti L, Brighenti A, Lacaze M, Lim V, Heinen JW, Berthelsen PA, Carstensen S, de Ridder EJ, van Bussel G, Tescione G. Deepwind - An innovative wind turbine concept for offshore, *European Wind Energy Association (EWEA) Annual Event*, Brussels, 2011.
11. Vita L, Paulsen US, Pedersen TF. A novel floating offshore wind turbine concept: new developments, *European Wind Energy Conference and Exhibition*, Poland, 2010.

12. Vita L, Paulsen US, Pedersen TF, Madsen HA, Rasmussen F. A novel floating offshore wind turbine concept, *European Wind Energy Conference and Exhibition*, Marseille, France, 16-19 March, 2009.
13. Cahay M, Luquiau E, Smadja C, SILVERT FCC. Use of a Vertical Wind Turbine in an Offshore Floating Wind Farm, *Offshore Technology Conference* Houston, Texas, USA, 2-5 May 2011.
14. 10MW Aerogenerator X © Wind Power Limited & Grimshaw at http://vimeo.com/13654447.
15. Paulsen US, Vita L, Madsen HA, Hattel J, Ritchie E, Leban KM, Berthelsen PA, Carstensen S. 1st DeepWind 5 MW Baseline design. *Energy Procedia* 2012; **24**: 27-35.
16. Robertson A, Jonkman J, Masciola M, Song H, Goupee A, Coulling A, Luan C. Definition of the Semisubmersible Floating System for Phase II of OC4. 2012.
17. Wang K, Moan T, Hansen MOL. A method for modeling of floating vertical axis wind turbine, *Proceedings of the 32nd International Conference on Ocean, Offshore and Arctic Engineering*, Nantes, France, June, 2013.
18. Berthelsen PA, Fylling I, Vita L, Paulsen US. Conceptual Design of a Floating Support Structure and Mooring System for a Vertical Axis Wind Turbine, *Proceedings of the 31st International Conference on Ocean, Offshore and Arctic Engineering*, Rio de Janeiro, Brazil, June, 2012.
19. Paulsen US, Madsen HA, Hattel JH, Baran I, Nielsen PH. Design optimization of a 5 MW floating offshore vertical-axis wind turbine. *Energy Procedia* 2013; **35**: 22-32.
20. Merz KO. A Method for Analysis of VAWT Aerodynamic Loads under Turbulent Wind and Platform Motion. *Energy Procedia* 2012; **24**: 44-51.
21. Collu M, Borg M, Shires A, Brennan FP. FLOVAWT: Progress on the development of a coupled model of dynamics for floating offshore vertical axis wind turbines, *Proceedings of the 32nd International Conference on Ocean, Offshore and Arctic Engineering*, Nantes, France, June, 2013.
22. Borg M, Wang K, Collu M, Moan T. A comparison of two coupled model of dynamics for offshore floating vertical axis wind turbines(VAWT), *Proceedings of the ASME 2014 33nd International Conference on Ocean, Offshore and Arctic Engineering*, San Francisco, California, USA, June, 2014.
23. Fischer T, Rainey P, Bossanyi E, Kühn M. Study on control concepts suitable for mitigation of loads from misaligned wind and waves on offshore wind turbines supported on monopiles. *Wind Engineering* 2011; **35**: 561-574.
24. Kuhn M. Dynamics and design optimization of offshore wind energy conversions systems. 2001, Ph. D. thesis, Delft University of Technology, Civil Engineering and Geosciences.
25. Bachynski EE, Kvittem MI, Luan C, Moan T. Wind-wave misalignment effects on floating wind turbines: motions and tower load effects. *Journal of Offshore Mechanics and Arctic Engineering* 2014; **136**: 12. DOI: 10.1115/1.4028028
26. Barj L, Stewart S, Lackner M, Jonkman J, Robertson A. Wind/wave misalignment in the loads analysis of a floating offshore wind turbine, *AIAA SciTech 2014*, National Harbor, Maryland 13-17 January 2014.
27. Vita L. Offshore Floating Vertical Axis Wind Turbines with Rotating Platform. *Risø-PhD-80(EN)*, National Laboratory for Sustainable Energy, DTU, 2011.
28. Ormberg H, Passano E, Luxcey N. Global analysis of a floating wind turbine using an aero-hydroelastic model. Part 1: Code development and case study, *Offshore Mechanics and Arctic Engineering Conference*, Rotterdam, The Netherlands, 2011.
29. Luxcey N, Ormberg H, Passano E. Global analysis of a floating wind turbine using an aero-hydro-elastic numerical model. Part 2: Benchmark study. *Offshore Mechanics and Arctic Engineering Conference*2011: Rotterdam, The Netherlands.
30. Paraschivoiu I. *Wind turbine design: with emphasis on Darrieus concept*. Polytechnic International Press: Montreal, 2002.
31. Jonkman B. TurbSim user's guide: version 1.50. *Tech. rep. NREL/TP-500-46198.*, National Renewable Energy Laboratory, 2009.
32. Wang K, Hansen MOL, Moan T. Model improvements for evaluating the effect of tower tilting on the aerodynamics of a vertical axis wind turbine. *Wind Energy* 2013. DOI: 10.1002/we.1685
33. Det Norske Veritas. Sesam user manual:Wadam. 2008.
34. Svendsen HG, Merz KO, Endegnanew AG. Control of floating vertical axis wind turbine, *European Wind Energy Conference and Exhibition*, Copenhagen, Denmark, 2012.
35. Merz K, Svendsen H. A control algorithm for the deepwind floating vertical-axis wind turbine. *Journal of Renewable and Sustainable Energy* 2013; **5**: 063136.
36. International Electrotechnical Commission (2009). *IEC61400-3 Wind turbines - Part 3: Design requirement for offshore wind turbines*.
37. Johannessen K, Meling TS, Haver S. Joint distribution for wind and waves in the northern north sea. *International Journal of Offshore and Polar Engineering* 2002; **12**.
38. MARINTEK. SIMO User's Manual. 2011.

Previous PhD theses published at the Department of Marine Technology
(Earlier: Faculty of Marine Technology)
NORWEGIAN UNIVERSITY OF SCIENCE AND TECHNOLOGY

Previous PhD theses published at the Department of Marine Technology
(Earlier: Faculty of Marine Technology)
NORWEGIAN UNIVERSITY OF SCIENCE AND TECHNOLOGY

Report No.	Author	Title
	Kavlie, Dag	Optimization of Plane Elastic Grillages, 1967
	Hansen, Hans R.	Man-Machine Communication and Data-Storage Methods in Ship Structural Design, 1971
	Gisvold, Kaare M.	A Method for non-linear mixed -integer programming and its Application to Design Problems, 1971
	Lund, Sverre	Tanker Frame Optimalization by means of SUMT-Transformation and Behaviour Models, 1971
	Vinje, Tor	On Vibration of Spherical Shells Interacting with Fluid, 1972
	Lorentz, Jan D.	Tank Arrangement for Crude Oil Carriers in Accordance with the new Anti-Pollution Regulations, 1975
	Carlsen, Carl A.	Computer-Aided Design of Tanker Structures, 1975
	Larsen, Carl M.	Static and Dynamic Analysis of Offshore Pipelines during Installation, 1976
UR-79-01	Brigt Hatlestad, MK	The finite element method used in a fatigue evaluation of fixed offshore platforms. (Dr.Ing. Thesis)
UR-79-02	Erik Pettersen, MK	Analysis and design of cellular structures. (Dr.Ing. Thesis)
UR-79-03	Sverre Valsgård, MK	Finite difference and finite element methods applied to nonlinear analysis of plated structures. (Dr.Ing. Thesis)
UR-79-04	Nils T. Nordsve, MK	Finite element collapse analysis of structural members considering imperfections and stresses due to fabrication. (Dr.Ing. Thesis)
UR-79-05	Ivar J. Fylling, MK	Analysis of towline forces in ocean towing systems. (Dr.Ing. Thesis)
UR-80-06	Nils Sandsmark, MM	Analysis of Stationary and Transient Heat Conduction by the Use of the Finite Element Method. (Dr.Ing. Thesis)
UR-80-09	Sverre Haver, MK	Analysis of uncertainties related to the stochastic modeling of ocean waves. (Dr.Ing. Thesis)
UR-81-15	Odland, Jonas	On the Strength of welded Ring stiffened cylindrical Shells primarily subjected to axial Compression
UR-82-17	Engesvik, Knut	Analysis of Uncertainties in the fatigue Capacity of

Welded Joints

UR-82-18	Rye, Henrik	Ocean wave groups
UR-83-30	Eide, Oddvar Inge	On Cumulative Fatigue Damage in Steel Welded Joints
UR-83-33	Mo, Olav	Stochastic Time Domain Analysis of Slender Offshore Structures
UR-83-34	Amdahl, Jørgen	Energy absorption in Ship-platform impacts
UR-84-37	Mørch, Morten	Motions and mooring forces of semi submersibles as determined by full-scale measurements and theoretical analysis
UR-84-38	Soares, C. Guedes	Probabilistic models for load effects in ship structures
UR-84-39	Aarsnes, Jan V.	Current forces on ships
UR-84-40	Czujko, Jerzy	Collapse Analysis of Plates subjected to Biaxial Compression and Lateral Load
UR-85-46	Alf G. Engseth, MK	Finite element collapse analysis of tubular steel offshore structures. (Dr.Ing. Thesis)
UR-86-47	Dengody Sheshappa, MP	A Computer Design Model for Optimizing Fishing Vessel Designs Based on Techno-Economic Analysis. (Dr.Ing. Thesis)
UR-86-48	Vidar Aanesland, MH	A Theoretical and Numerical Study of Ship Wave Resistance. (Dr.Ing. Thesis)
UR-86-49	Heinz-Joachim Wessel, MK	Fracture Mechanics Analysis of Crack Growth in Plate Girders. (Dr.Ing. Thesis)
UR-86-50	Jon Taby, MK	Ultimate and Post-ultimate Strength of Dented Tubular Members. (Dr.Ing. Thesis)
UR-86-51	Walter Lian, MH	A Numerical Study of Two-Dimensional Separated Flow Past Bluff Bodies at Moderate KC-Numbers. (Dr.Ing. Thesis)
UR-86-52	Bjørn Sortland, MH	Force Measurements in Oscillating Flow on Ship Sections and Circular Cylinders in a U-Tube Water Tank. (Dr.Ing. Thesis)
UR-86-53	Kurt Strand, MM	A System Dynamic Approach to One-dimensional Fluid Flow. (Dr.Ing. Thesis)
UR-86-54	Arne Edvin Løken, MH	Three Dimensional Second Order Hydrodynamic Effects on Ocean Structures in Waves. (Dr.Ing. Thesis)
UR-86-55	Sigurd Falch, MH	A Numerical Study of Slamming of Two-Dimensional Bodies. (Dr.Ing. Thesis)
UR-87-56	Arne Braathen, MH	Application of a Vortex Tracking Method to the Prediction of Roll Damping of a Two-Dimension Floating Body. (Dr.Ing. Thesis)

UR-87-57	Bernt Leira, MK	Gaussian Vector Processes for Reliability Analysis involving Wave-Induced Load Effects. (Dr.Ing. Thesis)
UR-87-58	Magnus Småvik, MM	Thermal Load and Process Characteristics in a Two-Stroke Diesel Engine with Thermal Barriers (in Norwegian). (Dr.Ing. Thesis)
MTA-88-59	Bernt Arild Bremdal, MP	An Investigation of Marine Installation Processes – A Knowledge - Based Planning Approach. (Dr.Ing. Thesis)
MTA-88-60	Xu Jun, MK	Non-linear Dynamic Analysis of Space-framed Offshore Structures. (Dr.Ing. Thesis)
MTA-89-61	Gang Miao, MH	Hydrodynamic Forces and Dynamic Responses of Circular Cylinders in Wave Zones. (Dr.Ing. Thesis)
MTA-89-62	Martin Greenhow, MH	Linear and Non-Linear Studies of Waves and Floating Bodies. Part I and Part II. (Dr.Techn. Thesis)
MTA-89-63	Chang Li, MH	Force Coefficients of Spheres and Cubes in Oscillatory Flow with and without Current. (Dr.Ing. Thesis
MTA-89-64	Hu Ying, MP	A Study of Marketing and Design in Development of Marine Transport Systems. (Dr.Ing. Thesis)
MTA-89-65	Arild Jæger, MH	Seakeeping, Dynamic Stability and Performance of a Wedge Shaped Planing Hull. (Dr.Ing. Thesis)
MTA-89-66	Chan Siu Hung, MM	The dynamic characteristics of tilting-pad bearings
MTA-89-67	Kim Wikstrøm, MP	Analysis av projekteringen for ett offshore projekt. (Licenciat-avhandling)
MTA-89-68	Jiao Guoyang, MK	Reliability Analysis of Crack Growth under Random Loading, considering Model Updating. (Dr.Ing. Thesis)
MTA-89-69	Arnt Olufsen, MK	Uncertainty and Reliability Analysis of Fixed Offshore Structures. (Dr.Ing. Thesis)
MTA-89-70	Wu Yu-Lin, MR	System Reliability Analyses of Offshore Structures using improved Truss and Beam Models. (Dr.Ing. Thesis)
MTA-90-71	Jan Roger Hoff, MH	Three-dimensional Green function of a vessel with forward speed in waves. (Dr.Ing. Thesis)
MTA-90-72	Rong Zhao, MH	Slow-Drift Motions of a Moored Two-Dimensional Body in Irregular Waves. (Dr.Ing. Thesis)
MTA-90-73	Atle Minsaas, MP	Economical Risk Analysis. (Dr.Ing. Thesis)
MTA-90-74	Knut-Aril Farnes, MK	Long-term Statistics of Response in Non-linear Marine Structures. (Dr.Ing. Thesis)
MTA-90-75	Torbjørn Sotberg, MK	Application of Reliability Methods for Safety Assessment of Submarine Pipelines. (Dr.Ing.

Thesis)

MTA-90-76	Zeuthen, Steffen, MP	SEAMAID. A computational model of the design process in a constraint-based logic programming environment. An example from the offshore domain. (Dr.Ing. Thesis)
MTA-91-77	Haagensen, Sven, MM	Fuel Dependant Cyclic Variability in a Spark Ignition Engine - An Optical Approach. (Dr.Ing. Thesis)
MTA-91-78	Løland, Geir, MH	Current forces on and flow through fish farms. (Dr.Ing. Thesis)
MTA-91-79	Hoen, Christopher, MK	System Identification of Structures Excited by Stochastic Load Processes. (Dr.Ing. Thesis)
MTA-91-80	Haugen, Stein, MK	Probabilistic Evaluation of Frequency of Collision between Ships and Offshore Platforms. (Dr.Ing. Thesis)
MTA-91-81	Sødahl, Nils, MK	Methods for Design and Analysis of Flexible Risers. (Dr.Ing. Thesis)
MTA-91-82	Ormberg, Harald, MK	Non-linear Response Analysis of Floating Fish Farm Systems. (Dr.Ing. Thesis)
MTA-91-83	Marley, Mark J., MK	Time Variant Reliability under Fatigue Degradation. (Dr.Ing. Thesis)
MTA-91-84	Krokstad, Jørgen R., MH	Second-order Loads in Multidirectional Seas. (Dr.Ing. Thesis)
MTA-91-85	Molteberg, Gunnar A., MM	The Application of System Identification Techniques to Performance Monitoring of Four Stroke Turbocharged Diesel Engines. (Dr.Ing. Thesis)
MTA-92-86	Mørch, Hans Jørgen Bjelke, MH	Aspects of Hydrofoil Design: with Emphasis on Hydrofoil Interaction in Calm Water. (Dr.Ing. Thesis)
MTA-92-87	Chan Siu Hung, MM	Nonlinear Analysis of Rotordynamic Instabilities in Highspeed Turbomachinery. (Dr.Ing. Thesis)
MTA-92-88	Bessason, Bjarni, MK	Assessment of Earthquake Loading and Response of Seismically Isolated Bridges. (Dr.Ing. Thesis)
MTA-92-89	Langli, Geir, MP	Improving Operational Safety through exploitation of Design Knowledge - an investigation of offshore platform safety. (Dr.Ing. Thesis)
MTA-92-90	Sævik, Svein, MK	On Stresses and Fatigue in Flexible Pipes. (Dr.Ing. Thesis)
MTA-92-91	Ask, Tor Ø., MM	Ignition and Flame Growth in Lean Gas-Air Mixtures. An Experimental Study with a Schlieren System. (Dr.Ing. Thesis)
MTA-86-92	Hessen, Gunnar, MK	Fracture Mechanics Analysis of Stiffened Tubular Members. (Dr.Ing. Thesis)

MTA-93-93	Steinebach, Christian, MM	Knowledge Based Systems for Diagnosis of Rotating Machinery. (Dr.Ing. Thesis)
MTA-93-94	Dalane, Jan Inge, MK	System Reliability in Design and Maintenance of Fixed Offshore Structures. (Dr.Ing. Thesis)
MTA-93-95	Steen, Sverre, MH	Cobblestone Effect on SES. (Dr.Ing. Thesis)
MTA-93-96	Karunakaran, Daniel, MK	Nonlinear Dynamic Response and Reliability Analysis of Drag-dominated Offshore Platforms. (Dr.Ing. Thesis)
MTA-93-97	Hagen, Arnulf, MP	The Framework of a Design Process Language. (Dr.Ing. Thesis)
MTA-93-98	Nordrik, Rune, MM	Investigation of Spark Ignition and Autoignition in Methane and Air Using Computational Fluid Dynamics and Chemical Reaction Kinetics. A Numerical Study of Ignition Processes in Internal Combustion Engines. (Dr.Ing. Thesis)
MTA-94-99	Passano, Elizabeth, MK	Efficient Analysis of Nonlinear Slender Marine Structures. (Dr.Ing. Thesis)
MTA-94-100	Kvålsvold, Jan, MH	Hydroelastic Modelling of Wetdeck Slamming on Multihull Vessels. (Dr.Ing. Thesis)
MTA-94-102	Bech, Sidsel M., MK	Experimental and Numerical Determination of Stiffness and Strength of GRP/PVC Sandwich Structures. (Dr.Ing. Thesis)
MTA-95-103	Paulsen, Hallvard, MM	A Study of Transient Jet and Spray using a Schlieren Method and Digital Image Processing. (Dr.Ing. Thesis)
MTA-95-104	Hovde, Geir Olav, MK	Fatigue and Overload Reliability of Offshore Structural Systems, Considering the Effect of Inspection and Repair. (Dr.Ing. Thesis)
MTA-95-105	Wang, Xiaozhi, MK	Reliability Analysis of Production Ships with Emphasis on Load Combination and Ultimate Strength. (Dr.Ing. Thesis)
MTA-95-106	Ulstein, Tore, MH	Nonlinear Effects of a Flexible Stern Seal Bag on Cobblestone Oscillations of an SES. (Dr.Ing. Thesis)
MTA-95-107	Solaas, Frøydis, MH	Analytical and Numerical Studies of Sloshing in Tanks. (Dr.Ing. Thesis)
MTA-95-108	Hellan, Øyvind, MK	Nonlinear Pushover and Cyclic Analyses in Ultimate Limit State Design and Reassessment of Tubular Steel Offshore Structures. (Dr.Ing. Thesis)
MTA-95-109	Hermundstad, Ole A., MK	Theoretical and Experimental Hydroelastic Analysis of High Speed Vessels. (Dr.Ing. Thesis)
MTA-96-110	Bratland, Anne K., MH	Wave-Current Interaction Effects on Large-Volume Bodies in Water of Finite Depth. (Dr.Ing. Thesis)
MTA-96-111	Herfjord, Kjell, MH	A Study of Two-dimensional Separated Flow by a Combination of the Finite Element Method and

Navier-Stokes Equations. (Dr.Ing. Thesis)

MTA-96-112	Æsøy, Vilmar, MM	Hot Surface Assisted Compression Ignition in a Direct Injection Natural Gas Engine. (Dr.Ing. Thesis)
MTA-96-113	Eknes, Monika L., MK	Escalation Scenarios Initiated by Gas Explosions on Offshore Installations. (Dr.Ing. Thesis)
MTA-96-114	Erikstad, Stein O., MP	A Decision Support Model for Preliminary Ship Design. (Dr.Ing. Thesis)
MTA-96-115	Pedersen, Egil, MH	A Nautical Study of Towed Marine Seismic Streamer Cable Configurations. (Dr.Ing. Thesis)
MTA-97-116	Moksnes, Paul O., MM	Modelling Two-Phase Thermo-Fluid Systems Using Bond Graphs. (Dr.Ing. Thesis)
MTA-97-117	Halse, Karl H., MK	On Vortex Shedding and Prediction of Vortex-Induced Vibrations of Circular Cylinders. (Dr.Ing. Thesis)
MTA-97-118	Igland, Ragnar T., MK	Reliability Analysis of Pipelines during Laying, considering Ultimate Strength under Combined Loads. (Dr.Ing. Thesis)
MTA-97-119	Pedersen, Hans-P., MP	Levendefiskteknologi for fiskefartøy. (Dr.Ing. Thesis)
MTA-98-120	Vikestad, Kyrre, MK	Multi-Frequency Response of a Cylinder Subjected to Vortex Shedding and Support Motions. (Dr.Ing. Thesis)
MTA-98-121	Azadi, Mohammad R. E., MK	Analysis of Static and Dynamic Pile-Soil-Jacket Behaviour. (Dr.Ing. Thesis)
MTA-98-122	Ulltang, Terje, MP	A Communication Model for Product Information. (Dr.Ing. Thesis)
MTA-98-123	Torbergsen, Erik, MM	Impeller/Diffuser Interaction Forces in Centrifugal Pumps. (Dr.Ing. Thesis)
MTA-98-124	Hansen, Edmond, MH	A Discrete Element Model to Study Marginal Ice Zone Dynamics and the Behaviour of Vessels Moored in Broken Ice. (Dr.Ing. Thesis)
MTA-98-125	Videiro, Paulo M., MK	Reliability Based Design of Marine Structures. (Dr.Ing. Thesis)
MTA-99-126	Mainçon, Philippe, MK	Fatigue Reliability of Long Welds Application to Titanium Risers. (Dr.Ing. Thesis)
MTA-99-127	Haugen, Elin M., MH	Hydroelastic Analysis of Slamming on Stiffened Plates with Application to Catamaran Wetdecks. (Dr.Ing. Thesis)
MTA-99-128	Langhelle, Nina K., MK	Experimental Validation and Calibration of Nonlinear Finite Element Models for Use in Design of Aluminium Structures Exposed to Fire. (Dr.Ing. Thesis)
MTA-99-	Berstad, Are J., MK	Calculation of Fatigue Damage in Ship Structures.

129		(Dr.Ing. Thesis)
MTA-99-130	Andersen, Trond M., MM	Short Term Maintenance Planning. (Dr.Ing. Thesis)
MTA-99-131	Tveiten, Bård Wathne, MK	Fatigue Assessment of Welded Aluminium Ship Details. (Dr.Ing. Thesis)
MTA-99-132	Søreide, Fredrik, MP	Applications of underwater technology in deep water archaeology. Principles and practice. (Dr.Ing. Thesis)
MTA-99-133	Tønnessen, Rune, MH	A Finite Element Method Applied to Unsteady Viscous Flow Around 2D Blunt Bodies With Sharp Corners. (Dr.Ing. Thesis)
MTA-99-134	Elvekrok, Dag R., MP	Engineering Integration in Field Development Projects in the Norwegian Oil and Gas Industry. The Supplier Management of Norne. (Dr.Ing. Thesis)
MTA-99-135	Fagerholt, Kjetil, MP	Optimeringsbaserte Metoder for Ruteplanlegging innen skipsfart. (Dr.Ing. Thesis)
MTA-99-136	Bysveen, Marie, MM	Visualization in Two Directions on a Dynamic Combustion Rig for Studies of Fuel Quality. (Dr.Ing. Thesis)
MTA-2000-137	Storteig, Eskild, MM	Dynamic characteristics and leakage performance of liquid annular seals in centrifugal pumps. (Dr.Ing. Thesis)
MTA-2000-138	Sagli, Gro, MK	Model uncertainty and simplified estimates of long term extremes of hull girder loads in ships. (Dr.Ing. Thesis)
MTA-2000-139	Tronstad, Harald, MK	Nonlinear analysis and design of cable net structures like fishing gear based on the finite element method. (Dr.Ing. Thesis)
MTA-2000-140	Kroneberg, André, MP	Innovation in shipping by using scenarios. (Dr.Ing. Thesis)
MTA-2000-141	Haslum, Herbjørn Alf, MH	Simplified methods applied to nonlinear motion of spar platforms. (Dr.Ing. Thesis)
MTA-2001-142	Samdal, Ole Johan, MM	Modelling of Degradation Mechanisms and Stressor Interaction on Static Mechanical Equipment Residual Lifetime. (Dr.Ing. Thesis)
MTA-2001-143	Baarholm, Rolf Jarle, MH	Theoretical and experimental studies of wave impact underneath decks of offshore platforms. (Dr.Ing. Thesis)
MTA-2001-144	Wang, Lihua, MK	Probabilistic Analysis of Nonlinear Wave-induced Loads on Ships. (Dr.Ing. Thesis)
MTA-2001-145	Kristensen, Odd H. Holt, MK	Ultimate Capacity of Aluminium Plates under Multiple Loads, Considering HAZ Properties. (Dr.Ing. Thesis)
MTA-2001-146	Greco, Marilena, MH	A Two-Dimensional Study of Green-Water Loading. (Dr.Ing. Thesis)

MTA-2001-147	Heggelund, Svein E., MK	Calculation of Global Design Loads and Load Effects in Large High Speed Catamarans. (Dr.Ing. Thesis)
MTA-2001-148	Babalola, Olusegun T., MK	Fatigue Strength of Titanium Risers – Defect Sensitivity. (Dr.Ing. Thesis)
MTA-2001-149	Mohammed, Abuu K., MK	Nonlinear Shell Finite Elements for Ultimate Strength and Collapse Analysis of Ship Structures. (Dr.Ing. Thesis)
MTA-2002-150	Holmedal, Lars E., MH	Wave-current interactions in the vicinity of the sea bed. (Dr.Ing. Thesis)
MTA-2002-151	Rognebakke, Olav F., MH	Sloshing in rectangular tanks and interaction with ship motions. (Dr.Ing. Thesis)
MTA-2002-152	Lader, Pål Furset, MH	Geometry and Kinematics of Breaking Waves. (Dr.Ing. Thesis)
MTA-2002-153	Yang, Qinzheng, MH	Wash and wave resistance of ships in finite water depth. (Dr.Ing. Thesis)
MTA-2002-154	Melhus, Øyvin, MM	Utilization of VOC in Diesel Engines. Ignition and combustion of VOC released by crude oil tankers. (Dr.Ing. Thesis)
MTA-2002-155	Ronæss, Marit, MH	Wave Induced Motions of Two Ships Advancing on Parallel Course. (Dr.Ing. Thesis)
MTA-2002-156	Økland, Ole D., MK	Numerical and experimental investigation of whipping in twin hull vessels exposed to severe wet deck slamming. (Dr.Ing. Thesis)
MTA-2002-157	Ge, Chunhua, MK	Global Hydroelastic Response of Catamarans due to Wet Deck Slamming. (Dr.Ing. Thesis)
MTA-2002-158	Byklum, Eirik, MK	Nonlinear Shell Finite Elements for Ultimate Strength and Collapse Analysis of Ship Structures. (Dr.Ing. Thesis)
IMT-2003-1	Chen, Haibo, MK	Probabilistic Evaluation of FPSO-Tanker Collision in Tandem Offloading Operation. (Dr.Ing. Thesis)
IMT-2003-2	Skaugset, Kjetil Bjørn, MK	On the Suppression of Vortex Induced Vibrations of Circular Cylinders by Radial Water Jets. (Dr.Ing. Thesis)
IMT-2003-3	Chezhian, Muthu	Three-Dimensional Analysis of Slamming. (Dr.Ing. Thesis)
IMT-2003-4	Buhaug, Øyvind	Deposit Formation on Cylinder Liner Surfaces in Medium Speed Engines. (Dr.Ing. Thesis)
IMT-2003-5	Tregde, Vidar	Aspects of Ship Design: Optimization of Aft Hull with Inverse Geometry Design. (Dr.Ing. Thesis)
IMT-2003-6	Wist, Hanne Therese	Statistical Properties of Successive Ocean Wave Parameters. (Dr.Ing. Thesis)

IMT-2004-7	Ransau, Samuel	Numerical Methods for Flows with Evolving Interfaces. (Dr.Ing. Thesis)
IMT-2004-8	Soma, Torkel	Blue-Chip or Sub-Standard. A data interrogation approach of identity safety characteristics of shipping organization. (Dr.Ing. Thesis)
IMT-2004-9	Ersdal, Svein	An experimental study of hydrodynamic forces on cylinders and cables in near axial flow. (Dr.Ing. Thesis)
IMT-2005-10	Brodtkorb, Per Andreas	The Probability of Occurrence of Dangerous Wave Situations at Sea. (Dr.Ing. Thesis)
IMT-2005-11	Yttervik, Rune	Ocean current variability in relation to offshore engineering. (Dr.Ing. Thesis)
IMT-2005-12	Fredheim, Arne	Current Forces on Net-Structures. (Dr.Ing. Thesis)
IMT-2005-13	Heggernes, Kjetil	Flow around marine structures. (Dr.Ing. Thesis
IMT-2005-14	Fouques, Sebastien	Lagrangian Modelling of Ocean Surface Waves and Synthetic Aperture Radar Wave Measurements. (Dr.Ing. Thesis)
IMT-2006-15	Holm, Håvard	Numerical calculation of viscous free surface flow around marine structures. (Dr.Ing. Thesis)
IMT-2006-16	Bjørheim, Lars G.	Failure Assessment of Long Through Thickness Fatigue Cracks in Ship Hulls. (Dr.Ing. Thesis)
IMT-2006-17	Hansson, Lisbeth	Safety Management for Prevention of Occupational Accidents. (Dr.Ing. Thesis)
IMT-2006-18	Zhu, Xinying	Application of the CIP Method to Strongly Nonlinear Wave-Body Interaction Problems. (Dr.Ing. Thesis)
IMT-2006-19	Reite, Karl Johan	Modelling and Control of Trawl Systems. (Dr.Ing. Thesis)
IMT-2006-20	Smogeli, Øyvind Notland	Control of Marine Propellers. From Normal to Extreme Conditions. (Dr.Ing. Thesis)
IMT-2007-21	Storhaug, Gaute	Experimental Investigation of Wave Induced Vibrations and Their Effect on the Fatigue Loading of Ships. (Dr.Ing. Thesis)
IMT-2007-22	Sun, Hui	A Boundary Element Method Applied to Strongly Nonlinear Wave-Body Interaction Problems. (PhD Thesis, CeSOS)
IMT-2007-23	Rustad, Anne Marthine	Modelling and Control of Top Tensioned Risers. (PhD Thesis, CeSOS)
IMT-2007-24	Johansen, Vegar	Modelling flexible slender system for real-time simulations and control applications
IMT-2007-25	Wroldsen, Anders Sunde	Modelling and control of tensegrity structures. (PhD Thesis, CeSOS)
IMT-	Aronsen, Kristoffer Høye	An experimental investigation of in-line and

2007-26		combined inline and cross flow vortex induced vibrations. (Dr. avhandling, IMT)
IMT-2007-27	Gao, Zhen	Stochastic Response Analysis of Mooring Systems with Emphasis on Frequency-domain Analysis of Fatigue due to Wide-band Response Processes (PhD Thesis, CeSOS)
IMT-2007-28	Thorstensen, Tom Anders	Lifetime Profit Modelling of Ageing Systems Utilizing Information about Technical Condition. (Dr.ing. thesis, IMT)
IMT-2008-29	Berntsen, Per Ivar B.	Structural Reliability Based Position Mooring. (PhD-Thesis, IMT)
IMT-2008-30	Ye, Naiquan	Fatigue Assessment of Aluminium Welded Box-stiffener Joints in Ships (Dr.ing. thesis, IMT)
IMT-2008-31	Radan, Damir	Integrated Control of Marine Electrical Power Systems. (PhD-Thesis, IMT)
IMT-2008-32	Thomassen, Paul	Methods for Dynamic Response Analysis and Fatigue Life Estimation of Floating Fish Cages. (Dr.ing. thesis, IMT)
IMT-2008-33	Pákozdi, Csaba	A Smoothed Particle Hydrodynamics Study of Two-dimensional Nonlinear Sloshing in Rectangular Tanks. (Dr.ing.thesis, IMT/ CeSOS)
IMT-2007-34	Grytøyr, Guttorm	A Higher-Order Boundary Element Method and Applications to Marine Hydrodynamics. (Dr.ing.thesis, IMT)
IMT-2008-35	Drummen, Ingo	Experimental and Numerical Investigation of Nonlinear Wave-Induced Load Effects in Containerships considering Hydroelasticity. (PhD thesis, CeSOS)
IMT-2008-36	Skejic, Renato	Maneuvering and Seakeeping of a Singel Ship and of Two Ships in Interaction. (PhD-Thesis, CeSOS)
IMT-2008-37	Harlem, Alf	An Age-Based Replacement Model for Repairable Systems with Attention to High-Speed Marine Diesel Engines. (PhD-Thesis, IMT)
IMT-2008-38	Alsos, Hagbart S.	Ship Grounding. Analysis of Ductile Fracture, Bottom Damage and Hull Girder Response. (PhD-thesis, IMT)
IMT-2008-39	Graczyk, Mateusz	Experimental Investigation of Sloshing Loading and Load Effects in Membrane LNG Tanks Subjected to Random Excitation. (PhD-thesis, CeSOS)
IMT-2008-40	Taghipour, Reza	Efficient Prediction of Dynamic Response for Flexible amd Multi-body Marine Structures. (PhD-thesis, CeSOS)
IMT-2008-41	Ruth, Eivind	Propulsion control and thrust allocation on marine vessels. (PhD thesis, CeSOS)
IMT-2008-42	Nystad, Bent Helge	Technical Condition Indexes and Remaining Useful Life of Aggregated Systems. PhD thesis, IMT

IMT- 2008-43	Soni, Prashant Kumar	Hydrodynamic Coefficients for Vortex Induced Vibrations of Flexible Beams, PhD thesis, CeSOS
IMT- 2009-43	Amlashi, Hadi K.K.	Ultimate Strength and Reliability-based Design of Ship Hulls with Emphasis on Combined Global and Local Loads. PhD Thesis, IMT
IMT- 2009-44	Pedersen, Tom Arne	Bond Graph Modelling of Marine Power Systems. PhD Thesis, IMT
IMT- 2009-45	Kristiansen, Trygve	Two-Dimensional Numerical and Experimental Studies of Piston-Mode Resonance. PhD-Thesis, CeSOS
IMT- 2009-46	Ong, Muk Chen	Applications of a Standard High Reynolds Number Model and a Stochastic Scour Prediction Model for Marine Structures. PhD-thesis, IMT
IMT- 2009-47	Hong, Lin	Simplified Analysis and Design of Ships subjected to Collision and Grounding. PhD-thesis, IMT
IMT- 2009-48	Koushan, Kamran	Vortex Induced Vibrations of Free Span Pipelines, PhD thesis, IMT
IMT- 2009-49	Korsvik, Jarl Eirik	Heuristic Methods for Ship Routing and Scheduling. PhD-thesis, IMT
IMT- 2009-50	Lee, Jihoon	Experimental Investigation and Numerical in Analyzing the Ocean Current Displacement of Longlines. Ph.d.-Thesis, IMT.
IMT- 2009-51	Vestbøstad, Tone Gran	A Numerical Study of Wave-in-Deck Impact usin a Two-Dimensional Constrained Interpolation Profile Method, Ph.d.thesis, CeSOS.
IMT- 2009-52	Bruun, Kristine	Bond Graph Modelling of Fuel Cells for Marine Power Plants. Ph.d.-thesis, IMT
IMT 2009-53	Holstad, Anders	Numerical Investigation of Turbulence in a Sekwed Three-Dimensional Channel Flow, Ph.d.-thesis, IMT.
IMT 2009-54	Ayala-Uraga, Efren	Reliability-Based Assessment of Deteriorating Ship-shaped Offshore Structures, Ph.d.-thesis, IMT
IMT 2009-55	Kong, Xiangjun	A Numerical Study of a Damaged Ship in Beam Sea Waves. Ph.d.-thesis, IMT/CeSOS.
IMT 2010-56	Kristiansen, David	Wave Induced Effects on Floaters of Aquaculture Plants, Ph.d.-thesis, CeSOS.
IMT 2010-57	Ludvigsen, Martin	An ROV-Toolbox for Optical and Acoustic Scientific Seabed Investigation. Ph.d.-thesis IMT.
IMT 2010-58	Hals, Jørgen	Modelling and Phase Control of Wave-Energy Converters. Ph.d.thesis, CeSOS.
IMT 2010- 59	Shu, Zhi	Uncertainty Assessment of Wave Loads and Ultimate Strength of Tankers and Bulk Carriers in a

IMT 2010-60	Shao, Yanlin	Reliability Framework. Ph.d. Thesis, IMT/ CeSOS Numerical Potential-Flow Studies on Weakly-Nonlinear Wave-Body Interactions with/without Small Forward Speed, Ph.d.thesis,CeSOS.
IMT 2010-61	Califano, Andrea	Dynamic Loads on Marine Propellers due to Intermittent Ventilation. Ph.d.thesis, IMT.
IMT 2010-62	El Khoury, George	Numerical Simulations of Massively Separated Turbulent Flows, Ph.d.-thesis, IMT
IMT 2010-63	Seim, Knut Sponheim	Mixing Process in Dense Overflows with Emphasis on the Faroe Bank Channel Overflow. Ph.d.thesis, IMT
IMT 2010-64	Jia, Huirong	Structural Analysis of Intect and Damaged Ships in a Collission Risk Analysis Perspective. Ph.d.thesis CeSoS.
IMT 2010-65	Jiao, Linlin	Wave-Induced Effects on a Pontoon-type Very Large Floating Structures (VLFS). Ph.D.-thesis, CeSOS.
IMT 2010-66	Abrahamsen, Bjørn Christian	Sloshing Induced Tank Roof with Entrapped Air Pocket. Ph.d.thesis, CeSOS.
IMT 2011-67	Karimirad, Madjid	Stochastic Dynamic Response Analysis of Spar-Type Wind Turbines with Catenary or Taut Mooring Systems. Ph.d.-thesis, CeSOS.
IMT - 2011-68	Erlend Meland	Condition Monitoring of Safety Critical Valves. Ph.d.-thesis, IMT.
IMT – 2011-69	Yang, Limin	Stochastic Dynamic System Analysis of Wave Energy Converter with Hydraulic Power Take-Off, with Particular Reference to Wear Damage Analysis, Ph.d. Thesis, CeSOS.
IMT – 2011-70	Visscher, Jan	Application of Particla Image Velocimetry on Turbulent Marine Flows, Ph.d.Thesis, IMT.
IMT – 2011-71	Su, Biao	Numerical Predictions of Global and Local Ice Loads on Ships. Ph.d.Thesis, CeSOS.
IMT – 2011-72	Liu, Zhenhui	Analytical and Numerical Analysis of Iceberg Collision with Ship Structures. Ph.d.Thesis, IMT.
IMT – 2011-73	Aarsæther, Karl Gunnar	Modeling and Analysis of Ship Traffic by Observation and Numerical Simulation. Ph.d.Thesis, IMT.
Imt – 2011-74	Wu, Jie	Hydrodynamic Force Identification from Stochastic Vortex Induced Vibration Experiments with Slender Beams. Ph.d.Thesis, IMT.
Imt – 2011-75	Amini, Hamid	Azimuth Propulsors in Off-design Conditions. Ph.d.Thesis, IMT.
IMT – 2011-76	Nguyen, Tan-Hoi	Toward a System of Real-Time Prediction and Monitoring of Bottom Damage Conditions During

Ship Grounding. Ph.d.thesis, IMT.

IMT-2011-77	Tavakoli, Mohammad T.	Assessment of Oil Spill in Ship Collision and Grounding, Ph.d.thesis, IMT.
IMT-2011-78	Guo, Bingjie	Numerical and Experimental Investigation of Added Resistance in Waves. Ph.d.Thesis, IMT.
IMT-2011-79	Chen, Qiaofeng	Ultimate Strength of Aluminium Panels, considering HAZ Effects, IMT
IMT-2012-80	Kota, Ravikiran S.	Wave Loads on Decks of Offshore Structures in Random Seas, CeSOS.
IMT-2012-81	Sten, Ronny	Dynamic Simulation of Deep Water Drilling Risers with Heave Compensating System, IMT.
IMT-2012-82	Berle, Øyvind	Risk and resilience in global maritime supply chains, IMT.
IMT-2012-83	Fang, Shaoji	Fault Tolerant Position Mooring Control Based on Structural Reliability, CeSOS.
IMT-2012-84	You, Jikun	Numerical studies on wave forces and moored ship motions in intermediate and shallow water, CeSOS.
IMT-2012-85	Xiang ,Xu	Maneuvering of two interacting ships in waves, CeSOS
IMT-2012-86	Dong, Wenbin	Time-domain fatigue response and reliability analysis of offshore wind turbines with emphasis on welded tubular joints and gear components, CeSOS
IMT-2012-87	Zhu, Suji	Investigation of Wave-Induced Nonlinear Load Effects in Open Ships considering Hull Girder Vibrations in Bending and Torsion, CeSOS
IMT-2012-88	Zhou, Li	Numerical and Experimental Investigation of Station-keeping in Level Ice, CeSOS
IMT-2012-90	Ushakov, Sergey	Particulate matter emission characteristics from diesel enignes operating on conventional and alternative marine fuels, IMT
IMT-2013-1	Yin, Decao	Experimental and Numerical Analysis of Combined In-line and Cross-flow Vortex Induced Vibrations, CeSOS
IMT-2013-2	Kurniawan, Adi	Modelling and geometry optimisation of wave energy converters, CeSOS
IMT-2013-3	Al Ryati, Nabil	Technical condition indexes doe auxiliary marine diesel engines, IMT
IMT-2013-4	Firoozkoohi, Reza	Experimental, numerical and analytical investigation of the effect of screens on sloshing, CeSOS
IMT-2013-5	Ommani, Babak	Potential-Flow Predictions of a Semi-Displacement Vessel Including Applications to Calm Water Broaching, CeSOS

IMT-2013-6	Xing, Yihan	Modelling and analysis of the gearbox in a floating spar-type wind turbine, CeSOS
IMT-7-2013	Balland, Océane	Optimization models for reducing air emissions from ships, IMT
IMT-8-2013	Yang, Dan	Transitional wake flow behind an inclined flat plate-----Computation and analysis, IMT
IMT-9-2013	Abdillah, Suyuthi	Prediction of Extreme Loads and Fatigue Damage for a Ship Hull due to Ice Action, IMT
IMT-10-2013	Ramìrez, Pedro Agustìn Pèrez	Ageing management and life extension of technical systems- Concepts and methods applied to oil and gas facilities, IMT
IMT-11-2013	Chuang, Zhenju	Experimental and Numerical Investigation of Speed Loss due to Seakeeping and Maneuvering. IMT
IMT-12-2013	Etemaddar, Mahmoud	Load and Response Analysis of Wind Turbines under Atmospheric Icing and Controller System Faults with Emphasis on Spar Type Floating Wind Turbines, IMT
IMT-13-2013	Lindstad, Haakon	Strategies and measures for reducing maritime CO2 emissons, IMT
IMT-14-2013	Haris, Sabril	Damage interaction analysis of ship collisions, IMT
IMT-15-2013	Shainee, Mohamed	Conceptual Design, Numerical and Experimental Investigation of a SPM Cage Concept for Offshore Mariculture, IMT
IMT-16-2013	Gansel, Lars	Flow past porous cylinders and effects of biofouling and fish behavior on the flow in and around Atlantic salmon net cages, IMT
IMT-17-2013	Gaspar, Henrique	Handling Aspects of Complexity in Conceptual Ship Design, IMT
IMT-18-2013	Thys, Maxime	Theoretical and Experimental Investigation of a Free Running Fishing Vessel at Small Frequency of Encounter, CeSOS
IMT-19-2013	Aglen, Ida	VIV in Free Spanning Pipelines, CeSOS
IMT-1-2014	Song, An	Theoretical and experimental studies of wave diffraction and radiation loads on a horizontally submerged perforated plate, CeSOS
IMT-2-2014	Rogne, Øyvind Ygre	Numerical and Experimental Investigation of a Hinged 5-body Wave Energy Converter, CeSOS
IMT-3-2014	Dai, Lijuan	Safe and efficient operation and maintenance of offshore wind farms ,IMT
IMT-4-2014	Bachynski, Erin Elizabeth	Design and Dynamic Analysis of Tension Leg Platform Wind Turbines, CeSOS
IMT-5-2014	Wang, Jingbo	Water Entry of Freefall Wedged – Wedge motions

and Cavity Dynamics, CeSOS

IMT-6-2014	Kim, Ekaterina	Experimental and numerical studies related to the coupled behavior of ice mass and steel structures during accidental collisions, IMT
IMT-7-2014	Tan, Xiang	Numerical investigation of ship's continuous- mode icebreaking in leverl ice, CeSOS
IMT-8-2014	Muliawan, Made Jaya	Design and Analysis of Combined Floating Wave and Wind Power Facilities, with Emphasis on Extreme Load Effects of the Mooring System, CeSOS
IMT-9-2014	Jiang, Zhiyu	Long-term response analysis of wind turbines with an emphasis on fault and shutdown conditions, IMT
IMT-10-2014	Dukan, Fredrik	ROV Motion Control Systems, IMT
IMT-11-2014	Grimsmo, Nils I.	Dynamic simulations of hydraulic cylinder for heave compensation of deep water drilling risers, IMT
IMT-12-2014	Kvittem, Marit I.	Modelling and response analysis for fatigue design of a semisubmersible wind turbine, CeSOS
IMT-13-2014	Akhtar, Juned	The Effects of Human Fatigue on Risk at Sea, IMT
IMT-14-2014	Syahroni, Nur	Fatigue Assessment of Welded Joints Taking into Account Effects of Residual Stress, IMT
IMT-1-2015	Bøckmann, Eirik	Wave Propulsion of ships, IMT
IMT-2-2015	Wang, Kai	Modelling and dynamic analysis of a semi-submersible floating vertical axis wind turbine, CeSOS